# TOPOLOGY OPTIMIZATION CONSIDERING CONSTRUCTABILITY OF TRUSS STRUCTURES AND MANUFACTURABILITY OF COMPOSITE COMPONENTS

by

Saranthip Koh

A dissertation submitted to The Johns Hopkins University in conformity with the requirements for the degree of Doctor of Philosophy.

Baltimore, Maryland

August, 2017

# Abstract

Topology optimization is a mathematical process that systematically searches for the 'best possible' solution to a specific engineering design problem. In discrete domains (such as truss or frame structures), topology optimization is used to determine optimal layout of structural members, while in continuum domains it is used to determine optimal material distribution. Due to its free-form and systematic nature, topology optimization has become a powerful computational tool in engineering design that is capable of discovering solutions that are both innovative and high performance.

Despite its potential capabilities, topology optimization has a tendency to produce structural solutions that are 'suboptimal' when considering constructability and manufacturability of solutions. This dissertation aims to address this fundamental challenge by proposing new topology optimization design methods and algorithms that consider constructability and manufacturability in the design of structures.

When optimizing structural layout in discrete design domains, topology optimization has a tendency to design structures that are topologically complex, which drives

ABSTRACT

construction costs significantly higher, potentially overtaking cost savings from reduced material usage and enhanced system performance. This dissertation examines opportunities to incorporate constructability metrics directly into the topology optimization of structures, such that the designer gains control and may explore potential constructability-performance tradeoffs. In particular, several new algorithms are proposed that incorporate cost metrics associated with section selection, including maximum member sizes, section repeatability, and connection complexity.

In continuum design domains, topology optimization is traditionally employed with an underlying assumption that structures have a continuous distribution and connectivity of material phases. Many engineering components and materials, however, gain strength and functionality through strategic placement of reinforcing objects. Often these objects are selected 'off-the-shelf' and thus come in fixed size and shapes, and are not permitted to overlap due to physical geometry or functionality requirements. This dissertation investigates the use of Discrete Object Projection (DOP) for optimizing the distribution of reinforcing objects within a structure and extends the DOP approach to simultaneously optimize the component topology. The approach is then tailored to the properties of a novel 3D printer developed at NASA capable of printing polymer selectively reinforced with carbon nanotube yarn.

Primary Reader: Dr. James K. Guest (Advisor)

Secondary Readers: Dr. Benjamin W. Schafer, Dr. Kristopher E. Wise

# Acknowledgements

I would like to express my deepest gratitude to my advisor, Dr. James K. Guest, for his support, enthusiasm, encouragement, and patience throughout the course of my graduate study. He is a great mentor who truly cares about and believes in his students, and his guidance has helped me towards realizing my potential.

I would also like to give my sincere thanks to Dr. Benjamin W. Schafer and Dr. Kristopher E. Wise for their valuable advice and insightful review of my dissertation.

I would also like to give a special thanks to Dr. Emilie J. Siochi, Dr. Kristopher E. Wise, and the rest of the 3DP/CNTs team at NASA LaRC Advanced Materials and Processing Branch for their generosity and hospitality during and after my visit and for the knowledge they shared with me.

I would like to acknowledge that this research was financially supported by Hoomes Rich Fellowship, the National Science Foundation's Modeling Complex System Integrative Graduate Education and Research Traineeship (NSF MSC IGERT), and the National Aeronautics and Space Administration (NASA) under Cooperative Agreement NNX16AC45A. This support is gratefully acknowledged.

ACKNOWLEDGEMENTS

I would also like to give special thanks to my TOPOPT family for their support, and to the rest of the faculty, staff, and friends in the Civil Engineering Department.

I am also grateful for my parents, my grandmother, my aunts and uncle, my in-laws, my siblings, and my cousins for their love, encouragement, and support. I would like to especially thank my parents for always believing in me.

Last but not least, I am most grateful to my beloved husband, Teng, for his immense patience, unwavering support, and unconditional love without whom I would not have reached this milestone.

# Dedication

To my incredible husband, Teng, and my wonderful family.

# Contents

# List of Tables

# List of Figures

# Chapter 1

# Introduction

Since the development of the first finite element based methods for generating optimal topologies in the work of Bendsøe and Kikuchi (1988), topology optimization is arising as a powerful tool for designing structures with extreme levels of structural efficiency. As a systematic and computationally driven approach, topology optimization seeks the 'best possible' design solution that satisfies structural requirements and criteria without trial and error or any prior knowledge of the solutions. Known for its ability to discover novel and high performance solutions to engineering design problems governed by a variety of physics, topology optimization has become increasingly popular in research and application in both academia and industry.

In mathematics, optimization is a mathematical process that seeks the best solutions from all possible solutions. A general optimization problem is formulated as:

$$\min_{\boldsymbol{x}} \ f(\mathbf{x}) \tag{1.1a}$$

$$\text{s.t.} \ \ h_i(\mathbf{x}) = 0 \qquad for \ \ i = 1, \ldots, N_{ec} \tag{1.1b}$$

$$g_j(\mathbf{x}) \leq 0 \qquad for \ \ i = 1, \ldots, N_{ic} \tag{1.1c}$$

where $f(\mathbf{x})$ is the objective function, $\mathbf{x}$ is a vector of independent design variables, $h_i(\mathbf{x})$ is the equality constraint, $g_j(\mathbf{x})$ is the inequality constraint, $x_{min}$ and $x_{max}$ are design variable upper and lower bounds, respectively, $N_{ec}$ is the number of equality constraints, $N_{ic}$ is the number of inequality constraints, and $e$ is the number of design variables. The constraints in Eqs. (1.1b)-(1.1c) together form a region which feasible solutions exist. While this general form of optimization is posed as a minimization problem, it can be turned into a maximization problem by simply taking negative of the objective function. In engineering, topology optimization is a mathematical process that optimizes structural layout and material distribution by identify the locations that material resource should exists within a design domain. This process can thus be formulated as an optimization problem with a specific objective and a given set of constraints.

The minimum compliance (maximize stiffness) problem is often used to benchmark topology optimization design problems due to its simplicity and relative importance of stiffness in design. In this problem, material volume is treated as a constraint and the internal strain energy is minimized. For building structures, minimizing

structural response at a location of interest is also a common optimization problem. Equivalently, this problem can be formulated as minimization of total material volume for a given displacement constraint. In conventional topology optimization (Bendsøe and Kikuchi, 1988), finite element method is used to evaluate structural performance. This generally involves discretization of design domain ($\Omega$) into either continuum finite elements or discrete members such as truss or frame elements, represented by $\rho^e$ for each element $e$. Traditionally, optimization problem is formulated as two material phase design problem, where one material phase represents a structural element (e.g. solid, truss, or frame element) and the other represents a void material (i.e. no material).

For minimum compliance problem or minimum displacement, the optimization formulation is expressed as:

$$\min_{\boldsymbol{\rho}} \quad f = \mathbf{L}^{\mathrm{T}}\mathbf{d} \tag{1.2a}$$

$$\text{s.t.} \quad \mathbf{K}(\boldsymbol{\rho})\mathbf{d} = \mathbf{F} \tag{1.2b}$$

$$\sum_{\forall e \in \Omega} \rho^e v^e \leq V \tag{1.2c}$$

$$0 < \rho_{min} \leq \rho^e \leq \rho_{max} \quad \forall i \in \Omega \tag{1.2d}$$

where $\boldsymbol{\rho}$ is design variable vector, $f$ is the objective function, $\mathbf{F}$ is a vector of nodal applied loads, $\mathbf{d}$ is a vector of the nodal displacements, $\mathbf{K}(\boldsymbol{\rho})$ is the global stiffness matrix, $V$ is the maximum allowable volume of the material in the structure, and $\rho_{min}$

and $\rho_{max}$ are the design variable bounds. In the case of minimum displacement, $\mathbf{L}$ is a unit vector that extracts displacement at the location of interest. For minimum compliance problem, we can simply set $\mathbf{L} = \mathbf{F}$. In this case, static equilibrium $\mathbf{K}(\boldsymbol{\rho})\mathbf{d} - \mathbf{F} = 0$ representing the governing mechanics is the equality constraints, and the volume constraint $\sum_{\forall e \in \Omega} \rho^e v^e - V \leq 0$ is the inequality constraints. In this problem, the the design variable lower bound $\rho_{min}$ must be a small positive number to maintain the positive definiteness of the global stiffness matrix $\mathbf{K}(\boldsymbol{\rho})$. For discrete structures (such as trusses and frames), $\rho^e$ and $v^e$ is cross-sectional area and the length of element, respectively. For continuum structure, $\rho^e$ and $v^e$ correspond to elemental volume fraction and volume of element $e$, respectively

As mentioned, minimum compliance problem can be equivalently formulated as minimum volume problem, which can be expressed as:

$$\min_{\boldsymbol{\rho}} \; V(\boldsymbol{\rho}) = \sum_{\forall e \in \Omega} \rho^e v^e \tag{1.3a}$$

$$\text{s.t.} \;\; \mathbf{K}(\boldsymbol{\rho})\mathbf{d} = \mathbf{f} \tag{1.3b}$$

$$d_i(\boldsymbol{\rho}) = {\mathbf{L}_i}^{\mathrm{T}}\mathbf{d} \leq d_{i,allow} \qquad for \;\; i = 1, \ldots, N \tag{1.3c}$$

$$\rho_{min} \leq \rho^e \leq \rho_{max} \quad \forall e \in \Omega \tag{1.3d}$$

In this case, $d_i$ is the nodal deflection for $i^{th}$ constraint, $\mathbf{L}_i$ is a unit vector that extracts displacement for $i^{th}$ constraint, $d_{i,allow}$ is the maximum allowable nodal deflection for $i^{th}$ constraint, and $N$ is the number of displacement constraints.

Even though the concept of topology optimization is straightforward, the use of finite element combined with the free-form nature of topology optimization often leads to a number of well-known challenges when solving these problems. In topology optimization of discrete structures, the ground structure approach is typically implemented (Achtziger, 1997; Bendsøe and Sigmund, 2003; Dorn et al., 1964), in which the design domain is discretized into a dense mesh of elements connecting (for example) every possible pair of nodes. The optimized topology (connectivity) is obtained by removing inefficient elements from the design domain. In order to keep the optimization as open as possible, the initial ground structure is typically defined as complex. As a result, using the ground structure approach for discrete structures, may lead to highly complex design solutions.

Topology optimization of continuum structures faces similar issues of complexity and mesh depencency. One of the most well-known issues is that the optimized solutions may contain regions of alternating solid and void elements arranged in checkerboard-like fashion caused by discretization error which overestimates the stiffness of two solid element connecting only at the corner (Bendsøe et al., 1993; Díaz and Sigmund, 1995; Jog and Haber, 1996). The solutions are also highly dependent on the density of the mesh. This is because the length scale of members is defined at the resolution of finite element (i.e. pixel for 2D and voxel for 3D). As the mesh becomes more refined, more smaller holes are introduced into the final design to improve stiffness (Sigmund and Petersson, 1998) and the members can become as thin

as the size of the finite element leading to solutions with high complexity.

As a consequence, the approach has a tendency to produce structurally efficient but complex solutions. These solutions may be impossible to construct or manufacture economically and efficiently, and may therefore require significant post-processing or re-designing to achieve workable solutions. These topology-optimized solutions are thus considered suboptimal considering real world conditions. This dissertation aims to address the challenges that arise when considering real-world operating conditions.

Over the past two decades, a significant amount of research has been conducted on improving design solutions for continuum structures. A notable progress has been made to combat these issues by considering manufacturability and constructability of design solutions mainly through geometric restriction of the design space. Examples of these works include, but not limited to, placing a upperbound costraint on the total perimeter of the structure (Ambrosio and Buttazzo, 1993; Haber et al., 1996), adding a constraint on minimum length scale of members to the optimization formulation (Poulsen, 2003), constraining minimum allowable feature sizes (Guest, 2009a; Guest et al., 2004; Sigmund, 2007) and maximum allowable feature sizes (Carstensen and Guest, 2014; Guest, 2009b), restricting the number of repeating pattern in the conceptual design of buildings (Stromberg et al., 2011), and restricting the design space to solutions that can be manufactured via multi-axis machining (Guest and Zhu, 2012), casting (Gersborg and Andreasen, 2011; Strömberg, 2010), Polyjet 3D printing (Gaynor et al., 2014), scaffoldless metal and polymer 3D printing (Gaynor and

Guest, 2016). The idea is that designers have ability to control design complexity and constructability by tailoring optimization algorithm out of manufacturing primitives.

On the contrary, significantly less work has been conducted concerning complexity and its relation to constructability in the topology optimization of truss and frame structures. A notable progress includes the works of Gaynor et al. (2013) and Yang et al. (2015b) in the topology optimization of 2D and 3D strut and tie models, respectively, for reinforced concrete design. In their work, a hybrid truss-continuum finite element mesh and bi-linear constitutive law was employed to ensure that the designed rebars resemble realistic straight steel bars. This methodology was later extended in Yang et al. (2015a) using an idea from Asadpoure et al. (2015) to reduce complexity and increase constructability of reinforced concrete by assigning lower construction cost to rebars that are easier to place than rebars that require more complicated placement. In the work of Asadpoure et al. (2015), both material cost and fabrication cost are combined to account for the cost of placing each member in the structure. The work shows that complexity can be reduced by adding a linear function relating cost to the number of elements in the structure.

Motivated by the ideas of Asadpoure et al. (2015), the first part of this dissertation highlights several constructability issues in topology-optimized solutions and its potential relation to construction cost, within the optimization formulation. This work will focus on three particular issues relating to design complexity and member sizes and propose several new algorithms that incorporate constructability metrics

directly into the topology optimization formulations. This gives designers an ability to explore potential tradeoffs between structural constructability and performance. The details of this part are presented in Chapter 2.

As discussed above, a significant amount of research has been conducted to incorporate manufacturability into topology optimization of continuum structures. Some of these includes designing directly for a specific manufacturing processes (see e.g. (Gaynor and Guest, 2016; Gaynor et al., 2014; Gersborg and Andreasen, 2011; Guest and Zhu, 2012; Strömberg, 2010)). All of these past work, however, has focused on single-component structures or structure that are monolithic in nature. This is because traditional topology optimization (Bendsøe, 1989; Bendsøe and Kikuchi, 1988) is employed with an underlying assumption that structures have a continuous distribution and connectivity of material phases throughout the given domain (i.e. monolithic design). This underlying assumption essentially allows the material features to take any arbitrary shape. Many engineering materials and components are, however, composite in nature. Such structures may be manufactured by emdedding pre-fabricated objects inside a monolithic material, such as particles- or fiber-reinforced composites and steel-reinforced concrete beams. These objects are not permitted to overlap or varied in size and shape. Topology optimization applied in a traditional manner cannot be used to solve such design problems.

Significantly less work has been conducted on design of multicomponent structures with embedded discrete objects using topology optimization. Some of these include

the already mentioned topology optimization of strut and tie models for reinforced concrete design (Gaynor et al., 2013; Yang et al., 2015a,b). In this case, discrete truss elements are embedded into continuum mesh and the topology of both types of elements are optimized simultaneously. Kato and Ramm (2010) proposed a material shape optimization to enhance the ductility of fiber-reinforced concrete with respect to fiber locations and orientations. In this method, the thickness and number of fibers are pre-fixed, and the fiber geometry is approximated using Bézier-splines, which permits the movement of fibers and the curvature of the fibers. This work is later extended by Kato and Ramm (2013) to allow for variation of fiber thickness. Qian and Ananthasuresh (2004) and Zhu et al. (2008) proposed methods that simultaneously optimize the locations and orientations of rigid objects and the connecting structures. In the former study, a peak function material interpolation scheme is use to approximate the geometry of embedded objects to overcome the discontinuity of material variation along the edges of the embeded objects as these object moves inside the domain (Qian and Ananthasuresh, 2004). In the latter study, an embbeded mesh is created on top of the basic mesh in which the finite element is remeshed to resemble the shape of the object as the object changes locations Zhu et al. (2008). In both of these works, the number of rigid objects are defined *a priori* and the overlapping of these objects are prevented by imposing additional constraints associated with each of the embedded objects.

Most recently, Guest (2011, 2015) introduced Discrete Object Projection (DOP)

method for optimizing the layout of discrete objects within a structure. In this method, objects of fixed shape and size are projected onto a monolithic material and are allowed to appear (or disappear) and move freely inside the design domain. Since this is a projection-based method, the length scales of embedded objects and minimum spacing between objects are naturally achieved through projection functions without any additional constraints. The approach was also extended to allow for the shape and size of the object to also be optimized (Guest and Ha, 2014), including selection among a set of objects (Guest, 2014). To date, however, the DOP approach applies topology optimization to only two phases: either two materials or one material and a void.

The second part of this dissertation proposes the extension of this idea to multi-material design where the topology of the components is also optimized. Chapter 3 will highlight the motivation of this work, which includes recent development in material and manufacturing technologies, discuss prior research on topology optimization of embedded objects, and outline the method for the simultaneous optimization of component topology and object layout within that topology. This chapter will also present the extension of the proposed methodology to multiple object types including discrete continuous fiber-like objects.

# Chapter 2

# Topology Optimization of Truss Structures Considering Constructability

This chapter addresses the issue of constructability in topology optimization of truss structures including connection complexity, use of non-standard sized members, and existence of many different section sizes, and proposes several new algorithms in relations to construction cost to improve topology-optimized solutions in this regards.

# 2.1 Topology Optimization of Truss Structures Considering Constructability Cost Metrics

## 2.1.1 Introduction

Topology optimization of discrete structures has been studied and used extensively in literature. For discrete structures, such as trusses and frames, the ground structure approach is typically implemented (Achtziger, 1997; Bendsøe and Sigmund, 2003; Dorn et al., 1964), in which optimization algorithm starts with a dense ground structure mesh, and as the optimization progresses, the inefficient elements are removed from the design domain until the optimized topology is found. The gradient based optimizers, which are preferred over non-gradient based optimizers for their speed, can be utilized by modeling the cross-sectional areas as continuous design variables. Using the ground structure approach, however, may lead to highly complex designs since this type of optimization searches for the optimal member placements and cross-sectional areas. The topological complexity of the solution is also highly dependent on the complexity of the initial ground structure. In order to keep the optimization as free as possible, the initial ground structure should be as complex as possible since new elements cannot be added nor removed elements be returned during the opti-

mization process. Therefore, the resulting topological complexity in the solution can be contributed from the initial ground structure.

One well-known strategy aiming at reducing topological complexity in topology optimization of discrete structures is to remove elements with cross-sectional areas that are lower than the threshold from the design domain at each optimization iteration and the problem is re-solved using the new design as the initial guess. While practical, this strategy has some shortcomings, including the possible loss of global optimality and the effect on the final optimal topology based on the chosen threshold magnitude. Another strategy is to use Solid Isotropic Material with Penalization (SIMP) method (Bendsøe, 1989; Zhou and Rozvany, 1991). In this method, the intermediate values between the minimum and maximum cross-sectional areas are penalized. This method is effective in continuum domains where the design variables must be either zero (void) or one (material). In its application to truss, the method has shown to reduce design complexity, but the solutions are still sensitive to the value of penalization (Amir and Sigmund, 2013). For discrete structures, the existence of intermediate cross-sectional areas in optimal solution is natural and to be expected.

In topology optimization of discrete structures, the minimum compliance (maximize stiffness) problem for a given total material volume is considered to be the typical optimal design problem formulation due to its simplicity and ability to handle problems of having a very dense mesh of elements (i.e. potential bars) in the ground structure approach (Achtziger, 1997; Bendsøe and Sigmund, 2003; Dorn et al., 1964).

# CHAPTER 2. TOPOLOGY OPTIMIZATION OF TRUSS STRUCTURES CONSIDERING CONSTRUCTABILITY

In the minimization of compliance problem, material volume is treated as a constraint. Equivalently, this problem can be formulated as minimization of total material volume problem for a given displacement constraint as previously discussed (see Section 1). The minimum total material volume formulation (Eq. (2.1)) can then be converted to a minimization of material cost formulation, which is a more suitable formulation when constructability is considered. This can be expressed as:

$$\min_{\boldsymbol{\rho}} \; M(\boldsymbol{\rho}) = \sum_{\forall e \in \Omega} \alpha_M^e \gamma^e \rho^e L^e \tag{2.1a}$$

$$\text{s.t.} \; \mathbf{K}(\boldsymbol{\rho})\mathbf{d} = \mathbf{f} \tag{2.1b}$$

$$d_i(\boldsymbol{\rho}) \leq d_{i,allow} \qquad for \;\; i = 1, \ldots, N \tag{2.1c}$$

$$\rho_{min} \leq \rho^e \leq \rho_{max} \quad \forall e \in \Omega \tag{2.1d}$$

where $M$ is the material cost of the structure, $\alpha_W^e$ is the material cost per unit weight ($\$/lb_w$), and $\gamma^e$ is material weight density for element $e$.

From a constructability point-of-view, the topological complexity in designs of discrete structures may be expensive to manufacture. For two designs with the same mass, the more complex design will be more expensive to construct since the cost to fabricate discrete structures relates directly to the number of elements and the intricacy of connection designs. To account for the fabrication cost associated with the existence of non-zero members in the domain, Asadpoure et al. (2015) propose a comprehensive cost function that combines both material cost and fabrication cost

by utilizing a regularized Heaviside step function. The work had illustrated the superiority of the proposed combined cost function, in which the tradeoff between the material cost and the fabrication cost is allowed to explore proposed (Asadpoure et al., 2015).

While this combined cost function worked effectively to reduce topological complexity in truss structures as unit fabrication cost increases, the optimal complexity reduced solution could still resulted in structures with large or oversized members, which can likely incur extra costs. In this work, we consider these extra costs and refer to these costs as cost premiums related to the existence of oversized members in structures. The cost premium for using oversized members are mainly influenced by the fabrication cost and construction cost. For fabrication cost, it will depend on the regional availability of resources, such as fabricators or steel, and the fabrication processes (the oversized members may need to be custom made into plate girders, which may require welding, which can be expensive). Using oversized members can also incur additional construction cost as they may require larger hoisting equipment which also depends on the location of the construction site. In this work, a hyperbolic tangent function is utilized to account for the cost premium associated with the use of oversized members. This cost function is a smooth continuous function, which allows a use of gradient-based optimizer.

Another cost associated with a complicated truss design is fabrication cost for connections for the reason that a connection that joins a lot of members together will

be more difficult to fabricate and labor intensive leading to higher total cost. The work by Asadpoure et al. (2015) shows that complexity can be reduced by adding a linear function relating cost to the number of elements in the structure. Essentially, a combination of material cost and fabrication cost is used to account for the cost of placing each member in the structure. In this work, we propose an alternative linear function for connections and show a direct relation between the two linear functions. We demonstrate the proposed function on two simple examples, the cantilever and simply supported beam problems, which correlate directly to the Asadpoure algorithm as expected.

The topological complexity in structures presents one additional potential issue: the existence of many different length members and cross-sectional areas. Structures with many different length members and cross-sectional areas will encounter costs associated with production, transportation, and storage, amongst many others. Thus repeatability in member lengths and areas becomes important. Not only may repeatability imply a structure with more topological simplicity, but it also cost advantages relating to the concept widely known as economies of scale. In this microeconomic concept, the average cost of a producing single member decreases as the production of quantity of the same members are produced.

One way to reduce a number of different cross-sectional areas is to constrain the number of different cross-sections allowed in the structure (Kanno, 2015). The minimum compliance problem was formulated as a mixed-integer second-order cone

programming (MISOCP) problem having an upper bound constraint on the number of different member cross-sectional areas. Formulating the problem as mixed-integer problem, however, means that gradient based optimizers cannot be used. Furthermore, this approach required additional design variables as well as predetermined the number of different cross-sectional areas, which can potential make optimization more constrictive.

Alternatively, we utilize the concept of economies of scale and propose cost function that take into account the reduction of total cost based on the repeatability of cross-sectional area. This approach allows the optimizer to freely determine the number of different cross-sectional areas that should exist in the optimized solution without constraining them in the beginning or adding any addition design variables.

In this dissertation, we consider constructability in topology optimization of discrete structures. Specifically, we aim to tackle three main areas of issues with regards to constructability: (1) the use of oversized members, (2) connection complexity, and (3) many different cross-sectional areas. In each of these issues, we propose either an additional cost function to or a different cost function than the traditional material cost function. The proposed formulations were applied to a simple "fan" structure, in which expected optimal solutions are known, to demonstrate the effectiveness of the proposed functions. Finally, we illustrate the advantages of the proposed approach with classic truss examples with more complicated initial ground structures.

Within each of the cost functions that we propose in this dissertation, there exist

unit cost, which is a predefined independent variable. These unit costs can be cost per unit volume of structure (i.e. $\$/lb$) or cost of producing each member in the structure. For different issues mentioned in the previous paragraph, the value of the unit cost will be different since there may be different factors involved. While the unit cost for using oversized members is mainly influenced by fabrication cost (relating to regional availability of resources and special fabrication processes) as well as construction cost (relating to construction location and possible requirement of bigger construction equipment), the unit cost of producing a member considering repeatability is influenced by cost of transportation and storage as well as cost of fabricating each of the member. Furthermore, the unit cost for each constructability issue can also vary. For instance, the unit cost for using oversized members may become low in areas with abundance of resources (such as steel, fabricators, space for large construction equipment, and cheap labor) and high in areas that lack resources.

Due to their sensitive nature to variability and many different factors involved, the quantification of these unit costs requires an expertise in market data and construction cost estimation. This nontrivial task, however, is not our current goal in this study. Our goal is to develop a tool that consider these very important (but difficult to quantify) factors in our optimization formulation and explore tradeoffs between material cost and design complexity, oversized members, and repeatability.

### 2.1.2 Cost Premium For Oversized Members

When a cross-sectional area of an element becomes larger than or equal to the cross-sectional area equal to that of the predefined oversized member $\rho_{OS}$, there is a cost incurred in addition to material cost. The cost premium term is added to the material cost term stated in Eq. (2.1) as follows:

$$\min_{\boldsymbol{\rho}} \; M(\boldsymbol{\rho}) + OS(\boldsymbol{\rho}) = \sum_{\forall e \in \Omega} \alpha_M^e \gamma^e \rho^e L^e + \sum_{\forall e \in \Omega} \alpha_{OS}^e H_{OS}(\rho^e, \rho_{OS}) \tag{2.2a}$$

$$\text{s.t. } \mathbf{K}(\boldsymbol{\rho})\mathbf{d} = \mathbf{f} \tag{2.2b}$$

$$d_i(\boldsymbol{\rho}) \leq d_{i,allow} \qquad for \;\; i = 1, \ldots, N \tag{2.2c}$$

$$\rho_{min} \leq \rho^e \leq \rho_{max} \quad \forall e \in \Omega \tag{2.2d}$$

where $\alpha_{OS}^e$ is the unit cost premium of element $e$ having cross-sectional area $\rho^e \geq \rho_{OS}$; and $H_{OS}(\rho^e, \rho_{OS})$ is the function that determines whether the cross-sectional area of element $e$ (or $\rho^e$) is smaller or larger than $\rho_{OS}$. This function can ideally be expressed as follows:

$$H_{OS}(\rho^e, \rho_{OS}) = \begin{cases} 0 & \text{if } \rho^e < \rho_{OS} \quad (2.3a) \\ 1 & \text{if } \rho^e \geq \rho_{OS} \quad (2.3b) \end{cases}$$

This step function, however, is discontinuous and, therefore, not differentiable. To implement gradient-based optimizer, $H_{OS}(\rho^e, \rho_{OS})$ is approximated by a smooth and

continuous Hyperbolic Tangent function as follows:

$$H_{OS}(\rho^e, \rho_{OS}) = \frac{1}{2}\left[1 + \tanh\Big(\beta_{OS}(\rho^e - \rho_{OS})\Big)\right] \tag{2.4}$$

where $\beta_{OS}$ is the shaping parameter that dictates the aggressiveness of the step function. As $\beta_{OS} \to \infty$, the Hyperbolic Tangent function approaches the step function in Eq. (2.3). Essentially, this function count the existence of oversized member in the structure and ensures that the cost premium incurred only when oversized member exists. Figure 2.1 shows the cost premium function, respectively, with $\rho_{OS} = 1$ and $\beta_{OS} = \{10^0, 10^1, 10^2, 10^3\}$.

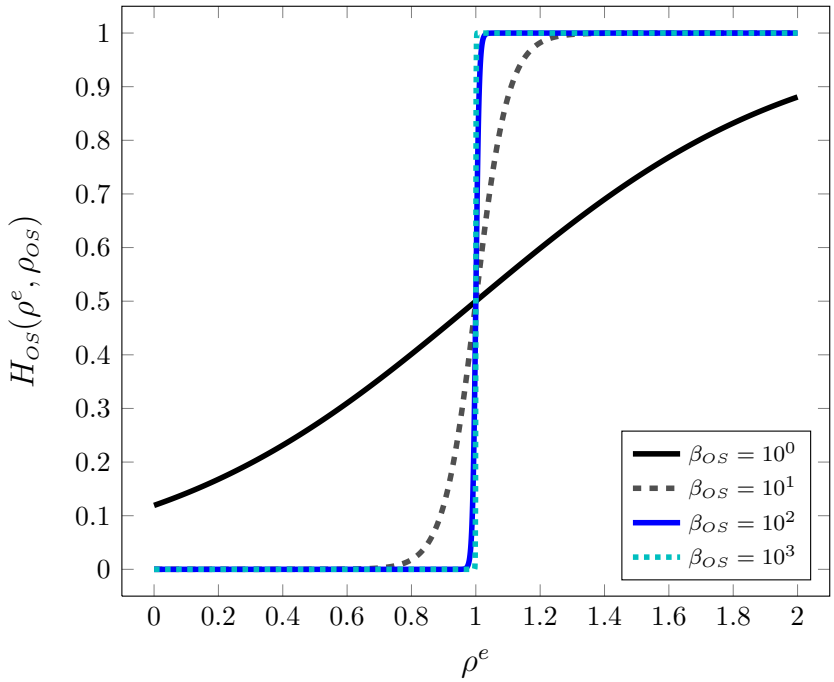


**Figure 2.1:** Hyperbolic tangent function used for oversized member cost premium.

It is important to note that the oversized cross-sectional area $\rho_{OS}$ is not a con-

straint. This approach allows the algorithm to choose oversized members if it is more cost-efficient as unit cost premium changes. Our focus here is on how unit cost premium influence the topology and when it becomes more efficient to use oversized members.

Derivatives of Eq. (2.2a) with respect to cross-sectional area $\rho^e$ can be computed as follows:

$$\frac{d}{d\rho^e}\Big(M(\boldsymbol{\rho}) + OS(\boldsymbol{\rho})\Big) = \alpha_{_M}^e \gamma^e L^e + \alpha_{OS}^e \frac{\beta_{OS}}{2}\Big[1 - \tanh^2(\rho^e - \rho_{OS})\Big]. \tag{2.5}$$

All problems tested using this proposed methodology are solved using MATLAB's fmincon with the interior-point method as the optimization algorithm. To help avoid convergence to low quality local minima, a continuation method on the shaping parameter $\beta$ is traditionally applied. This is done by gradually increasing the shaping parameter to prevent the continuous approximation from approaching the step function too quickly. While the work of Guest et al. (2011) proposed simple modifications that can be applied to allow designers to avoid using a continuation method on the shaping parameter $\beta$ in regularized Heaviside function, the continuation method is found to improves convergence in this application.

It is also worth noting that we have tried solving these problems using Method of Moving Asymptotes (MMA) (Svanberg, 1987, 1995), but run into some convergence difficulties and found MATLAB's fmincon to be much more suitable when the regularized Hyperbolic Tangent is used. Our extensive testing suggests that it is more

difficult for MMA to stay below the oversized member threshold $\rho_{OS}$ or come back down once it crosses over the threshold value. We found that to help with convergence, adjustment to several MMA parameters were required (such as continuation of MMA parameters). Since this was found less robust than fmincon, MMA was not used for this proposed algorithm.

### 2.1.3 Numerical Examples and Solutions For Oversized Members

To illustrate the effectiveness of the proposed combined material cost and oversized cost premium optimization formulation (Eqs. (2.2)), we apply the algorithm to a simple structure consisting of 11 elements with a horizontal point load $P = 20$ kips applied at the far right node as shown in Figure 2.2. We refer to this example as the *fan* problem. The threshold for removal of element from the structure is set at $\rho^e_{th} = 10^{-5}$ in. and a maximum allowable deflection constraint is applied at the node at which the load is applied with $d_{allow} = 1740P/EL$ where $L$ is the length of the shortest element equaled to 60 in. and $E$ is the Young's modulus of material assumed to be that of steel (i.e. $E = 29000$ ksi).

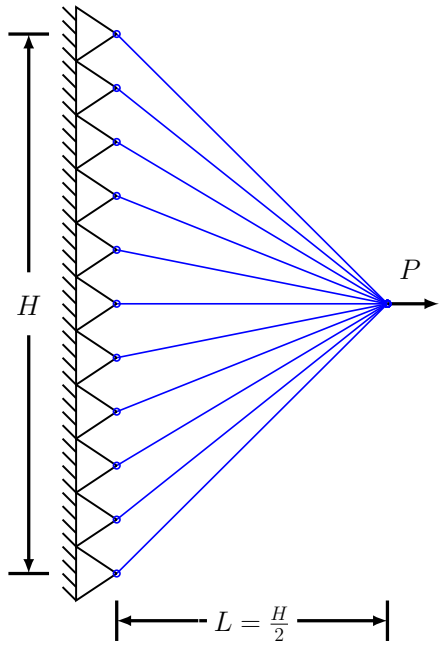


**Figure 2.2:** Initial mesh for the *fan* problem.

For this example, the optimization is performed for varying the oversized members $\rho_{OS}$ from 2 in$^2$ to 0.282 in$^2$ while keeping $\alpha_W$ and $\alpha_{OS}$ constant. The optimized structures for different values of $\rho_{OS}$ are shown in Figure 2.3. When there is no cost premium applied (i.e. $\alpha_{OS} = 0$), the optimal solution is one bar with $\rho^e = 2.0684$ in$^2$. As expected, the number of element increases as the oversize member $\rho_{OS}$ decreases to avoid using the given oversized member. As a consequence, the material cost also increases because more material is required to meet the same stiffness constraint (Figure 2.4).

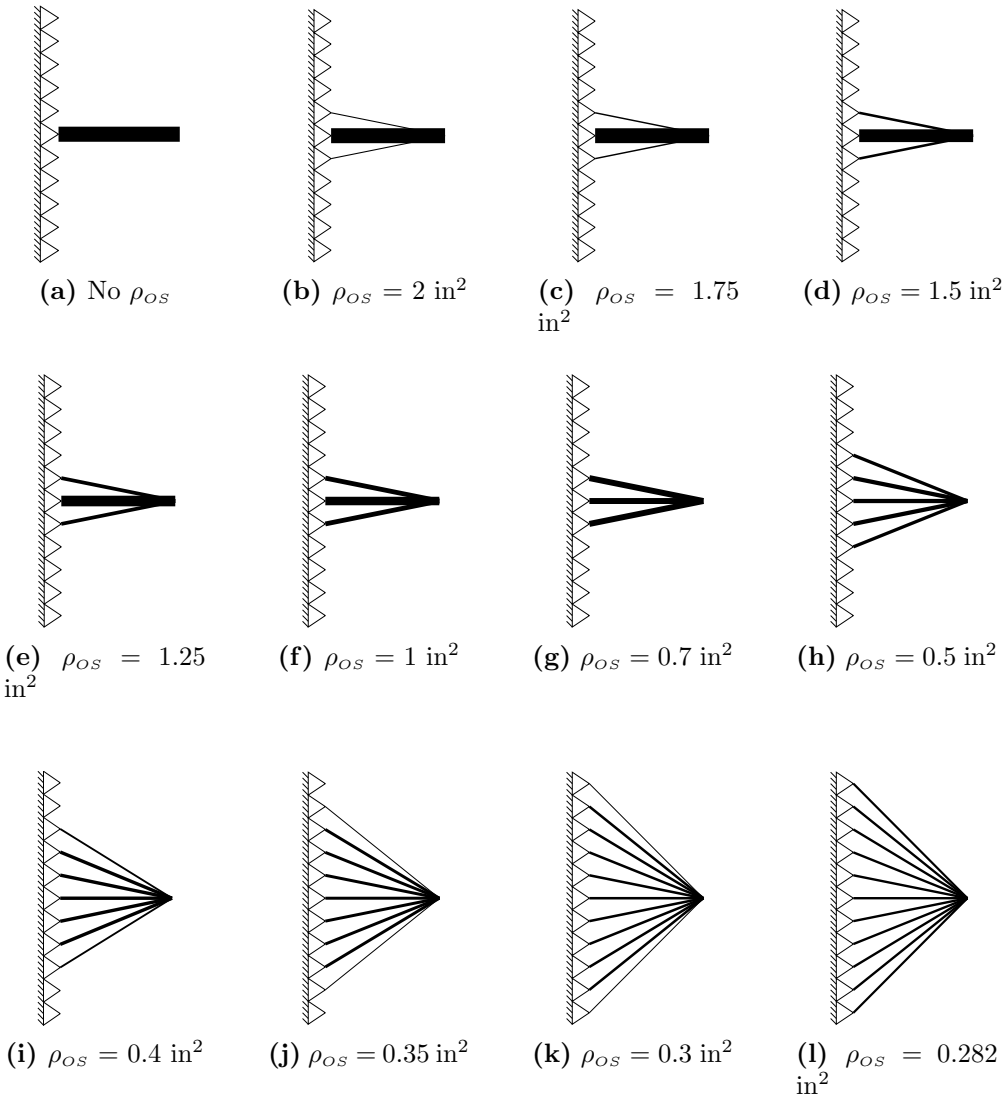


**Figure 2.3:** Optimized *fan* structures for different values of oversized members $\rho_{OS}$.

It is worth mentioning, however, that at a certain small value of oversized member (in this case, some small value of $\rho_{OS} < 0.282$ in$^2$), the optimization finds the optimized structure to be the same as when $\alpha_{OS} = 0$ as seen in Figure 2.4. This happens at the cost of satisfying the maximum allowable displacement constraint,

i.e. it is no longer possible to maintain cross-sectional area of any element below $\rho_{OS}$ without violating the deflection constraint. The optimizer, therefore, choose to incur the lowest possible cost premium, which resulted in optimized solution of a one-bar structure.

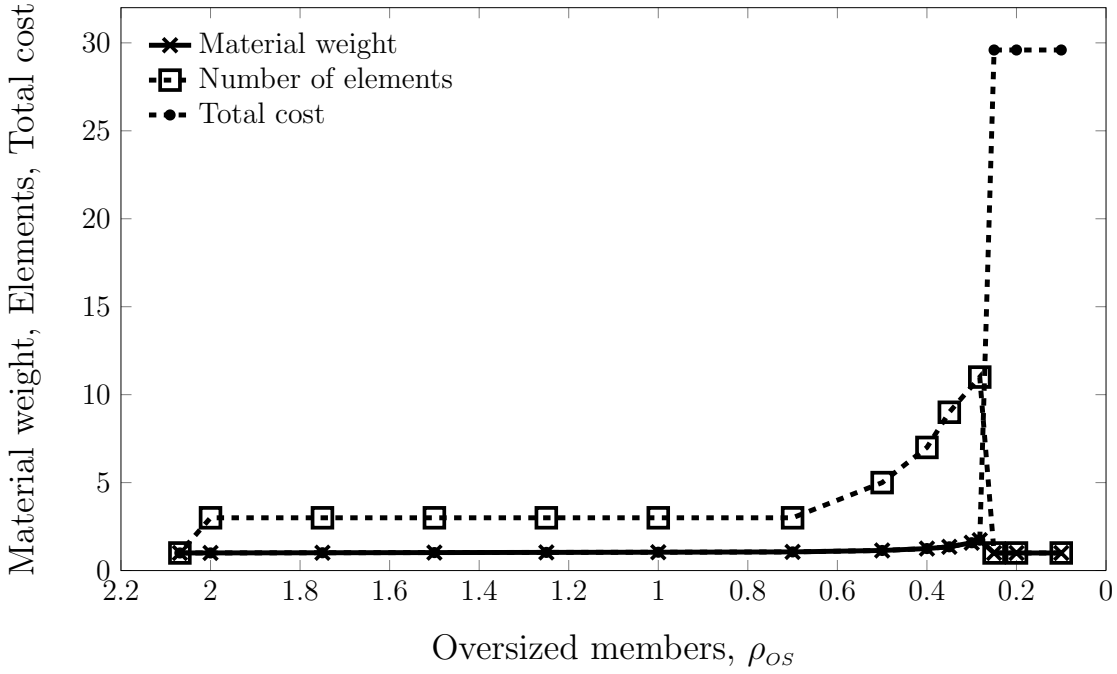


**Figure 2.4:** Total cost (material + cost premium) of and the number of elements in optimized structure for the domain shown in Figure 2.2 for different value of oversized member $\rho_{OS}$; All values are normalized with the corresponding value for the optimized structure shown in Figure 2.3a with no cost premium applied, i.e. $\alpha_{OS} = 0$.

To further illustrate the effectiveness the proposed combined material cost and oversized cost premium optimization formulation (Eqs. (2.2)), we now perform the optimization algorithm for a constant value of unit material cost $\alpha_W = 1$ while varying unit cost premium $\alpha_{OS} = \left\{10^{-7}, 10^{-6}, 10^{-5}, 10^{-4}, 10^{-3}, 10^{-2}, 10^{-1}, 10^{0}\right\}$ for each of the $fan$ problems with $\rho_{OS} = \{1, 0.4\}$ in$^2$.

Figures 2.5 and 2.6 show the optimized *fan* solution for different values of $\alpha_{OS}$ while keeping unit material cost a constant value of 1. As expected, for small values of unit cost premium, the algorithm determines that it is more cost-efficient to use the oversized member. For this example, the optimal solution is that of one-bar truss structure with $\rho^e = 2.0684$ in$^2$. When the unit cost premium is increased to a certain larger value, the structure with oversized member is avoided and the optimal structure remains unchanged for any larger value of unit cost premium. While there is no cost premium incurred, the total cost increases at the cost of a heavier structure as previously explained.

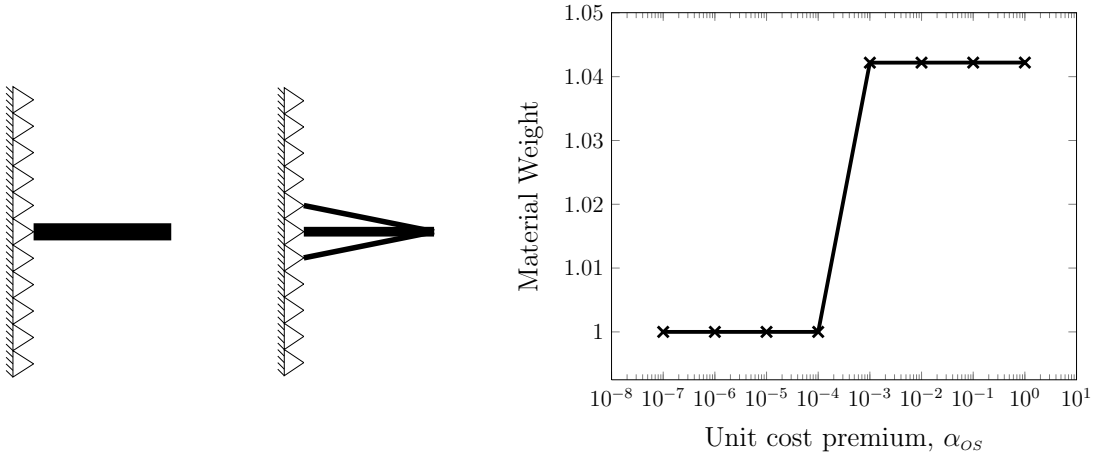


**(a)** $\alpha_{OS} \leq 10^{-4}$ **(b)** $\alpha_{OS} > 10^{-4}$ **(c)** Total cost of the optimized structures for *fan* structures

**Figure 2.5:** Optimized *fan* structures and normalized weight for different values of unit cost premium $\alpha_{OS}$ and oversized members $\rho_{OS} = 1$ in$^2$.

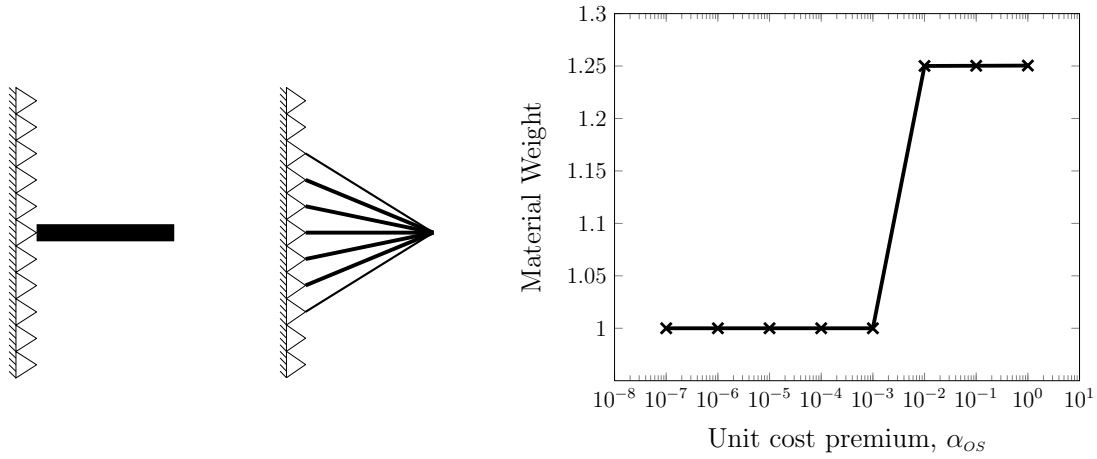


**(a)** $\alpha_{OS} \leq 10^{-3}$ **(b)** $\alpha_{OS} > 10^{-3}$ **(c)** Total cost of the optimized structures for *fan* structures

**Figure 2.6:** Optimized *fan* structures and normalized weight for different values of unit cost premium $\alpha_{OS}$ and oversized members $\rho_{OS} = 0.4$ in$^2$.

We also apply the algorithm to a simply supported truss structure with a point load on top boundary as shown in Figure 2.7. The ground structure consists of 11 $\times$ 3 nodes with 332 elements connecting every pair of nodes without overlapping of elements. The removal threshold for the elements is the same as the one set in the *fan* problem and the maximum allowable deflection a the midspan of the top boundary is $d_{allow} = 6960P/EL$, where $L = 120$ in. With this example, we set the oversized members $\rho_{OS} = \{1, 0.75\}$ in$^2$.

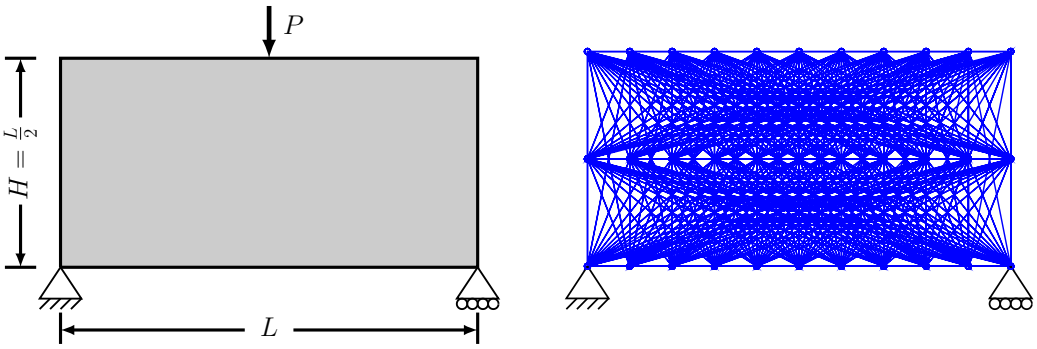


**(a)** Geometry and boundary conditions **(b)** Initial mesh

**Figure 2.7:** A simply supported domain with a point load applied at top boundary (a) geometry and boundary conditions; (b) initial ground structure mesh with 11 × 3 nodes and 332 truss elements.

Similar to the *fan* problem, the algorithm determines that it is more cost-efficient to for the optimal truss structure to have the oversized member for the small values of unit cost premium. For this example, the optimal structure consists of 3-bar truss elements with the maximum cross-sectional area $\rho_{\max} = 2.195$ in$^2$ (See Figures 2.8a and 2.9a). As unit cost premium becomes larger past a certain value, the optimizer avoid using elements with cross-sectional areas larger than the given $\rho_{OS}$ and choose the heavier structure with more number of elements (See Figures 2.8b-2.8c and Figures 2.9b-(2.9c).

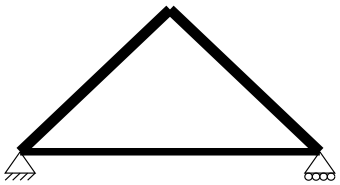

**(a)** $\alpha_{OS} \leq 10^{-4}$

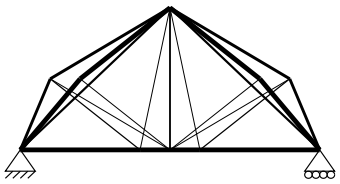

**(b)** $\alpha_{OS} > 10^{-4}$

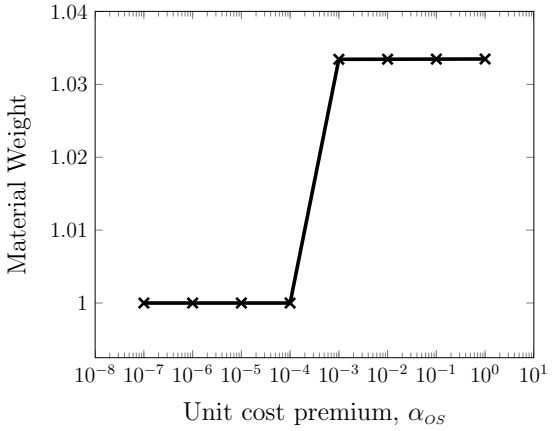


**(c)** Total cost of the optimized structures for $11 \times 3$-node structure

**Figure 2.8:** Optimized $11 \times 3$-node structures and normalized weight for different values of unit cost premium $\alpha_{OS}$ and oversized members $\rho_{OS} = 0.75$ in$^2$.

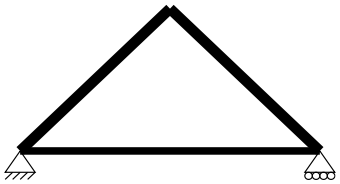

**(a)** $\alpha_{OS} \leq 10^{-4}$

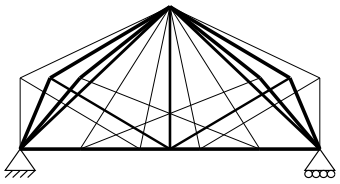

**(b)** $\alpha_{OS} > 10^{-4}$

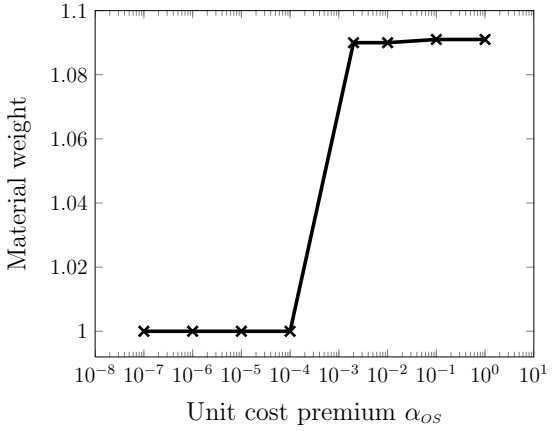


**(c)** Total cost of the optimized structures for $11 \times 3$-node structure

**Figure 2.9:** Optimized $11 \times 3$-node structures and normalized weight for different values of unit cost premium $\alpha_{OS}$ and oversized members $\rho_{OS} = 1$ in$^2$.

Based on these solutions and their trends, it could be said that our proposed optimization formulation (Eqs. (2.2)) allows the optimizer to explore tradeoffs between the structural and cost efficiency and the use of oversized members. It is important to note that this comes at no cost of constraining the value of the design variables (i.e. the cross-sectional area of each element $\rho^e$), which keeps the algorithm to freely choose optimal values of the design variables.

### 2.1.4 Cost Premium For Connection Complexity

The work of Asadpoure et al. (2015) propose adding a fabrication cost to material cost formulation in Eq. (2.1). This fabrication cost is proportional to the total number of members in the structure, estimated by counting the number of structural members with non-zero cross-sectional areas. The underlying idea is that each member in the structure requires a placement and two connections. The number of non-zero elements connected to a node can be estimated by using a regularized Heaviside step function (Guest et al., 2004), as follows:

$$H(\rho^e) = 1 - \exp(-\beta\rho^e) + \rho^e \exp(-\beta) \tag{2.6}$$

where $\beta$ is a regularization parameter. As $\beta \to \infty$, Eq. (2.6) approaches the step function and the function will count any non-zero element towards the total number of element at a connection as seen in Figure 2.10.

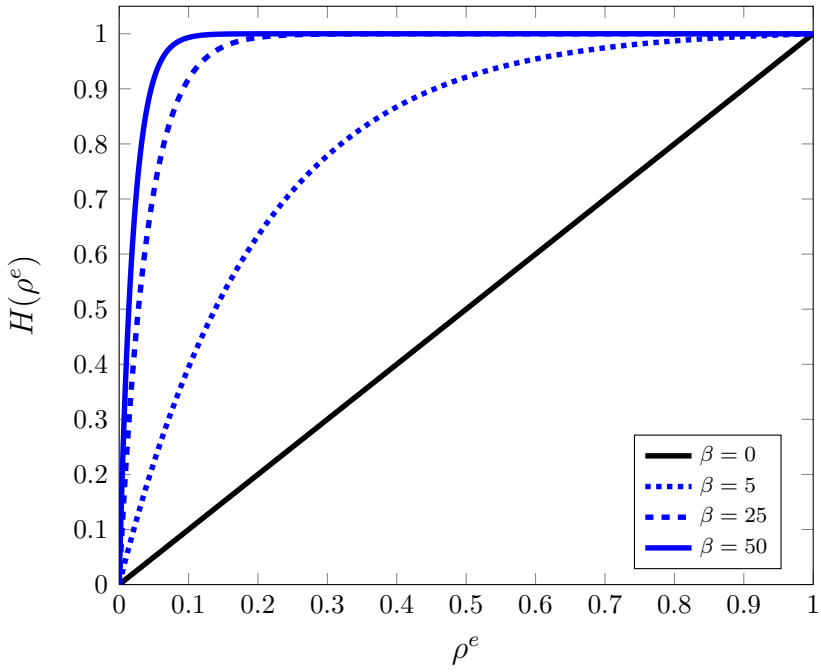


**Figure 2.10:** Regularized Heaviside step function.

This idea can be applied to account for cost associated with a complicated truss design in terms of connections. From the constructability point-of-view, a location requiring larger number of elements incurs higher cost associated with making a connection at that location. In this work, the fabrication cost at a connection is estimated by accounting for the presence of non-zero members connected at a node and the total fabrication cost associated with connection complexity in the structure is obtained by summing up the cost of the individual connection. This total cost can be expressed as:

$$C(\boldsymbol{\rho}) = \sum_{i=1}^{nnp} \alpha_C^i \left[ \sum_{\forall e \in S_i} H(\rho^e) \right] \tag{2.7}$$

where $\alpha_C^i$ is the unit connection cost associated with node $i$; $nnp$ is the total number of nodes in the structure; $S_i$ is the set of element connected to node $i$.

The gradient of Eq. (2.7) can be solved using chain rule as follows:

$$\frac{\partial C(\boldsymbol{\rho})}{\partial \rho^e} = \frac{\partial C(\boldsymbol{\rho})}{\partial H(\rho^e)} \cdot \frac{\partial H(\rho^e)}{\partial \rho^e} \tag{2.8}$$

where

$$\frac{\partial C(\boldsymbol{\rho})}{\partial H(\rho^e)} = \sum_{i=1}^{nnp} \alpha_C^i \sum_{\forall e \in S_i} \frac{\partial H(\rho^e)}{\partial H(\rho^e)} \tag{2.9}$$

and

$$\frac{\partial H(\rho^e)}{\partial \rho^e} = \beta \exp(-\beta \rho^e) + \exp(-\beta) \tag{2.10}$$

Equation (2.9) can be simplified since $\frac{\partial H(\rho^e)}{\partial H(\rho^e)} = 1$ and using the fact that each element is connected by two nodes (i.e. $nnp = 2$). Eq. (2.9) becomes

$$\frac{\partial C(\boldsymbol{\rho})}{\partial H(\rho^e)} = \sum_{j=1}^{2} \alpha_C^i \tag{2.11}$$

where index $i$ in Eq. (2.11) represent the node numbers associated with element $e$ (i.e. $i = ien(j, e)$ where $ien$ is a matrix relating element $e$ with the node numbers at each end of the element).

Substituting Eqs. (2.10)-(2.11) into Eq. (2.8), we can rewritten the derivative as:

$$\frac{\partial C(\boldsymbol{\rho})}{\partial \rho^e} = \left( \sum_{j=1}^{2} \alpha_C^i \right) \Big( \beta \exp(-\beta \rho^e) + \exp(-\beta) \Big) \tag{2.12}$$

For the case where $\alpha_C^i = \alpha_C$, Eq. (2.12) can be simplified further to

$$\frac{\partial C(\boldsymbol{\rho})}{\partial \rho^e} = 2\alpha_C \Big( \beta \exp(-\beta \rho^e) + \exp(-\beta) \Big) \tag{2.13}$$

and the total connection cost in Eq. (2.7) can also be simplified to

$$C(\boldsymbol{\rho}) = 2\alpha_C \sum_{\forall e \in \Omega} H(\rho^e) \tag{2.14}$$

It is important to note here that Eqs. (2.13) and (2.14) are the simpler forms of Eqs. (2.12) and (2.7), respectively, and only valid if $\alpha_C^i = \alpha_C$.

From a general observation between Eq. (2.7) and Eq. (2.14), it can be seen that when the connection cost function is linear and the unit cost is the same for all connection locations (i.e. $\alpha_C^i = \alpha_C$), the formulation reduces to a linear scaling of Asadpoure et al. (2015). In this particular case, the cost of fabricating all connections is twice the cost of fabricating all members in the structure. This makes logical sense since each member in the structure will require fabrication of two connections (one at each end of the member). In the cases where $\alpha_C$ is different for each connection, the cost would incur at a different rate for different connections. Realistically, the fabrication cost would increase more rapidly (i.e. nonlinearly) with the number of members at a connection.

Combining material cost (Eq. (2.1a)) and a general fabrication cost for connection (Eq. (2.7)), an optimization problem for a discretized domain ($\Omega$) can be expressed

follows:

$$\min_{\boldsymbol{\rho}} \; M(\boldsymbol{\rho}) + C(\boldsymbol{\rho}) = \sum_{\forall e \in \Omega} \alpha_{_M}^{e} \gamma^{e} \rho^{e} L^{e} + \sum_{i=1}^{nnp} \alpha_{C}^{i} \left[ \sum_{\forall e \in S_i} H(\rho^{e}) \right] \tag{2.15a}$$

$$\text{s.t. } \mathbf{K}(\boldsymbol{\rho})\mathbf{d} = \mathbf{f} \tag{2.15b}$$

$$d_i(\boldsymbol{\rho}) \leq d_{i,allow} \qquad for \;\; i = 1, \ldots, N \tag{2.15c}$$

$$\rho_{min} \leq \rho^{e} \leq \rho_{max} \quad \forall e \in \Omega \tag{2.15d}$$

and the derivatives of Eq. (2.15a) with respect to cross-sectional area $\rho^e$ is expressed as follows:

$$\frac{d}{d\rho^{e}} \Big( M(\boldsymbol{\rho}) + C(\boldsymbol{\rho}) \Big) = \alpha_{_M}^{e} \gamma^{e} L^{e} + \left( \sum_{j=1}^{2} \alpha_{C}^{i} \right) \Big( \beta \, \exp(-\beta \rho^{e}) + \exp(-\beta) \Big) \tag{2.16}$$

### 2.1.5 Numerical Examples and Solutions For Connection Complexity

The proposed minimum cost formulation for connection complexity is applied to two classic 2D truss problems: cantilever truss (Figure 2.11) and simply supported truss (Figure 2.12) structures. These problems are solved using Method of Moving Asymptotes (MMA) (Svanberg, 1987, 1995) with a modification of MMA proposed by (Guest et al., 2011). This modification eliminates continuation scheme on the parameter $\beta$ in Eq. (2.7) that is typically required to ensure convergence (Guest et al., 2011).

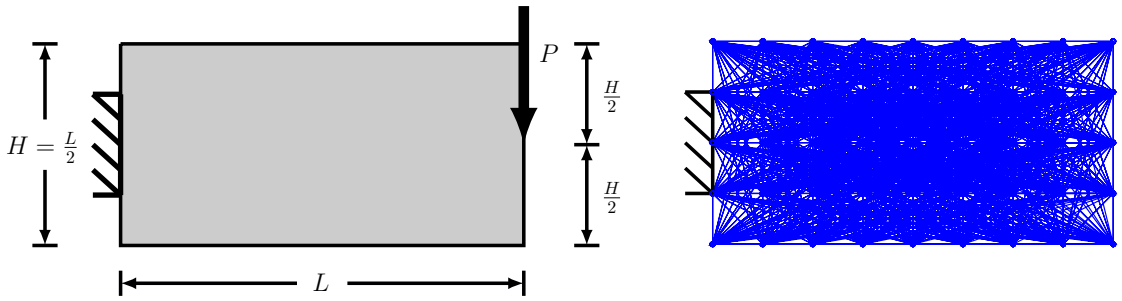


**(a)** Geometry and boundary condition **(b)** Initial ground structure

**Figure 2.11:** A cantilever design domain with a vertical point load applied: (a) geometry and boundary conditions; (b) initial ground structure mesh with 632 truss elements.

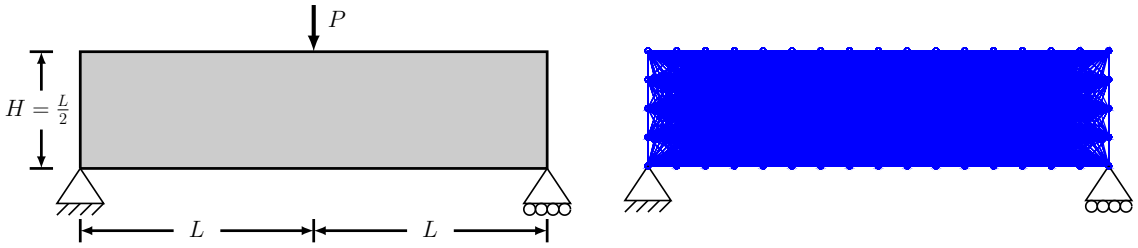


**(a)** Geometry and boundary condition **(b)** Initial ground structure

**Figure 2.12:** A cantilever design domain with a vertical point load applied: (a) geometry and boundary conditions; (b) initial ground structure mesh with 3,570 truss elements.

In practice, the unit cost parameters, $\alpha_M^e$ and $\alpha_C^i$, are estimated by experts in construction and local market, and input by designers. However, to illustrate the effectiveness of the algorithm, we fix the magnitude of material unit cost and vary the magnitude of connection unit cost with uniform weight and connection cost for all the elements and connections (i.e. $\alpha_M^e = \alpha_M$ and $\alpha_C^i = \alpha_C$), respectively. To

reduce computational expense in the simply supported truss problem (with 3,570 truss elements), we also impose symmetry about the axis passing through the location of the applied loads, where elements crossing the line of symmetry are allowed.

Figures 2.13 and 2.14 show the optimized solutions for cantilever truss structures and simply supported truss structures, respectively, for different ratios of connection unit cost and material unit cost (i.e. $\frac{\alpha_C}{\alpha_M}$). Here, we are essentially varying the contribution and significance of connection complexity towards the total cost. As expected, the number of connections in the optimized design decreases as connection unit cost increases. The simpler, less complex designs comes at a higher material cost as seen in Figure 2.15 for both examples. This is because more material is required to maintain the same level of structural performance. As expected, similar trends were reported in Asadpoure et al. (2015) for the simply supported truss structures.

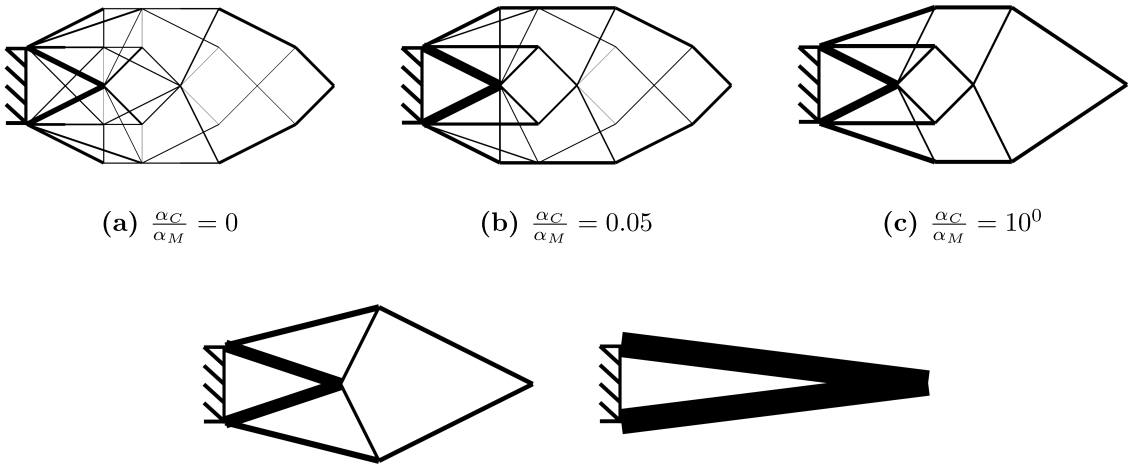

**(a)** $\frac{\alpha_C}{\alpha_M} = 0$ **(b)** $\frac{\alpha_C}{\alpha_M} = 0.05$ **(c)** $\frac{\alpha_C}{\alpha_M} = 10^0$

**(d)** $\frac{\alpha_C}{\alpha_M} = 10^1$ **(e)** $\frac{\alpha_C}{\alpha_M} = 10^2$

**Figure 2.13:** Examples of optimized truss structures for the cantilever domain for different ratios of connection unit cost and material cost $\frac{\alpha_C}{\alpha_M}$ under a deflection constraint (neglecting buckling). As this ratio increases the topological complexity decreases.

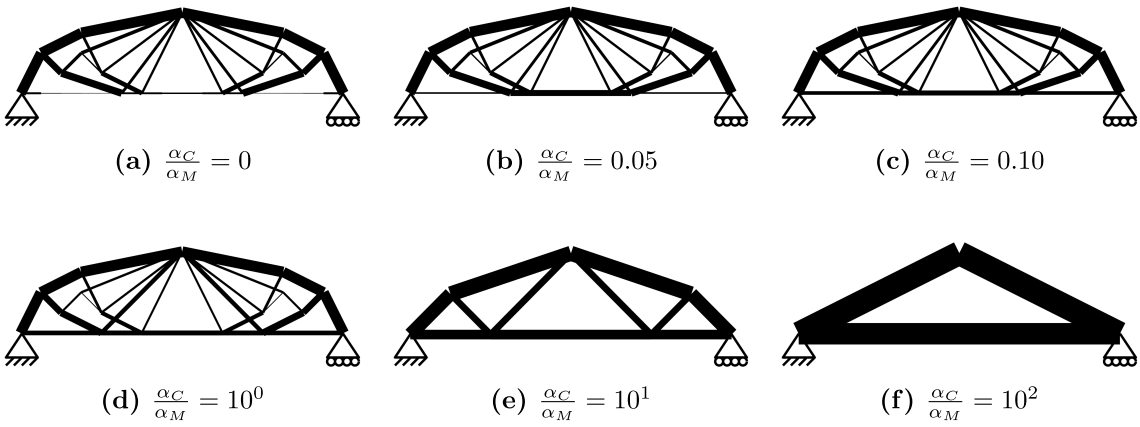

**(a)** $\frac{\alpha_C}{\alpha_M} = 0$ **(b)** $\frac{\alpha_C}{\alpha_M} = 0.05$ **(c)** $\frac{\alpha_C}{\alpha_M} = 0.10$

**(d)** $\frac{\alpha_C}{\alpha_M} = 10^0$ **(e)** $\frac{\alpha_C}{\alpha_M} = 10^1$ **(f)** $\frac{\alpha_C}{\alpha_M} = 10^2$

**Figure 2.14:** Examples of optimized truss structures for the simply supported domain for different ratios of connection unit cost and material cost $\frac{\alpha_C}{\alpha_M}$ under a deflection constraint (neglecting buckling). As this ratio increases the topological complexity decreases.

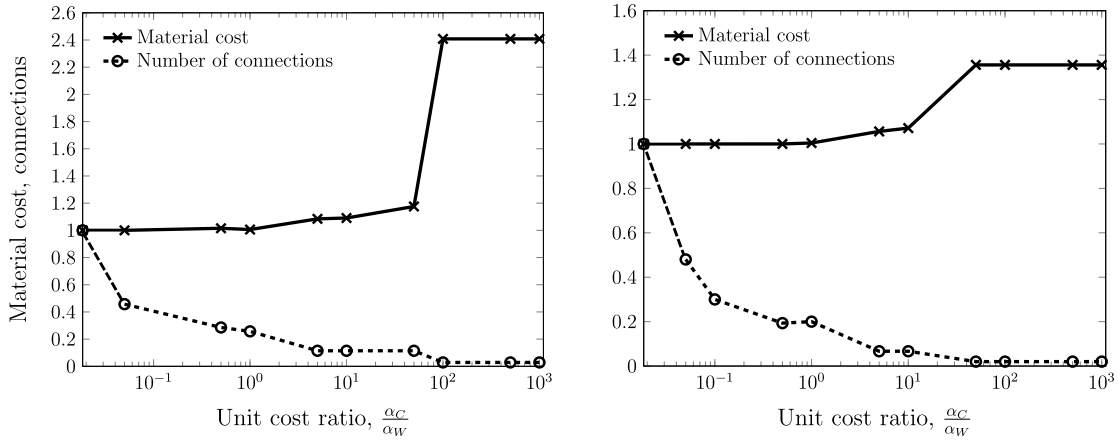


**(a)** Cantilever domain

**(b)** Simply supported domain

**Figure 2.15:** Normalized material cost and normalized number of connections for optimized structures for different ratios of connection unit cost and material cost $\frac{\alpha_C}{\alpha_M}$; All values are normalized with the corresponding values for the optimized structure with zero connection cost (i.e. $\alpha_C = 0$).

These results demonstrate the capability of the proposed cost function, where a slight increase in connection unit cost reduces the number of connections by almost 50% with very little increase in material cost. The plots in Figure 2.15 indicate a constructability-performance tradeoff in terms of connection complexity versus the use of material.

Finally, it is worth noting that while the evolution of optimal topology for the cantilever domain is more or less straightforward, it is not as obvious in the case of simply supported domain. In particular, the evolution of designs seen in Figures 2.14a-2.14d, where the topologies do not look much different, but the number of connections decreases drastically. Upon closer inspection, it was found that there are several

shorter elements overlapping the element at the bottom chord in the cases where the connection unit cost is not considered (i.e. $\alpha_C = 0$). As the connection unit cost slowly increases, the algorithm reduces the number of connections by removing the overlapping elements at the bottom chord, which can be visually observed by the increasing thickness of the bottom chord. This further emphasizes the capability of this algorithm in incorporating constructability into topology optimization.

### 2.1.6 Cost Reduction Considering Repeatability In Section Sizes

Using ground structure approach in topology optimization of discrete structures, the finer the mesh, the less constrictive the optimization becomes; however, as a consequence, the approach allows for the design that is topologically complex with many different member lengths. In addition, when topology optimization with continuous design variables is applied to discrete structures, the optimal solution often results in designs that are difficult to construct because the cross-sectional areas of each member can essentially take all different values.

From a practical perspective, structure having elements with numerous different cross-sectional areas is not desirable due to manufacturability and constructability reasons. To tackle this issue without constraining the value of the design variables, we refer to concept of economy of scale. Producing members of the same property in

large quantity will reduce the cost of manufacturing, transporting, and storing each of these members, which, in turn, reduces the total cost of the structure as a whole. In other words, quantity discount needs to be considered in calculating the material cost in order to obtain structure with optimum design and lowest cost.

Examples of different quantity discounts could be found online from several metal supply websites such as onlinemetalsupply.com and discountsteel.com. Figure 2.16 shows an example of the quantity discounts from Discount Steel (Discount Steel, 2017). It can be seen here that for a certain range and number of products purchased, different discount percentages are applied. The more number of products purchased, the higher discount percentage is applied. These quantity discount percentages can be presented as actual discounted unit cost factors for different range of quantity purchased as seen in Table 2.1, where $\alpha_k$ denotes discounted unit cost factor within range $k$, and $N_k$ denotes the number of element at the end of range $k$.


**Figure 2.16:** Example quantity discount Discount Steel (2017).

When these discounted unit cost factors $\alpha_k$ are plotted against the number of

repeating elements (i.e. number of elements having the same cross-sectional areas or section size), it resembles a downward staircase step function as seen in Figure 2.17, where we will denote the final discounted unit cost factor (i.e. $\alpha_5$) as $\alpha_{k_D}$.

**Table 2.1:** Example discounted unit cost factors.

| Range | $\boldsymbol{\alpha_k}$ | $\boldsymbol{N_k}$ |
|---|---|---|
| 0 | 1 | 5 |
| 1 | 0.95 | 10 |
| 2 | 0.91 | 20 |
| 3 | 0.87 | 50 |
| 4 | 0.83 | 100 |
| 5 | 0.79 | $\infty$ |

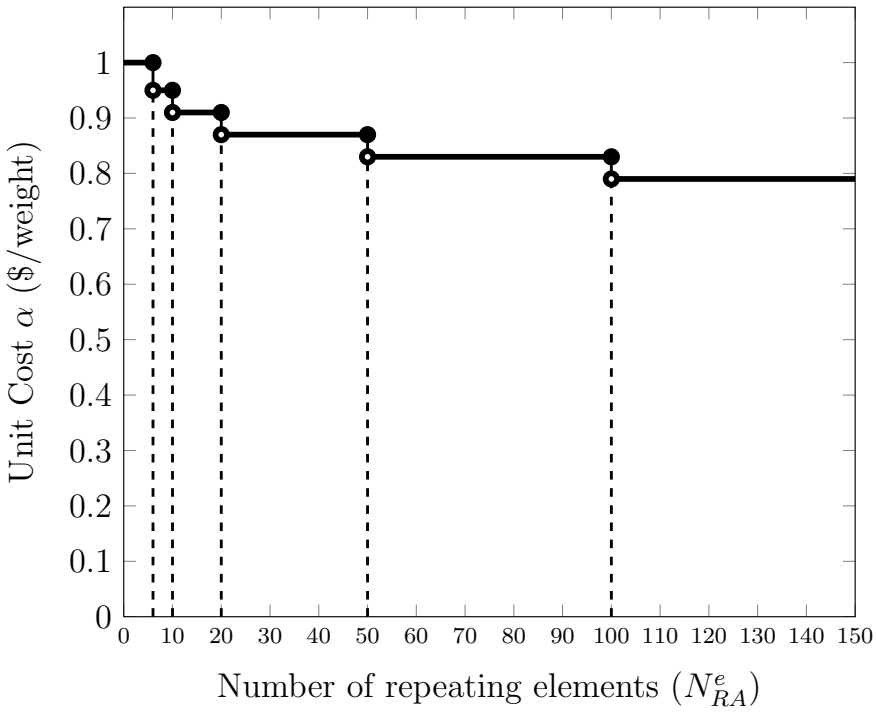


**Figure 2.17:** Example discounted unit cost function.

Here we proposed a way to calculate the reduced material cost when considering quantity discount. Suppose we have 110 elements of the same cross-sectional area and the base cost of producing each element be \$1. The unit cost of producing the first 5 elements would be $\alpha_0 = \$1$/element. The cost of producing elements 6 - 10 would be $\alpha_1 = \$0.95$/element. The cost of producing elements 11 - 20 would be $\alpha_2 = \$0.91$/element. The cost of producing elements 21 - 50 would be $\alpha_3 = \$0.87$/element. The cost of producing elements 51 - 100 would be $\alpha_4 = \$0.83$/element. Lastly, the cost of producing elements 101 - 110 would be $\alpha_5 = \$0.79$/element. Here, we calculate the total cost for producing 110 repeating elements as:

$$RC = \alpha_0(5) + \alpha_1(5) + \alpha_2(10) + \alpha_3(30) + \alpha_4(50) + \alpha_5(10) = \$94.35 \tag{2.17}$$

Equivalently, we can calculate the total cost for producing 32 elements as:

$$\begin{aligned} RC = \alpha_0(110) &- (\alpha_0 - \alpha_1)(110 - 5) - (\alpha_1 - \alpha_2)(110 - 10) \\ &- (\alpha_2 - \alpha_3)(110 - 20) - (\alpha_3 - \alpha_4)(110 - 50) \\ &- (\alpha_4 - \alpha_5)(110 - 100) = \$94.35 \end{aligned} \tag{2.18}$$

Equation (2.18) calculates first the total cost of producing all 110 elements without any discount. The total cost is then deducted by considering the discounted unit

costs for each of the ranges. Equation (2.18) can be rewritten in terms of $N_k$ as:

$$\begin{aligned} RC = \alpha_0 N_{RA} &- (\alpha_0 - \alpha_1)(N_{RA} - N_0) - (\alpha_1 - \alpha_2)(N_{RA} - N_1) \\ &- (\alpha_2 - \alpha_3)(N_{RA} - N_2) - (\alpha_3 - \alpha_4)(N_{RA} - N_3) \\ &- (\alpha_4 - \alpha_5)(N_{RA} - N_4) \end{aligned} \tag{2.19}$$

which can be simplified as:

$$RC = \alpha_0 N_{RA} - \sum_{k=1}^{n_D} (\alpha_{k-1} - \alpha_k)(N_{RA} - N_{k-1}) \tag{2.20}$$

where $N_{RA}$ is the total number of repeating element and $n_D$ is the total number of discount range.

Equation (2.20) is, however, only applicable in cases where $N_{RA} > N_{n_D-1}$. For Eq. (2.20) to work with any value of $N_{RA}$, we introduce a function $\phi_k$ that determines whether $N_{RA}$ is greater than or equal to $N_{k-1}$. This function can be ideally be expressed as follows:

$$\phi_k(N_{RA}, N_{k-1}) = \begin{cases} 0 & \text{if } N_{RA} < N_{k-1} \quad (2.21a) \\ 1 & \text{if } N_{RA} \geq N_{k-1} \quad (2.21b) \end{cases}$$

Equation (2.21) can be approximated by a Hyperbolic Tangent function, which is smooth and continuous, as follows:

$$\phi_k(N_{RA}, N_{k-1}) = \frac{1}{2}\left[1 + \tanh\Big(\beta_{RA}(N_{RA} - N_{k-1})\Big)\right] \tag{2.22}$$

where $\beta_{RA}$ dictates the aggressiveness of the Hyperbolic Tangent function. Notice

that Eq. (2.22) is exactly the same as Eq. (2.4) with different input variables in Section 2.1.2. For convenience, we show here in Figure 2.18 the value of $\phi_k$ for $N_{k-1} = 1$ and $\beta_{RA} = \{10^0, 10^1, 10^2, 10^3\}$. For high value of $\beta_{RA}$, if $N_{RA} \geq N_{k-1}$, then $\phi_k = 1$ meaning that discount in range $k$ should be applied. On the other hand if $N_{RA} < N_{k-1}$, then $\phi_k = 0$ meaning that the number of elements with the same cross-sectional area is not high enough to receive discount in range $k$.

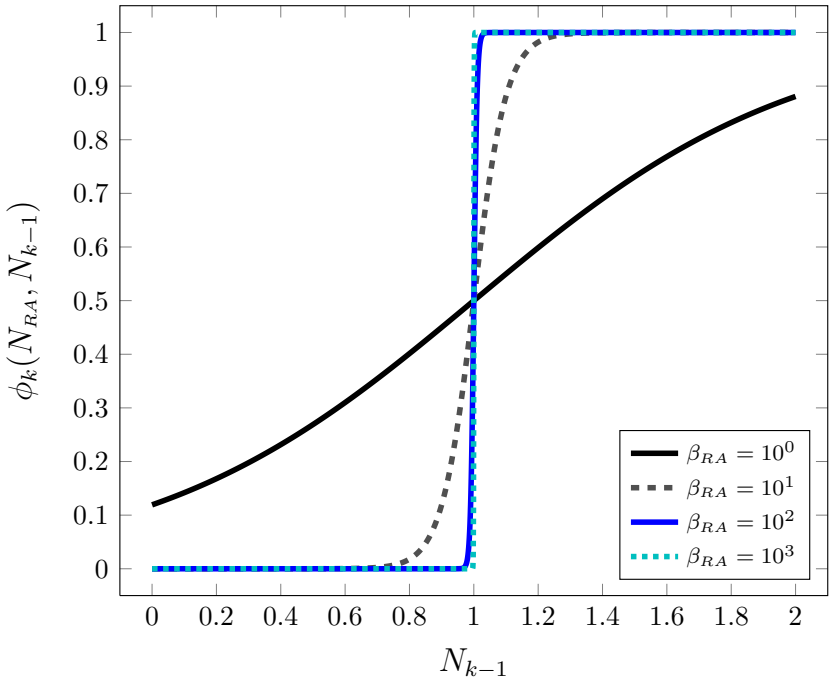


**Figure 2.18:** Hyperbolic tangent function used for repeatability in member sizes.

Equation (2.20) can be rewritten to calculate total cost for any value of $N_{RA}$ as:

$$RC = \alpha_0 N_{RA} - \sum_{k=1}^{n_D} \phi_k(\alpha_{k-1} - \alpha_k)(N_{RA} - N_{k-1}) \tag{2.23}$$

Equation (2.23) represents the total cost of producing all the elements having

the same specific property, but not the cost reduction from overall material cost itself. To account for the cost reduction, we replace the material cost per unit weight, $\alpha_M^e$, in Eq. (2.1a), with the reduced material cost per unit weight $\alpha_{RA}^e$ considering repeatability in section sizes. This cost reduction formulation can be expressed as:

$$\min_{\boldsymbol{\rho}} \;\; RA(\boldsymbol{\rho}) = C_{\text{base}} \sum_{\forall e \in \Omega} \alpha_{RA}^e \gamma^e \rho^e L^e \tag{2.24a}$$

$$\text{s.t.} \;\; \mathbf{K}(\boldsymbol{\rho})\mathbf{d} = \mathbf{f} \tag{2.24b}$$

$$d_i(\boldsymbol{\rho}) \leq d_{i,allow} \qquad for \;\; i = 1, \ldots, N \tag{2.24c}$$

$$\rho_{min} \leq \rho^e \leq \rho_{max} \quad \forall e \in \Omega \tag{2.24d}$$

where $C_{\text{base}}$ is the base cost of each element $e$; and $\alpha_{RA}^e$ is the adjusted unit cost for element $e$ due to repeatability in section sizes, which can be calculated using the total cost of producing all the elements having the same cross-sectional areas (Eq. (2.23)) as:

$$\begin{aligned} \alpha_{RA}^e &= \frac{RC}{N_{RA}^e} \\ &= \frac{\alpha_0 N_{RA}^e - \sum_{k=1}^{n_D} \phi_k^e (\alpha_{k-1} - \alpha_k)\Big(N_{RA}^e - N_{k-1}\Big)}{N_{RA}^e} \\ &= \alpha_0 - \sum_{k=1}^{n_D} \phi_k^e (\alpha_{k-1} - \alpha_k)\left(1 - \frac{N_{k-1}}{N_{RA}^e}\right) \end{aligned} \tag{2.25}$$

where Eq. (2.22) is used to calculate $\phi_k^e$ as

$$\phi_k^e = \frac{1}{2}\left[1 + \tanh\Big(\beta_{RA}(N_{RA}^e - N_{k-1})\Big)\right] \tag{2.26}$$

and $N_{RA}^{e}$ is the number of elements that have cross-sectional area as element $e$, which is estimated as follows:

$$N_{RA}^{e} = \sum_{j=1}^{nel} \exp\Big( - \beta_{RA}^{\eta} (\rho^{e} - \rho^{j})^{\eta} \Big). \tag{2.27}$$

In Eq. (2.27), $nel$ is the total number of element in the domain; $\beta_{RA}$ is the curvature parameter for the exponential function that dictates how close $\rho^{e}$ and $\rho^{j}$ has to be to consider that elements $e$ has similar cross-sectional area as element $j$; and $\eta$ is an exponent that is an even number to make $\rho^{e} - \rho^{j}$ positive value.

Using the chain rule and product rule, the derivatives of total cost of a structure considering repeatability in member cross-sectional area (Eq. (2.24a)) with respect to cross-sectional area $\rho^{e}$ can be expressed as follows:

$$\frac{\partial RA(\boldsymbol{\rho})}{\partial \rho^{e}} = C_{\text{base}} \left[ \alpha_{RA}^{e} L^{e} \gamma^{e} + \sum_{i=1}^{nel} \left( \frac{\partial \alpha_{RA}^{i}}{\partial \rho^{e}} \rho^{i} L^{i} \gamma^{i} \right) \right] \tag{2.28}$$

The derivative of the unit cost reduction function for element $i$ with respect to cross-sectional area $\rho^{e}$ is calculated as follows:

$$\frac{\partial \alpha_{RA}^{i}}{\partial \rho^{e}} = - \sum_{k=1}^{n_D} \left[ (\alpha_{k-1} - \alpha_{k}) \left( \frac{\partial \phi_{k}^{i}}{\partial \rho^{e}} \left( 1 - \frac{N_{k-1}}{N_{RA}^{i}} \right) + \frac{\phi_{k}^{i} N_{k-1}}{\left( N_{RA}^{i} \right)^{2}} \frac{\partial N_{RA}^{i}}{\partial \rho^{e}} \right) \right] \tag{2.29}$$

where

$$\frac{\partial \phi_{k}^{i}}{\partial \rho^{e}} = \frac{\beta_{N}}{2} \left[ \left( 1 - \tanh^{2}\Big( \beta_{N} (N_{RA}^{i} - N_{k-1}) \Big) \right) \frac{\partial N_{RA}^{i}}{\partial \rho^{e}} \right] \tag{2.30}$$

and $N_{RA}^{i}$ is the function that counts the number of element that has similar cross-

sectional areas as element $i$ and its the derivative with respect to cross-sectional area $\rho^e$ can be calculated as:

$$\frac{\partial N^i_{RA}}{\partial \rho^e} = \begin{cases} \sum_{j=1}^{nel} -\beta_{RA}^{\eta}\, \eta(\rho^i - \rho^j)^{\eta-1} \exp\Big( -\beta_{RA}^{\eta}(\rho^i - \rho^j)^{\eta}\Big) & \text{if } i = e \quad (2.31a) \\ \beta_{RA}^{\eta}\, \eta(\rho^i - \rho^e)^{\eta-1} \exp\Big( -\beta_{RA}^{\eta}(\rho^i - \rho^e)^{\eta}\Big) & \text{if } i \neq e \quad (2.31b) \end{cases}$$

### 2.1.7 Numerical Examples and Solutions Repeatability In Section Sizes

Similar to the proposed oversize member cost premium methodology, the problems tested using this proposed methodology are solved using fmincon with the interior-point method as the optimization algorithm. The continuation method on the shaping parameter $\beta_{RA}$ is also found to improves convergence in this application.

To illustrate the effectiveness of our proposed reduced material cost formulation (Eqs. (2.24)), we apply the algorithm to a classic cantilever beam problem as seen in Figure 2.19. The ground structure consists of 9 $\times$ 5 nodes with 632 elements connecting every pair of nodes without overlapping of elements. The removal threshold for the element is set at $\rho^e_{th} = 10^{-4}$ in. A point load of $P = 1$ kip is applied and the maximum allowable deflection at the location of the load is $d_{allow} = 464000P/EL$, where $L = 160$ in.

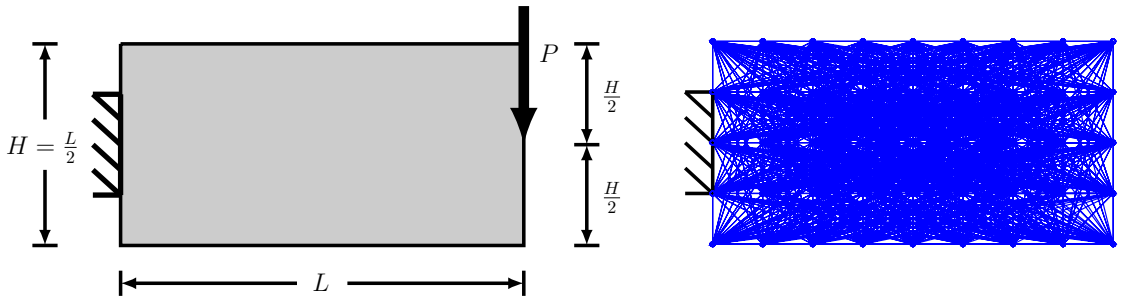


**(a)** Geometry and boundary condition

**(b)** Initial ground structure

**Figure 2.19:** A cantilever design domain with a vertical point load applied: (a) geometry and boundary conditions; (b) initial ground structure mesh with 632 truss elements.

Here we perform optimization for different final discounted unit cost $\alpha_{k_D}$ ranged from 1 to 0.2 as seen in Figure 2.20. The resulting optimized cantilever structure are shown in Figure 2.21, where the thickness of each element corresponds to the value of cross-sectional area, i.e. the thicker the element, the larger the cross-sectional area. The values of total discounted cost, weight, number of element, and number of different area types in the optimized structures for different values of final discounted unit cost $\alpha_{k_D}$ are plotted in Figure 2.22.

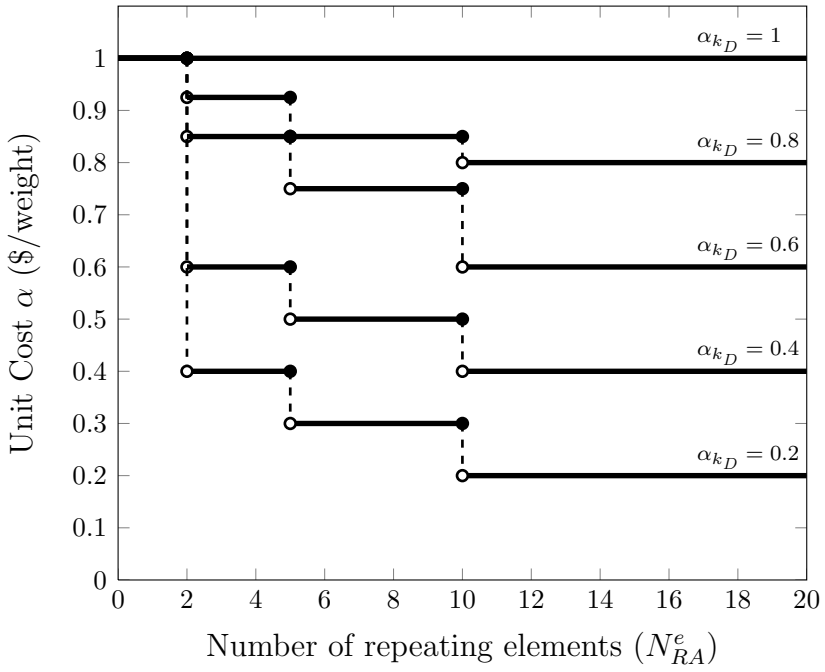


**Figure 2.20:** Example discounted unit cost function with different values of final discounted unit cost $\alpha_{k_D}$.

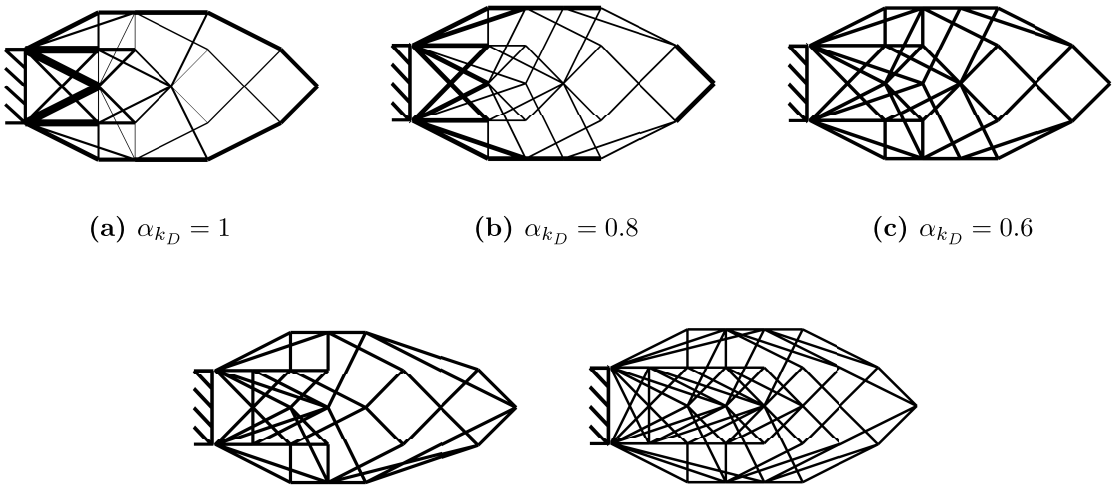

**(a)** $\alpha_{k_D} = 1$ **(b)** $\alpha_{k_D} = 0.8$ **(c)** $\alpha_{k_D} = 0.6$

**(d)** $\alpha_{k_D} = 0.4$ **(e)** $\alpha_{k_D} = 0.2$

**Figure 2.21:** Examples of optimized cantilever structures for domain shown in Figure 2.19 for different values of final discounted unit cost $\alpha_{k_D}$.

As expected, both the number of different area types in the optimal design and the total cost of the structure is reduced as the final discounted unit factors decreases. This is because the material cost can be reduced when more elements with the same cross-sectional areas are produced. However, this occurs at the cost of increasing material weight, which comes at the cost of reducing the number of different area types that exists in the optimal designs. Notice that for a small value of the final discounted unit cost factor $\alpha_{k_D} = 0.2$, the number of elements increase drastically. This happens because the algorithm takes advantage of the low final discounted unit cost and adds more elements having the same cross-sectional areas into the structure to reduce the total cost as a whole.

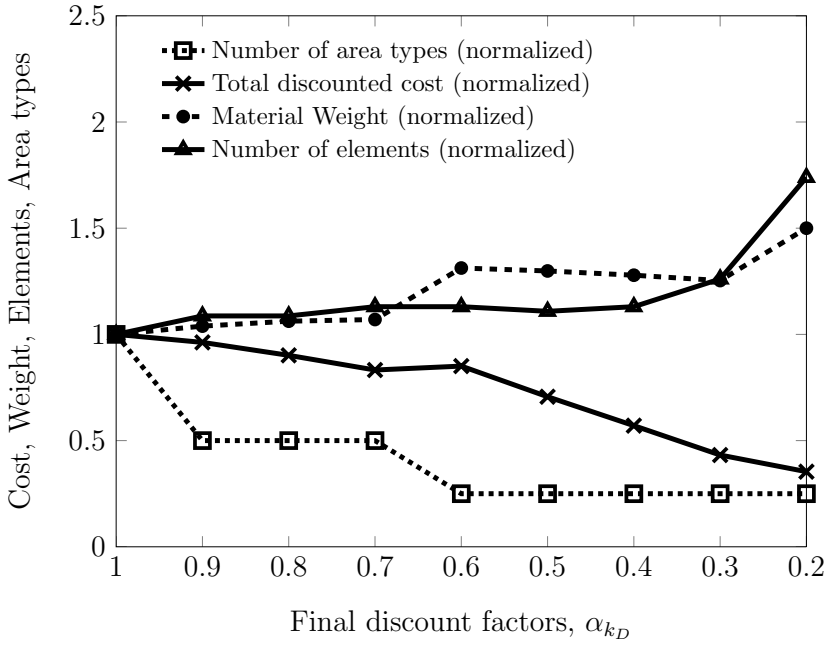


**Figure 2.22:** Total discounted cost, weight, number of element, and number of different area types in optimized structures for the domain shown in Figure 2.19 for different values of final discounted unit cost $\alpha_{k_D}$; all values are normalized with the corresponding value for the optimized structure shown in Figure 2.21a with no quantity discount applied, i.e. $\alpha_{k_D} = 1$.

While this behavior does not reflect the desire property (i.e. adding more elements than actually needed), it only occurs at a small value of $\alpha_{k_D}$ and it also shows that the proposed formulation is effective in considering repeatability and quantity discount. In practice, the discount values are at a much higher values as seen in Figure 2.16 and Table 2.1. The low values of $\alpha_{k_D}$ were only used here to explore the effectiveness of this proposed formulation. This behavior can also be avoided by simply adding the fabrication cost term proposed by Asadpoure et al. (2015) to our proposed reduced material cost algorithm (Eq. (2.24a)).

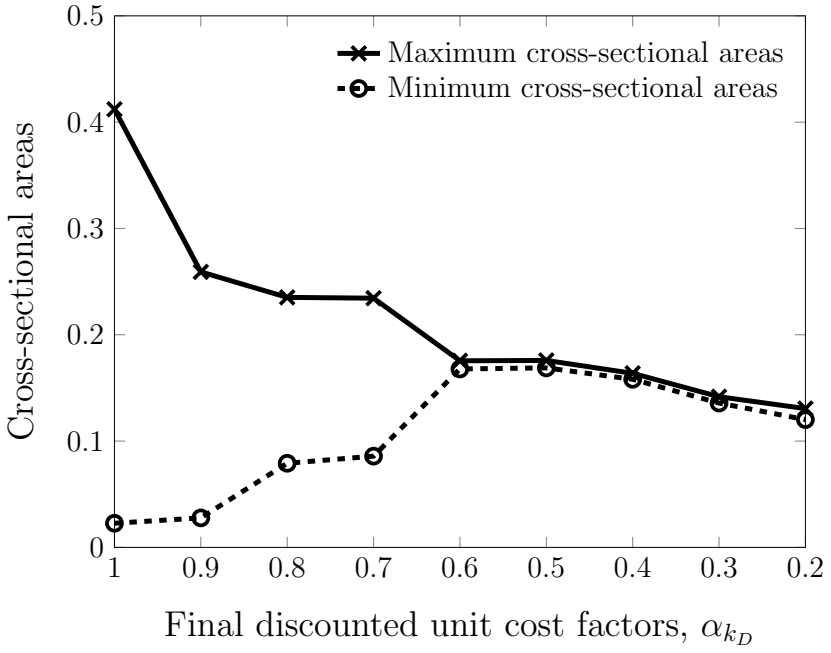


**Figure 2.23:** Maximum and minimum cross-sectional areas in optimized structures for the domain shown in Figure 2.19 for different values of final discounted unit cost $\alpha_{k_D}$.

Interestingly, when the values of maximum and minimum cross-sectional areas in optimized structures are compared (Figure 2.23), these areas converge to relatively the same values at $\alpha_{k_D} = 0.6$. This clearly illustrates the ability of this algorithm to reduce the total number of different cross-sectional area types by finding an optimal values of cross-sectional areas that should be repeated. It should be noted that the values of cross-sectional area continue to decrease after converging as $\alpha_{k_D}$ decreases. This can be explained by looking at Eq. (2.24a), where the reduced material cost is not only depended on the adjusted unit cost $\alpha_{RA}$ which is a function of $\alpha_k$, but it is also depended on the cross-sectional area of each element. Therefore, it makes

sense that the algorithm would decrease the cross-sectional area while at the same time increase the number of elements to reduce the total cost as can be seen in both Figures 2.22 and 2.23.

## 2.2 Summary

In this chapter, the author proposes methods to incorporate costs associated with constructability in topology optimization of truss structures. Specifically, the goal is to solve the following issues that may arise with regards to constructability: (1) the use of oversized members, (2) connection complexity, and (3) many different cross-sectional areas.

The cost associated with the use of oversized members is modeled by assigning a unit cost premium to elements having cross-sectional areas greater than the cross-sectional area of a predefined oversized member. In other words, the cost premium is only incurred when there exists members that are larger than the predefined oversized member. A regularized Hyperbolic Tangent function is utilized in order to implement gradient-based optimizer (i.e. the objective function is smooth and differentiable). Most importantly, the predefined oversized member is not a constraint in this proposed algorithm. The advantage here is twofold: firstly, it allows the algorithm to choose an optimized design with oversized members if it deems to be more cost-efficient, and, secondly, no computational complexity is increased since

no additional constraints is introduced. The proposed algorithm is performed on a simple *fan* structure as well as a more complex truss structure. As expected, the algorithm avoid using the oversized member in the optimized structures when the value of unit cost premium makes the design with oversized member cost-inefficient. This, however, comes at the cost of heavier structure (i.e. higher material cost) to satisfy structural constraints. It is important to note that even for the cases where the unit cost premium is not yet quantified by experts, the proposed approach can help designers assess the tradeoffs and cost benefits between structural efficiency and constructability cost.

This work also extends the idea of Asadpoure et al. (2015) for incorporating constructability in truss and frame topology optimization to considering connections. The idea is that the cost of each connection depends on the number of elements connected to it and that increasing connection unit costs leads to structures with simpler topologies. This, however, comes with a higher material cost because the topologies are less structurally efficient and thus require more to maintain the same stiffness requirement. In its simplest form of uniform, linear cost functions, the algorithm reduces to a scaled version of Asadpoure et al. (2015), and thus it is expected that these solutions and trends are similar to those reported in that work. However, the cost functions can be extended to more complex formulations to provide a more comprehensive constructability-performance tradeoff study.

We also propose an approach to reduce construction complexity in designs with

regards to the existence of many different cross-sectional areas by considering the concept of economy of scale. Here, the unit material cost is adjusted to reflect the quantity discount given for different ranges of total number of elements having the same cross-sectional areas. The proposed approach is demonstrated on a classic cantilever beam problem with decreasing quantity discounts. As expected, the number of different cross-sectional area types is reduced as the value of quantity discounts become smaller. The cross-sectional areas also converges to having roughly the same value at the certain small quantity discount. This illustrates the algorithm's ability to reduce the number of different cross-sectional area type by finding an optimal cross-sectional area value for the entire structure.

In addition to the proposed algorithm that considers the existence of oversized member, it would be useful to consider minimum member size as well. This is a nontrivial task because we cannot simply set the minimum member size as minimum design variable bound. Alternatively, we can create a potential cost premium function as illustrated in Figure 2.24 where subscript '$NS$' denotes non-standard member sizes, 'small' denotes minimum member size, and 'large' denotes oversize member.

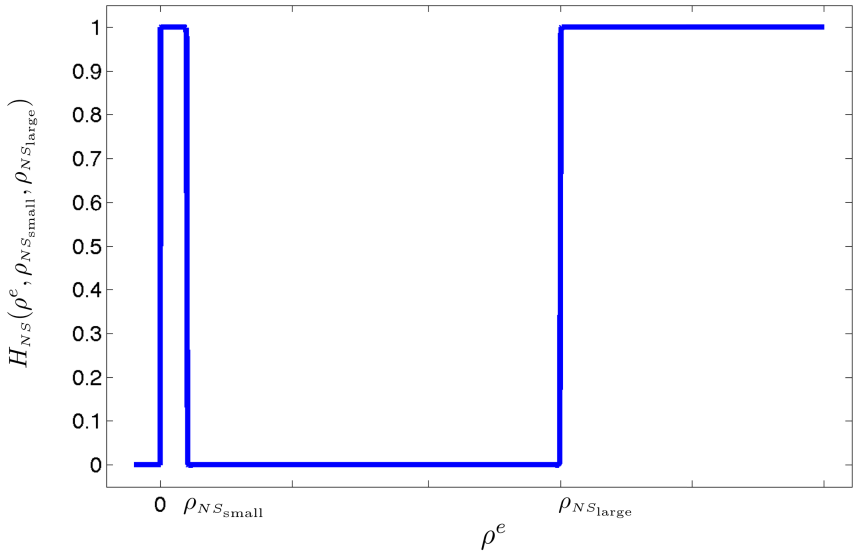


**Figure 2.24:** Hyperbolic tangent function used for non-standard member sizes.

Although this cost function makes sense, applying this cost function to the algorithm will, however, not work because of a fundamental issue relating to enforcing minimum member size. This is because we have to allow the cross-sectional area to take on the value of zero, but penalize any value between zero and minimum member size. During topology optimization process, design variables can take on any value including zero and are allowed to change to any values within the design variable bounds. With this cost function, however, it is extremely difficult for the design variables to cross over the barrier and take on take on the value of zero, which incur no extra cost premium. Due to this fundamental problem, a different penalization strategy is needed to enforce minimum member size and deserve further investigation.

In the case of connection cost, a more realistic cost function would increase more rapidly (i.e. nonlinearly) with the number of members at a connection. One way that

one may consider the nonlinear relationship between cost and the number of element is expressed in equation below:

$$C(\boldsymbol{\rho}) = \sum_{i=1}^{nnp} \alpha_C^i \left[ \sum_{\forall e \in S_i} H_C(\rho^e) \right]^p \tag{2.32}$$

where the fabrication cost at an individual node $i$ is raised to an exponent $p$. Here, when $p > 1$, the cost associated with a node with many elements is significantly higher, depending on the value of $p$, than of a node with very few elements connected to it. We have tried applying this cost function to the proposed algorithm, but ran into issues of non-convergence, which deserves additional attention in future research.

Lastly, it is important to note that the presented topology optimization algorithm for truss structures does not currently consider buckling constraints. While the buckling issues are an important consideration in truss structures, we want to demonstrate that the proposed algorithms perform as expected before considering additional criteria. Buckling constraints should be included in the future work.

# Chapter 3

# Topology Optimization of Components with Embedded Objects

## 3.1 Introduction

### 3.1.1 Motivation

Topology optimization is an extremely powerful mathematical design approach that allows designers to define any design problems in terms of design objective and specifications. Due to its free-form and systematic nature, topology optimization is capable of discovering new and innovative solutions; however, despite its potential as

a design tool, topology optimized solutions tends to be suboptimal when considering real-world operating conditions such as manufacturability. This disadvantage is the direct result of the complexity of the topology optimized solutions, which are theoretically optimal, but may be impractical or impossible to manufacture efficiently. Designers are therefore often required to perform manual post-processing and redesigning, which ultimately leads to workable, but suboptimal solutions. This chapter aims to address this particular challenge by proposing methodology that fully leverage the capabilities of modern manufacturing methods, such as additive manufacturing. In particular, we will discuss how we tailor topology optimization algorithm to conform to a particular additive manufacturing process that is capable of fabricating high-strength fiber-reinforced polymer components.

Additive manufacturing (AM), or more popularly known as 3D printing (3DP), is a manufacturing processes that builds parts by adding material layer-by-layer. In other words, 3D objects are created by adding material in a 2D plane layer-by-layer. Parts that are usually composed of assemblies can now be manufactured as one single 'end-use' part. Over the past two decades, 3DP technology has dramatically expanded its application from rapid prototyping to fabrication of end-use aerospace components, such as jet engine fuel nozzles (Kellner, 2014) and rocket engine injectors (Aerojet Rocketdyne, 2015), to potential long-term space expeditions as evidenced by the existence of 3D printer at the International Space Station (Hubscher, 2014).

While several 3DP technologies exists on the market, fused deposition model-

ing (FDM) is amongst the most widely used 3DP technologies in the present day. FDM was developed in the late 1980s by Scott Cramp, founder of Stratasys Inc. (Chua et al., 2003; Stratasys Ltd., 2017a). In FDM, parts are created by passing thermoplastic filament through a heated extrusion nozzle, which heats the materials above their glass transition temperature and deposits it layer-by-layer (Stratasys Ltd., 2017a). This process is also commonly known as Fused Filament Fabrication (FFF). Polylactic acid (PLA) and acrylonitrile butadiene styrene (ABS) are among the two most common thermoplastics used in FFF because of their low glass transition temperatures (Tymrak et al., 2014). High-performance and engineering-grade thermoplastics like Ultem® (polyetherimide) have higher glass transition temperatures thus require more expensive FFF equipments that can handle higher processing temperature (Gardner et al., 2016b,c). The FFF can also be tailored to allow for deposition of multiple materials by installing additional print heads one for each type of material.

Recently, research scientists at National Aeronautics and Space Administration (NASA) Langley Research Center (LaRC) have developed FFF technology that can fabricate multifunctional load bearing component parts (Gardner et al., 2016b,c). In their work, continuous carbon nanotube (CNT) yarn filament was chosen as multifunctional feedstock due to its high strength and electrical/thermal conductivity. These discrete continuous CNT yarns can be embedded at any location inside the component parts without manual intervention by user as typically required when

embedding discrete objects during the printing process in other techniques (see e.g. (Meisel et al., 2015)). The new capabilities of NASA's 3DP of CNT-based materials, so called 3DP nanocomposites, has enabled fabrication of parts with customized topology built from high strength and multifunctional material and expanded the feasible design space for engineers.

This dissertation aims to develop a computational design tool that efficiently navigate this newfound design space. Specifically, a topology optimization-based design methodology will be developed to integrate the constraints and capabilities of this type of 3DP technology. Particular emphasis will be on the method that simultaneously optimizes the component topology and layout of discrete objects and projection scheme that create discrete continuous yarn-like objects. While the 3DP nanocomposite technology developed by NASA LaRC researchers is the main motivation of this work, the author would like to note that there are similar 3DP technologies with an ability to print continuous fiber composites (see e.g. Markforged (2017); Matsuzaki et al. (2016)). These other technologies, however, prints with material such as carbon fiber, Kevlar®, and fiberglass, all of which possess only one functionality (Gardner et al., 2016b; Markforged, 2017). Compare to others, NASA's 3DP nanocomposite technology with multifunctional CNT yarns is thus more superior.

#### 3.1.1.1 NASA LaRC 3DP Nanocomposite Technologies

The 3D printing of multifunctional load bearing components developed by NASA LaRC combines the printing of high-performance and engineering-grade thermoplastic with conductive and high-strength CNT yarn. The use of single material (i.e. CNT yarn) to provide multiple functionalities in a component part can lead to cost reduction in manufacturing as well as enhancement in performance. As a step towards this 3DP nanocomposite technology, the NASA LaRC team first created a low-cost, desktop sized FFF 3D printer with an ability to fabricate functional components made from high-performance and engineering-grade thermoplastics like Ultem® (polyetherimide). As previously mentioned, these engineering polymers can withstand high temperature and mechanical loading, but also require more expensive industrial machines (e.g. Stratasys Fortus 900mc) that are equipped to handle high processing temperature (Stratasys Ltd., 2017b). Potential cost savings can thus be realized by creating commercially accessible machine that can print these engineering-grade materials.

Researchers at NASA LaRC chose low-cost open-source Lulzbot Taz 4 3D printer developed by Aleph Objects and made several modifications that allow the printer to process high heat-resistant thermoplastic polymer. Figures 3.1a and 3.1b show the original and the modified Lulzbot Taz 4 3D printer, respectively. To increase the processing temperature, twelve direct infrared (IR) heating lamps were installed in the area surrounding the build volume. The original hot end nozzle was also upgraded

to a higher temperature hot end nozzle that that provide temperatures above 400° (from the original of 300°). To prevent outside drafts that could potentially cause parts to warp during printing and retain heat, an enclosure box made from aluminum frame and cardboard foam sidewalls with see-through front is installed around the machine. The original printer parts made from ABS were also replaced with Ultem® which possesses much higher glass transition temperature and better suited for higher temperature printing environment. The NASA LaRC researchers also performed a test to evaluate the effectiveness of the modifications. They printed parts from Ultem® 1010 with and without RI heating lamps and enclosure systems, and found that parts printed without the modifications experience delamination and warping issues while neither of the issues were observed in parts printed with modification. For more details parameters and specification of this printer, the readers are referred to Gardner et al. (2016c).

Since their discovery in 1991, carbon nanotube (CNT) have attracted interest in the scientific community due to their remarkable mechanical, thermal and electrical properties (Baughman et al., 2002; Iijima, 1991). As its name implies, CNT is made of carbon arranged in a tube shape with a diameter in the nanometer scale. These CNTs can be made with one layer or with multiple layers of carbon, formally referred to as single-walled (SWCNT) or multi-walled (MWCNT). Studies on properties of individual CNTs have shown that their elastic modulus and tensile strengths can be in the scale of 1 TPa and of 50 GPa, respectively, and a fracture strength of 100 GPa

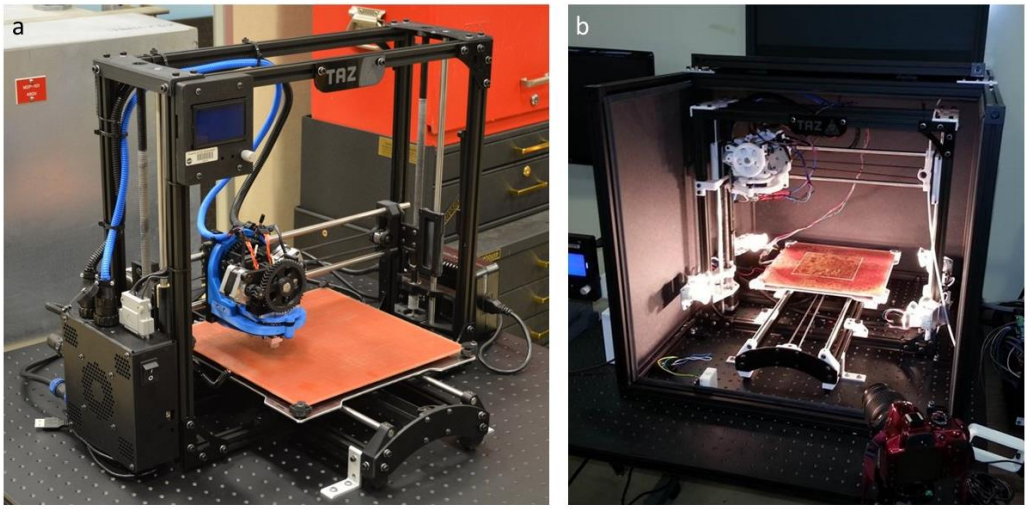


**Figure 3.1:** (a) Original and (b) modified Lulzbot Taz 3D printer. Image Credit: NASA (Gardner et al., 2016c)

have been measured for MWCNTs (Peng et al., 2008; Yu et al., 2000a,b). With their incredible high strength-to-weight ratios, CNTs thus have great potential for enabling development of enhanced lightweight, multifunctional materials and components for air and spacecraft (Baughman et al., 2002).

It is not until recently that CNTs in macroscale bulk format has become available in forms of sheets, tapes, and yarns (Gurau, 2014). So far, the existing 3DP nanocomposite technologies have been using CNTs at nanoscale format (e.g. Campbell and Ivanova (2013); Chizari et al. (2016); Farahani et al. (2012a,b); Guo et al. (2015); Kim et al. (2016); Postiglione et al. (2015)). In these studies, the CNTs are mixed with polymer creating a monolithic nanocomposite, which is then used for printing. In contrast, 3DP nanocomposite technology proposed by NASA LaRC

utilizes CNT yarns and gives users direct control over the placement of these yarns within a component (Gardner et al., 2016a,b).

The CNT yarn used in NASA 3DP nanocomposite technology is fabricated by Nanocomp Technologies, Inc., Merrimack, NH. The purchased CNT yarn is highly densified with specific strength and specific modulus ranged from 1.33 to 1.59 N/tex and from 69 to 102 N/tex, respectively, and linear densities of 24-29g/km. The CNT yarns are made into printable filament by coating them with 3D printable polyetherimide made with 50 mg/ml Ultem® 1010 (Stratasys, Eden Prairie, MN) in dimethylacetamide (DMAc). The printable Ultem®/CNT filaments preparation is completed by heating coated CNT yarns to 250°. The average diameter of Ultem®/CNT filaments is approximately 350 µm with 10-20 wt.% resin content. Figure 3.2 shows printable CNT yarn filaments ready for printing.

**Figure 3.2:** Printable CNT yarn filaments (Gardner et al., 2016a).

To enable 3D printing of CNT yarn-reinforced parts, additional high tempera-

ture hot end nozzle is installed into the modified 3DP machine outlined above (see Figure 3.1b and Gardner et al. (2016c)). Utilized two separate nozzles, the latest modified 3DP machine can print components consisting of both neat Ultem® resin and Ultem®/CNT yarn, where each nozzle is dedicated to one of two materials. The extrusion nozzle for Ultem®/CNT yarns is shown in Figure 3.3.

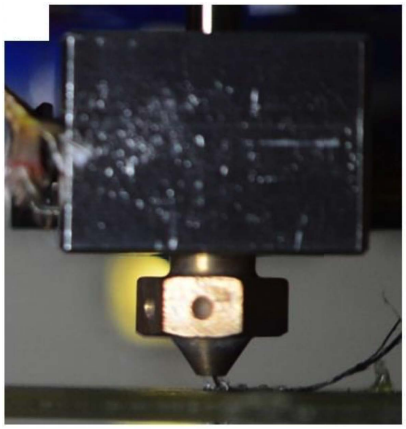

**Figure 3.3:** Extrusion nozzle for Ultem®/CNT yarns (Gardner et al., 2016a).

To print CNT yarn-reinforced parts, a layer of Ultem® is printed on the movable glass print bed as an initial part layer, then either Ultem® or Ultem®/CNT yarn is printed on top layer-by-layer. Two methods are used in this 3DP machine to print the CNT yarns: (1) selective compaction and (2) continuous compaction. In selective compaction, the CNT yarn nozzle is lowered onto the previous layer at 45° angle until contact is made, then the yarn is pushed on top of the previous layer for approximately 1 second to anchor the yarn to the substrate before a single long pass across the printing surface. This anchoring process can be repeated as many times

as required to ensure sufficient bonding before the pass. The selective compaction method is illustrated in Figure 3.4. In continuous compaction, the anchoring process is repeated for the entire CNT yarn filament trace. The latter method is recommended for printing CNT yarns in locations that require structural reinforcement, while the former method is used for printing conductive traces and in locations that does not require robust adhesion. In this printer, resistive (Joule) heating is used to cut the continuous CNT yarns.

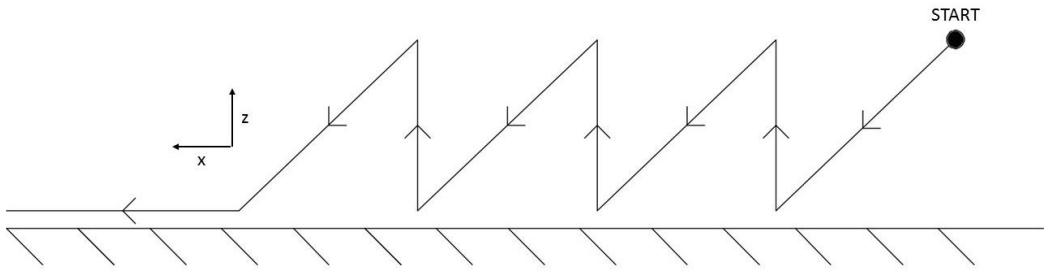


**Figure 3.4:** Illustration of selective compaction method for printing Ultem®/CNT filament (Gardner et al., 2016a).

Several specimens with embedded CNT yarns were printed and tested by the NASA LaRC researchers. In their studies, it is shown that the printer has an ability to print CNT yarns at various angles and allows for very tight turns (Figure 3.5).

The researchers at NASA LaRC also performed mechanical testing and electrical testing of the 3D printed parts (Gardner et al., 2016a,b). In the mechanical testing, a dog-bone shape tensile specimen were cut from the 3D printed coupon and tested in accordance with ASTM D638 standard. They found that the tensile strength

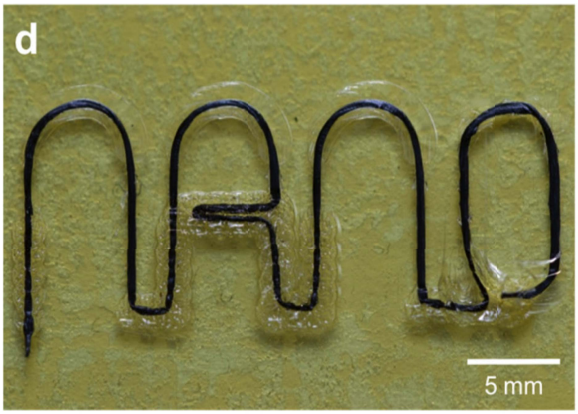


**Figure 3.5:** Illustration of single printed CNT yarn showing 90°, 180°, and large radius turns (Gardner et al., 2016b).

increased 26% using only 4.7% CNT yarn reinforcement (Gardner et al., 2016b). In the conductivity test, the embedded CNT yarn part is shown to power a 1W lamp by successfully acting as current carrying path. The researchers also demonstrate the multifunctionality of 3D printed CNT yarn-reinforced composites on a 3D printed quadcopter with embedded CNT yarns, which acts as both mechanical reinforcement and current carrying conductor. Figure 3.6a shows the quadcopter frame made of Ultem® and CNT yarn and Figure 3.6b shows a fully assembled quadcopter in motion. For more details on this 3DP nanocomposite technology developed by NASA LaRC, the readers are referred to Gardner et al. (2016a,b).

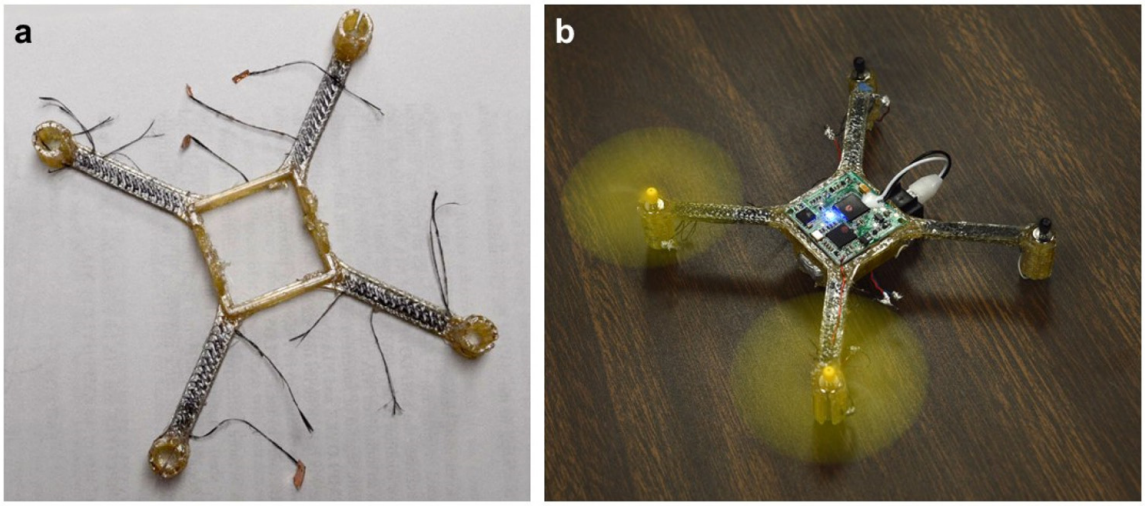


**Figure 3.6:** (a) 3D printed quadcopter frame with Ultem® and CNT yarn and (b) fully-functional quadcopter in motion (Gardner et al., 2016b).

### 3.1.2 Prior Research on Topology Optimization of Embedded Objects

Traditional topology optimization (Bendsøe, 1989; Bendsøe and Kikuchi, 1988) is employed with an underlying assumption that structures have a continuous distribution and continuous connectivity of material phases. In other words, structures are assumed to be monolithic in nature. Many engineering components and materials, however, are not monolithic in nature. They are instead manufactured by distributing pre-fabricated discrete objects inside a monolithic matrix material, such as fiber-reinforced composites and steel-reinforced concrete beams. Topology optimization applied in a traditional manner is thus not equipped to handle such design

problems.

Two notable preliminary works in the topology optimization of material systems with embedded reinforcing or functional objects are mentioned here by the author: (i) Discrete Element Projection and (ii) Discrete Object Projection. These works provide the groundwork towards addressing the fundamental challenge of topology of optimization of components with embedded objects.

#### 3.1.2.1 Discrete Element Projection

Discrete Element Projection is a topology optimization method which was developed as a way to optimize structures that are composed of discrete elements and continuum elements having significantly different functionalities and material properties. In this method, discrete finite elements are embedded inside continuum finite element mesh, creating one hybrid structural model. In this discrete-continuum hybrid model, the layout of discrete elements and the topology of the continuum component are simultaneously optimized using ground structure topology optimization approach (Achtziger, 1997; Bendsøe and Sigmund, 2003; Dorn et al., 1964) for discrete elements and continuum topology optimization for continuum elements.

This method was first demonstrated in the application of 2D steel-reinforced concrete design (Gaynor et al., 2013) and was later extend to 3D design domain (Yang et al., 2015b). Figure 3.7 shows illustration of discrete-continuum hybrid model in 2D and 3D design domains, respectively. In this application, the continuum concrete ma-

terial phase is assumed to carry only compressive forces and the discrete steel rebars are assumed to carry only tensile forces. Both studies shows that discrete element projection methods was successful at optimizing both the concrete topology and the placements of discrete steel rebars. Figure 3.8 shows example solutions of optimized steel-reinforced concrete structures in 2D.

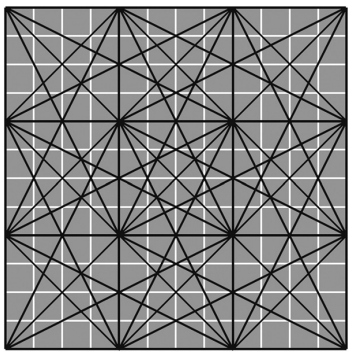

**Figure 3.7:** Illustration of 2D hybrid truss-continuum domain (Gaynor et al., 2013).

As a way to consider constructability of the embedded objects, the Discrete Element Projection approach was extended to include a cost function that promote placement of steel rebars that are easy to construct (Yang et al., 2015b). In this work, horizontal and vertical steel bars are cheaper than inclined steel bars. Similar to the first part of this dissertation, the tradeoff between performance and constructability can be explored by the designers.

Although the Discrete Element Projection can be extended to consider other combinations of material functionalities and interactions, there are limitations to this method when considering other types of reinforced composites. One of these limita-

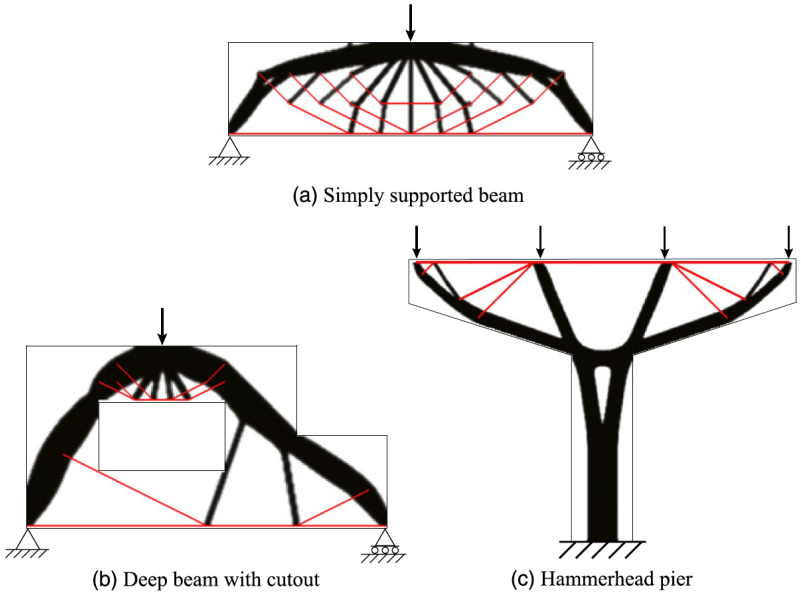


**Figure 3.8:** Example solutions of optimized steel-reinforced concrete structures in 2D (Gaynor et al., 2013).

tions is that the embedded objects are permitted to be placed outside of the component topology. This behavior is not permitted in, for example, fiber-reinforced composites. While it is possible to modify the method to ensure that the embedded objects are completely surrounded by continuum material phase, the nature of ground structure approach representing discrete elements in Discrete Element Projection is the limiting factor in extending this method to other applications.

One byproduct of using ground structure approach is that only bar-like or fiber-like objects are allowed. Another, perhaps the biggest disadvantage, is that the solutions are mesh dependent. This means that the minimum length of objects depends on the resolution of the mesh, which also directly influence the complexity of object layout.

In addition, the minimum spacing between these objects cannot be defined, meaning that objects are allowed to overlap and that one object can "grow" into multiple objects at its ends as evident in Figure 3.8 where a single bar can be connected at its ends by two or more bars.

With these limitations, the author of this dissertation chose to leverage another existing method called Discrete Object Projection, which has shown to be free of these limitations and allow for more freedom in design.

#### 3.1.2.2 Discrete Object Projection

Discrete Object Projection (DOP) method (Guest, 2011, 2014, 2015; Guest and Ha, 2014) was developed to expand monolithic topology optimization to the design of materials and components containing reinforcing objects. The DOP approach utilizes and extends the Heaviside Projection Method (HPM) (Guest et al., 2004) to ensure that stiff (or compliant) material having fixed shape and size are projected onto a compliant (or stiff) matrix material while satisfying specified minimum spacing (Guest, 2011, 2015). For a complete understanding of the reader, two-phase DOP method is explained here in details including several numerical example problems tested by the author.

HPM was developed by Guest et al. (2004) as a way to tackle the complexity and manufacturability issue by controlling the minimum length scale of structural members. This is made possible by projecting design variables onto physical element

space via mesh independent functions defined by minimum length scale. Typically, these functions are regularized Heaviside functions, which can be used with gradient-based optimizer and can be tailored to achieve user-defined length scale criterion without additional constraints or filters as may be required by other methods (see e.g (Haber et al., 1996; Poulsen, 2003)). This projection technique also eliminates well-known issues in topology optimization concerning numerical instabilities that arise from mesh dependency and checkerboard patterns (Díaz and Sigmund, 1995; Sigmund and Petersson, 1998).

HPM has since been extended to further improve manufacturability of topology optimized solutions of continuum structures. Some of these extended works include, but not limited to, allowing a complete control over member sizes through the control of minimum length scale of holes (Guest, 2009a; Sigmund, 2007) and maximum length scale of members (Carstensen and Guest, 2014; Guest, 2009a,b), tailoring projection domains to mimic several manufacturing technologies such as casting (Gersborg and Andreasen, 2011) multi-axis machining (or 3D milling) (Guest and Zhu, 2012), Poly-Jet 3D Printing (Gaynor et al., 2014), and using the projection technique to eliminate the need of temporary support material in metal and polymer additive manufacturing process Gaynor and Guest (2016). It also has been successfully implemented in wide range of problems such as fluids (Guest and Prévost, 2006; Lin et al., 2015), thermal (Deaton and Grandhi, 2013; Guest, 2009a), stochastic dynamics (Yang et al., 2017), and transient (Behrou and Guest, 2017) problems.

In HPM, the topology optimization problem is divided into two spaces: an independent design variable space $\Phi$ where the optimization is performed, and a physical finite element space $\Omega$ where the physics is solved. These spaces are connected by projecting the design variables $\phi$ onto the finite element $\rho$ via projection function. These design variables may be located anywhere but typically are placed at the nodes or element centroids of the finite element mesh. Material is projected from their locations onto the physical element space if and only if their magnitude $\phi_i$ is non-zero. Figure 3.9 illustrates the projection of design variable $\phi_i$ placed at element nodes to physical element space $\Omega$ over prescribed length scale $r_{\min}$.

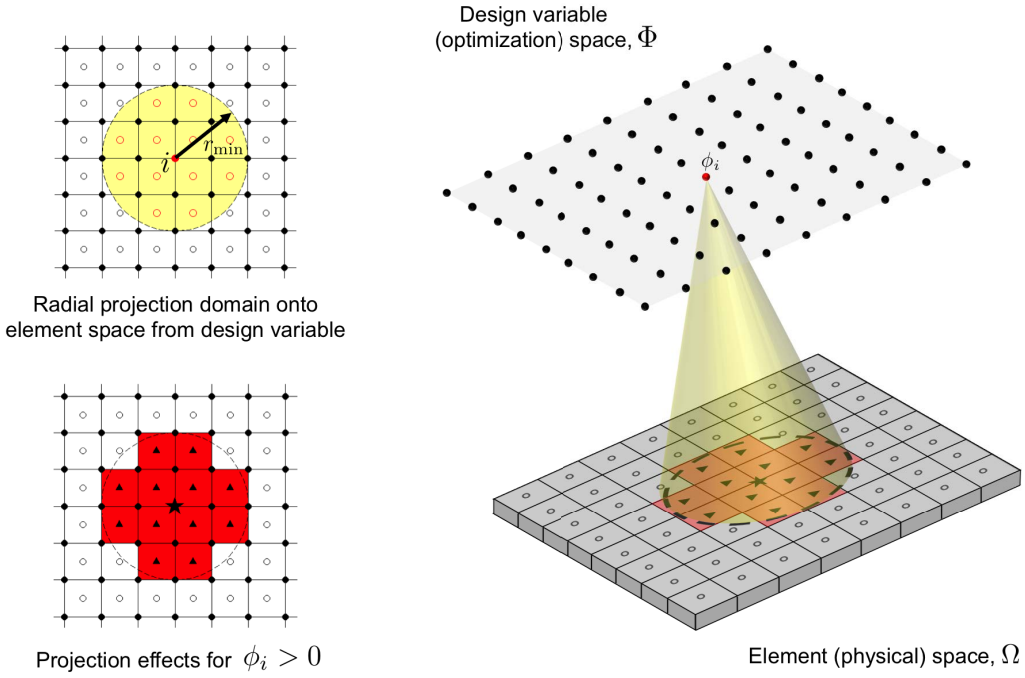


**Figure 3.9:** Illustration of radial projection of length scale $r_{\min}$ from design variable $\phi_i$ onto finite element space $\Omega$ and the projection effect for non-zero $\phi_i$.

The quality that made HPM a powerful approach is that it allows designers to have direct control over the thickness of structural members and this length scale restriction is naturally achieved without any additional constraints, penalty functions, or sensitivity filters. This means that designs obtained using this approach can be manufactured without the need of post-processing because it is optimized directly for the capabilities of the specific manufacturing process. Another key advantage that becomes significant to DOP method is that this method can be extended to other projection shapes (see Figure 3.10) and to multiple design variable spaces.

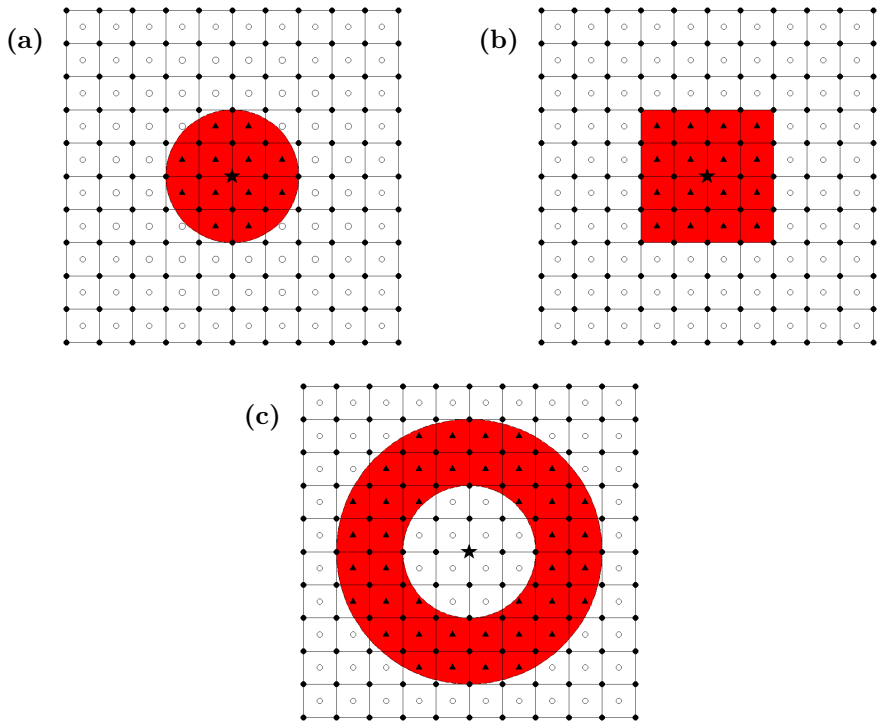


**Figure 3.10:** Examples of different projection shapes: (a) radial projection, (b) square projection, and (c) oculus projection.

In traditional projection method, the design variable is projected in a radial shape over a prescribed length scale $r_{\min}$, which represents the minimum allowable thickness of the designed features (Figure 3.11a). Without any geometric restriction, projected objects can be overlapped to create any arbitrary shape (Figure 3.11b). Discrete objects with fixed shape and size can be created by projecting one material phase locally and enclosing this material inside another material phase (Guest, 2011, 2014, 2015; Guest and Ha, 2014). For instance, stiff material (red) is locally projected and enclosed in compliant material (Figure 3.11c). The equations developed in this work are for the case of stiff features enclosed in compliant matrix material.

For the discrete stiff enclosure case, the mapping of independent design variables $\boldsymbol{\phi}_D$ to element volume fraction $\rho_D^e$ is stored in two elemental neighborhood sets: (1) the local neighborhood set $N_L^e$ and (2) enclosure neighborhood set $N_E^e$. For each design variable in $\boldsymbol{\phi}_D$, the local neighborhood set project stiff circular object (Figure 3.12a) and the enclosure neighborhood set projects oculus compliant enclosure (Figure 3.12b). The ability to define multiple projection shapes for each design variable is a direct benefit of HPM, where the extension to projections other than radial projections is very important when it comes to designing components with embedded objects. This is because the geometries, such as sizes and orientations, of these objects are most likely be predefined by designers and cannot be changed throughout the design process.

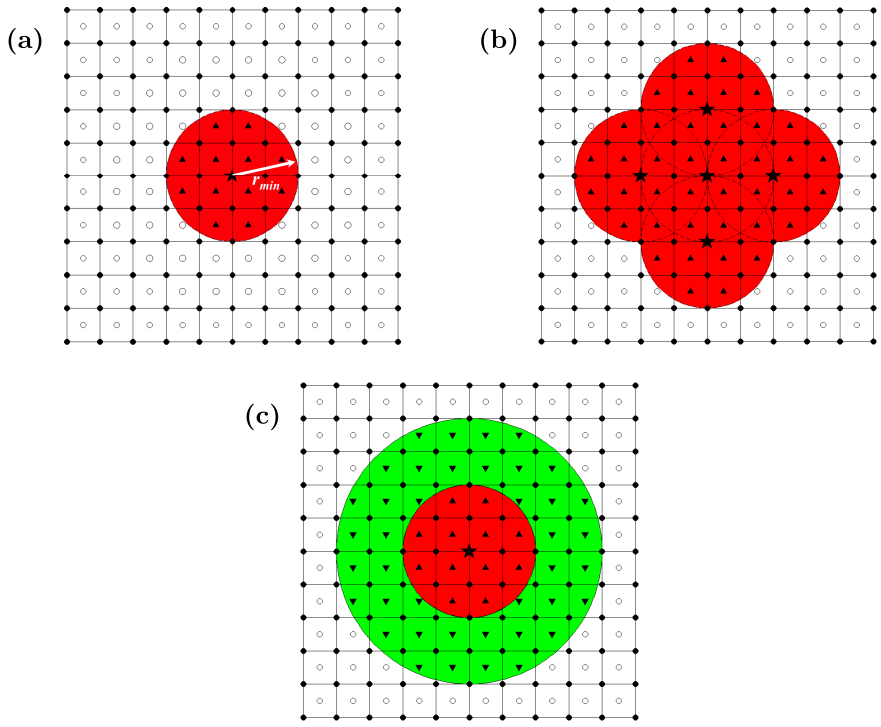


**Figure 3.11:** Illustration of circular projection onto design domain: (a) projection of single design variable, (b) projection of multiple design variables without any geometric restriction creating arbitrary shape, and (c) projection of circular object enclosed inside a layer of matrix material creating discrete object of fixed size and shape.

The local and enclosure neighborhood sets are defined, respectively, as:

$$i \in N_L^e \qquad \text{if } \|\mathbf{x}_i - \bar{\mathbf{x}}^e\| \leq r_{\min_D} \tag{3.1a}$$

$$i \in N_E^e \qquad \text{if } r_{\min_D} < \|\mathbf{x}_i - \bar{\mathbf{x}}^e\| \leq r_{\min_D} + t_E \tag{3.1b}$$

where $\mathbf{x}_i$ is the location of design variable $i$, $\bar{\mathbf{x}}^e$ is the location of the centroid of element $e$, $r_{\min_D}$ is the length scale of the discrete object, and $t_E$ is the thickness of the oculus enclosure, which dictates minimum required distance between discrete

objects (Figure 3.12).

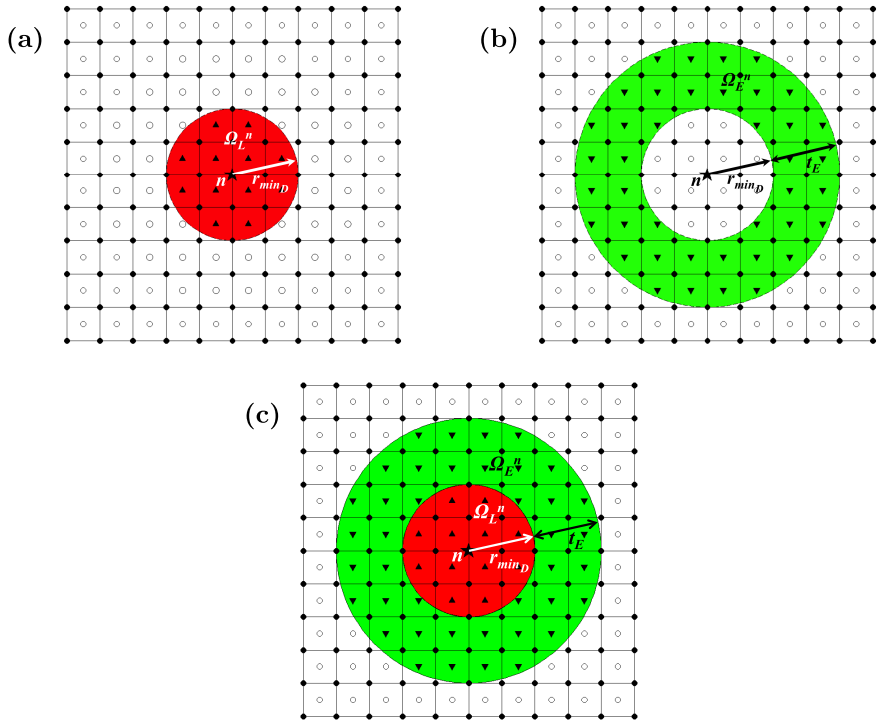


**Figure 3.12:** Discrete circular projection from design variable $n$: (a) a projection of circular stiff phase (red) of length scale $r_{\min_D}$ onto the local domain $\Omega_l^i$ as expressed in Eq. 3.1a, (b) a projection of oculus compliant phase (green) onto the enclosure domain $\Omega_E^i$ as expressed in Eq. 3.1a, and (c) a illustration of final projection.

Densities of elements inside each of the two neighborhoods can be computed using Heaviside projection function the design variable set $\boldsymbol{\phi}_D$ using the standard regular-

ized Heaviside functions (Guest et al., 2004) as follows:

$$\rho_L^e = 1 - e^{-\beta_L \mu_L^e(\boldsymbol{\phi}_D)} + \frac{\mu_L^e}{\phi_{\max}}(\boldsymbol{\phi}_D) e^{-\beta_L \phi_{\max}} \tag{3.2a}$$

$$\rho_E^e = 1 - e^{-\beta_E \mu_E^e(\boldsymbol{\phi}_D)} + \frac{\mu_E^e}{\phi_{\max}}(\boldsymbol{\phi}_D) e^{-\beta_E \phi_{\max}} \tag{3.2b}$$

where $\beta_L$ and $\beta_E$ dictate the aggressiveness in the regularization of the Heaviside function for local and enclosure neighborhood sets, respectively, and $\phi_{\max}$ is the upper bound on design variables $\phi_i$.

The variables $\mu_L^e$ and $\mu_E^e$ are the "filtered" variables (Bruns and Tortorelli, 2001) that essentially measure projection intensity for each element in local and enclosure domains, respectively, and are calculated by averaging the magnitudes of $\boldsymbol{\phi}_D$ over the respective domains as follow:

$$\mu_L^e = \frac{\sum\limits_{i \in N_L^e} \phi_{D,i} w_L(\mathbf{x}_i - \bar{\mathbf{x}}^e)}{\sum\limits_{i \in N_L^e} w_L(\mathbf{x}_i - \bar{\mathbf{x}}^e)} \tag{3.3a}$$

$$\mu_E^e = \frac{\sum\limits_{i \in N_E^e} \phi_{D,i} w_E(\mathbf{x}_i - \bar{\mathbf{x}}^e)}{\sum\limits_{i \in N_E^e} w_E(\mathbf{x}_i - \bar{\mathbf{x}}^e)} \tag{3.3b}$$

The functions $w_L$ and $w_E$ in Eq. (3.3) represents the weighting function associated with each design variable and here uniform weighting function is chosen, which can

be computed simply as:

$$w_{_L}(\mathbf{x}_i - \bar{\mathbf{x}}^e) = \left\{ \begin{array}{ll} 1 & \text{if } \mathbf{x}_i \in \Omega^i_{_L} \\ \\ 0 & \text{otherwise} \end{array} \right\} \tag{3.4a}$$

$$w_{_E}(\mathbf{x}_i - \bar{\mathbf{x}}^e) = \left\{ \begin{array}{ll} 1 & \text{if } \mathbf{x}_i \in \Omega^i_{_E} \\ \\ 0 & \text{otherwise} \end{array} \right\} \tag{3.4b}$$

We refer to the elemental densities in Eq. (3.2) as pseudo-densities because they are used to calculate the final desired elemental phase decomposition (either stiff or compliant phase), $\rho^e_{_D}$, as expressed in Eq. (3.5) below:

$$\rho^e_{_D} = \frac{\rho^e_{_L}(2 - \rho^e_{_E})}{2} \tag{3.5}$$

This equation is designed to maintain a binary phase distribution. In other words, it is to prevent design variable from projecting different phase onto the same element. Figures 3.13a and 3.13b illustrate examples of acceptable projections of discrete stiff particles from two design variables having magnitude greater than zero that results in the binary phase distribution. For this to happen, the distance between the projecting design variables must be at least $2r_{\min_{_D}} + t_{_E}$ (see Figure 3.13b). In the case where the distance between the design variable is less than the required value, phase mixing occurs as illustrated in Figure 3.13c. This phase mixing is due to the projection of stiff phase from one of the design variables and the projection of compliant phase from the other design variable onto the same element. Equation (3.5) therefore facilitates

prevention of overlapping objects by enforcing the minimum distance of $t_E$ between the discrete objects.

The relationship between the pseudo-densities, $\rho_L^e$ and $\rho_E^e$, and the final elemental density, $\rho_D^e$, is summarized in Table 3.1. For instance, if $\rho_L^e = 1$ and $\rho_E^e = 0$, the stiff phase is projected at element $e$. If $\rho_L^e = 0$, the projected phase at element $e$ would be the compliant phase, regardless of value of $\rho_E^e$. If both pseudo-densities are equaled to 1, we set the value of $\rho_D^e$ equal to 0.5. This makes the projection two different phases onto the same element undesirable as gray region would be in regular continuum monolithic topology optimization.

**Table 3.1:** Projection relationships between pseudo-densities and final density for creating stiff discrete objects.

| $\rho_L^e$ | $\rho_E^e$ | Desired phase | $\rho_D^e$ |
|---|---|---|---|
| 1 | 0 | *stiff* | 1 |
| 0 | 0 | *compliant* | 0 |
| 0 | 1 | *compliant* | 0 |
| 1 | 1 | *mixed* | 0.5 |

Using Eq. (3.5), designers can thus prevent occurrence of phase mixing by applying penalization method. In the two-phase DOP method, the Rational Approximation of Material Properties (RAMP) (Stolpe and Svanberg, 2001) is employed to produce discrete objects. This is done by penalizing the intermediate volume fraction that

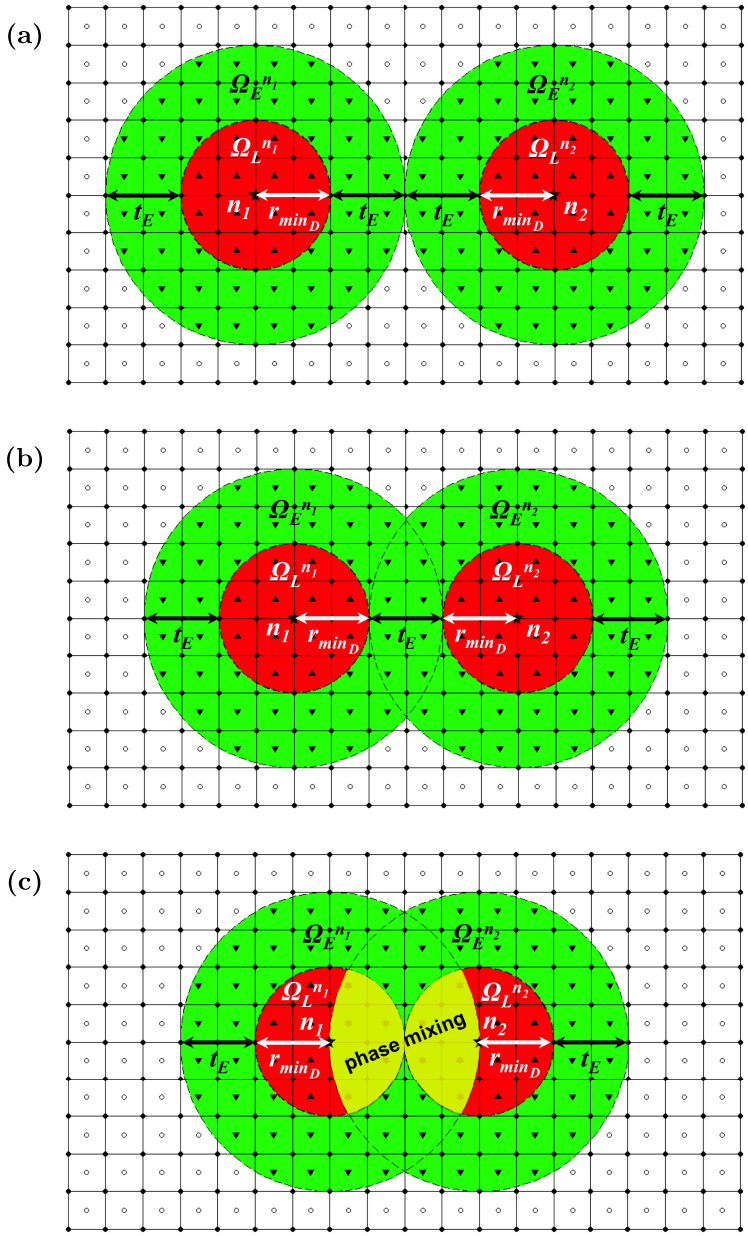


**Figure 3.13:** Illustration of projections from two non-zero design variables: (a)-(b) binary phase distribution is created when projecting design variables are at least $2r_{\min_D} + t_E$ apart, and (c) phase mixing occurs as the distance between the design variable is less than the required value.

produces gray region and phase mixing as expressed in the following equation:

$$E^e(\boldsymbol{\phi}_D = E_1 + \frac{\rho_D^e(\boldsymbol{\phi}_D)}{1 \ + \ \eta\Big(1 - \rho_D^e(\boldsymbol{\phi}_D)\Big)}(E_2 - E_1) \tag{3.6}$$

where $E_1$ and $E_2$ are Young's modulus of the compliant and stiff phases, respectively. If $\rho_D$ is equal to 1, then the element takes on a modulus of the stiff phase $E_2$ and if $\rho_D = 0$, then the element takes the modulus of the compliant phase $E_1$. In RAMP, $\eta$ is the penalty term. When $\eta > 0$, the penalization makes the intermediate volume fraction uneconomical, which help facilitate 0/1 topologies. As discuss in detail by Guest (2015), RAMP method is preferred over the Solid Isotropic Material with Penalization (SIMP) method (Bendsøe, 1989) in topology optimization of embedded discrete objects. This is because the derivation of element stiffness is non-zero when $\rho^e = 0$ in RAMP, which allows the algorithm to create material at these location, whereas in SIMP, the derivative is zero when $\rho^e = 0$ when the exponential penalty term $p > 1$, making it more difficult for discrete objects to be created.

The two-phase DOP algorithm is tested on minimum compliance topology optimization problem for three benchmark problems: cantilever beam, MBB beam, and

L-bracket. The problem formulation is expressed formally as:

$$\min_{\boldsymbol{\phi}_D} \; C = \mathbf{F}^{\mathrm{T}}\mathbf{d} \tag{3.7a}$$

$$\text{s.t.} \;\; \mathbf{K}(\boldsymbol{\phi}_D)\mathbf{d} = \mathbf{F} \tag{3.7b}$$

$$\sum_{\forall e \in \Omega} \rho_D^e(\boldsymbol{\phi}_D) v^e \leq V_s \tag{3.7c}$$

$$0 \leq \phi_i \leq \phi_{max} \quad \forall i \in \Omega \tag{3.7d}$$

where $C$ is compliance, $\mathbf{F}$ are the nodal applied loads, $\mathbf{d}$ are the nodal displacements, $\mathbf{K}$ is the global stiffness matrix, $v^e$ is the elemental volume, $V_s$ is the maximum allowable volume of the stiff phase, and $\phi_{max}$ is the upper bound of the design variable. In this work, the magnitude of $\phi_{max}$ is chosen based on the finite element mesh size as outlined in Guest (2015). The sensitivity of the objective and constraint functions in Eq. (3.7) with respect to $\boldsymbol{\phi}_D$ can be found in Section 3.2.1.2 as well as in the works of Guest (2014, 2015).

The Method of Moving Asymptotes (MMA) (Svanberg, 1987, 1995) is used to solve the optimization problem. We consider various the magnitude of the maximum allowable volume of the embedded stiff particles $V_s$ to see its effect on the optimal layout of the stiff reinforcing particles inside the domain of each benchmark example problem. All example problems use four-node quadrilateral elements and plane stress conditions are assumed with Poisson's ration of 0.3. The Young's moduli of stiff and compliant phases are one and one-third, respectively (i.e. $E_2/E_1 = 3$). Here, we

set the upperbound on design variable $\phi_{\max} = 4$. In this work, we use technique proposed by Guest (2015) to prevent partial objects near the domain boundaries. This technique is described in detail in Section 3.2.1.4.

#### 3.1.2.2.1 Cantilever Beam

The geometry and loading condition for the cantilever beam problem is illustrated in Figure 3.14. The domain is fixed at one end and a point load is applied at the midpoint of the free end. The domain length $L = 40$, height $H = 25$, unit load $P$ and the finite element mesh for this problem is $200 \times 125$. For this problem, we perform topology optimization for two different stiff particle sizes: (1) $r_{\min_D} = 0.4$ units with minimum spacing between discrete stiff objects $t_E = 2 * r_{\min_D} = 0.8$ units, and (2) $r_{\min_D} = 0.6$ units with minimum spacing between discrete stiff objects $t_E = 2 * r_{\min_D} = 1.2$ units. We also vary the maximum volume of the stiff phase to be 2.5%, 5%, 12.5%, and 15%.

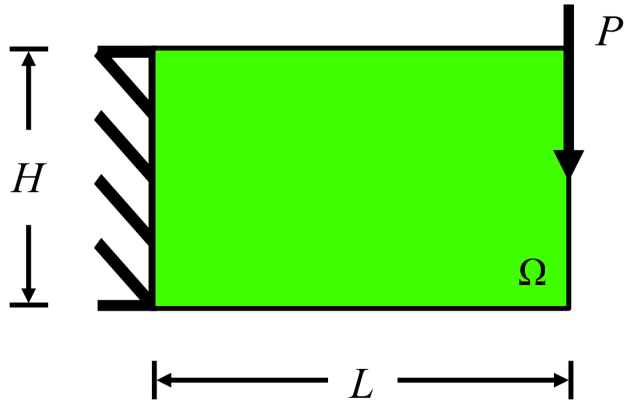


**Figure 3.14:** Cantilever beam domain for two-phase design.

Table 3.2 shows the optimal solutions for the two different particle sizes and four different reinforcement particle volume fractions. We obtain solutions with clearly identifiable discrete circular objects that satisfy the prescribed length scale $r_{\min_D}$ and minimum discrete objects spacing $t_E$. These objects are also logically placed in the location of high stress. For small reinforcement volume fraction, the objects are placed near the top and the bottom of the fixed support and near the applied load, where the stress are the highest as can be seen in the von Mises stress plot in Figure 3.15. As the reinforcement volume increases, the solutions start to resemble the traditional topology-optimized solution for the cantilever problem.

**Figure 3.15:** Plot of von Mises stress of cantilever beam with boundary and loading conditions in Figure 3.14.

As expected, the compliance decreases as reinforcement volume increases and we gain substantial stiffness over the unreinforced structure even for small reinforcement volumes. In this example, the stiffness of the cantilever beam increased by 11.4% and 12.5% using only 2.5% reinforcement volume fraction for $r_{\min_D} = 0.4$ and $r_{\min_D} = 0.6$,

**Table 3.2:** Optimized solutions for cantilever beam problem using two-phase DOP method for $r_{\min_D} = [0.4, 0.6]$ and $V_s = [2.5\%, 5\%, 12.5\%, 15\%]$.

| $V_{s,\text{given}}$ (%)* | $r_{\min_D} = 0.4$ | $r_{\min_D} = 0.6$ |
|---|---|---|
| 2.5 | 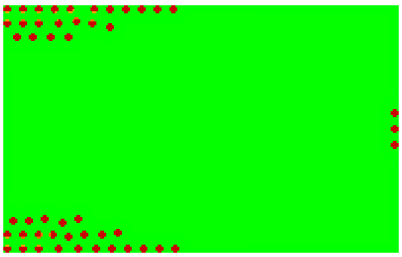 | 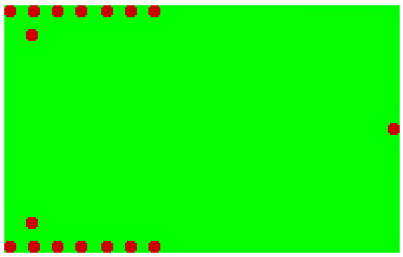 |
| 5 | 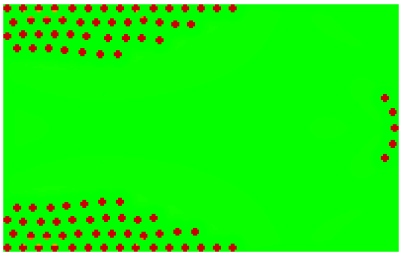 | 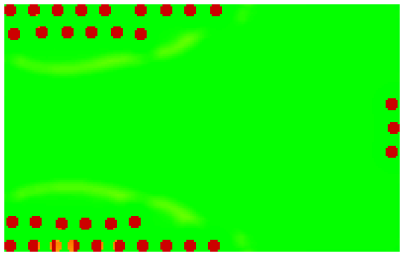 |
| 12.5 | 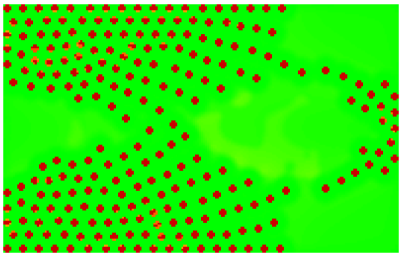 | 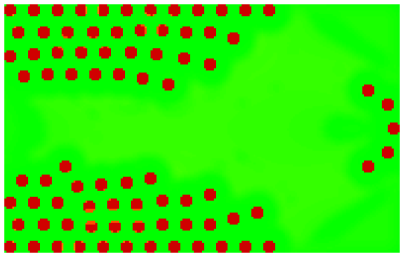 |
| 15 | 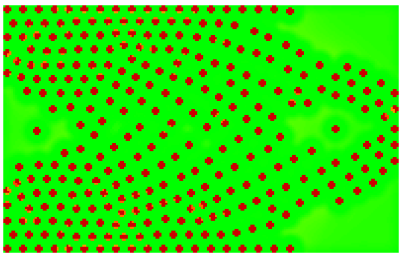 | 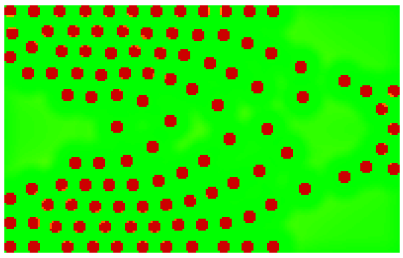 |

* $V_{s,\text{given}}$ is presented as % of $V_T$.

respectively. Interestingly, we observe that cantilever beams with larger reinforcement particles perform better than those with smaller reinforcement particles. This is because, with larger particles, there are larger area of stiff phase near the locations of highest stress, such as at the applied load and near the top and bottom corners of the fix support, which yields stiffer structure.

**Table 3.3:** Compliance and stiffness gain of optimized cantilever beam solutions using two-phase DOP method for $r_{\min_D} = [0.4, 0.6]$ and $V_s = [2.5\%, 5\%, 12.5\%, 15\%]$.

| $V_s$ (%) | $r_{\min_D} = 0.4$ | | $r_{\min_D} = 0.6$ | |
|---|---|---|---|---|
| | Compliance | Stiffness gain (%)† | Compliance | Stiffness gain (%)† |
| 0 | 23.74 | 0 | 23.74 | 0 |
| 2.5 | 21.03 | 11.4 | 20.76 | 12.5 |
| 5 | 20.23 | 14.8 | 19.76 | 16.8 |
| 12.5 | 19.17 | 19.3 | 18.62 | 21.5 |
| 15 | 18.98 | 20.0 | 18.48 | 22.2 |

† These values represent percent stiffness gains over the unreinforced cantilever beam.

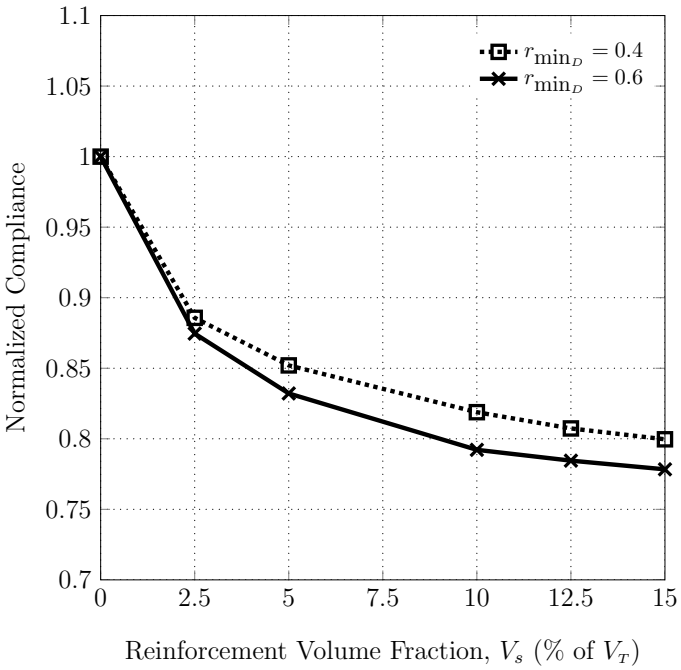


**Figure 3.16:** Normalized compliance for optimized cantilever beam solutions for different particle sizes and reinforcement volume fractions; All values are normalized with the corresponding values for the unreinforced cantilever beam.

#### 3.1.2.2.2 MBB Beam

The geometry and loading condition of the simply supported beam problem is shown in Figure 3.17 with domain length $L = 60$, height $H = 20$, and unit load $P$. The finite element mesh for this problem is $240 \times 80$. For this problem, we perform topology optimization for two different stiff particle sizes: (1) $r_{\min_D} = 0.5$ units with minimum spacing between discrete stiff objects $t_E = 2 * r_{\min_D} = 1.0$ units, and (2) $r_{\min_D} = 0.75$ units with minimum spacing between discrete stiff objects $t_E = 2 * r_{\min_D} = 1.5$ units. We also vary the maximum volume of the stiff phase

to be 2.5%, 7.5%, 10%, and 15% for both particle size, with an extra case of 20% reinforcement volume fraction for $r_{\min_D} = 0.75$. We also impose symmetry about vertical axis passing through the applied load (i.e. only right-half of the beam is considered) to reduce the number of design variables, and apply a technique proposed in Section 3.2.1.4 to prevent overlapping objects near the line of symmetry.

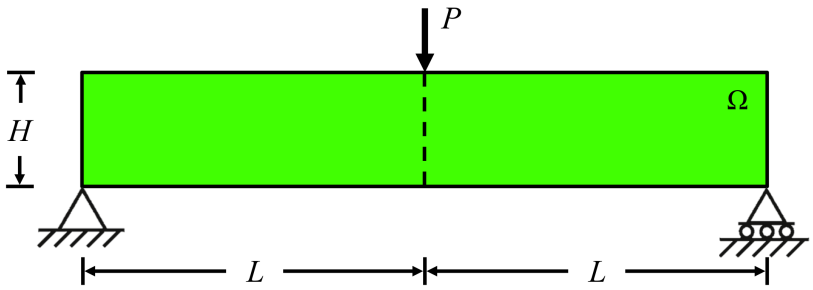


**Figure 3.17:** MBB beam domain for two-phase design.

Table 3.4 shows the optimized solutions for the two different particle sizes and five different reinforcement particle volume fractions. As in the case of cantilever beam, we again see that the algorithm produce solutions that have identifiable discrete circular objects and these objects satisfy the given length scale $r_{\min_D}$ and minimum required spacing $t_E$. We also see that in the case of low particle volume fraction, the algorithm places the stiff object in high strain energy regions first. The placement of these particles matches the location of the applied load, the regions hear the boundary conditions, and the upper and lower edges where highest stress and bending moment exist (see Figure 3.18). We also observe a similar trend for MBB problem where

the layout of these particles resembles the traditional topology-optimized MBB beam solution as the volume of stiff phase increases. Looking at the von Mises stress plot in Figure 3.18 and the optimized solutions in Table 3.4, we can see that the layout of these particles follows the contour of the stress plot, which is as expected.

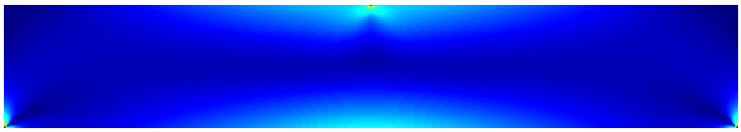

**Figure 3.18:** Plot of von Mises stress of MBB beam with boundary and loading conditions in Figure 3.14.

Similar to the cantilever beam problem, we observe a remarkable improvement in stiffness as reinforcement volume increases. In this example, the stiffness of the cantilever beam increased by 11.7% and 12.8% using only 2.5% reinforcement volume fraction for $r_{\min_D} = 0.5$ and $r_{\min_D} = 0.75$, respectively. Again, we see that solutions with larger reinforcement particles yield better performance compared to those with smaller reinforcement particles. Looking at the optimized solutions for reinforcement volume fraction of 2.5%, we can see that one large stiff particle is preferred over two smaller ones at the supports since the area of one large stiff particle is larger than the combined area of two smaller particles. This makes sense because larger particles can provide stiffness over the larger area inside high stress region.

**Table 3.4:** Optimized solutions for MBB beam problem using two-phase DOP method for $r_{\min_D} = [0.5, 0.675]$ and $V_s = [2.5\%, 7.5\%, 10\%, 15\%, 20\%]$.

| $V_{s,\text{given}}$ (%)* | $r_{\min_D} = 0.5$ | $r_{\min_D} = 0.75$ |
|---|---|---|
| 2.5 | 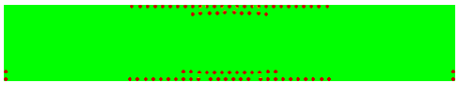 | 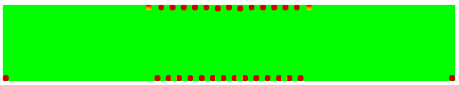 |
| 7.5 | 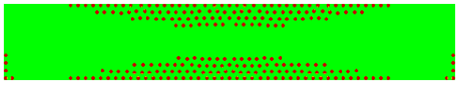 | 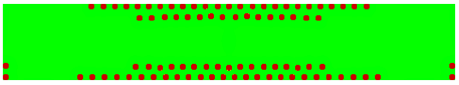 |
| 10 | 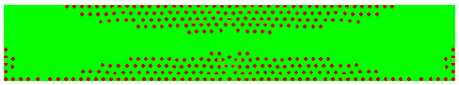 | 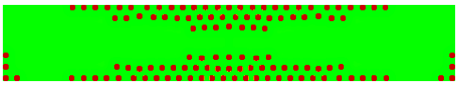 |
| 15 | 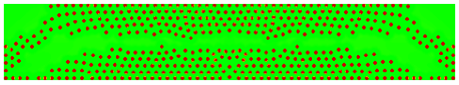 | 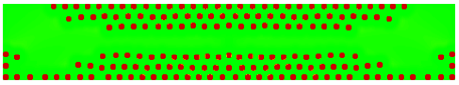 |
| 20 | | 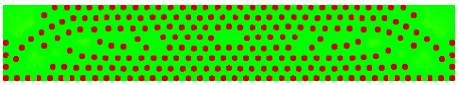 |

* $V_{s,\text{given}}$ is presented as % of $V_T$.

**Table 3.5:** Compliance and stiffness gain of optimized MBB beam solutions using two-phase DOP method for $r_{\min_D} = [0.5, 0.675]$ and $V_s = [2.5\%, 7.5\%, 10\%, 15\%, 20\%]$.

| $V_s$ (%) | $r_{\min_D} = 0.5$ | | $r_{\min_D} = 0.75$ | |
|---|---|---|---|---|
| | Compliance | Stiffness gain (%)† | Compliance | Stiffness gain (%)† |
| 0 | 130.76 | 0 | 130.76 | 0 |
| 2.5 | 115.43 | 11.7 | 114.01 | 12.8 |
| 7.5 | 107.58 | 17.7 | 105.06 | 19.7 |
| 10 | 106.03 | 18.9 | 103.03 | 21.2 |
| 15 | 103.97 | 20.5 | 100.84 | 22.9 |
| 20 | | | 99.70 | 23.8 |

† These values represent percent stiffness gains over the unreinforced MBB beam.

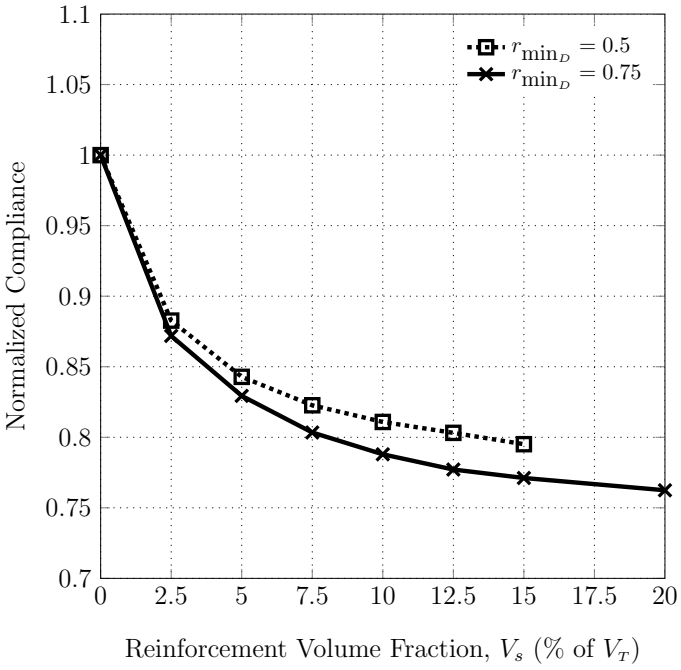


**Figure 3.19:** Normalized compliance for optimized MBB beam solutions for different particle sizes and reinforcement volume fractions; All values are normalized with the corresponding values for the unreinforced MBB beam.

#### 3.1.2.2.3 L-Bracket

The geometry and loading condition for the L-bracket problem is illustrated in Figure 3.20 with domain length $L = 40$, height $H = 20$, and unit load $P \times 10$ and the size of each finite element for this problem is 0.2 unit by 0.2 unit. Like the cantilever beam problem, we perform topology optimization for two different stiff particle sizes $r_{\min_D}$ of 0.4 and 0.6 units with minimum spacing between discrete stiff objects $t_E$ of 0.8 and 1.2 units, respectively. We also vary the maximum volume of the stiff phase to be 2.5%, 5%, 12.5%, and 15%.

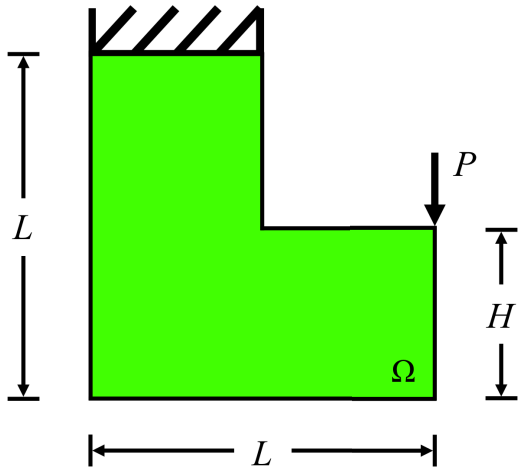


**Figure 3.20:** L-bracket domain for two-phase design.

Table 3.6 shows the optimal L-bracket solutions for the two different particle sizes and four different reinforcement particle volume fractions. As in the case of cantilever beam and MBB beam problems, we again clearly see non-overlapping circular objects. These reinforcing objects are placed in the order of strain energy magnitudes, which

are the highest at the location of the point load, the vertical faces near the supports, and the inner corner where stress concentration occurs (see Figure 3.21). We especially see higher concentration of particles near the inner corner for this problem. As the volume of the stiff phase becomes more available, the optimized layout of these particles resemble the traditional topology-optimized L-bracket solutions.

**Figure 3.21:** Plot of von Mises stress of L-bracket with boundary and loading conditions in Figure 3.20.

Similar to the cantilever beam and MBB beam problems, the compliance decreases as the reinforcement volume increases. In this example, the stiffness of the cantilever beam is improved by 11.6% and 13.0% using only 2.5% reinforcement volume fraction for $r_{\min_D} = 0.4$ and $r_{\min_D} = 0.6$, respectively. We again observe that optimized L-brackets with bigger reinforcing particles are stiffer than those with smaller particles.

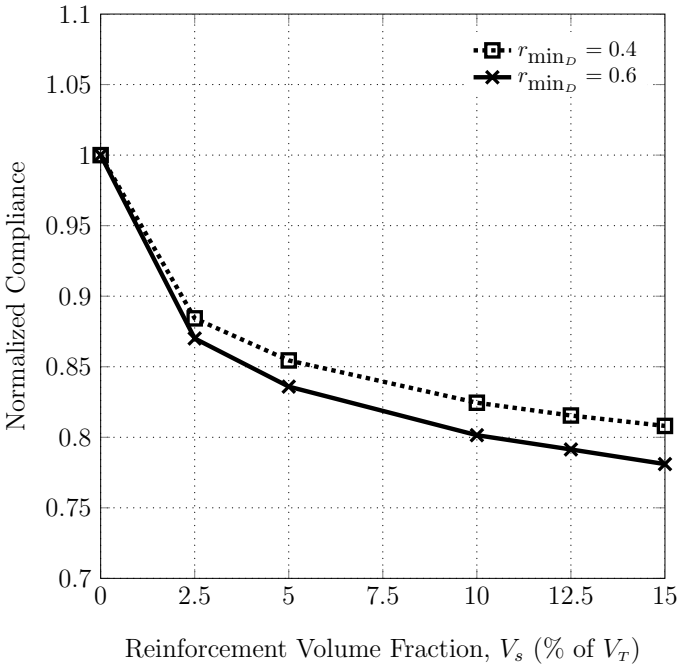


**Figure 3.22:** Normalized compliance for optimized L-bracket solutions for different particle sizes and reinforcement volume fractions; All values are normalized with the corresponding values for the unreinforced L-bracket.

**Table 3.6:** Optimized solutions for L-bracket problem using two-phase DOP method for $r_{\min_D} = [0.4, 0.6]$ and $V_s = [2.5\%, 5\%, 12.5\%, 15\%]$.

| $V_{s,\text{given}}$ (%)* | $r_{\min_D} = 0.4$ | $r_{\min_D} = 0.6$ |
|---|---|---|
| 2.5 | 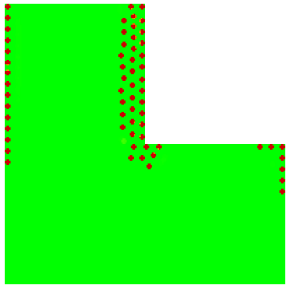 | 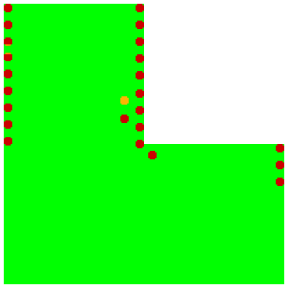 |
| 5 | 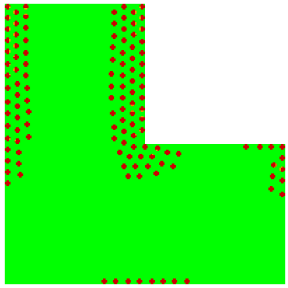 | 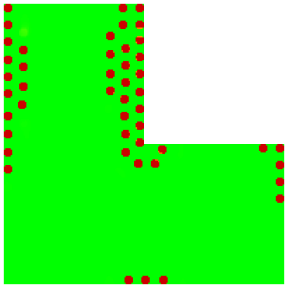 |
| 12.5 | 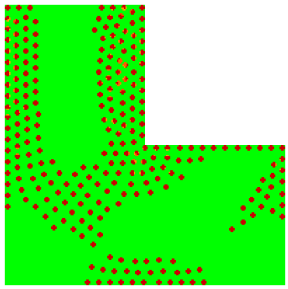 | 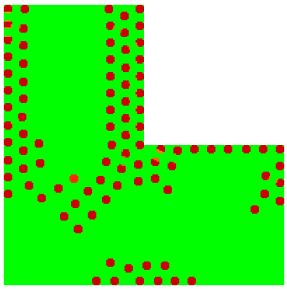 |
| 15 | 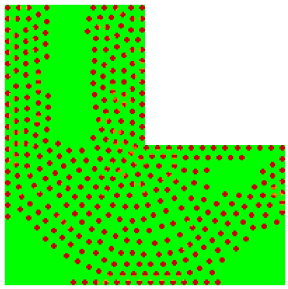 | 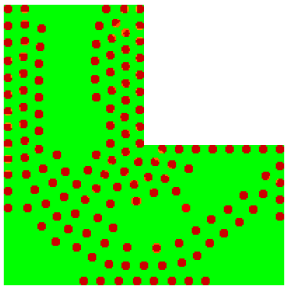 |

* $V_{s,\text{given}}$ is presented as % of $V_T$.

**Table 3.7:** Compliance and stiffness gain of optimized L-bracket solutions using two-phase DOP method for $r_{\min_D} = [0.4, 0.6]$ and $V_s = [2.5\%, 5\%, 12.5\%, 15\%]$.

| $V_s$ (%) | $r_{\min_D} = 0.4$ | | $r_{\min_D} = 0.6$ | |
|---|---|---|---|---|
| | Compliance | Stiffness gain (%)† | Compliance | Stiffness gain (%)† |
| 0 | 58.31 | 0 | 58.31 | 0 |
| 2.5 | 51.56 | 11.6 | 50.73 | 13.0 |
| 5 | 49.83 | 14.6 | 48.74 | 16.4 |
| 12.5 | 47.55 | 17.5 | 46.15 | 19.9 |
| 15 | 47.12 | 19.2 | 45.54 | 21.9 |

† These values represent percent stiffness gains over the unreinforced L-bracket.

#### 3.1.2.2.4 Summary

The author performed and tested the DOP method originally proposed by Guest (2011, 2015) for optimizing the placement of discrete reinforcing objects in structure on several benchmark example problems. Similar solution trends can be observed between all different benchmark example problems in which the particles are strategically placed in the locations of high strain energy when reinforcement volume is limited. These results also show similar trends in optimal layout of discrete objects as presented in Guest (2015), where the objects are clearly identifiable and satisfy prescribed minimum spacing $t_E$. This is made possible by allowing each design variable to project stiff phase enclosed inside compliant phase and tailoring the projection interactions so that discrete objects are achieved implicitly without any constraint on the design variables.

The advantage of this approach is that the free-form nature of traditional topology optimization is maintained since no additional constraint is required. This approach has been extended to allow the shape and size of the object to also be optimized (Guest and Ha, 2014), including selection among a set of objects (Guest, 2014). To date, however, the DOP approach applies topology optimization to only two phases: either two materials or one material and a void. This work proposes the extension of this idea to multi-material design where the topology of the components is also optimized.

## 3.2 Three-Phase Discrete Object Projection

Although significant research has been conducted on improving design solutions by considering manufacturability, past work has focused mostly on single-component structures or structures that are monolithic in nature. Besides the aforementioned work by (Gaynor et al., 2013; Guest, 2011, 2014, 2015; Guest and Ha, 2014; Yang et al., 2015b), significantly less work has been conducted in the area of topology optimization of embedded objects and multicomponent structures.

Kato and Ramm (2010) proposed a material shape optimization to maximize the ductility of fiber-reinforced concrete with respect to fiber locations and orientations. This method approximates the fiber geometry using a quadratic Bézier-splines, which is defined by a set of control points. The locations of the control points of the splines are optimized to obtain the optimal fiber lengths, locations, and curvatures. This work is later extended by Kato and Ramm (2013) to allow for variation of fiber thickness, where the fibers with thickness close to zero are considered to have no physical contributions. While the latter approach allows for fibers to disappear, the fiber thicknesses are no longer fixed, which may not be a desire quality in certain manufacturing processes. In both of these approaches, topology of the concrete is not optimized.

Qian and Ananthasuresh (2004) propose a methodology in which the locations and orientations of rigid objects are optimized simultaneously with the topology of the connecting structure. In their work, the design variables are defined with respect to fixed finite element mesh, which causes a discontinuity of material variation along the edges of the embedded objects when the objects move around the design domain during topology optimization. To overcome this discontinuity, they approximate the geometric domains of embedded objects using a peak function material interpolation scheme (Yin and Ananthasuresh, 2001). This essentially permits the use of gradient-based optimization and allows the embedded objects to freely move around the design domain during topology optimization iterations without the need for finite element remeshing. One of the disadvantages of this method is that avoiding mesh dependency comes at a cost of the exact shape of the embedded objects being neglected.

To circumvent the discontinuity of material variation, Zhu et al. (2008) propose an alternative method called coupled shape and topology optimization, in which a density point and embedded mesh technique is introduced. In this technique, the design variables are associated with density points, which are a set of points defined on a fixed finite element mesh referred to as basic mesh. As the embedded objects change location within the design domain, another mesh, called embedded mesh, is created on top of the basic mesh and the finite element region inside the objects is remeshed to matched the shape of the object. Each element in the embedded mesh then receives its pseudo-density value from the density point closest to it. This technique is similar

to the HPM methodology with regards to defining design variables separately from the physical design domain. One major difference, however, lies in that the density point and embedded mesh technique requires remeshing of the embedded objects at every optimization iteration, which can be computationally expensive, while HPM creates and stores projection information prior to optimization.

One of the most important aspects in the design of multicomponent structures or structures with discrete embedded objects is to keep the objects from overlapping. Both Qian and Ananthasuresh (2004) and Zhu et al. (2008) impose additional constraints associated with each of the embedded objects inside the design domain. The former encloses each object inside a circle or an ellipse, while the latter uses a family of circumcircles to define both the shape of the embedded objects and the overlapping constraints. In Kato and Ramm (2010, 2013), the fiber objects in can be overlapped and merge into one fiber with multiple ends that can have different lengths and curvatures. Unlike the DOP method, the minimum distance between each objects cannot be defined in these methods, at least not without adding more constraints to the problem.

Another major difference between the DOP method and the above methods is that the DOP method posses the free-from nature that exists in traditional topology optimization. This simply means that the embedded objects can be created, removed, or translated at any point during optimization without requiring any remeshing or any additional constraints (Guest, 2015). More importantly, DOP method does not

require predefining the number of embedded objects inside the design domain, which can be a major advantage in the cases where optimal number of discrete objects are not known *a priori* or is of interest, such as minimizing the number of objects to achieve a target performance metric. In the above methods, the numbers of objects are prefixed, and while objects are allowed to disappear in Kato and Ramm (2013), new objects cannot be created.

### 3.2.1 Three-Phase Discrete Object Projection Formulations

The key difference between the original DOP design method and the multi-material DOP design method is that the latter has an option to project three, instead of two, different phases which are: (1) discrete object phase, which is assumed stiff herein, (2) continuous compliant phase, and (3) void phase (see Figure 3.23). To implement the multi-material DOP method, we utilize a multi-phase topology optimization method proposed by Bendsøe and Sigmund (Bendsøe and Sigmund, 1999), in which an additional set of design variables, which we refer to as $\boldsymbol{\phi}_T$, is used to determine optimal topology of the structure (either material or void). Figure 3.24 illustrate the concept of additional design variable space. Each of these spaces has its own projection mapping information independent from one another.

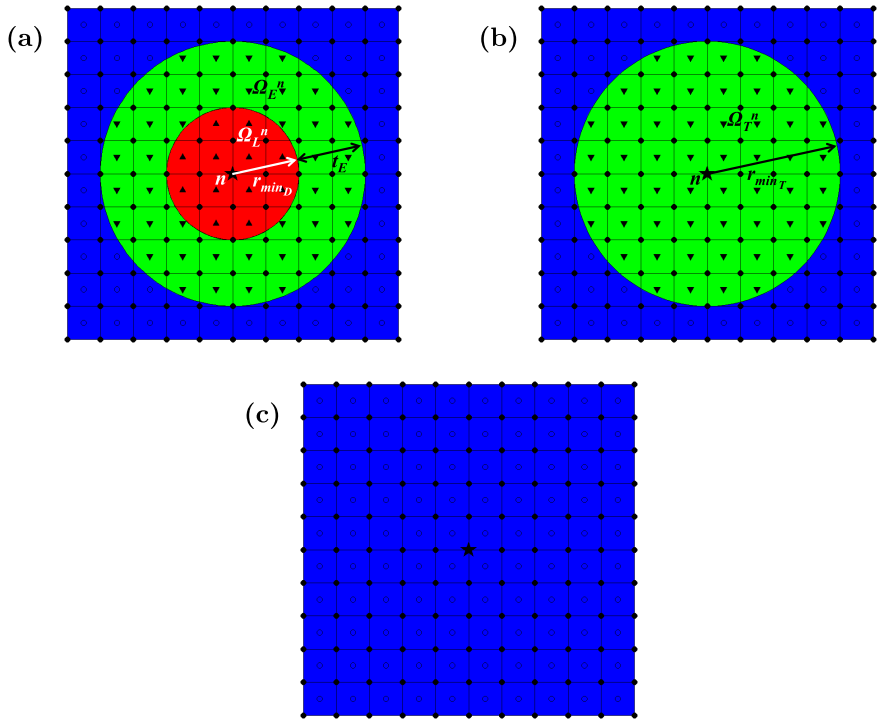


**Figure 3.23:** Discrete object projection from design variable $n$. (a) a projection of discrete stiff object (red) enclosed in compliant material (green), (b) a projection of compliant material, and (c) no projection resulting in void (blue).

The mapping of $\boldsymbol{\phi}_T$ to the physical design space is expressed, similar to Eq. (3.1), as:

$$i \in N_T^e \qquad \text{if } \|\mathbf{x}_i - \bar{\mathbf{x}}^e\| \leq r_{\min_T} \tag{3.8}$$

where $N_T^e$ is the topology neighborhood set and $r_{\min_T}$ is the minimum length scale (or thickness) of the design feature as illustrated in Fig. 3.23b. The element's topology $\rho_T$ is determined from design variable set $\boldsymbol{\phi}_T$ using standard regularized Heaviside

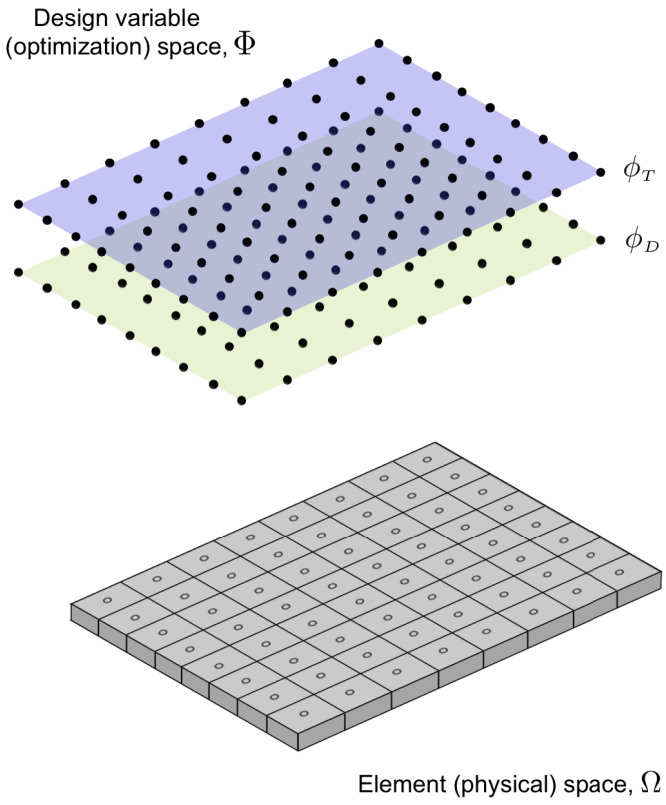


**Figure 3.24:** Illustration of design variable (optimization) space $\Phi$ and physical element space $\Omega$ for three-phase DOP method projecting a single discrete object type, where design variable $\boldsymbol{\phi}_T$ projects component topology (Figures 3.23b-3.23c) and design variable $\boldsymbol{\phi}_D$ projects circular discrete object (Figure 3.23a).

functions, similar to Eq. (3.2), as:

$$\rho_T^e = 1 - e^{-\beta_T \mu_T^e(\boldsymbol{\phi}_T)} + \frac{\mu_T^e}{\phi_{\max}}(\boldsymbol{\phi}_T) e^{-\beta_T \phi_{\max}} \tag{3.9}$$

and $\mu_T^e$ corresponding to topology is calculated using standard weighted averaging similar to Eq. (3.3):

$$\mu_T^e = \frac{\sum\limits_{i \in N_T^e} \phi_{T,i} w_T(\mathbf{x}_i - \bar{\mathbf{x}}^e)}{\sum\limits_{i \in N_T^e} w_T(\mathbf{x}_i - \bar{\mathbf{x}}^e)} \tag{3.10}$$

The function $w$ in Eq. (3.10) represents the weighting function associated with each design variable and here uniform weighting function is chosen, which can be computed similar to Eq. (3.4) as:

$$w_T(\mathbf{x}_i - \bar{\mathbf{x}}^e) = \left\{ \begin{array}{ll} 1 & \text{if } \mathbf{x}_i \in \Omega_T^i \\ \\ 0 & \text{otherwise} \end{array} \right\}. \tag{3.11}$$

In the multi-material DOP method, the material stiffness of an element can be expressed as (Bendsøe and Sigmund, 1999):

$$E^e(\boldsymbol{\phi}_D, \boldsymbol{\phi}_T) = \rho_T^e(\boldsymbol{\phi}_T)\Big(E_1 + \rho_D^e(\boldsymbol{\phi}_D)(E_2 - E_1)\Big) \tag{3.12}$$

where $E_1$ and $E_2$ are Young's modulus of the compliant and stiff phases, respectively. As can be observed in Eq. (3.12), the modulus of each element $E^e$ is the function of both $\rho_D$ and $\rho_T$ (and their corresponding independent design variables $\boldsymbol{\phi}_D$ and $\boldsymbol{\phi}_T$). If both $\rho_D$ and $\rho_T$ are equal to 1, then the element takes on a modulus of $E_2$. If $\rho_D = 0$ and $\rho_T = 1$, then $E^e = E_1$. If $\rho_T = 0$, then $E^e = 0$ (i.e. void), regardless of the value of $\rho_D$.

In free-form topology optimization, the design evolution can take on intermediate volume fractions (or gray regions), which are undesireable. In the proposed method, these gray regions can also result from an element receiving both stiff and compliant materials or phase mixing (i.e. $\rho_D^e = 0.5$ if both $\rho_L^e$ and $\rho_E^e$ are equal to 1) (Guest,

2015), creating overlapping objects instead of discrete objects. Here, we apply the Rational Approximation of Material properties (RAMP) method (Stolpe and Svanberg, 2001) to prevent the intermediate volume fractions and, consequentially, produce clear discrete objects. The penalization of element phase stiffness (Eq. (3.12)) using RAMP method can be expressed as:

$$E^e(\boldsymbol{\phi}_D, \boldsymbol{\phi}_T) = \frac{\rho_T^e(\boldsymbol{\phi}_T)}{1 \ + \ \eta\Big(1 - \rho_T^e(\boldsymbol{\phi}_T)\Big)} \left( E_1 + \frac{\rho_D^e(\boldsymbol{\phi}_D)}{1 \ + \ \eta\Big(1 - \rho_D^e(\boldsymbol{\phi}_D)\Big)} (E_2 - E_1) \right) \quad (3.13)$$

where $\eta \geq 0$ is the penalty term. When $\eta > 0$, the stiffness of phase mixing or gray regions is reduced resulting in inefficient material and driving the solutions to 0/1 topologies. In the previous work related to DOP done by Guest (2015), it was found that the optimization generally performs better using RAMP method than the Solid Isotropic Material with Penalization (SIMP) method (Bendsøe, 1989) in the context of a stiff feature enclosed in compliant matrix material. This is because there is a need to create material at locations where $\rho^e = 0$. In the RAMP method, the derivative of the modulus is non-zero at this point, compared to SIMP where the derivative is zero when the exponential penalty term $p > 1$ at these locations.

#### 3.2.1.1 Objective Function and Constraints

The proposed multi-material design algorithm is demonstrated on minimum compliance (maximum stiffness) topology optimization problems. The problem formula-

tion can be expressed as:

$$\min_{\boldsymbol{\phi}_D, \boldsymbol{\phi}_T} \quad C = \mathbf{F}^{\mathrm{T}}\mathbf{d} \tag{3.14a}$$

$$\text{s.t.} \quad \mathbf{K}(\boldsymbol{\phi}_D, \boldsymbol{\phi}_T)\mathbf{d} = \mathbf{F} \tag{3.14b}$$

$$\sum_{\forall e \in \Omega} \rho_T^e(\boldsymbol{\phi}_T) v^e \leq V_T \tag{3.14c}$$

$$\sum_{\forall e \in \Omega} \rho_D^e(\boldsymbol{\phi}_D) \rho_T^e(\boldsymbol{\phi}_T) v^e \leq V_s \tag{3.14d}$$

$$0 \leq \phi_i \leq \phi_{max} \quad \forall i \in \Omega \tag{3.14e}$$

where $C$ is compliance, $\mathbf{F}$ are the nodal applied loads, $\mathbf{d}$ are the nodal displacements, $\mathbf{K}$ is the global stiffness matrix, $v^e$ is the elemental volume, $V_T$ is the maximum allowable volume of the total material used in the structure, $V_s$ is the maximum allowable volume of the stiff phase, and $\phi_{max}$ is the upper bound of the design variable. In this work, we follow the guideline established by Guest (2015) on the choice of magnitude of $\phi_{max}$ in relation to finite element mesh size.

We also demonstrate our proposed algorithm on maximum negative displacement topology optimization problems for design of compliant mechanism or inverter. The

general formulation of this problem can be expressed as:

$$\min_{\boldsymbol{\phi}_D, \boldsymbol{\phi}_T} \quad C = \mathbf{L}^{\mathrm{T}}\mathbf{d} \tag{3.15a}$$

$$\text{s.t.} \quad \mathbf{K}(\boldsymbol{\phi}_D, \boldsymbol{\phi}_T)\mathbf{d} = \mathbf{F} \tag{3.15b}$$

$$\sum_{\forall e \in \Omega} \rho_T^e(\boldsymbol{\phi}_T) v^e \leq V_T \tag{3.15c}$$

$$\sum_{\forall e \in \Omega} \rho_D^e(\boldsymbol{\phi}_D)\rho_T^e(\boldsymbol{\phi}_T) v^e \leq V_s \tag{3.15d}$$

$$0 \leq \phi_i \leq \phi_{max} \quad \forall i \in \Omega \tag{3.15e}$$

where $\mathbf{d}$ is the nodal displacement vector and $L$ is a unit vector that extracts displacement at the output port. Solutions obtained using Eq. (3.15) may contain one-node connected hinges, which is when two solid elements are connected at the corner node. This issue is related to the hinges in the well-known checkerboard problem in topology optimization where the stiffness of these one-node hinges is overestimated when modeled with low-order finite elements (such as four-node or nine-node quadratic displacement finite elements) (Díaz and Sigmund, 1995; Jog and Haber, 1996; Sigmund, 1997; Sigmund and Petersson, 1998; Yin and Ananthasuresh, 2003). While introducing additional constraints (Haber et al., 1996; Petersson and Sigmund, 1998; Poulsen, 2003) or using filtering techniques (Bruns and Tortorelli, 2001; Guest et al., 2004; Sigmund, 2007) is successful in eliminating checkerboard issues, they are not entirely successful in removing one-node hinges. In projection methods, for instance, a one-node hinge can manifest from projections of two tangent circles (Guest et al., 2004).

Moreover, these one-node hinges present further problem in regards to manufacturability and manufacturing uncertainties. In particular, even if the device containing one-node hinges is manufactured without any imperfection, it would fail instantly due to high stress concentration at the hinges.

A number of studies have been conducted to combat the vulnerability to manufacturing uncertainties due to one-node hinges in the context of compliant inverter (Gaynor et al., 2014; Jansen et al., 2013; Lou et al., 2008; Schevenels et al., 2011; Sigmund, 2009). In this work, we apply a robust formulation proposed by Gaynor et al. (2014), which is based on idea proposed by Sigmund (2009). In the work of Sigmund (2009), manufacturing uncertainties is included in the topology optimization process by using morphology operators "erode" and "dilate" to simulate over-etching and over-depositing. The objective of the optimization problem becomes a min-max formulation, i.e. maximization of negative displacement for the worst case of the erode, dilate, and original density distributions. The key idea is that if one-node hinges exists in the structure, the "erode" operator makes the structure disconnected and not functional. While this method successfully prevent the presence of one-node hinges, over-etching modeled by the erode operator uses an inverse of the Heaviside filter, which represent subtractive manufacturing process instead of additive manufacturing process.

Gaynor et al. (2014) proposed a slightly different version of Sigmund's formulation, which better represent the additive manufacturing process. The idea in Gaynor et al.

(2014) is to represent manufacturing uncertainties as the under-depositing and over-depositing of material in the additive manufacturing process by varying the minimum length scale $r_{\min_T}$. The resulting min-max problem formulation combined with multi-phase DOP method is expressed as:

$$\min_{\boldsymbol{\phi}_D, \boldsymbol{\phi}_T} \quad C = \max \left\{ \mathbf{L}^{\mathrm{T}} \mathbf{d}_{\left(r_{\mathrm{minsmall}_T}\right)}, \mathbf{L}^{\mathrm{T}} \mathbf{d}_{\left(r_{\mathrm{minlarge}_T}\right)} \right\} \tag{3.16a}$$

$$\text{s.t.} \quad \mathbf{K}\left( \boldsymbol{\phi}_D, \boldsymbol{\phi}_{T_{\left(r_{\mathrm{minsmall}_T}\right)}} \right) \mathbf{d}_{\left(r_{\mathrm{minsmall}_T}\right)} = \mathbf{F} \tag{3.16b}$$

$$\mathbf{K}\left( \boldsymbol{\phi}_D, \boldsymbol{\phi}_{T_{\left(r_{\mathrm{minlarge}_T}\right)}} \right) \mathbf{d}_{\left(r_{\mathrm{minlarge}_T}\right)} = \mathbf{F} \tag{3.16c}$$

$$\sum_{\forall e \in \Omega} \rho_T^e \left( \boldsymbol{\phi}_{T_{\left(r_{\min_T}\right)}} \right) v^e \leq V_T \tag{3.16d}$$

$$\sum_{\forall e \in \Omega} \rho_D^e \left( \boldsymbol{\phi}_D \right) \rho_T^e \left( \boldsymbol{\phi}_{T_{\left(r_{\min_T}\right)}} \right) v^e \leq V_s \tag{3.16e}$$

$$0 \leq \phi_i \leq \phi_{max} \quad \forall i \in \Omega \tag{3.16f}$$

where the two additional length scales $r_{\mathrm{minsmall}_T}$ and $r_{\mathrm{minlarge}_T}$ are the smaller and larger projections of design variable $\phi_T$. These lengths scales are defined as:

$$r_{\mathrm{minsmall}_T} = r_{\min_T} - \Delta r \tag{3.17a}$$

$$r_{\mathrm{minlarge}_T} = r_{\min_T} + \Delta r \tag{3.17b}$$

where $\Delta r$ is a small positive variation in the length scale. For this problem, the projection information must be obtained and stored for $r_{\mathrm{minsmall}_T}$ and $r_{\mathrm{minlarge}_T}$ in addition to $r_{\min_T}$.

As seen in Eqs. (3.14) and (3.16), the proposed multi-material DOP algorithm gives designer control over the volume of the stiff objects in addition to the volume of the entire structure. When $V_s$ is set to be at 100% of the total allowable volume of material used in the structure $V_T$ (i.e. $V_s = V_T$), we have what we refer to as a "packing" problem, where we expect to see the algorithm pack as many discrete objects into the structure as it can without violating the required minimum distance between each discrete objects ($t_E$) since the constraint on the volume of stiff material is inactive in this particular case.

#### 3.2.1.2 Sensitivities

The sensitivities of the objective function $C$ in the multi-material DOP method follows the original DOP method outlined in the previous works (Guest, 2014, 2015; Guest and Ha, 2014) with additional sensitivity terms on $\boldsymbol{\phi}_T$ and the sensitivity terms on $\boldsymbol{\phi}_D$ are also included here for convenience:

$$\frac{\partial C}{\partial \phi_{D,i}} = \sum_{\forall e \in \Omega} \frac{\partial C}{\partial \rho_D^e} \frac{\partial \rho_D^e}{\partial \phi_{D,i}} \qquad \forall i \in \boldsymbol{\phi}_D \tag{3.18}$$

and

$$\frac{\partial C}{\partial \phi_{T,i}} = \sum_{\forall e \in \Omega} \frac{\partial C}{\partial \rho_T^e} \frac{\partial \rho_T^e}{\partial \phi_{T,i}} \qquad \forall i \in \boldsymbol{\phi}_T \tag{3.19}$$

where the derivatives of the objective function with respect to $\rho_D^e$ and $\rho_T^e$ can be calculated using the adjoint method. For the minimum compliance formulation (Eq. (3.14),

the sensitivities of the objective function can be expressed as:

$$\frac{\partial C}{\partial \rho_D^e} = -\frac{\rho_T^e(\boldsymbol{\phi}_T)}{1+\eta\Big(1-\rho_T^e(\boldsymbol{\phi}_T)\Big)}\left(\frac{1+\eta}{\Big(1+\eta\Big(1-\rho_D^e(\boldsymbol{\phi}_D)\Big)\Big)^2}(E_2-E_1)\right)\mathbf{d}^{e^T}\mathbf{K}_0^e\mathbf{d}^e \quad (3.20)$$

$$\frac{\partial C}{\partial \rho_T^e} = -\frac{1+\eta}{\Big(1+\eta\Big(1-\rho_T^e(\boldsymbol{\phi}_T)\Big)\Big)^2}\left(E_1+\frac{\rho_D^e(\boldsymbol{\phi}_D)}{1+\eta\Big(1-\rho_D^e(\boldsymbol{\phi}_D)\Big)}(E_2-E_1)\right)\mathbf{d}^{e^T}\mathbf{K}_0^e\mathbf{d}^e \quad (3.21)$$

where $\mathbf{K}_0^e$ is the un-scaled element stiffness matrix for element $e$ and $\mathbf{d}^e$ is the nodal displacement vector for element $e$. For the maximum negative displacement formulation, the sensitivities of the objective function are expressed as:

$$\frac{\partial C}{\partial \rho_D^e} = -\frac{\rho_T^e(\boldsymbol{\phi}_T)}{1+\eta\Big(1-\rho_T^e(\boldsymbol{\phi}_T)\Big)}\left(\frac{1+\eta}{\Big(1+\eta\Big(1-\rho_D^e(\boldsymbol{\phi}_D)\Big)\Big)^2}(E_2-E_1)\right)\boldsymbol{\lambda}^{e^T}\mathbf{K}_0^e\mathbf{d}^e \quad (3.22)$$

$$\frac{\partial C}{\partial \rho_T^e} = -\frac{1+\eta}{\Big(1+\eta\Big(1-\rho_T^e(\boldsymbol{\phi}_T)\Big)\Big)^2}\left(E_1+\frac{\rho_D^e(\boldsymbol{\phi}_D)}{1+\eta\Big(1-\rho_D^e(\boldsymbol{\phi}_D)\Big)}(E_2-E_1)\right)\boldsymbol{\lambda}^{e^T}\mathbf{K}_0^e\mathbf{d}^e \quad (3.23)$$

where $\boldsymbol{\lambda}^e$ is the adjoint vector associated with element $e$ obtained from the global adjoint vector $\boldsymbol{\lambda}$, which is a solution to the adjoint problem $\mathbf{K}\boldsymbol{\lambda} = -\mathbf{L}$.

The partial derivative of element volume fraction for placing discrete object $\rho_D^e$ in Eq. (3.5) with respect to its corresponding design variable $\phi_{D,i}$ is computed using chain rule (Guest, 2014, 2015):

$$\frac{\partial \rho_D^e}{\partial \phi_{D,i}} = \frac{1}{2}\left(\Big(2-\rho_E^e\Big)\frac{\partial \rho_L^e}{\partial \phi_{D,i}} - \rho_L^e\frac{\partial \rho_E^e}{\partial \phi_{D,i}}\right) \quad (3.24)$$

where the inner partial derivative expressions for region $R$ where $R = L$ for local regions and $R = E$ for enclosure regions are:

$$\frac{\partial \rho_R^e}{\partial \phi_{D,i}} = \left( \beta_R e^{-\beta_R \mu_R^e(\boldsymbol{\phi}_D)} + \frac{1}{\phi_{\max}} e^{-\beta_R \phi_{\max}} \right) \frac{\partial \mu_R^e}{\partial \phi_{D,i}} \tag{3.25}$$

and the derivative of $\mu_R^e$ in Eq. (3.3) with uniform weighting function $w = 1$ (Eq. (3.4)) is

$$\frac{\partial \mu_R^e}{\partial \phi_{D,i}} = \frac{1}{\sum\limits_{i \in N_R^e} w_R(\mathbf{x}_i - \bar{\mathbf{x}}^e)} \tag{3.26}$$

The partial derivative of element volume fraction for creating topology $\rho_T^e$ in Eq. (3.9) with respect to its corresponding design variable $\phi_{T,i}$ is

$$\frac{\partial \rho_T^e}{\partial \phi_{T,i}} = \left( \beta_T e^{-\beta_T \mu_T^e(\boldsymbol{\phi}_D)} + \frac{1}{\phi_{\max}} e^{-\beta_T \phi_{\max}} \right) \frac{\partial \mu_T^e}{\partial \phi_{D,i}} \tag{3.27}$$

and the derivative of $\mu_T^e$ in Eq. (3.10) is

$$\frac{\partial \mu_T^e}{\partial \phi_{D,i}} = \frac{1}{\sum\limits_{i \in N_T^e} w_T(\mathbf{x}_i - \bar{\mathbf{x}}^e)} \tag{3.28}$$

Since the constraint function on the total volume $V_T$ in Eq. (3.14), which we will refer to as constraint function $g_T$, depends only on the design variables responding for placing material (i.e. creating topology), the sensitivity is thus:

$$\frac{\partial g_T}{\partial \phi_{T,i}} = \sum_{\forall e \in \Omega} v^e \frac{\partial \rho_T^e}{\partial \phi_{T,i}} \qquad \forall i \in \boldsymbol{\phi}_T \tag{3.29}$$

On the contrary, the constraint function on the stiff material volume $V_s$ in

Eq. (3.14), which we will refer to as constraint function $g_s$, depends on both sets of design variables and the sensitivities are expressed as:

$$\frac{\partial g_s}{\partial \phi_{D,i}} = \sum_{\forall e \in \Omega} \rho_T^e v^e \frac{\partial \rho_D^e}{\partial \phi_{D,i}} \qquad \forall i \in \boldsymbol{\phi}_D \tag{3.30}$$

and

$$\frac{\partial g_s}{\partial \phi_{T,i}} = \sum_{\forall e \in \Omega} \rho_D^e v^e \frac{\partial \rho_T^e}{\partial \phi_{T,i}} \qquad \forall i \in \boldsymbol{\phi}_T \tag{3.31}$$

#### 3.2.1.3 Optimizer

All problems in this work are solved using Method of Moving Asymptotes (MMA) (Svanberg, 1987, 1995) as the optimization algorithm. Although using continuation method on the Heaviside variable $\beta$ (i.e. $\beta_L$, $\beta_E$, and $\beta_T$) can be avoided as outlined in Guest et al. (2011), we have found that the continuation method generally improves convergence in this application. For most of problems and reinforcement volume fractions, we found that setting the HPM parameters $\beta_L$, $\beta_E$, and $\beta_T$ to gradually increase from 5 to 20 and set RAMP parameter $\eta$ to gradually increases from 0 to 15 in 9 continuation steps are sufficient to produce solutions with clear identifiable objects. In certain cases where solution contain discrete objects with intermediate volume fraction, increasing these parameters helps generate binary solutions. We also found that higher magnitudes of both parameters were needed in the case of the packing problems and also in the case of the compliant inverter. In the latter case, the higher penalization was needed to create binary solutions near the hinges.

#### 3.2.1.4 Restricting length scale near boundaries

As discussed in Guest (2015), applying the algorithm as presented will allow creation of partial objects, such as quarter- and semi-circular objects near the domain boundaries (see Figure 3.25a and 3.25b). To prevent development of partial discrete objects, a technique outlined in the 2-phase DOP method by Guest (2015) for restrict length scale near the design domain boundaries can be implemented in the proposed algorithm if full discrete objects are required. This is done by "turning off" the design variables located within the distance of $r_{\min_D} + s_{\text{edge}}$ from the domain boundary, where $s_{\text{edge}}$ is the minimum distance from the domain boundary to the edge of discrete object. Figures 3.25c and 3.25d illustrate this technique for $s_{\text{edge}} = 0$ and $s_{\text{edge}} = t_E$ where design variables marked with gray x-in-square symbols represent design variables that are "turned off". In this work, we set $s_{\text{edge}} = 0$, therefore requiring development of full discrete objects near the boundaries of the design domain.

With the implementation of symmetry in some benchmark examples, we need to restrict the length scale of stiff objects near the symmetry axis (in addition to restricting length scale near design domain boundaries) because the overlapping of objects can occur and different size objects may be created when the problem is in full view (see Figure 3.26a). In this work, we prevent this violation by "turning off" the design variables located between the symmetry line and $r_{\min_D} + t_E/2$ distance away from the symmetry line. In other words, the minimum distance from the symmetry line to the edge of a discrete object $s_{\text{edge}}$ equal to $t_E/2$ (see Figure 3.26b). The key

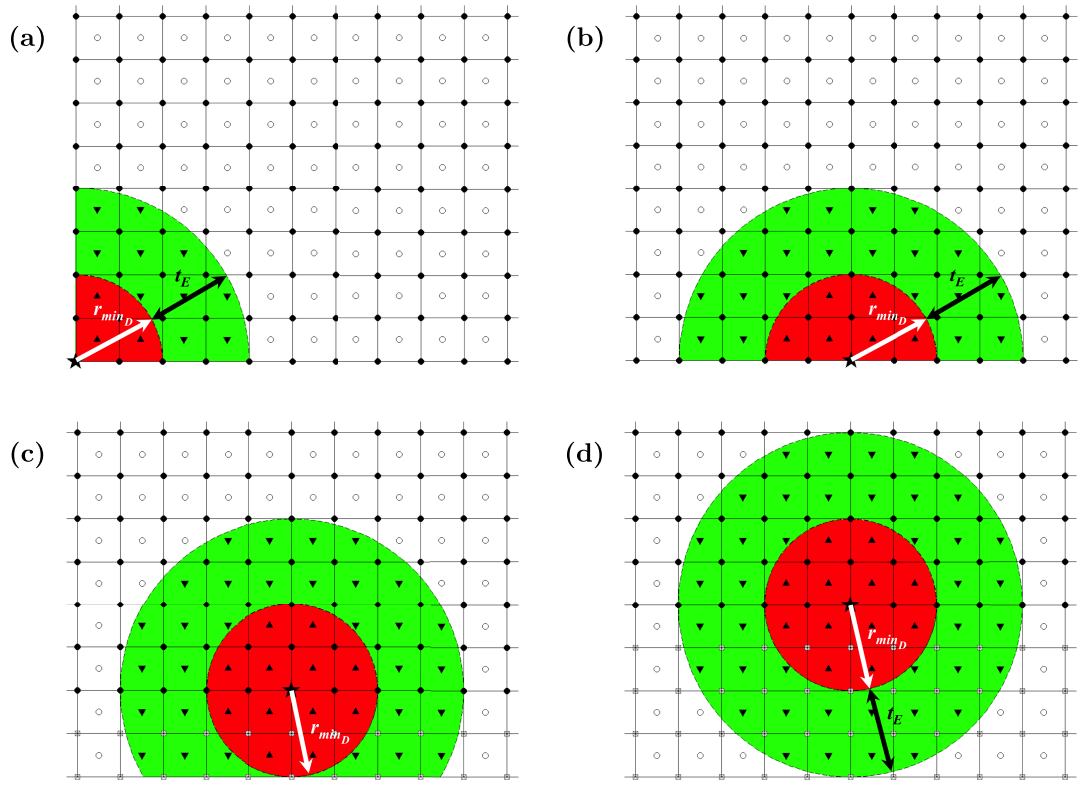


**Figure 3.25:** Boundary effects: (a) quarter-circular objects of radius $r_{\min_D}$, (b) semi-circular objects of radius $r_{\min_D}$, (c) full circular objects with $s_{\text{edge}} = 0$, (d) full circular objects with $s_{\text{edge}} = t_e$.

here is to leave design variables located on the symmetry line "turned on" to allow for creation of full discrete objects on symmetry line (see Figure 3.26c). When the domain is view in full, the minimum distance between the discrete objects between either side of the symmetry line satisfies minimum spacing $t_E$ and full objects are allowed to be created directly on the symmetry line (see Figures 3.26b and 3.26c).

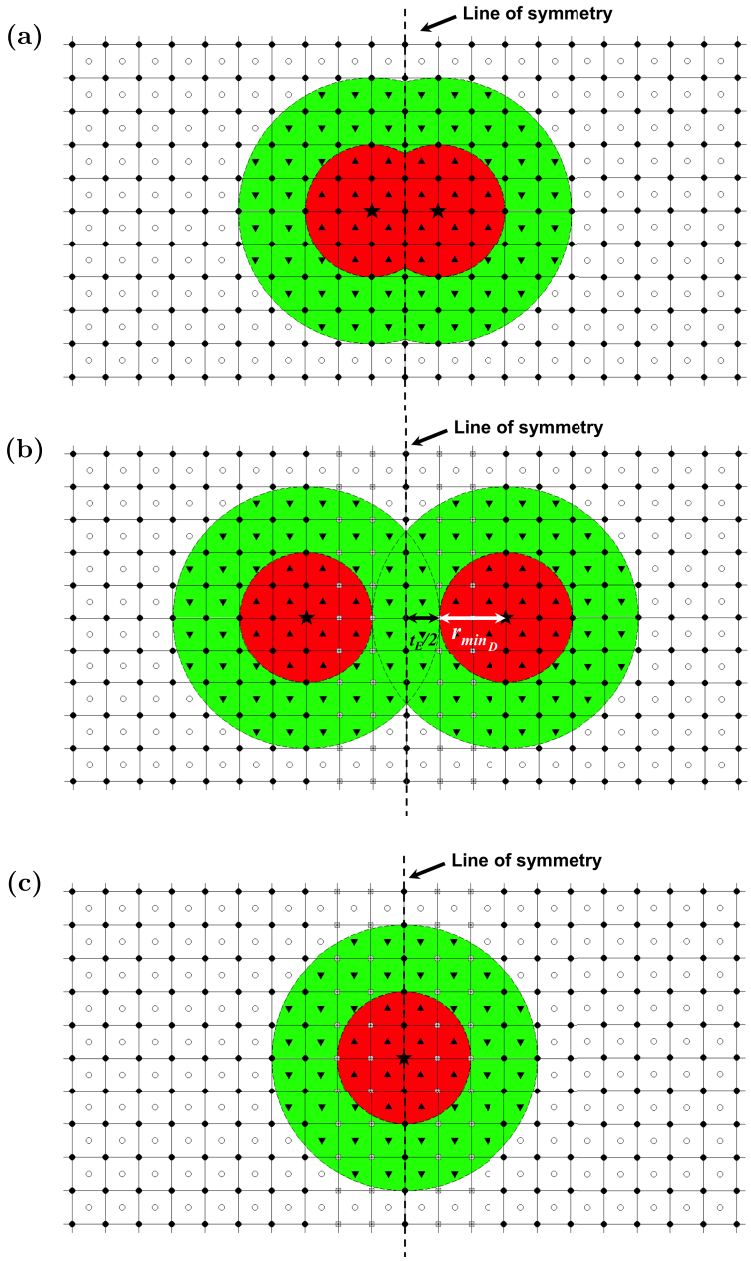


**Figure 3.26:** Boundary effects at the line of symmetry: (a) an example of objects overlapping when projecting design variables are located less than $r_{\min_D} + t_E/2$ distance away from the symmetry line, (b) an example of acceptable projection full circles satisfying minimum spacing $t_E$, and (c) a projection of circular discrete objects from design variable on the line of symmetry.

### 3.2.2 Numerical Examples and Solutions For Three-Phase Discrete Object Projection

The proposed multi-material DOP algorithm is demonstrated on benchmark cantilever beam, simply supported beam (MBB), L-bracket, and compliant inverter problems. All example problems use four-node quadrilateral elements and plane stress conditions are assumed with Poisson's ration of 0.3. The Young's moduli of stiff and compliant phases are one and one-third, respectively (i.e. $E_2/E_1 = 3$). Here, we set the upperbound on design variable $\phi_{\max} = 4$. We impose symmetry in the cases of MBB beam and compliant inverter, and therefore apply technique outlined in Section 3.2.1.4 for restricting length scale near the line of symmetry.

#### 3.2.2.1 Minimum compliance design of cantilever beam

The geometry and loading condition for the cantilever beam problem is illustrated in Figure 3.27. The domain is fixed at one end and a point load is applied at the midpoint of the free end. The domain length $L = 40$, height $H = 25$, unit load $P$ and the finite element mesh for this problem is $200 \times 125$. For this problem, we perform topology optimization for minimum discrete stiff object radius $r_{\min_D} = 0.4$ units, minimum spacing between discrete stiff objects $t_E = 2 * r_{\min_D} = 0.8$ units, and minimum topology feature radius $r_{\min_T} = r_{\min_D} + t_E = 1.2$ units. The allowable volume of the structure $V_T$ is 40%.

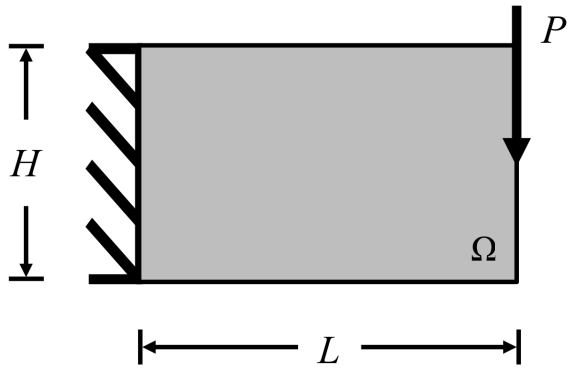


**Figure 3.27:** Cantilever beam domain.

Figure 3.28c shows the solution with circular stiff inclusion with fixed diameter of 0.8 units using the multi-material DOP formulation (Eq. (3.14)) with $V_s = 100\%$ of $V_T$. Comparing this solution to the solution obtained from the traditional two-phase topology optimization (shown in Figure 3.28a), we see that the algorithm successfully optimizes both the placement of stiff objects and the topology of the structure simultaneously. For this packing problem, the algorithm packs as many stiff objects as it could fit inside the component topology without violating the prescribed enclosure region length scale $t_E$ as expected because adding stiff objects will improve overall structural performance (i.e. the compliance is reduced). Since the volume of stiff material cannot be equal to the maximum allowable volume without violating discrete object condition, the constraint function on stiff material volume $V_s$ is inactive for the packing problem. The volume of stiff reinforcement for the packing problem is found to be at approximately 23% of $V_T$ (see Table 3.8 and Figure 3.29).

To illustrate the algorithm more effectively, we consider the case where the volume

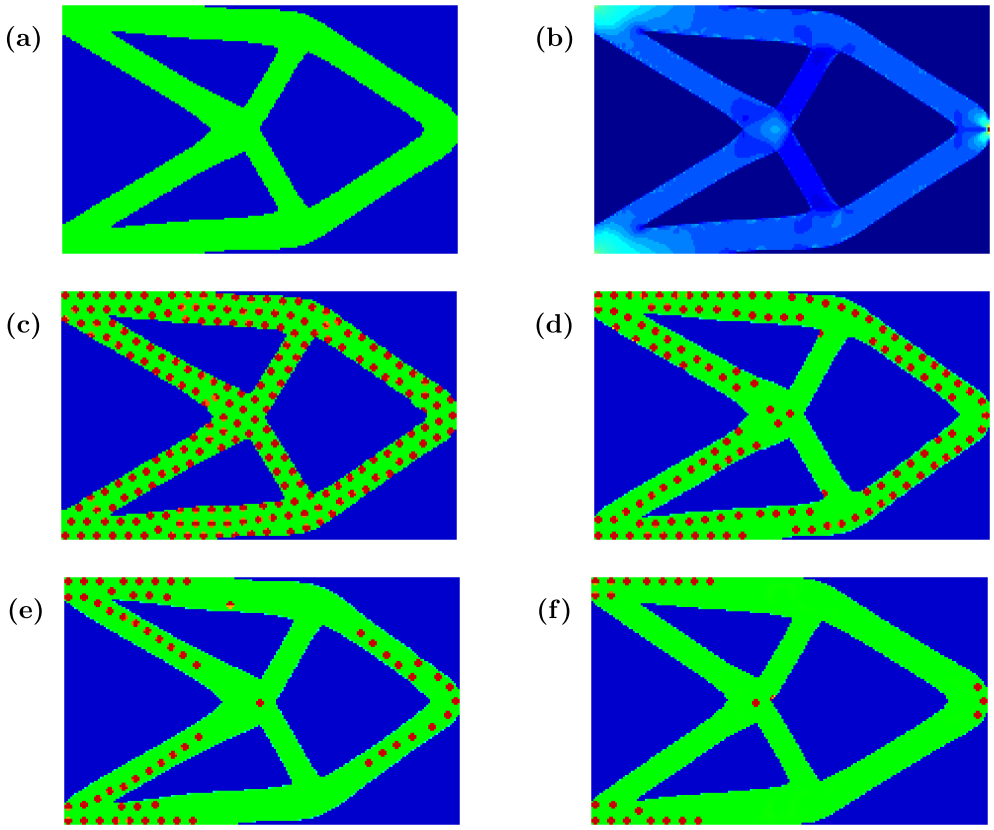


**Figure 3.28:** Cntilever beam results: (a) optimized solution using traditional monolithic formulation composed of compliant material with allowable total volume fraction $V_T = 40\%$, (b) von Mises stress plot for structure in (a), and optimized solution using the multi-material DOP formulation (Eq. (3.14)) with allowable volume of stiff material (c) $V_s = 100\%$ of $V_T$ (i.e. packing problem), (d) $V_s = 15\%$ of $V_T$, and (e) $V_s = 7.5\%$ of $V_T$, and (f) $V_s = 3\%$ of $V_T$.

of stiff material constraint becomes active. For this problem, volume fractions of the stiff material are set at 15%, 7.5%, and 3% of total topology volume $V_T$ (See Figure 3.28d-3.28f). We see that as the volume fraction decreases, the stiff objects

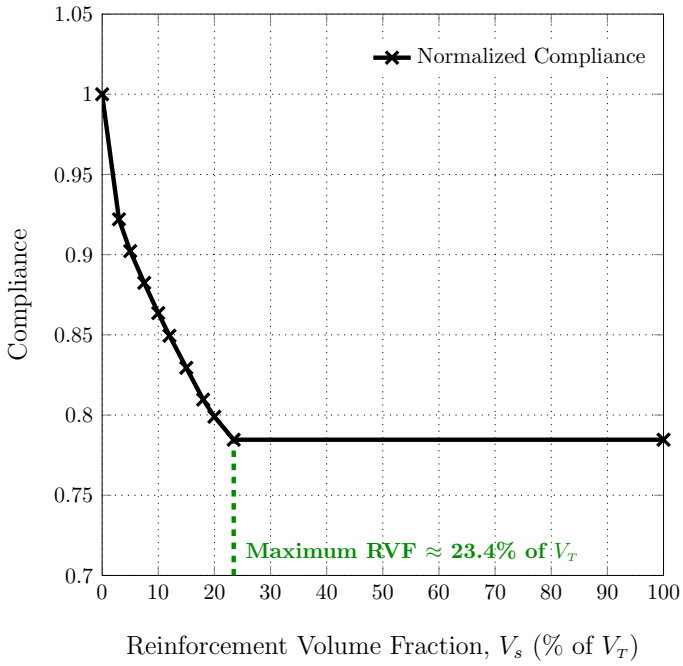


**Figure 3.29:** Normalized compliance for optimized cantilever beam solutions for different reinforcement volume fractions; All values are normalized with the corresponding values for the optimized unreinforced cantilever beam.

are logically placed in the regions with high strain energies as represented by the von Mises stress plot for the unreinforced structure in Figure 3.28b. This is illustrated most clearly when the volume fraction is small and the stiff discrete objects are placed at the location of the applied load and the regions near the boundary conditions where highest stress exists (see Figure 3.28f).

We also observed that the compliance increases as the percent volume fraction of stiff material decreases (see Table 3.8), which is as expected because structures will be less stiff with less available reinforcement. More importantly, however, is that

stiffness can be enhanced by placing the reinforcement strategically. For this example, the stiffness of cantilever beam increases by 7.8% using only 3% reinforcement and the beam can gain its stiffness up to 21.5% as seen from the packing problem result.

**Table 3.8:** Cantilever beam results: compliance and final reinforcement percent volume fraction inside optimal component topology for different given reinforcement percent volume fractions.

| $V_{s,\text{given}}$ (%)* | Fig. | Compliance | $V_{s,\text{used}}$ (%)* | % Stiffness gain† |
|---|---|---|---|---|
| 0 | 3.28a | 45.43 | 0 | 0 |
| 3 | 3.28f | 41.89 | 3 | 7.8 |
| 7.5 | 3.28e | 40.08 | 7.5 | 11.8 |
| 15 | 3.28d | 37.68 | 15 | 17.1 |
| 100 | 3.28c | 35.64 | 23.4 | 21.5 |

* $V_{s,\text{given}}$ and $V_{s,\text{used}}$ are presented as % of $V_T$.

† These values represent percent stiffness gains over the optimized unreinforced cantilever beam.

#### 3.2.2.2 Minimum compliance design of MBB beam

The geometry and loading condition of the simply supported beam problem is shown in Figure 3.30 with domain length $L = 60$, height $H = 20$, and unit load $P$. The finite element mesh for this problem is $240 \times 80$, with minimum discrete

stiff object radius $r_{\min_D} = 0.5$ units, minimum spacing between discrete stiff objects $t_E = 2 * r_{\min_D} = 1$ units, and minimum topology feature radius $r_{\min_T} = 2$ units. The allowable volume of the structure $V_T$ is set to be at 50%. For this problem, we impose symmetry about vertical axis passing through the applied load (i.e. only right-half of the beam is considered) in order to reduce the number of design variables.

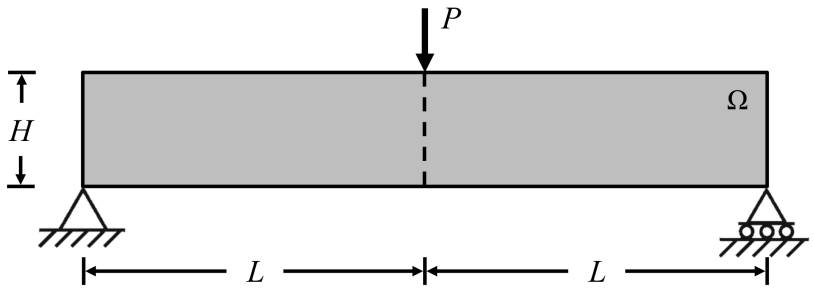


**Figure 3.30:** MBB beam domain.

Figure 3.31c shows the solution with circular stiff inclusion with fixed diameter of 1 unit using the multi-material DOP formulation (Eq. (3.14)) with $V_s = 100\%$ of $V_T$. Comparing this solution with the solution obtained from the traditional two-phase topology optimization (shown in Figure 3.31a), we see again that the algorithm has optimized both the placement of stiff objects and topology of the structure simultaneously. The result also shows a similar trend of the packing problem to the result in the cantilever beam problem. The optimal volume of stiff reinforcement for the packing problem is found to be at approximately 23% of $V_T$ (see Table 3.9 and Figure 3.32).

For this problem, we consider volume fraction of the stiff material at 15%, 12.5%,

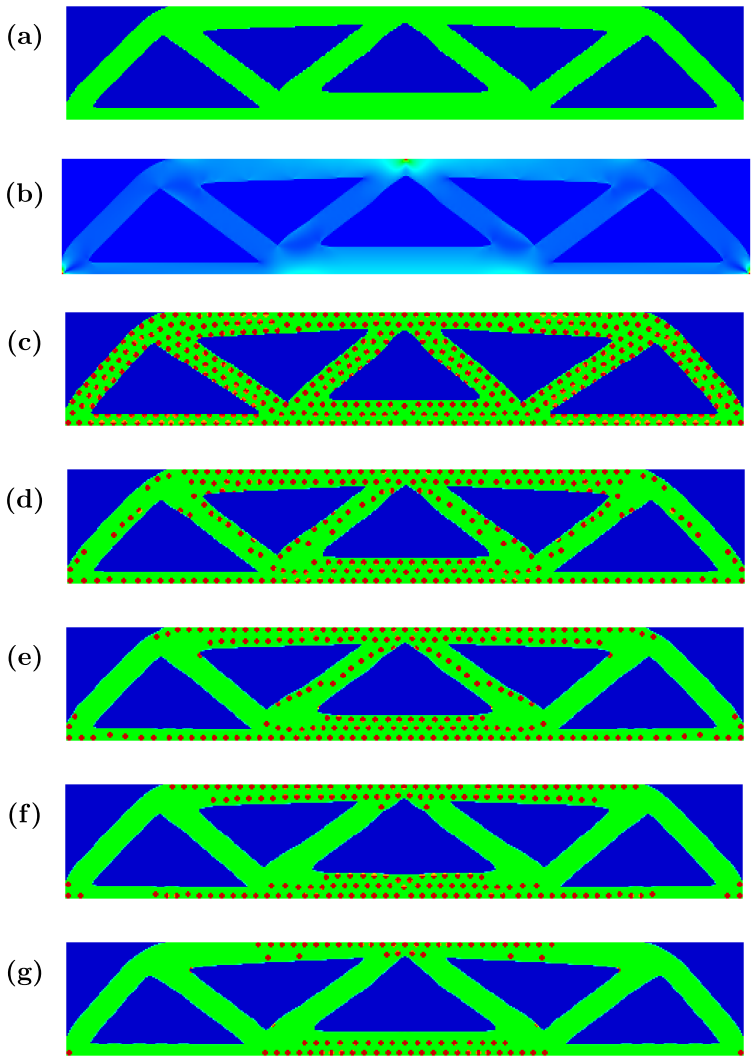


**Figure 3.31:** MBB beam results: (a) optimized solution using traditional monolithic formulation composed of compliant material with allowable total volume fraction $V_T = 50\%$, (b) von Mises stress plot for structure in (a), and optimized solution using the multi-material DOP formulation (Eq. (3.14)) with allowable volume of stiff material (c) $V_s = 100\%$ of $V_T$ (i.e. packing problem), (d) $V_s = 15\%$ of $V_T$, (e) $V_s = 12.5\%$ of $V_T$, (f) $V_s = 10\%$ of $V_T$, and (g) $V_s = 5\%$ of $V_T$.

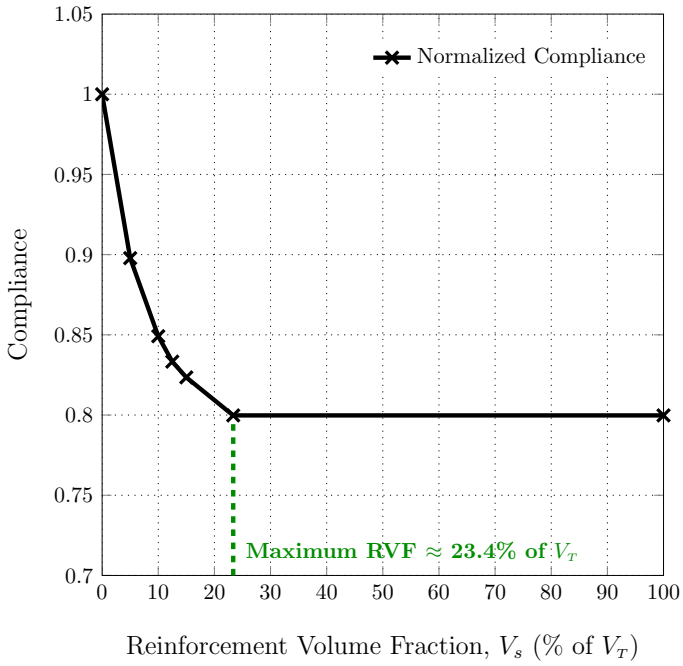


**Figure 3.32:** Normalized compliance for optimized MBB beam solutions for different particle sizes and reinforcement volume fractions; All values are normalized with the corresponding values for the optimized unreinforced MBB beam.

10%, and 5% of $V_T$ (See Figure 3.31d-3.31g). Again, we see that as the volume fraction decreases, the algorithm places the stiff objects in high strain energy region (see von Mises stress plot in Figure 3.31b). This becomes very apparent in the case of low particle volume fraction (see Figure 3.31g) where the stiff objects are placed at the location of the applied load, the regions near the boundary conditions, and the upper and lower chords where highest stress and bending moment exist.

Similar to the cantilever beam problem, we see the improvement in stiffness as more reinforcement becomes available (see Table 3.9). For this example problem,

the stiffness of MBB beam increases by 10.2% using only 5% reinforcement and the maximum stiffness gain over the unreinforced MBB beam is 20%.

**Table 3.9:** MBB beam results: compliance and final reinforcement percent volume fraction inside optimal component topology for different given reinforcement percent volume fractions.

| $V_{s,\text{given}}$ (%)* | Fig. | Compliance | $V_{s,\text{used}}$ (%)* | % Stiffness gain† |
|---|---|---|---|---|
| 0 | 3.31a | 194.50 | 0 | 0 |
| 5 | 3.31g | 174.62 | 5 | 10.2 |
| 10 | 3.31f | 165.16 | 10 | 15.1 |
| 12.5 | 3.31e | 162.07 | 12.5 | 16.7 |
| 15 | 3.31d | 160.16 | 15 | 17.7 |
| 100 | 3.31c | 155.55 | 23.4 | 20.0 |

* $V_{s,\text{given}}$ and $V_{s,\text{used}}$ are presented as % of $V_T$.

† These values represent percent stiffness gains over the optimized unreinforced MBB beam.

#### 3.2.2.3 Minimum compliance design of L-bracket

The geometry and loading condition for the L-bracket problem is illustrated in Figure 3.33 with domain length $L = 40$, height $H = 20$, and unit load $P \times 10$ and the size of each finite element for this problem is 0.2 unit by 0.2 unit. Like the cantilever beam problem, we perform topology optimization for minimum discrete

stiff object radius $r_{\min_D} = 0.4$ units, minimum spacing between discrete stiff objects $t_E = 2 * r_{\min_D} = 0.8$ units, and minimum topology feature radius $r_{\min_T} = r_{\min_D} + t_E = 1.2$ units. The allowable volume of the structure $V_T$ is 50%.

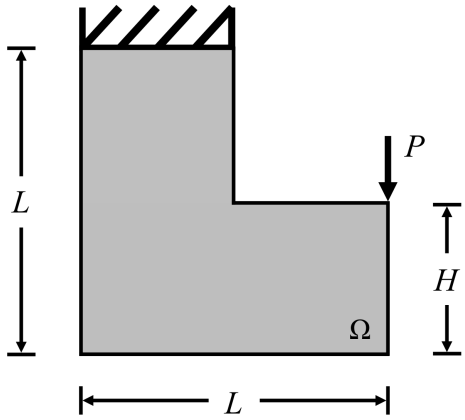


**Figure 3.33:** L-bracket domain.

Figure 3.34c shows the solution with circular stiff inclusion with fixed diameter of 0.8 unit using the multi-material DOP formulation (Eq. (3.14)) with $V_s = 100\%$ of $V_T$. Comparing this solution with the solution obtained from the traditional two-phase topology optimization (shown in Figure 3.34a), we see again that the both the component topology and the layout of the reinforcing particles are optimized. The result also shows a similar trend of the packing problem to the result in the cantilever beam and MBB beam problems, where the algorithms fit as many stiff particles as it can inside the component topology. The optimal volume of stiff reinforcement for the packing problem is found to be at approximately 23% of $V_T$ (see Table 3.10 and Figure 3.35).

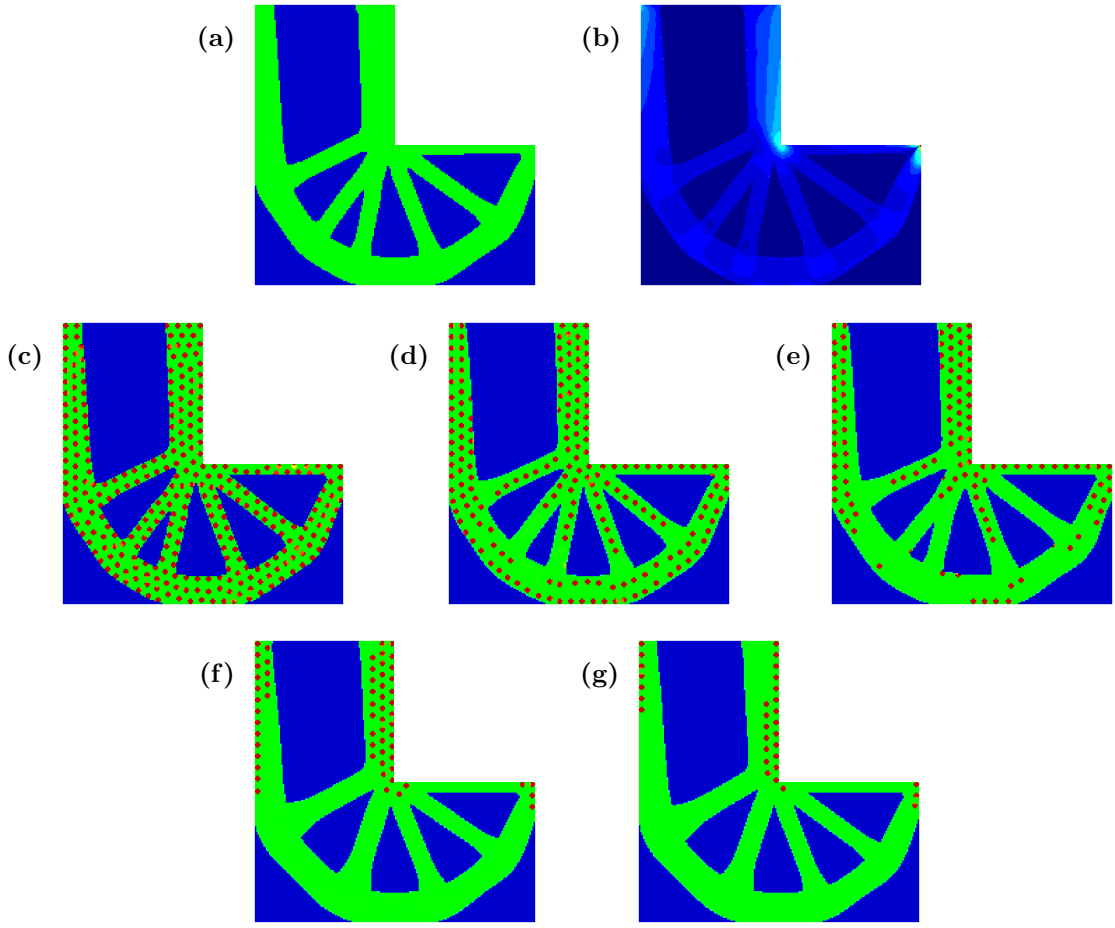


**Figure 3.34:** L-bracket results: (a) optimized solution using traditional monolithic formulation composed of compliant material with allowable total volume fraction $V_T = 50\%$, (b) von Mises stress plot for structure in (a), and optimized solution using the multi-material DOP formulation (Eq. (3.14)) with allowable volume of stiff material (c) $V_s = 100\%$ of $V_T$ (i.e. packing problem), (d) $V_s = 15\%$ of $V_T$, (e) $V_s = 10\%$ of $V_T$, (f) $V_s = 5\%$ of $V_T$, and (g) $V_s = 2.5\%$ of $V_T$.

For this problem, we varied the volume fraction of the reinforcing particles at 15%, 12.5%, 10%, and 5% of $V_T$. The optimized solutions are shown in Figure 3.34d-3.34f.

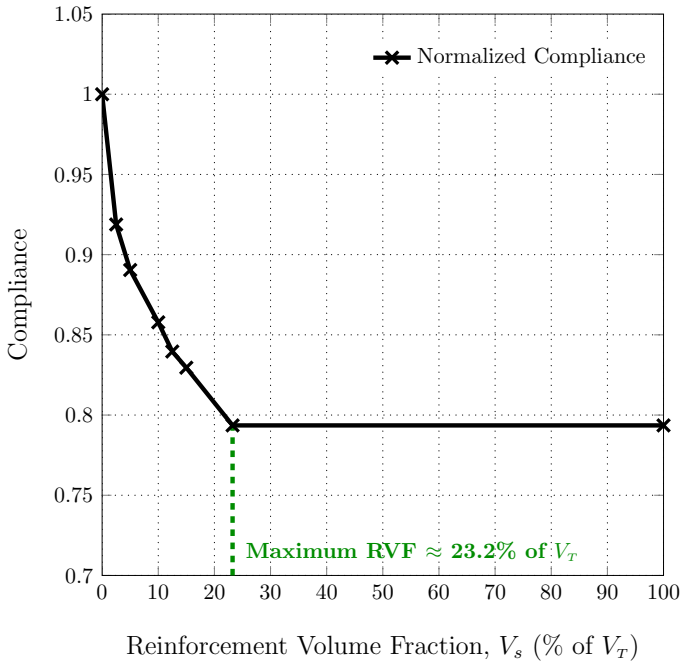


**Figure 3.35:** Normalized compliance for optimized L-bracket solutions for different particle sizes and reinforcement volume fractions; All values are normalized with the corresponding values for the optimized unreinforced L-bracket.

Again, we observe that as the volume fraction becomes less available, the algorithm places the stiff objects in high strain energy region (see von Mises stress plot in Figure 3.34b). In the case of very low particle volume fraction (see Figure 3.34f), the reinforcing objects are placed at the location of the point load, the vertical faces near the supports, and the inner corner where stress concentration occurs. These layout of these discrete objects also follow the optimal load path as seen in Figures 3.34d and 3.34e where the particles are place right at the middle of bracket's branch-like members.

While the differences between the optimized component topologies for different reinforcement volume fractions is not very noticeable in the cantilever beam and MBB beam problems, we observe that the optimized component topologies vary between different reinforcement volume fractions for the L-bracket problems. We believe that this slight variations between the optimized topologies imply that the final component topologies do not have to exactly match the optimized unreinforced topology upon the introduction of stiff particles. In fact, we the reinforcements were removed from the optimized component topologies, the compliances would be higher than that of optimized unreinforced topology. This is because we do not optimize the component topology first then reinforcement, but actually optimize both component topology and placement of reinforcing particles at the same time.

Similar to the cantilever beam and MBB beam problems, we see the improvement in stiffness as more reinforcement becomes available (see Table 3.10). For this example problem, the stiffness of L-bracket increases by 11.0% using only 5% reinforcement and the maximum stiffness gain over the unreinforced L-bracket is 23.2%.

**Table 3.10:** L-bracket results: compliance and final reinforcement percent volume fraction inside optimal component topology for different given reinforcement percent volume fractions.

| $V_{s,\text{given}}$ (%)* | Fig. | Compliance | $V_{s,\text{used}}$ (%)* | % Stiffness gain† |
|---|---|---|---|---|
| 0 | 3.34a | 80.95 | 0 | 0 |
| 2.5 | 3.34g | 74.38 | 2.5 | 8.1 |
| 5 | 3.34f | 72.08 | 5 | 11.0 |
| 10 | 3.34e | 69.44 | 10 | 14.2 |
| 15 | 3.34d | 67.15 | 15 | 17.0 |
| 100 | 3.34c | 64.24 | 23.2 | 20.6 |

* $V_{s,\text{given}}$ and $V_{s,\text{used}}$ are presented as % of $V_T$.

† These values represent percent stiffness gains over the optimized unreinforced L-bracket.

#### 3.2.2.4 Maximum Negative Displacement design of compliant inverter

The geometry and loading condition of the compliant inverter is shown in Figure 3.36 with a square domain with length $L = 50$, and unit load $P \times 100$. The finite element mesh for this problem is $250 \times 125$, with minimum discrete stiff object radius $r_{\min_D} = 0.4$ units, minimum spacing between discrete stiff objects $t_E = 2 * r_{\min_D} = 0.8$ units, minimum topology feature radius $r_{\min_T} = 1.2$ units, and the length scale vari-

able $\Delta r$ of 0.2 units . The objective of this problem is to maximize negative displacement (i.e. minimize positive displacement) at the output port $d_{out}$ under a given load $P$ at the input port. The input spring stiffnesses at the input and output ports are $k_{in} = 1$ and $k_{out} = 0.001$, respectively. The allowable volume of the structure $V_T$ is set to be at 30%. For this problem, we utilize symmetry about horizontal axis passing through the applied load (i.e. only the bottom-half of the inverter is modeled) in order to reduce the number of design variables.

The inverter problem is generally difficult to solve since it tends to get stuck at the local minimum in which the solution produce zero displacement at the output port by disconnecting it from the rest of the structure. Sigmund (2009) suggests minimizing the sum of the objective functions (i.e. instead of the maximum of the objective functions) for the first several iterations then switch to min-max formulation to overcome this issue. While this helps the algorithm from getting stuck in the local minimum for two-phase design (i.e. solid-void), we found that the combination of multi-material DOP and robust formulation proposed in this work is still susceptible to this issue. To circumvent this, we perform optimization using only two phases as in traditional monolithic topology optimization (i.e. only the compliant and void phases, and without the stiff phase) for the first continuation (i.e. $\beta = 5$ and $\eta = 0$) and thereafter switched to the proposed combined multi-phase DOP formulation.

Figure 3.37c shows the solution with circular stiff inclusion with fixed diameter of 0.8 unit using the combination of robust formulation and the proposed multi-material

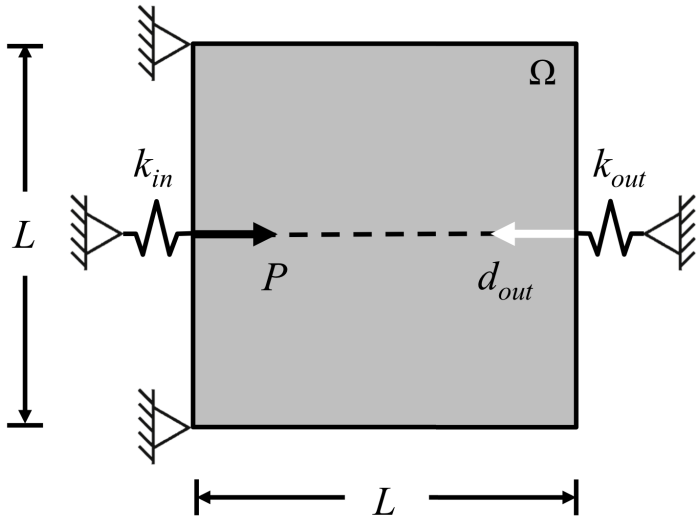


**Figure 3.36:** Compliant inverter domain.

DOP formulation (Eq. (3.16)) with $V_s = 100\%$ of $V_T$. Comparing this solution with the solution obtained from the traditional monolithic two-phase topology optimization (shown in Figure 3.37a), we see again that the algorithm has optimized both the placement of stiff objects and topology of the structure simultaneously. The result also shows a similar trend of the packing problem to all of the other test cases. The maximum volume of stiff reinforcement for the packing problem is found to be at approximately 23% of $V_T$ (see Table 3.11 and Figure 3.38).

For this problem, we consider reinforcement volume fraction at 12.5%, 10%, 5%, and 2.5% of $V_T$ (See Figure 3.37d-3.37g). Again, we see that as the volume fraction decreases, the algorithm places the stiff objects in high strain energy region (see von Mises stress plot in Figure 3.37b). In the case of compliant inverter, high strain energies are located around the applied load, the supports, and the hinge regions, and we

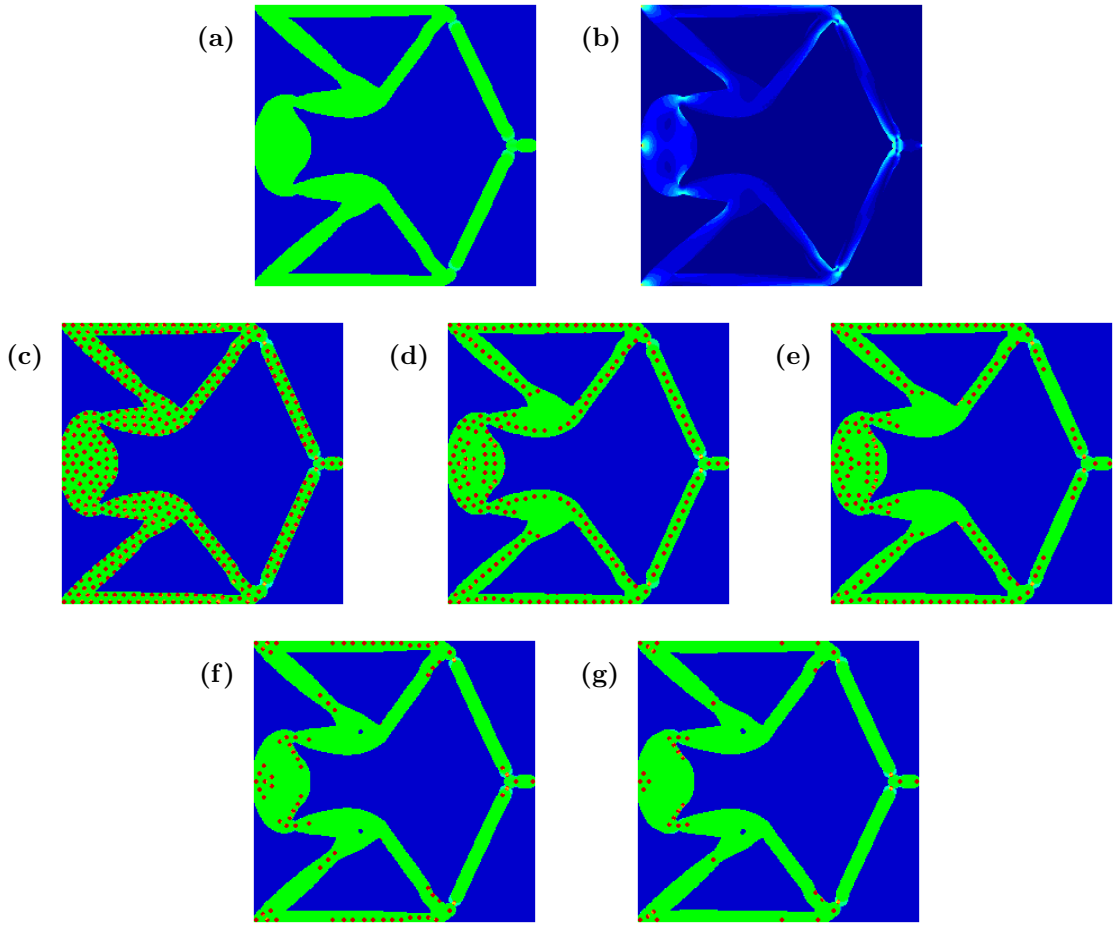


**Figure 3.37:** Compliant inverter results: (a) optimized solution using traditional monolithic formulation composed of compliant material with allowable total volume fraction $V_T = 30\%$, (b) von Mises stress plot for structure in (a), and optimized solution using the multi-material DOP formulation (Eq. (3.16)) with allowable volume of stiff material (c) $V_s = 100\%$ of $V_T$ (i.e. Packing problem), (d) $V_s = 12.5\%$ of $V_T$, (e) $V_s = 10\%$ of $V_T$, (f) $V_s = 5\%$ of $V_T$, and (g) $V_s = 2.5\%$ of $V_T$.

can see that the reinforcements are placed at these locations first when reinforcement volume fraction is low (see Figure 3.37g). The well-known two-node hinge issue is

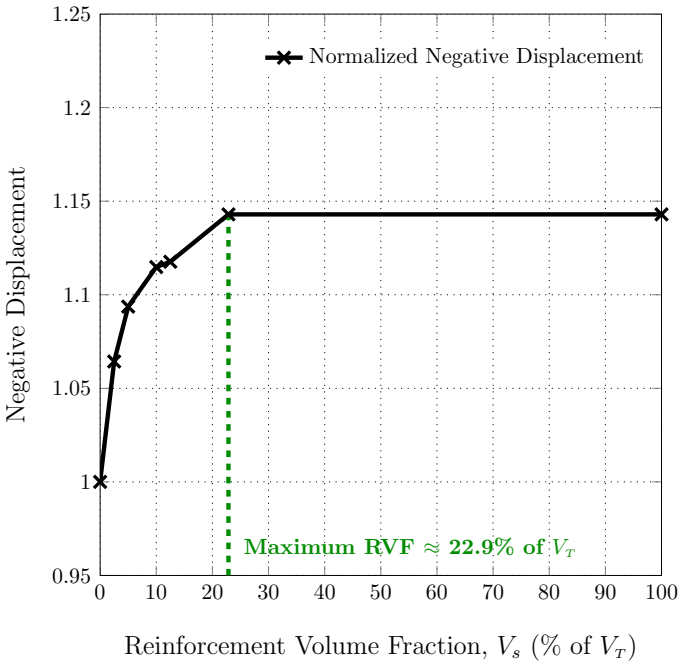


**Figure 3.38:** Normalized negative displacement for optimized compliant inverter solutions structures for different particle sizes and reinforcement volume fractions; All values are normalized with the corresponding values for the optimized unreinforced compliant inverter.

also successfully eliminated with the use of robust formulation (Gaynor et al., 2014; Sigmund, 2009).

While it makes sense that stiff objects are place along the load-carrying members, it may seem counter-intuitive to put stiff material at the hinges when the work of Gaynor et al. (2014); Sigmund (2009) shows that compliant material is concentrated in the hinge region, but embedding stiff materials at hinges increases the inverter's movement in the context of this work, which is to improve performance of the com-

ponent through the inclusion of discrete reinforcing objects. This essentially means that the component is made up of material that is much weaker than the material that made up the reinforcing objects. In the absence of any reinforcements, less force can be transferred through the inverter because the entire component is made of compliant material, resulting in small displacement at the output port. Embedding stiff objects at the hinges would therefore help transfer the forces and increase the inverter's movement, but only as long as the objects are placed in center or along the centerline of the hinges. This is because placing stiff material along the edges of the hinge would stiffen up the hinge rather than facilitate its movement. The optimized inverter solutions obtained in this work thus make sense from structural efficiency point of view.

As in the case of L-bracket, we observe slight variation of optimized component topologies in the cases of small reinforcement volume fractions. In this case, small-sized void are present in the areas that are low in strain energy. This is most likely due to solutions being in different local minima. Another observation made from the optimized compliant inverter solutions is that the they contain some "orange" particles, which indicates intermediate volume fraction, at the hinge regions. Upon closer inspection, these particles are partially orange, meaning that the intermediate volume fraction is a result from projecting entirely stiff particles onto a region of component topology that contains intermediate volume fraction, which happens to be at hinges. While these hinges are not one-node hinges that manifest from projections

of two tangent circles, the thickness of the hinges is slightly less than the minimum length scale of $2 \times r_{\min_T}$. This is most likely due to the choice of the length scale variable $\Delta r$ as it might not be high enough to create hinge feature that completely satisfy the minimum length scale. Increasing RAMP penalization parameter *eta* would likely help get rid intermediate volume fraction as well. Nevertheless, these particles are projected as discrete objects in the locations of high strain energy, as would be expected.

Like in other benchmark examples, we see the improvement in target performance as more reinforcement becomes available (see Table 3.11). For this example problem, the displacement of compliant inverter increases by 9.4% using only 5% reinforcement and the maximum displacement gain over the unreinforced compliant inverter is approximately 23%.

**Table 3.11:** Compliant inverter results: displacement at the output port and final reinforcement percent volume fraction inside optimal component topology for different given reinforcement percent volume fractions.

| $V_{s,\text{given}}$ (%)* | Fig. | Compliance | $V_{s,\text{used}}$ (%)* | % Displacement gain† |
|---|---|---|---|---|
| 0 | 3.37a | -191.68 | 0 | 0 |
| 2.5 | 3.37g | -204.01 | 2.5 | 6.4 |
| 5 | 3.37f | -209.63 | 5 | 9.4 |
| 10 | 3.37e | -213.68 | 10 | 11.5 |
| 12.5 | 3.37d | -214.23 | 12.5 | 11.8 |
| 100 | 3.37c | -216.08 | 22.8 | 14.3 |

* $V_{s,\text{given}}$ and $V_{s,\text{used}}$ are presented as % of $V_T$.

† These values represent percent displacement gains over the optimized unreinforced compliant inverter.

### 3.2.2.5 Example Design Evolutions

The design evolutions for the optimized cantilever beam and L-bracket solutions with stiff circular reinforcement volume fraction of 15% (Figures 3.28d and 3.34d), respectively) are illustrated in Figures 3.39 and 3.40, respectively. The designs begins with uniform initial guess without any discrete object. In the first continuation step, the topology of the component begins to take shape and the stiff phase is place at the location of high strain energies (Figures 3.39b and 3.40b). Both component topology

and the stiff phase, however, contain intermediate volume fraction since there is no penalty applied (i.e. $\eta = 0$).

As both RAMP penalty term $\eta$ and Heaviside curvature parameter $\beta$ increase (the former increases the penalization of intermediate volume fraction and the latter facilitates the projection of discrete objects), the topology of the component becomes more defined first, creating well-defined stress trajectories and load paths. The stiff phase then begins to translate creating string-like shape with the thickness of prescribed minimum length scale $r_{\min_D}$ (Figures 3.39c and Figures 3.40c-3.40d). The stiff phase continues to translate and break into individual discrete objects (Figures 3.39d-3.39i and Figures 3.40e-3.40i).

It is important to note that in this method, translation of discrete objects is facilitated by decreasing and increasing the magnitudes of the design variable magnitudes, not by changing their locations. This is one of the key advantages of this approach because it does not require the number of discrete objects to be fixed or predefined *a priori*. This approach also allows for the objects to be created out of the background topology (i.e. not from translation of nearby objects) as seen in, for example, Figures 3.39h-3.39i and Figure 3.40i, or disappear, as observed in Figure 3.39e. The design evolution of the discrete objects are in agreement with the illustrations in Guest (2014, 2015).

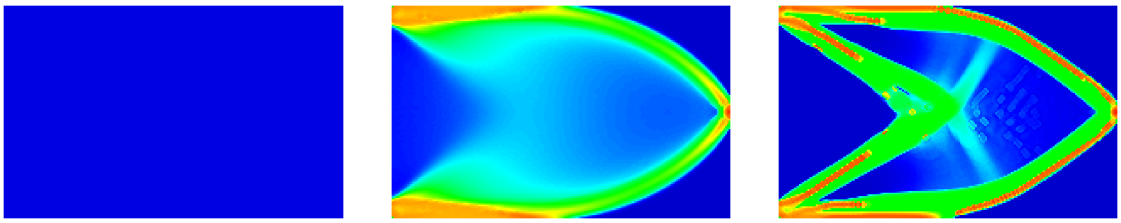

**(a)** Initial guess



**(b)** Continuation step 1 ($\eta = 0$, $\beta = 5$)



**(c)** Continuation step 2 ($\eta = 1$, $\beta = 6$)

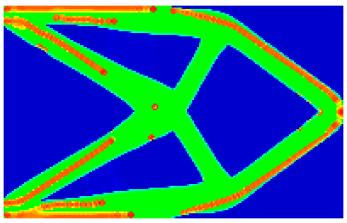

**(d)** Continuation step 3 ($\eta = 2$, $\beta = 7$)

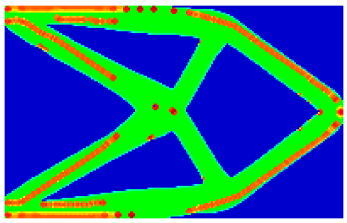

**(e)** Continuation step 4 ($\eta = 3$, $\beta = 8$)

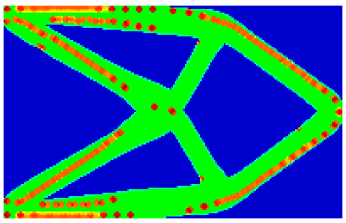

**(f)** Continuation step 5 ($\eta = 4$, $\beta = 9$)

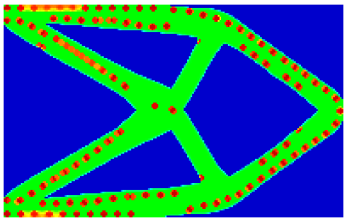

**(g)** Continuation step 6 ($\eta = 5$, $\beta = 10$)

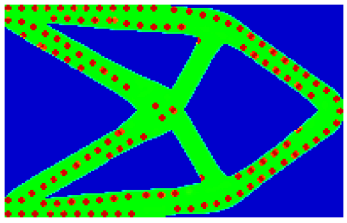

**(h)** Continuation step 7 ($\eta = 7$, $\beta = 12$)

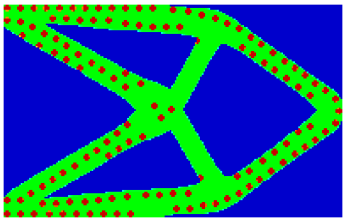

**(i)** Continuation step 9 ($\eta = 15$, $\beta = 20$)

**Figure 3.39:** Design evolution for the topology shown in Figure 3.28d. Note: initial guess is uniform.

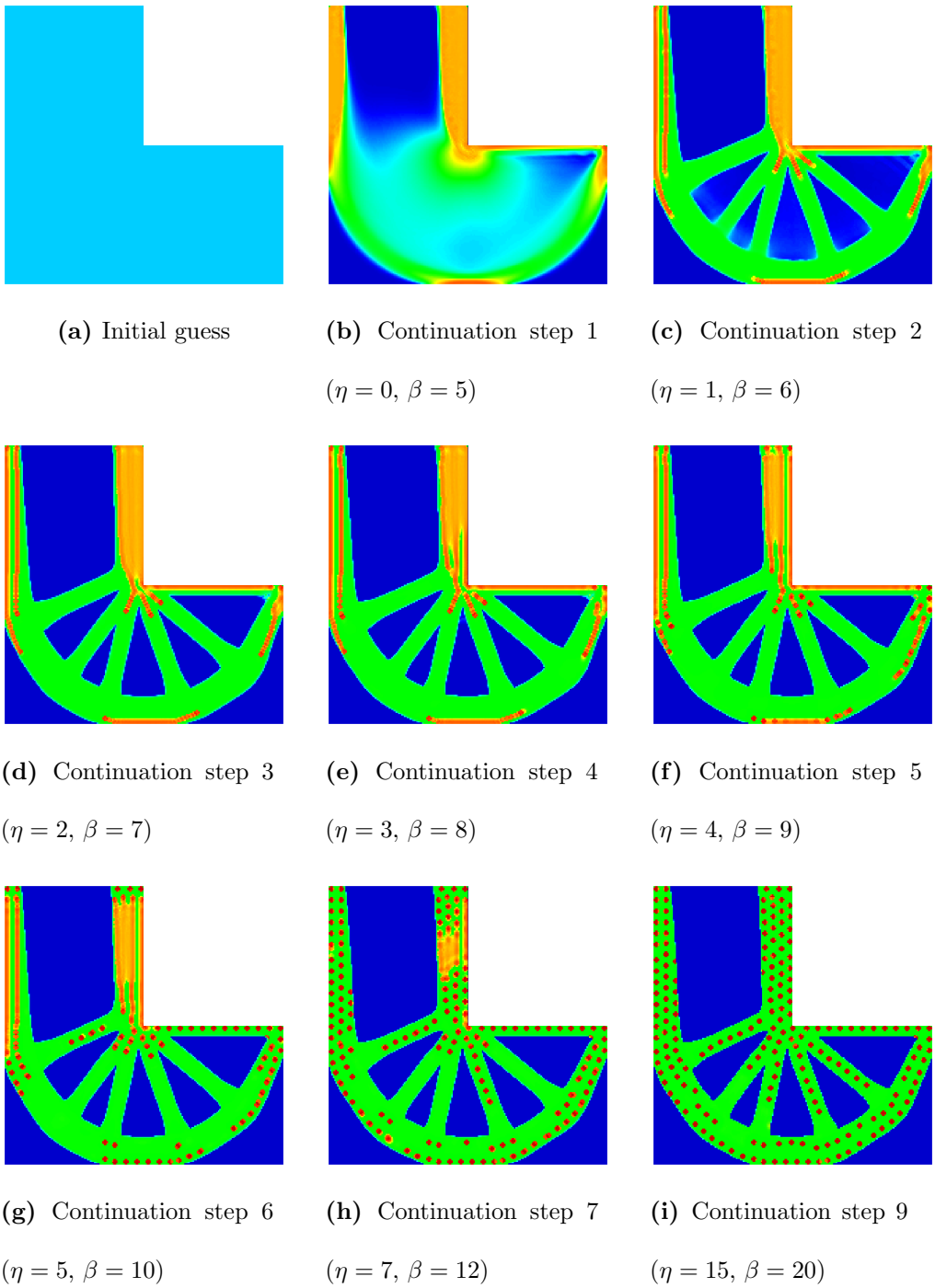

**(a)** Initial guess

**(b)** Continuation step 1 ($\eta = 0$, $\beta = 5$)

**(c)** Continuation step 2 ($\eta = 1$, $\beta = 6$)

**(d)** Continuation step 3 ($\eta = 2$, $\beta = 7$)

**(e)** Continuation step 4 ($\eta = 3$, $\beta = 8$)

**(f)** Continuation step 5 ($\eta = 4$, $\beta = 9$)

**(g)** Continuation step 6 ($\eta = 5$, $\beta = 10$)

**(h)** Continuation step 7 ($\eta = 7$, $\beta = 12$)

**(i)** Continuation step 9 ($\eta = 15$, $\beta = 20$)

**Figure 3.40:** Design evolution for the topology shown in Figure 3.34d. Note: initial guess is uniform.

# 3.3 Discrete Object Projection with Discrete Object Sets

## 3.3.1 Discrete Object Sets

In this work, we further extend the proposed DOP method to cases where embedded objects are chosen from predefined set of objects with fixed size and shape. This idea, originally put forth by Guest (2014), is to consider at set of objects that are selected from database described by designers. Some examples include circular objects of different sizes and non-circular objects with multiple orientations. This can be easily achieved by using the same logic as the proposed multi-material DOP method where an additional set of design variables is used to represent component topology. In the case of object sets, there will now be multiple sets of design variables, each of which corresponds to an object in an object set.

Figures 3.41 and 3.42 illustrate the idea of this DOP extension. In the case where we have a predefined set of objects composed of square and diamonds (i.e. square rotated at 45°), design variables for projecting discrete objects $\boldsymbol{\phi}_D$ will consist of two design variable "layers", one for square objects and another for diamond objects (Figure 3.41). In another case, we have short fiber objects permitted to be place at four different orientations (0°, −45°, 45°, and 90°). The design variables for projecting discrete objects $\boldsymbol{\phi}_D$ will then consist of four design variable layers, one for each of the

orientation (Figure 3.42).

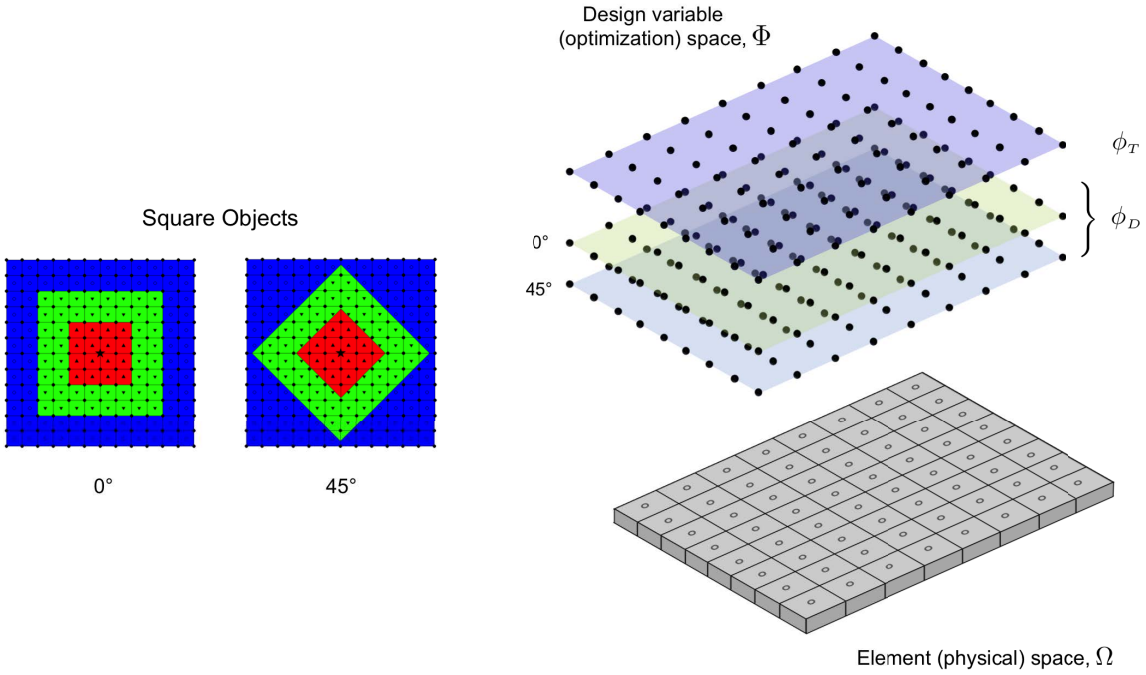


**Figure 3.41:** Illustration of design variable (optimization) space $\Phi$ and physical element space $\Omega$ for three-phase DOP method projecting two different discrete object sets, where design variable $\boldsymbol{\phi}_T$ projects component topology and design variable $\boldsymbol{\phi}_D$ projects square discrete object at either 0° or 45° orientation.

The projection of only one object at a single location is automatically achieved in this extension to the DOP method. This is because multiple projections of different objects onto a single element will lead to objects being overlapped and thus phase mixing (i.e. projection of two different phases onto the same element), which resulted in inefficient topology. Since the original DOP method has the ability to prevent phase mixing, this extension does as well.

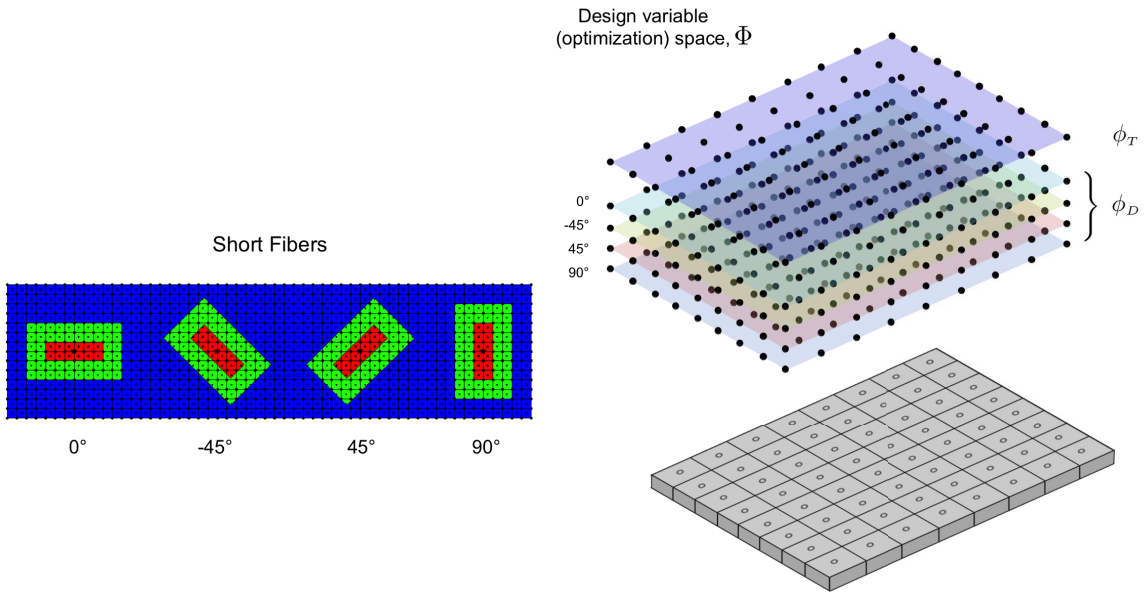


**Figure 3.42:** Illustration of design variable (optimization) space $\Phi$ and physical element space $\Omega$ for three-phase DOP method projecting two different discrete object sets, where design variable $\boldsymbol{\phi}_T$ projects component topology and design variable $\boldsymbol{\phi}_D$ projects short fiber object at either $0°$, $-45°$, $45°$, or $90°$ orientation.

In this section, we demonstrate this extension on a cantilever beam and L-bracket. For the cantilever beam example, the reinforcing objects are either squares or diamonds (Figure 3.41). For the L-bracket problem, we have short fibers that are permitted to be placed at four different orientations: $0°$, $-45°$, $45°$, and $90°$ (Figure 3.42).

The square objects and short fiber objects are considered to be of rectangular projection. The local and enclosure neighborhood sets for any arbitrary size rectangular

projection at 0° can be defined, respectively, as:

$$i \in N_L^e \qquad \text{if} \quad \left\{ \begin{array}{l} \|\mathbf{x}_{i,x} - \bar{\mathbf{x}}_x^e\| \leq r_{\min_{D,x}} \\ \\ \|\mathbf{x}_{i,y} - \bar{\mathbf{x}}_y^e\| \leq r_{\min_{D,y}} \end{array} \right\} \tag{3.32a}$$

$$i \in N_E^e \qquad \text{if} \quad \left\{ \begin{array}{l} r_{\min_{D,x}} < \|\mathbf{x}_{i,x} - \bar{\mathbf{x}}_x^e\| \leq r_{\min_{D,x}} + t_{E,x} \\ \\ r_{\min_{D,y}} < \|\mathbf{x}_{i,y} - \bar{\mathbf{x}}_y^e\| \leq r_{\min_{D,y}} + t_{E,y} \end{array} \right\} \tag{3.32b}$$

where $\mathbf{x}_{i,x}$ and $\mathbf{x}_{i,x}$ are the x- and y-coordinates of design variable $i$, $\bar{\mathbf{x}}_x^e$ and $\bar{\mathbf{x}}_y^e$ are the x- and y-coordinates of the centroid of element $e$, $r_{\min_{D,x}}$ and $r_{\min_{D,y}}$ are the length scale of the discrete object in the x- and y-directions, and $t_{E,x}$ and $t_{E,y}$ are the thickness of enclosure in the x- and y-directions, which dictates minimum required distance between discrete objects (Figure 3.43). The projection of rectangular objects at different angles other than 0° can be obtained by simply rotating the horizontal rectangular projection by desired orientations.

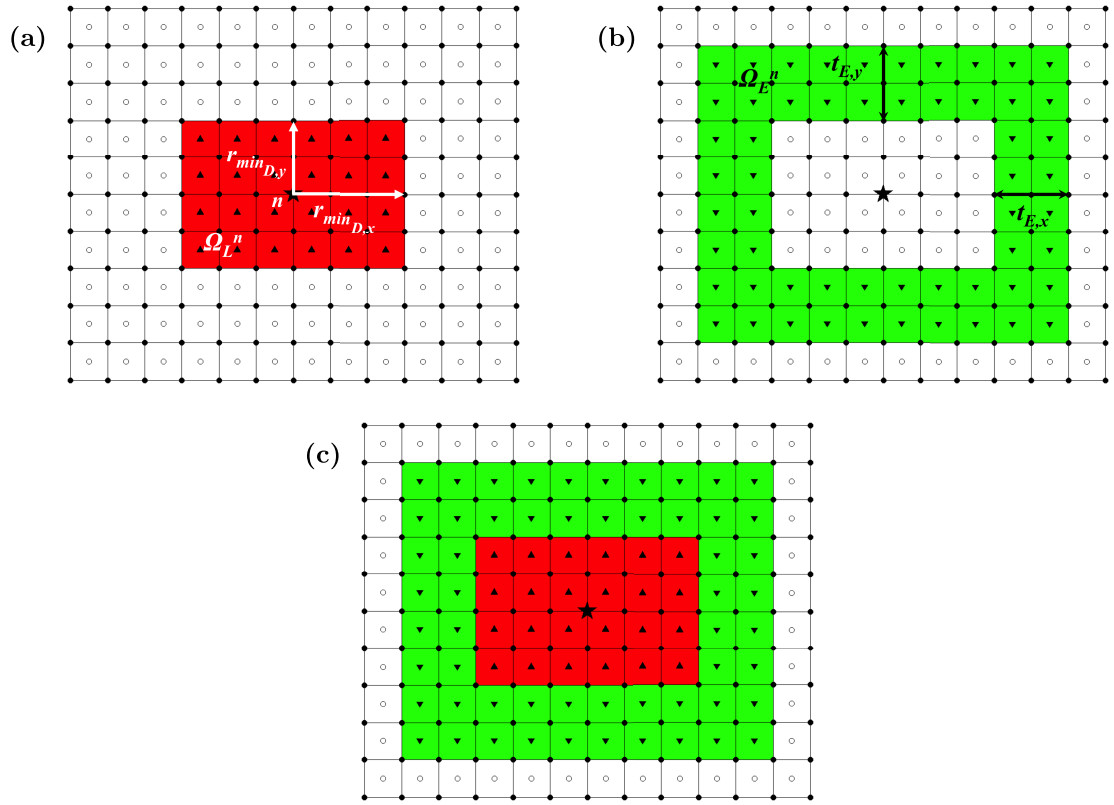


**Figure 3.43:** Discrete rectangular projection from design variable $n$: (a) a projection of rectangle stiff phase (red) of length scale $r_{\min_{D,x}}$ and $r_{\min_{D,y}}$ onto the local domain $\Omega_l^i$ as expressed in Eq. 3.32a, (b) a projection of hollow rectangle compliant phase (green) onto the enclosure domain $\Omega_E^i$ as expressed in Eq. 3.32b, and (c) a illustration of final projection.

### 3.3.2 Numerical Examples and Solutions For Discrete Object Sets

To illustrate the algorithm ability to project different objects from a prescribed set, the example presented in this section will focus on the optimization of embedded objects only (i.e. no optimization on the component topology). All problems here are solved using Method of Moving Asymptotes (MMA) by Svanberg (1987, 1995). In these examples, we found that while penalization of phase mixing with RAMP is sufficient, we found that higher values of the Heaviside variable $\beta$ and RAMP parameter $\eta$ are needed than previously used in Section 3.2.1.3 for single object projection. This is most likely because at each design variable location, there are now several options of objects that can be projected therefore it is more difficult and higher penalization is needed. For these problems, we gradually increase $\beta$ from 5 to 50 in 12 continuation steps and RAMP parameter $\eta$ from 0 to 40 in 12 continuation steps.

#### 3.3.2.1 Minimum compliance design of cantilever beam

The geometry and loading condition for the cantilever beam problem is the same as the one illustrated in Section 3.1.2.2.1 Figure 3.14. The size of these objects are $r_{\min_{D,x}} = r_{\min_{D,y}} = 0.6$ units and the minimum distance between the discrete objects is $t_{E,x} = t_{E,y} = 1.2$ units. For this problem, we consider cases where reinforcing objects are either squares or diamonds (Figure 3.41).

Table 3.12 shows solutions for cases of permitting square objects only, diamond objects only, and both square and diamond objects for 5%, 12.5%, and 15% reinforcement volume fractions. These solutions show similar trends to solutions with circular reinforcing objects (Table 3.2) where the algorithm places most of the stiff objects at the upper and lower left corners of the beam where strain energies are highest, and the layout of the objects resemble classic topology-optimized cantilever beam solution as the volume fraction increases.

It is interesting and as expected to see that the algorithm chooses the type of objects that best align with the principle stress trajectories as seen in the case where both square and diamond objects are permitted. This is most apparent in the optimized solution for 15% reinforcement volume fraction where square objects are placed in the location of largest bending stress and diamond objects are placed near the applied loads and towards the web. This trend is also in agreement with findings in Guest (2014).

In all of the cases, we observe that the solutions with both square and diamond objects perform better than those with square objects only or with diamond objects only (Figure 3.44). This is as expected because the algorithm now has more options to chose the objects that are best align with principle stress trajectories, which is the most efficient. We can also see that the performance of cantilever beam solutions with only stiff diamond objects perform the worst out of the three cases. This makes sense because square objects are much preferred by the optimizer since they are best

**Table 3.12:** Optimized solutions for cantilever beam problem using stiff square objects, stiff diamond objects, and both stiff square and diamond objects.

| $V_{s,\text{given}}$ (%)* | Square objects only | Diamond objects only | Square or diamond objects |
|---|---|---|---|
| 5 | 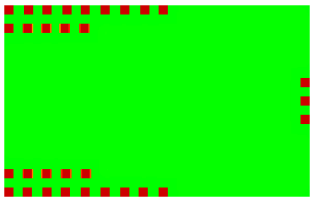 | 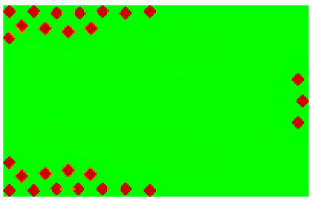 | 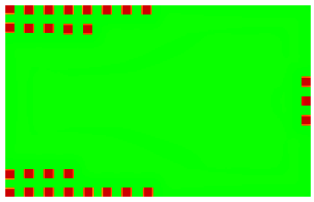 |
| 12.5 | 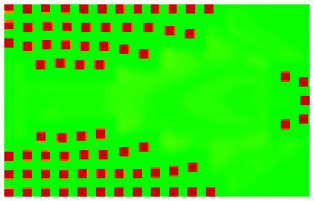 | 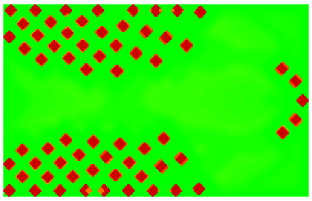 | 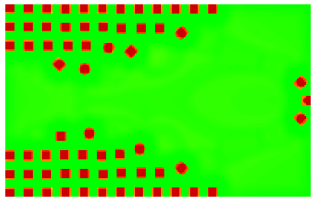 |
| 15 | 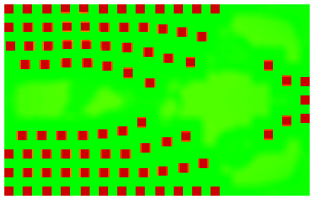 | 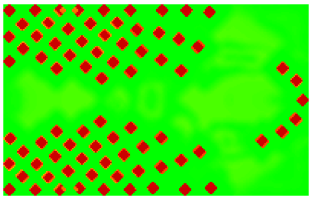 | 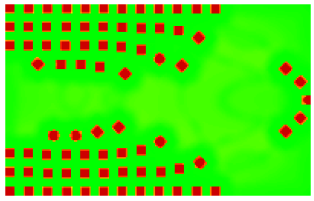 |

* $V_{s,\text{given}}$ is presented as % of $V_T$.

aligned with the stress trajectories at the locations where the strain energies are largest, which in this case are the upper and lower left corners of the beam (as seen in von Mises stress plot in Figure 3.15). This is further illustrated by Figure 3.44 in which we see that adding diamond objects to the square object set provide only slight improvement in stiffness, while adding square objects to the diamond object

sets provide substantial improvement in stiffness.

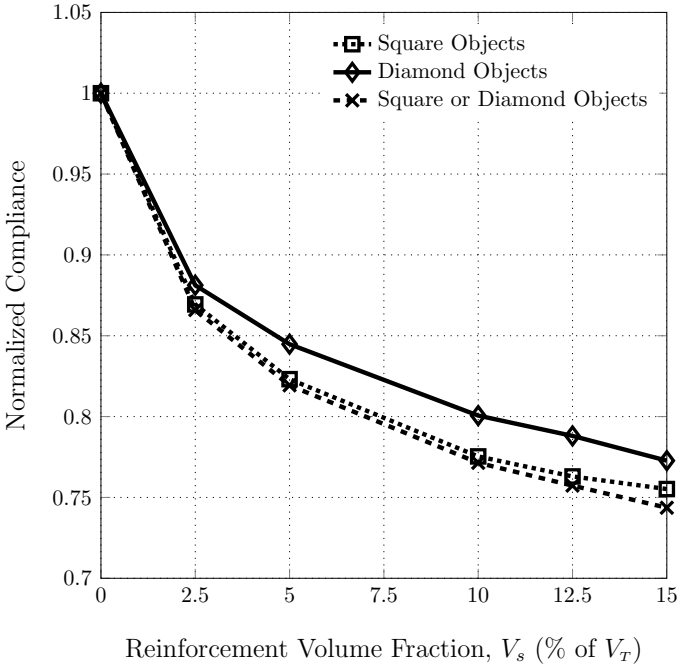


**Figure 3.44:** Normalized compliance for optimized cantilever beam solutions for different object sets and reinforcement volume fractions; All values are normalized with the corresponding values for the unreinforced cantilever beam.

### 3.3.2.2 Minimum compliance design of L-bracket

The geometry and loading condition for the L-bracket problem is the same as the one illustrated in Section 3.1.2.2.3 Figure 3.20. The size of these short fibers are $r_{\min_{D,x}} = 0.6$ units and $r_{\min_{D,y}} = 0.2$ units. The minimum distance between the discrete objects in local x- and y-directions are $t_{E,x} = 1.2$ units and $t_{E,y} = 0.8$ units, respectively. For this problem, we consider cases where reinforcing objects are short

fibers permitted to be placed at four different orientations: $0°$, $-45°$, $45°$, or $90°$ orientations (Figure 3.42).

Table 3.12 shows solutions for three different combinations of short fibers orientations: (a) $0°$ and $90°$ (horizontal/vertical fibers) only, (b) $-45°$ and $45°$ (inclined fibers) only, and (c) all four different orientations (horizontal/vertical/inclined fibers). The solutions shown are performed with 2.5%, 7.5%, and 12.5% reinforcement volume fractions. The solutions in all of the cases show similar trends to solutions with circular reinforcing objects (Table 3.6) where the algorithm places most of the stiff objects at the upper left and right corners near the supports and at the inner sharp corner where strain energies are highest. As the volume fraction of reinforcing objects increases, the optimized layout of the objects also resemble classic topology-optimized L-bracket solution.

As expected, algorithm successfully projected objects from the predefined object sets. We again see that the solutions in case (c) perform better than two other cases (Figure 3.44). While the solutions consist of only inclined fibers (case (b)) have the largest compliances for all volume fractions, the compliances of the optimized L-brackets in cases (a) and (c) are relatively close for small reinforcement volume fractions. With all four different orientations of fibers in case (c), the compliances is significantly reduced for larger reinforcement volume fractions. This indicates that horizontal/vertical fibers are best aligned with the stress trajectories at the locations where the strain energies are largest, which is near the upper left and right corners

**Table 3.13:** Optimized solutions for L-bracket problem using 0°/90° stiff short fiber objects, −45°/45° stiff short fiber objects, and 0°/−45°/45°/90° stiff short fiber objects.

| $V_{s,\text{given}}$ (%)* | 0°/90° Short Fibers | −45°/45° Short Fibers | 0°/−45°/45°/90° Short Fibers |
|---|---|---|---|
| 2.5 | 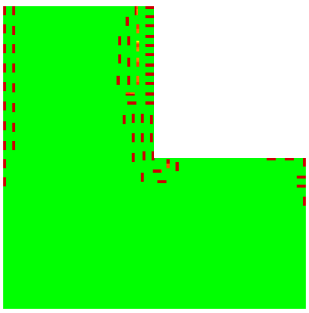 | 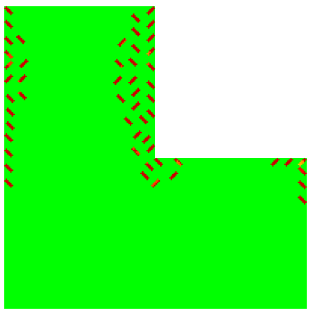 | 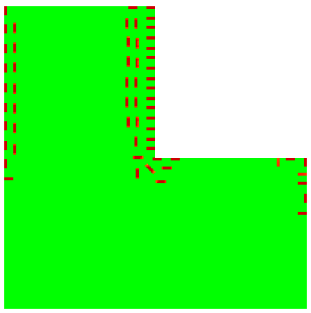 |
| 7.5 | 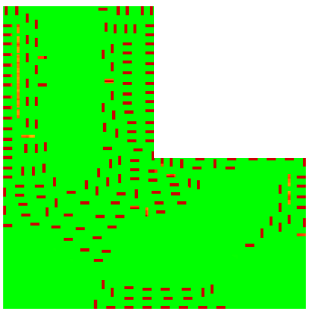 | 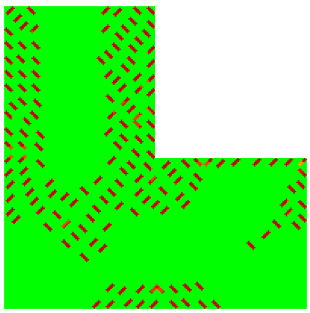 | 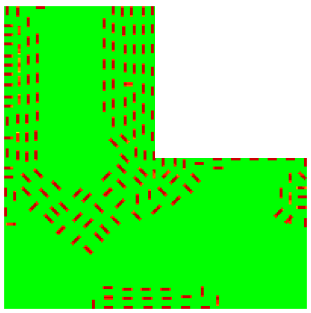 |
| 12.5 | 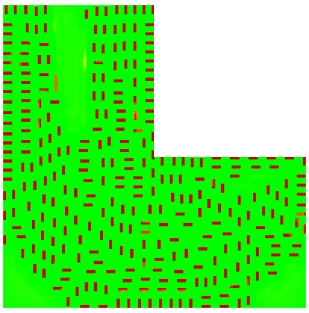 | 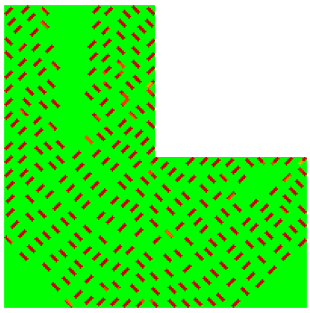 | 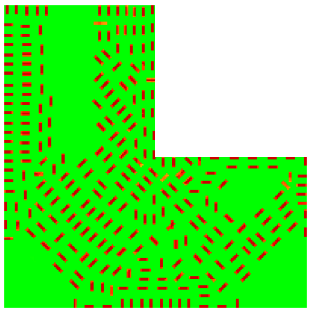 |

* $V_{s,\text{given}}$ is presented as % of $V_T$.

near the supports (as seen in von Mises stress plot in Figure 3.15). The stiffness of the structures can be greatly improve by adding the inclined fibers into the set since these objects will align with the stress trajectories in the web.

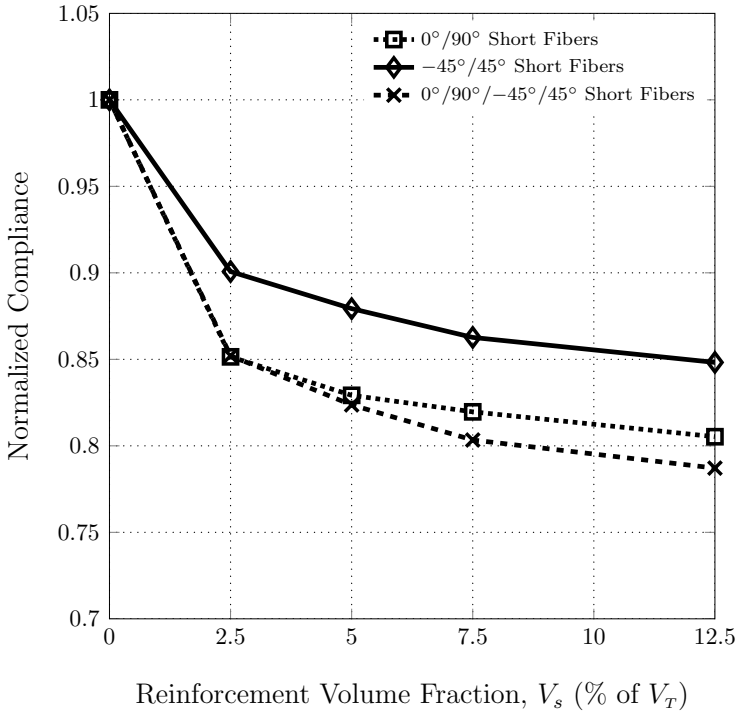


**Figure 3.45:** Normalized compliance for optimized L-bracket solutions for different object sets and reinforcement volume fractions; All values are normalized with the corresponding values for the unreinforced L-bracket.

### 3.3.3 Discrete Continuous Fibers

In this section, we introduce an extension of multi-phase DOP method for object sets to discrete continuous fibers. The key motivation of this extension comes from

the need of an algorithm that mimics the 3D-printing technique that can create component parts reinforced with yarn-like objects such as the carbon nanotube (CNT) yarns. The creation of discrete continuous fibers can be achieved using a projection of short fiber objects, where the thickness of the fiber is much smaller than its length (i.e. $r_{\min_{D,y}} \ll r_{\min_{D,x}}$) and the compliant enclosure is on the longitudinal surfaces only. The projection of this object is illustrated in Figure 3.46.

The local and enclosure neighborhood sets for longitudinally enclosed short fiber projection at 0° can be defined, respectively, as:

$$i \in N_L^e \qquad \text{if} \quad \left\{ \begin{array}{l} \|\mathbf{x}_{i,x} - \bar{\mathbf{x}}_x^e\| \leq r_{\min_{D,x}} \\ \\ \|\mathbf{x}_{i,y} - \bar{\mathbf{x}}_y^e\| \leq r_{\min_{D,y}} \end{array} \right\} \tag{3.33a}$$

$$i \in N_E^e \qquad \text{if} \quad \left\{ \begin{array}{l} r_{\min_{D,x}} < \|\mathbf{x}_{i,x} - \bar{\mathbf{x}}_x^e\| \leq r_{\min_{D,x}} \\ \\ r_{\min_{D,y}} < \|\mathbf{x}_{i,y} - \bar{\mathbf{x}}_y^e\| \leq r_{\min_{D,y}} + t_{E,y} \end{array} \right\} \tag{3.33b}$$

This equation is almost exactly the same as Eq. (3.32) except that $t_{E,x} = 0$ and $r_{\min_{D,y}}$ ¡¡ $r_{\min_{D,x}}$. Removing the enclosure at the fiber cross-sectional ends allows the end of these short fiber objects to overlap, essentially creating a chain of objects that represent continuous fibers. The objects also need not be overlapped, which would represent the end of the yarn and the yarn cutting action in the 3DP process. It is essential to maintain the compliant shell along the longitudinal surfaces as this prevents adjacent fibers from overlapping, thus keeping these continuous yarns discrete.

In the 3DP of continuous fiber composite materials, we have an option to deposit

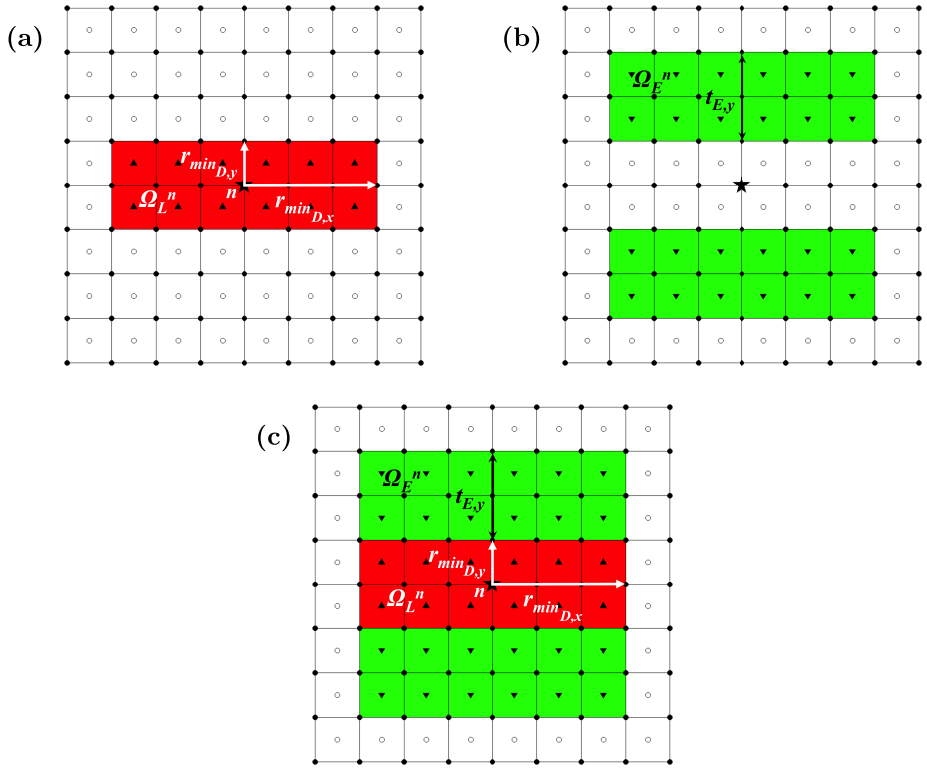


**Figure 3.46:** Projection of longitudinally enclosed short fiber from design variable $n$: (a) a projection of stiff phase (red) of length scale $r_{\min_{D,x}}$ and $r_{\min_{D,y}}$ onto the local domain $\Omega_l^i$ as expressed in Eq. 3.33a, (b) a projection of longitudinal compliant phase (green) onto the enclosure domain $\Omega_E^i$ as expressed in Eq. 3.33b, and (c) a illustration of final projection.

three different material phases: (1) short stiff fibers enclosed longitudinally inside a layer of polymer, (2) compliant material that makes up component topology, and (3) void phase (see Figure 3.47). To closely mimic the ability of 3DP machine to print the yarns at various angles, we provide the total of twelve possible orientations for placement of each of the short fibers (see Figure 3.48). The projection of fibers at

these different angles can be obtained by simply rotating the horizontal projection by desired orientations.

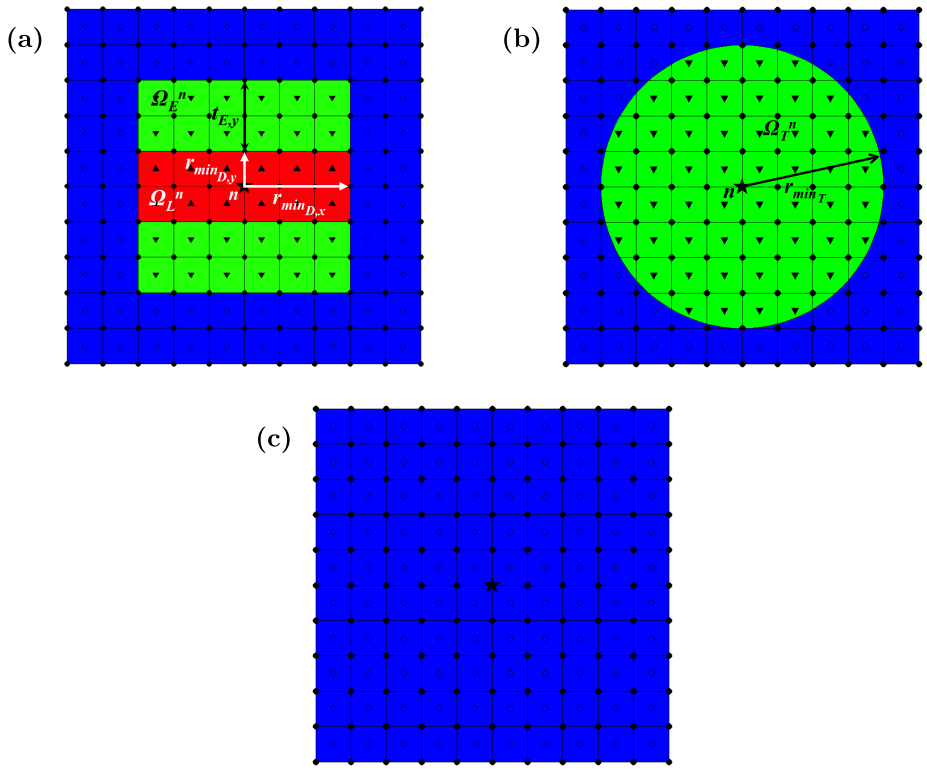


**Figure 3.47:** Discrete object projection from design variable $n$. (a) a projection of fiber (red) enclosed longitudinally inside a layer of compliant material (green), (b) a projection of compliant material (green), and (c) no projection resulting in void (blue).

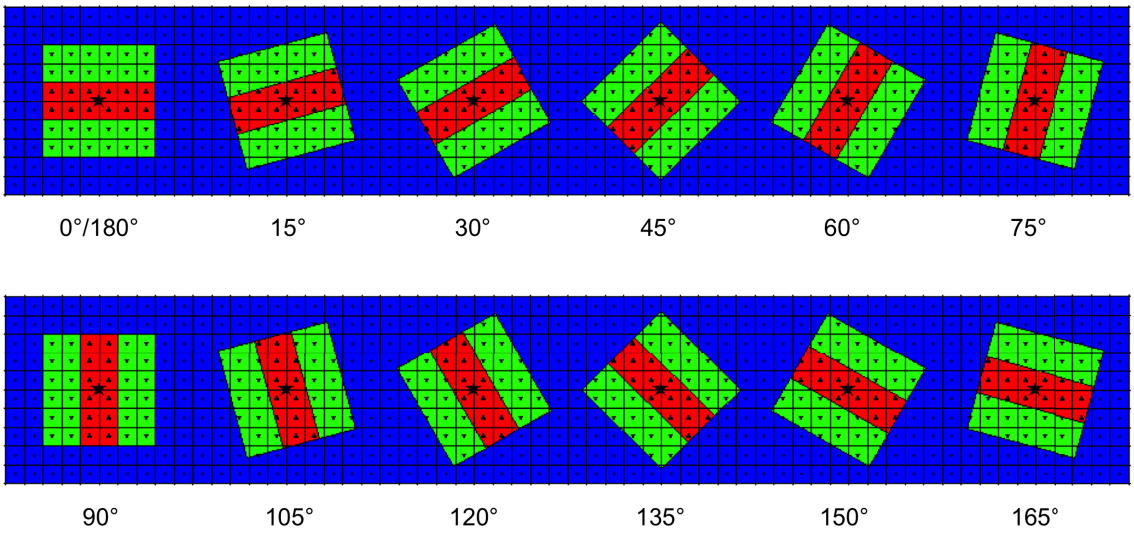


**Figure 3.48:** The predefined set of orientations for discrete continuous fibers.

### 3.3.4 Numerical Examples and Solutions For Discrete Continuous Fibers

The proposed multi-material DOP algorithm with discrete continuous fibers is demonstrated on benchmark cantilever beam, MBB beam, L-bracket, and compliant inverter problems. In these examples, we gradually increase $\beta$ from 5 to 50 in 12 continuation steps and RAMP parameter $\eta$ from 0 to 40 in 12 continuation steps as we did previously for optimization with discrete object sets (See Section 3.3.2).

#### 3.3.4.1 Cantilever Beam

The geometry and loading condition for the cantilever beam problem is the same as the one illustrated in Section 3.2.2.1 Figure 3.27. The half length scales of individual

fiber segment are $r_{\min_{D,x}} = 0.2$ units and $r_{\min_{D,y}} = 0.6$ units, and the minimum distance between each yarn is $t_E = 0.4$ units. The minimum topology feature radius $r_{\min_T}$ remains the same at 1.2 units.

Figure 3.49 shows the solution with discrete continuous fiber inclusion using the multi-material DOP formulation (Eq. (3.14)) for 5%, 7.5%, 15%, 25% and 35% reinforcement volume fractions. We can see that the algorithm successfully produce a long continuous yarn of stiff phase out of the short fiber projection. For small reinforcement volume of yarn, the algorithm places the longest yarns on the outermost top and bottom edges of the cantilever beam where bending stresses are highest, and shorter yarns on the interior and at the applied load (see Figures 3.49c and 3.49d). For larger yarn volume, these yarns begin to lengthen and appear along the webs of the cantilever beam. In the case of 35% volume fraction, the short fibers form continuous yarns that travel all the way from top support to applied load to bottom support, creating one long continuous load path.

As expected, cantilever beam with continuous fiber reinforcements perform significantly better than those with particle reinforcement as seen in Figure 3.50. This is because continuous fibers provide uninterrupted load path. By comparison, yarn reinforcements provide almost 20% gain in stiffness using only 7.5% volume fraction of stiff phase (see Table 3.14) while particle reinforcements provide only 11.4% gain, and the differences between the stiffness gains of these two different reinforcements get larger as the volume of reinforcement increases.

**Table 3.14:** Cantilever beam results with discrete continuous fibers: compliance and final reinforcement percent volume fraction inside optimal component topology for different given reinforcement percent volume fractions.

| $V_{s,\text{given}}$ (%)* | Fig. | Compliance | $V_{s,\text{used}}$ (%)* | % Stiffness gain† |
|---|---|---|---|---|
| 0 | 3.49a | 45.43 | 0 | 0 |
| 5 | 3.49c | 38.17 | 5 | 16.0 |
| 7.5 | 3.49d | 36.41 | 7.5 | 19.8 |
| 15 | 3.49e | 32.49 | 15 | 28.5 |
| 25 | 3.49f | 28.53 | 25 | 37.2 |
| 35 | 3.49g | 25.85 | 35 | 43.1 |

* $V_{s,\text{given}}$ and $V_{s,\text{used}}$ are presented as % of $V_T$.

† These values represent percent stiffness gains over the optimized unreinforced cantilever beam.

It is interesting to note that while the component topology resemble the traditional two-phase topology optimization (shown in Figure 3.28a) and exhibit symmetry, the placement of the yarns are not entirely symmetrical. This is most noticeable in Figure 3.49g for the case of 35% volume fraction at the web joint. At this location, the algorithm would most likely prefer for the fiber to cross, but this cannot be done because of the compliant shell along the longitudinal surfaces of the fiber. This behavior is further discussed in Section 3.3.4.5. Nevertheless, this behavior shows that the algorithm is successful in keeping each yarn from overlapping.

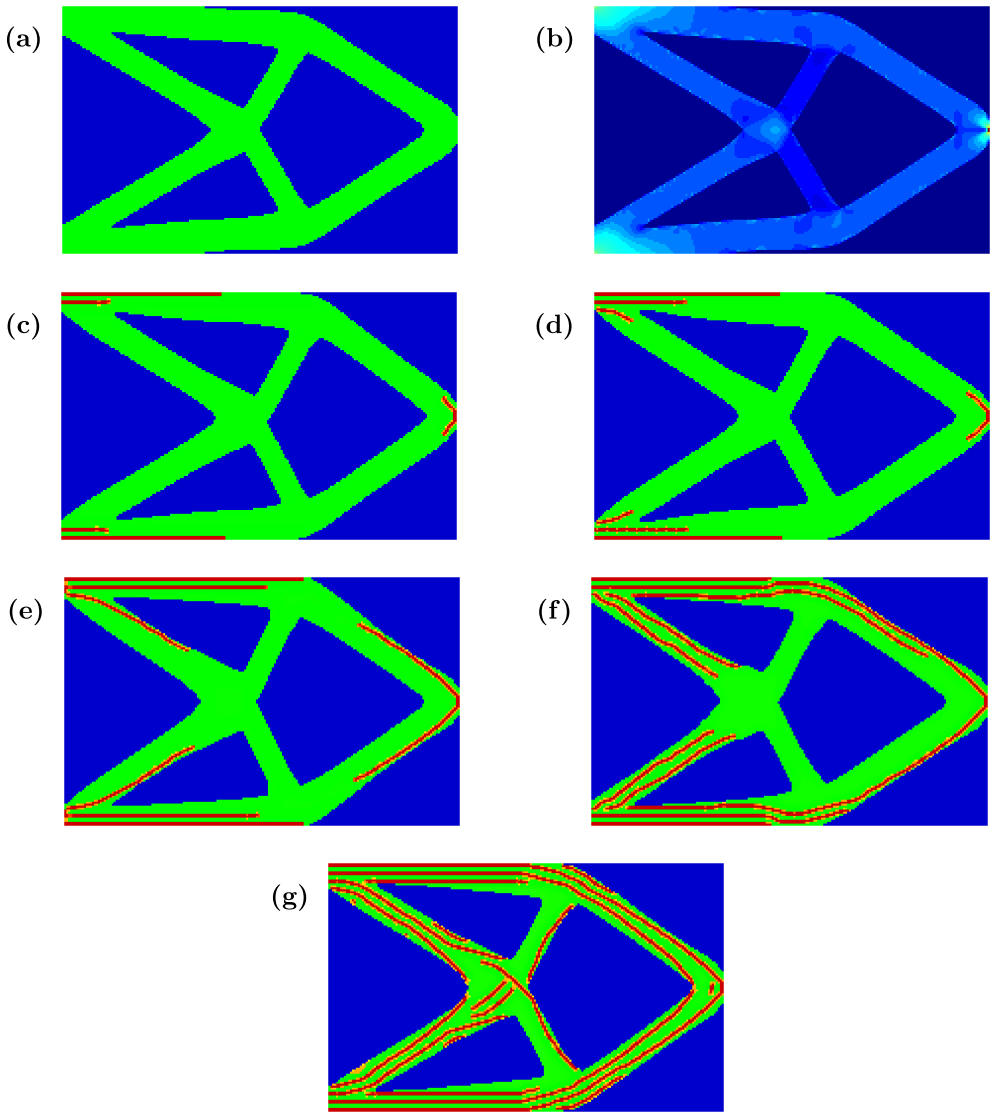


**Figure 3.49:** Cantilever beam results with discrete continuous fibers: (a) optimized solution using traditional monolithic formulation composed of compliant material with allowable total volume fraction $V_t = 40\%$, (b) von Mises stress plot for structure in (a), and optimized solutions using the multi-material DOP formulation (Eq. (3.14)) with allowable volume of stiff material (c) $V_s = 5\%$ of $V_T$, (d) $V_s = 7.5\%$ of $V_T$, (e) $V_s = 15\%$ of $V_T$, (f) $V_s = 25\%$ of $V_T$, and (g) $V_s = 35\%$ of $V_T$.

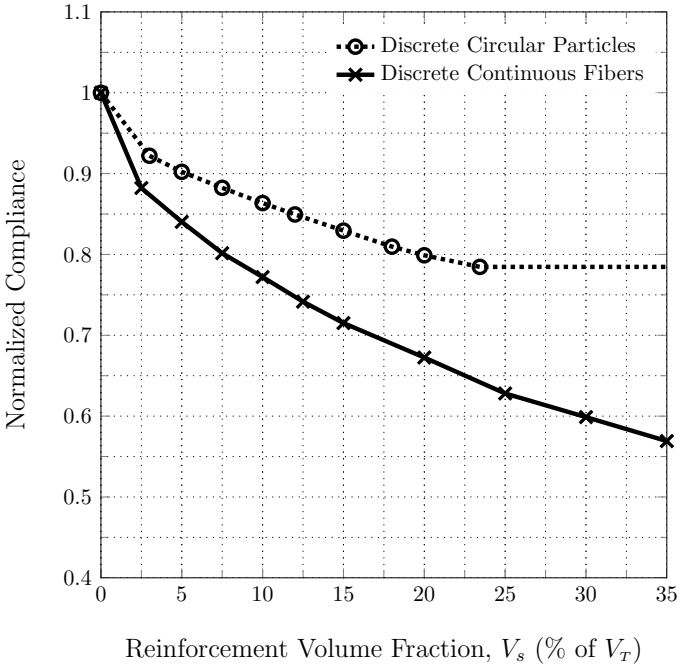


**Figure 3.50:** Normalized compliance for optimized cantilever beam solutions with stiff circular particles and with discrete continuous fibers for different reinforcement volume fractions; All values are normalized with the corresponding values for the optimized unreinforced cantilever beam.

#### 3.3.4.2 MBB Beam

The geometry and loading condition for the MBB beam problem is the same as the one illustrated in Section 3.2.2.2 Figure 3.30. The length scales of individual fiber segment are $r_{\min_{D,x}} = 0.25$ units and $r_{\min_{D,y}} = 0.75$ units, and the minimum distance between each yarn is $t_E = 0.5$ units.

Figure 3.51 shows the solution with discrete continuous fiber inclusion using the multi-material DOP formulation (Eq. (3.14)) for 5%, 12.5%, 15%, 20%, and 25% reinforcement volume fractions. We again see that the algorithm successfully create a long continuous yarn reinforcement from short fiber projection. Solutions also show that both component topology and placement of reinforcement are optimized simultaneously. The long fibers are placed first at the top and bottom chords where bending stress are largest. Shorter fibers are placed at the support and on the interiors of the chords. Similar to cantilever beam solutions, the length of these yarns gets longer as reinforcement volumes become higher and the webs are reinforced.

We again observe similar expected trend where MBB beam with continuous fiber reinforcements perform much better than those with particle reinforcement as seen in Figure 3.52. This is because of the continuous load path provided by the fibers. In this example problem, we see almost 35% gain in stiffness using only 15% reinforcement volume fraction (see Table 3.14) while particle reinforcements provide only 17.7%.

It can be observed in the optimized solution for MBB beam problem with 5% fiber volume fraction in Figure 3.51c that the algorithm chooses to place two short

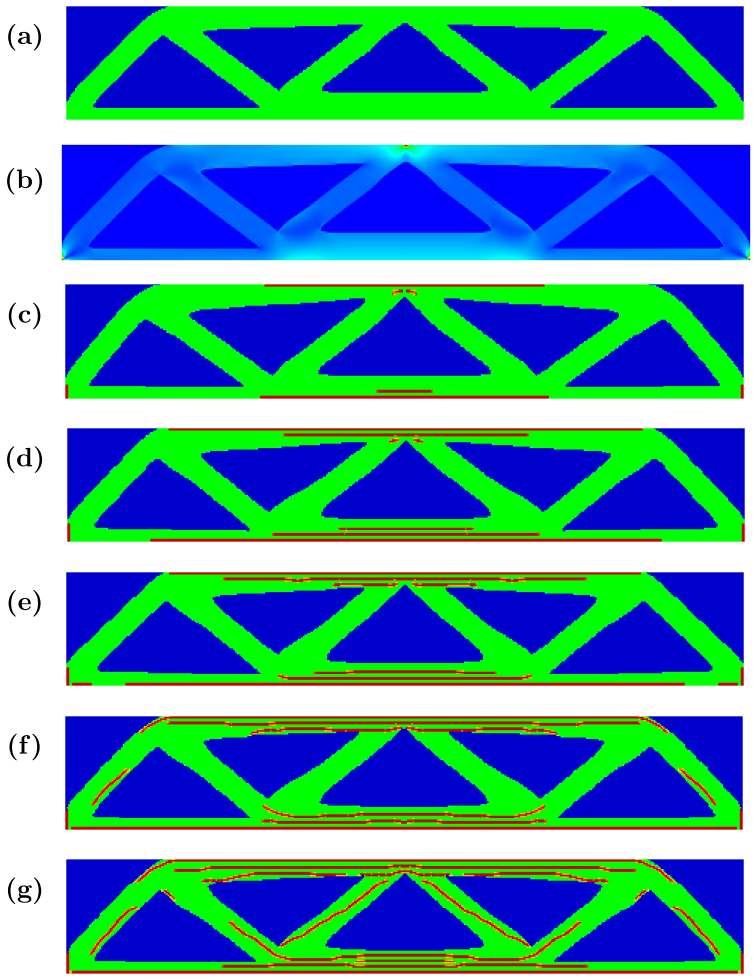


**Figure 3.51:** MBB beam results with discrete continuous fibers: (a) optimized solution using traditional monolithic formulation composed of compliant material with allowable total volume fraction $V_t = 50\%$, (b) von Mises stress plot for structure in (a), and optimized solutions using the multi-material DOP formulation (Eq. (3.14)) with allowable volume of stiff material (c) $V_s = 5\%$ of $V_T$, (d) $V_s = 12.5\%$ of $V_T$, (e) $V_s = 15\%$ of $V_T$, (f) $V_s = 20\%$ of $V_T$, and (g) $V_s = 25\%$ of $V_T$.

**Table 3.15:** MBB beam results with discrete continuous fibers: compliance and final reinforcement percent volume fraction inside optimal component topology for different given reinforcement percent volume fractions.

| $V_{s,\text{given}}$ (%)* | Fig. | Compliance | $V_{s,\text{used}}$ (%)* | % Stiffness gain† |
|---|---|---|---|---|
| 0 | 3.51a | 194.50 | 0 | 0 |
| 5 | 3.51c | 156.27 | 5 | 19.7 |
| 12.5 | 3.51d | 132.71 | 12.5 | 31.8 |
| 15 | 3.51e | 127.52 | 15 | 34.4 |
| 20 | 3.51f | 121.01 | 20 | 37.8 |
| 25 | 3.51g | 115.47 | 25 | 40.6 |

* $V_{s,\text{given}}$ and $V_{s,\text{used}}$ are presented as % of $V_T$.

† These values represent percent stiffness gains over the optimized unreinforced MBB beam.

fibers at the top chord instead of one continuous longer fiber. To ensure that the solution with two short fibers is truly optimized, we compare the compliance of this solution to the one where the two short fibers are connected. Figures 3.53a and 3.53b show the fibers from the optimized solution and from manually connecting the two fibers, respectively, overlaying the von Mises stress plot (as seen in Figure 3.51b). The resulting compliance for solution with two short fibers is 156.285 and for solution with one continuous longer fiber is 156.292. Although the difference between the two compliances are small, it validates that the solution from the algorithm is optimized

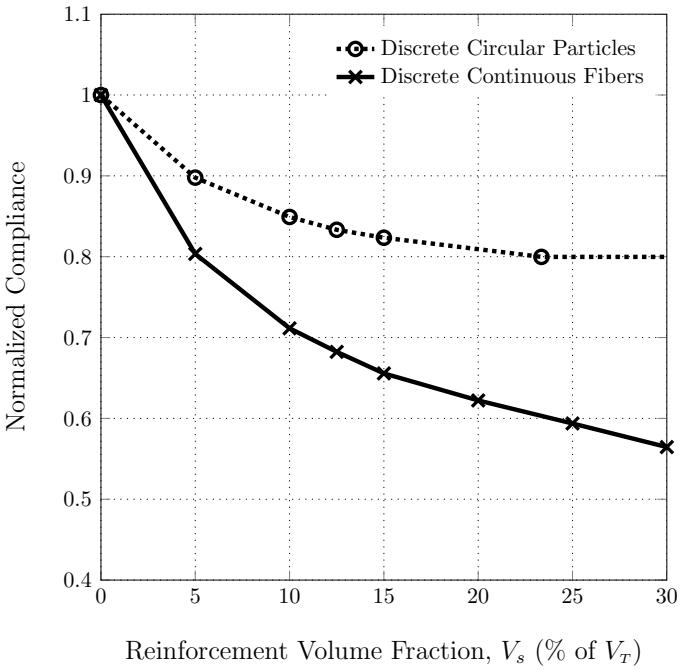


**Figure 3.52:** Normalized compliance for optimized MBB beam solutions with stiff circular particles and with discrete continuous fibers for different reinforcement volume fractions; All values are normalized with the corresponding values for the optimized unreinforced MBB beam.

and that the placement of these yarns is truly driven by the stresses.

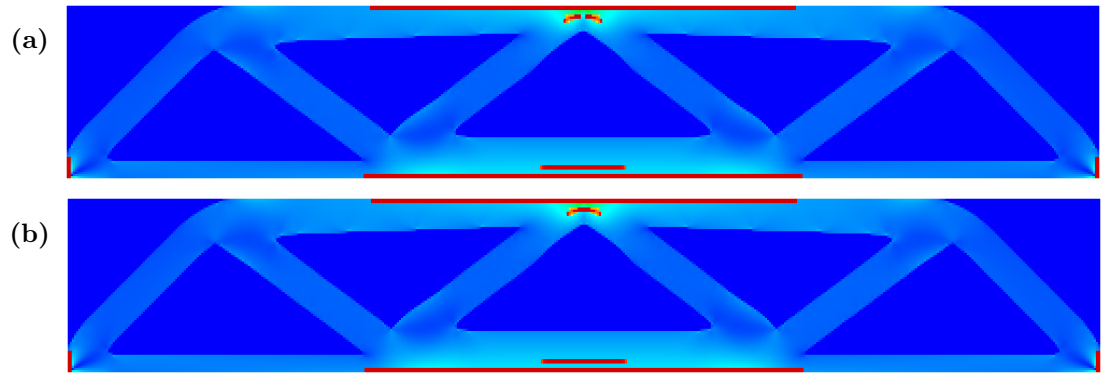


**Figure 3.53:** Illustration of (a) the fibers from the optimized solution and (b) from manually connecting the two fibers, overlaying the von Mises stress plot (as seen in Figure 3.51b). Both solutions contain 5% yarn volume fraction.

#### 3.3.4.3 L-Bracket

The geometry and loading condition for the L-bracket is the same as the one illustrated in Section 3.2.2.3 Figure 3.33. The half length scales of individual fiber segment are $r_{\min_{D,x}} = 0.2$ units and $r_{\min_{D,y}} = 0.6$ units, and the minimum distance between each yarn is $t_E = 0.4$ units.

Figure 3.54 shows the solution with discrete continuous fiber inclusion using the multi-material DOP formulation (Eq. (3.14)) for 5%, 10%, 15%, 20% and 35% reinforcement volume fractions. Creation of discrete continuous fibers can be seen in all of the solutions. As expected, long vertical fibers are placed along the outer edges of the vertical members from the supports, which experience high strain energy. We also observe that the yarns are essentially branching out at the stress concentration point and continue through the webs reinforcing the component. Similar to the cantilever

solutions, we again see short fibers form continuous yarns that trace the interior edge of the component topology all the way from top left support to applied load, creating one long continuous load path.

Similar to the optimized cantilever beam and MBB beam solutions, the compliance of the optimized L-brackets with continuous fiber reinforcements are significantly lower than those with particle reinforcement as seen in Figure 3.50. With only 5% of yarn reinforcements, the compliance of L-bracket is reduced by 22.3% (see Table 3.14) while particle reinforcements of the same volume reduces by only 10.7%.

**Table 3.16:** L-bracket results with discrete continuous fibers: compliance and final reinforcement percent volume fraction inside optimal component topology for different given reinforcement percent volume fractions.

| $V_{s,\text{given}}$ (%)* | Fig. | Compliance | $V_{s,\text{used}}$ (%)* | % Stiffness gain† |
|---|---|---|---|---|
| 0 | 3.54a | 80.95 | 0 | 0 |
| 5 | 3.54c | 62.88 | 5 | 22.3 |
| 10 | 3.54d | 57.35 | 10 | 29.2 |
| 15 | 3.54e | 53.49 | 15 | 33.9 |
| 20 | 3.54f | 50.40 | 20 | 37.7 |
| 35 | 3.54e | 44.32 | 35 | 45.3 |

* $V_{s,\text{given}}$ and $V_{s,\text{used}}$ are presented as % of $V_T$.

† These values represent percent stiffness gains over the optimized unreinforced L-bracket.

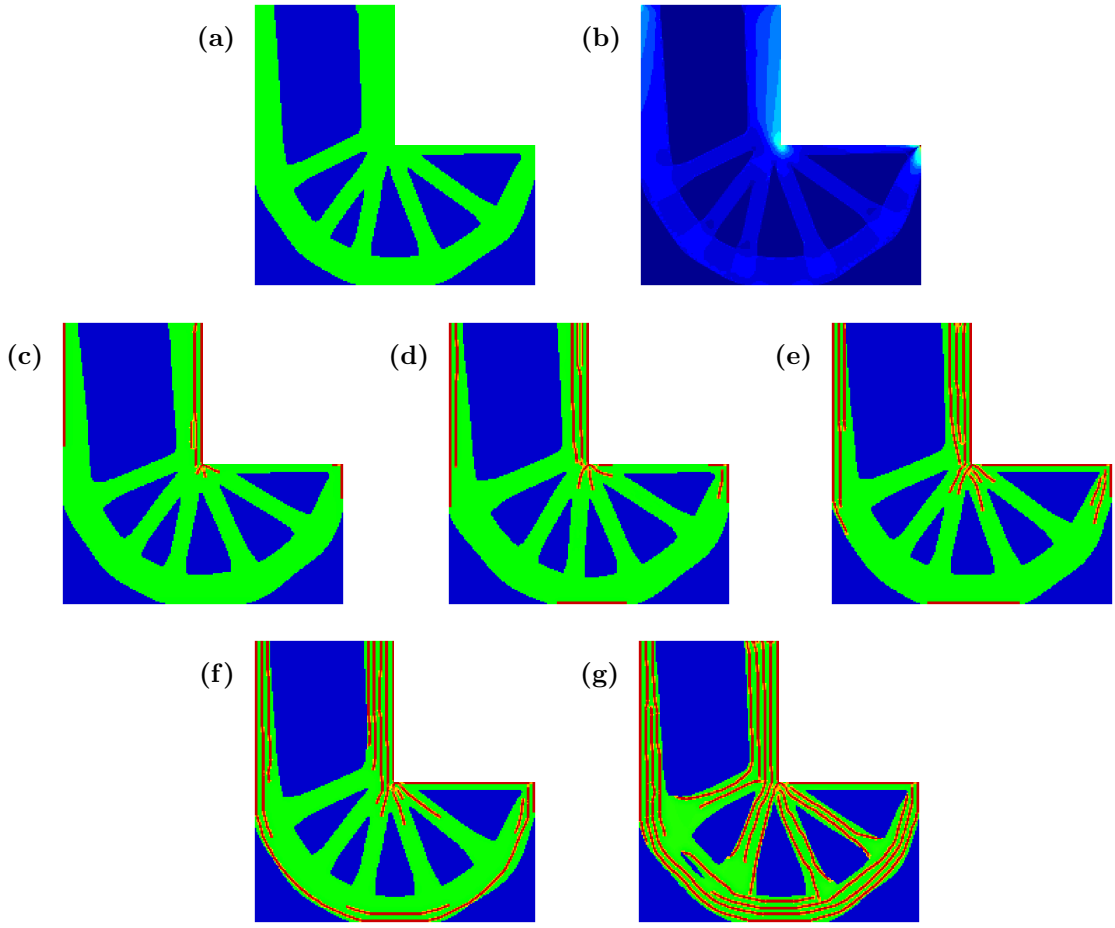


**Figure 3.54:** L-bracket results with discrete continuous fibers: (a) optimized solution using traditional monolithic formulation composed of compliant material with allowable total volume fraction $V_t = 40\%$, (b) von Mises stress plot for structure in (a), and optimized solutions using the multi-material DOP formulation (Eq. (3.14)) with allowable volume of stiff material (c) $V_s = 5\%$ of $V_T$, (d) $V_s = 10\%$ of $V_T$, (e) $V_s = 15\%$ of $V_T$, (f) $V_s = 20\%$ of $V_T$, and (g) $V_s = 35\%$ of $V_T$.

It is important to note that the optimized L-bracket topology with 35% volume fraction slightly differs than the rest of the solution shown here. Since the topology of

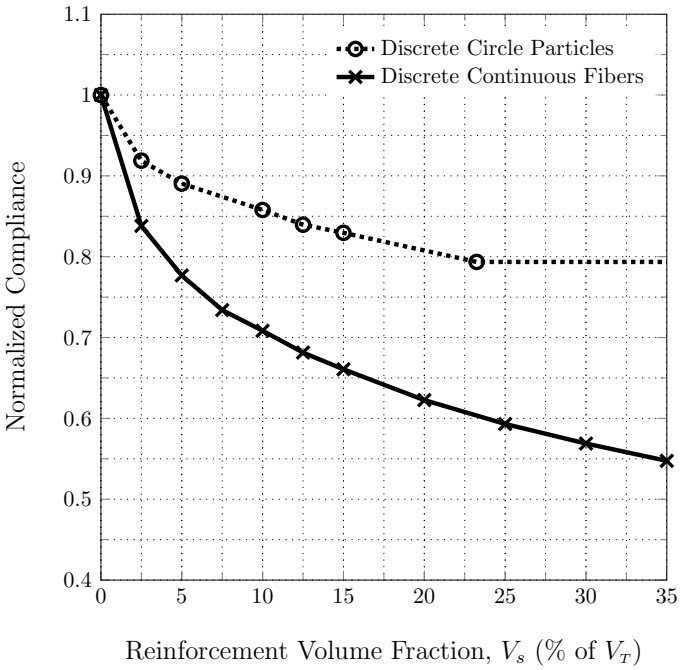


**Figure 3.55:** Normalized compliance for optimized L-bracket solutions with stiff circular particles and with discrete continuous fibers for different reinforcement volume fractions; All values are normalized with the corresponding values for the optimized unreinforced L-bracket beam.

component and the layout of reinforcement are optimized simultaneously (i.e. not in succession where component topology is optimized first then the reinforcements), the optimized component topologies can vary. Base of observation made from the design evolution for this case (see Figure 3.59 in Section 3.3.4.5), the existence of hole in Figure 3.54g may be contributed from ending the continuation step 2 too early (i.e. not enough iterations) for the algorithm to create one large hole (see Figure 3.59c). Increasing the number of iterations at this continuation step would likely have allowed

the algorithm to continue removing the solid region between the small and large hole, creating single triangular void region.

#### 3.3.4.4 Compliant Inverter

The geometry and loading condition for the compliant inverter problem is the same as the one illustrated in Section 3.2.2.4 Figure 3.36. The half length scales of individual fiber segment are $r_{\min_{D,x}} = 0.2$ units and $r_{\min_{D,y}} = 0.6$ units, and the minimum distance between each yarn is $t_E = 0.4$ units.

Figure 3.56 shows the solution with discrete continuous fiber inclusion using the multi-material DOP formulation (Eq. (3.16)) for 2.5%, 10%, 15%, 25% and 35% reinforcement volume fractions. We can see that for very low reinforcement volume, the algorithm places the all available stiff fibers at the locations of high strain energy, which are the locations of all the hinges, the supports, and the input port. As previously discussed in Section 3.2.2.4, placing stiff reinforcement at the hinges increases the performance of the inverter as long as the objects are place along the centerline of the hinges, and here we can see that the algorithm places the yarn right along centerline of the hinges. With only 2.5% reinforcement, the displacement at the output port increases by 9.3%.

As the reinforcement becomes more available, the yarns increases in length and are place along top and bottom load-carrying members, then the webs, then the inclined members. It is very interesting to see how the placement of these yarns

closely matches the contour of the stress plot. This is best illustrated by the yarn placement along the inclined members in Figure 3.56g. In this case, the yarns from the two ends of the inclined members are not placed at the center of the members as one would assume. Instead, the yarns coming from the top and bottom hinge are placed closer to the right edge of the inclined members, while the yarns coming from the hinge near the output port are placed closer to the left edge of the inclined members. This directly corresponds to the fact that the stresses are higher at those edges as can be observed from the von Mises stress plot in Figure 3.56b. Rather than connecting these yarns, another longer yarn is placed on the inclined members allowing for presence of more volume of stiff material in these members.

As expected, the performance of inverter with continuous fiber reinforcements surpasses those with discrete particle reinforcements as seen in Figure 3.50. It should be noted that the optimized topologies of the component slight varies for different reinforcement volume fractions, where extra voids appear in the topologies. This is most likely due to solutions being in different local minima.

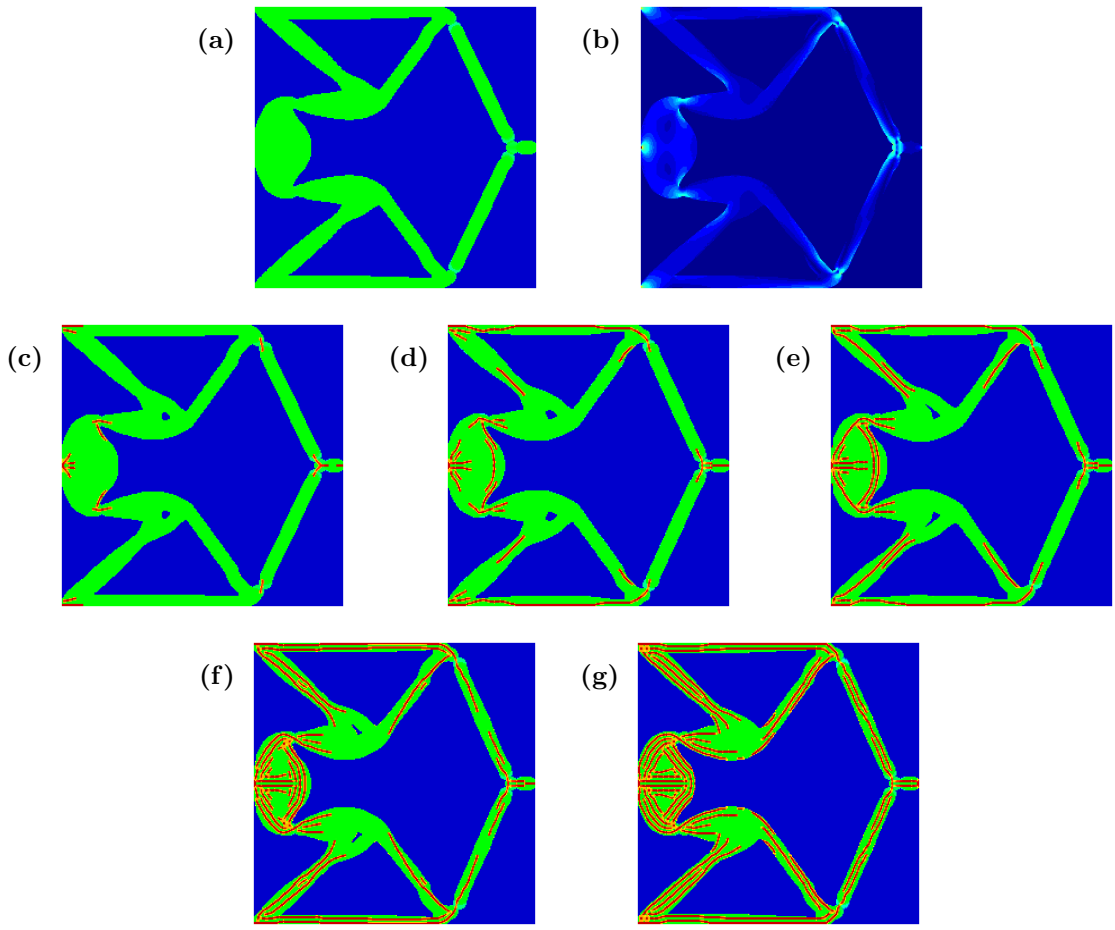


**Figure 3.56:** Compliant inverter results with discrete continuous fibers: (a) optimized solution using traditional monolithic formulation composed of compliant material with allowable total volume fraction $V_t = 30\%$, (b) von Mises stress plot for structure in (a), and optimized solutions using the multi-material DOP formulation (Eq. (3.16)) with allowable volume of stiff material (c) $V_s = 2.5\%$ of $V_T$, (d) $V_s = 10\%$ of $V_T$, (e) $V_s = 15\%$ of $V_T$, (f) $V_s = 25\%$ of $V_T$, and (g) $V_s = 35\%$ of $V_T$.

**Table 3.17:** Compliant inverter results with discrete continuous fibers: displacement at the output port and final reinforcement percent volume fraction inside optimal component topology for different given reinforcement percent volume fractions.

| $V_{s,\text{given}}$ (%)* | Fig. | Compliance | $V_{s,\text{used}}$ (%)* | % Displacement gain† |
|---|---|---|---|---|
| 0 | 3.56a | -191.68 | 0 | 0 |
| 2.5 | 3.56c | -209.52 | 2.5 | 9.3 |
| 10 | 3.56d | -227.97 | 10 | 18.9 |
| 15 | 3.56e | -231.72 | 15 | 20.9 |
| 25 | 3.56f | -246.80 | 25 | 28.8 |
| 35 | 3.56g | -253.18 | 35 | 32.1 |

* $V_{s,\text{given}}$ and $V_{s,\text{used}}$ are presented as % of $V_T$.

† These values represent percent displacement gains over the optimized unreinforced compliant inverter.

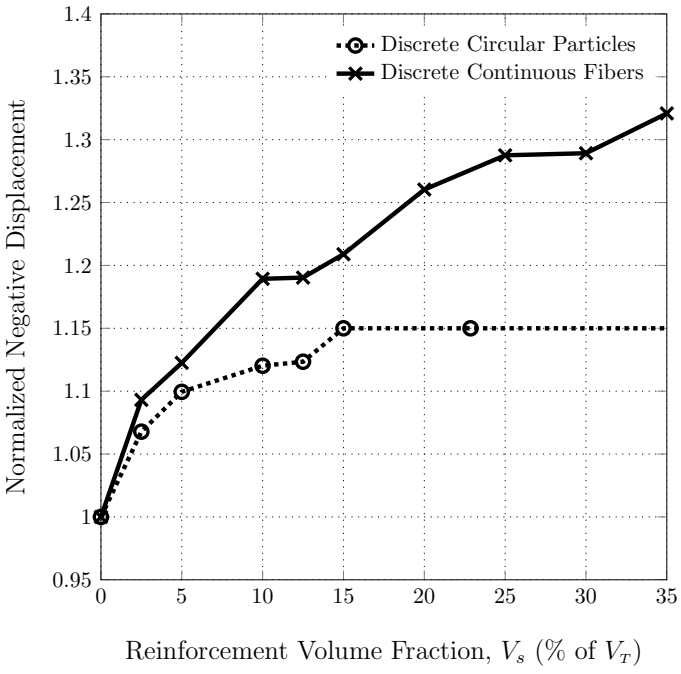


**Figure 3.57:** Normalized negative displacement for optimized compliant inverter solutions with stiff circular particles and with discrete continuous fibers for different reinforcement volume fractions; All values are normalized with the corresponding values for the optimized unreinforced compliant inverter.

#### 3.3.4.5 Example Design Evolutions

The design evolutions for the optimized cantilever beam and L-bracket solutions with discrete continuous fibers for reinforcement volume fraction of 35% (Figures 3.49g and 3.54g, respectively) are shown in Figures 3.58 and 3.59, respectively. The designs begins with uniform initial guess without any discrete object.

Some similar trends to the design evolution for solutions with discrete circular particles (Figures 3.39 and 3.40) can be seen for those with discrete continuous fiber. Mainly, the evolution of component topology resembles the free-form evolution of traditional topology optimization. During the first continuation steps, both component topology and the stiff phase contain intermediate volume fraction as expect since there is no penalty applied (i.e. $\eta = 0$).

One difference between the design evolutions for discrete circular particles and discrete continuous fiber we found is that clearer definite of discrete yarn can be observed at the locations of largest stresses even when $\eta = 0$ (Figures 3.39). This behavior makes sense because continuous fibers provide continuous load path making it easier for the algorithm to place them at the locations where they are most needed.

It can, however be observed that larger values of both RAMP penalty term $\eta$ and Heaviside curvature parameter $\beta$ are required to obtain crisp yarn edges. This is most likely related to the the larger numbers of design variable set because the possibility of overlapping between objects would increase with the number of additional design variable set. As the large penalty create crisp yarn edges by removing intermediate

volume fraction around the edge of the yarn, those volumes are then added back into the structure resulting in longer yarns (Figures 3.58h and 3.58i) or connections of yarn (Figures 3.59h and 3.59i) in certain places.

As mentioned previously in Section 3.3.4.1 that in the cantilever beam problem, the placement of the yarns are not entirely symmetrical even though the component topology exhibit symmetry. Looking at the design evolution for the cantilever beam, we can see that the yarns are placed symmetrically during the early steps of continuation (Figures 3.58b-3.58d). The evolution of designs from continuation steps 3 to 4 shows that short yarns at web joint and yarns at short webs would prefer to be joined to create two symmetric longer yarns. This would, however, mean that these yarns will be crossed, leading to phase mixing which would be inefficient. The algorithm thus avoid phase mixing by choosing to connect only one of the yarn at web joint to one of the yarn at web. This demonstrate the effectiveness of the proposed algorithm to create non-overlapping objects.

In the case of the existence of small void region in optimized L-bracket topology with 35% stiff volume fraction (Figure 3.54g), we believe that this is most likely due to insufficient number of iterations within the early continuation steps. This is based on the observations made from the evolution of designs from continuation steps 2, where the the void regions start to appear, but not quite finished forming when penalization increases causing the solid member to form creating an extra small void region. This solid member is right away reinforced by the stiff yarn because it is now in load path.

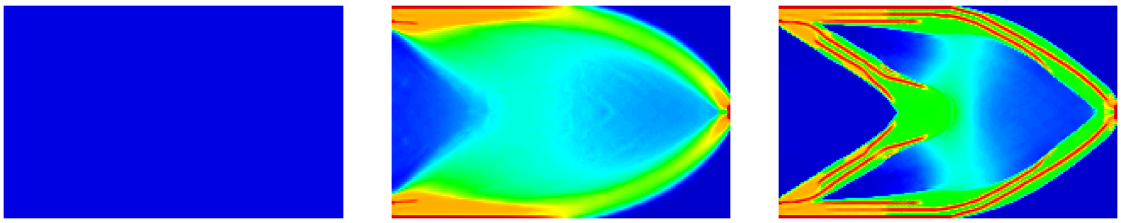

**(a)** Initial guess



**(b)** Continuation step 1 ($\eta = 0$, $\beta = 5$)



**(c)** Continuation step 2 ($\eta = 1$, $\beta = 6$)

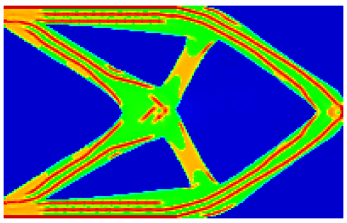

**(d)** Continuation step 3 ($\eta = 2$, $\beta = 7$)

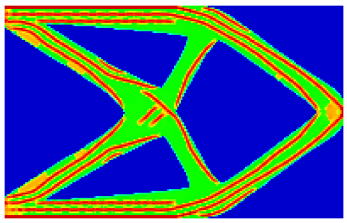

**(e)** Continuation step 4 ($\eta = 3$, $\beta = 8$)

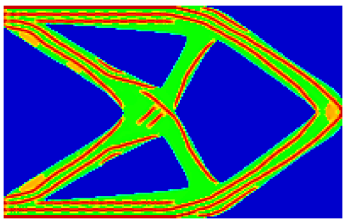

**(f)** Continuation step 5 ($\eta = 4$, $\beta = 9$)

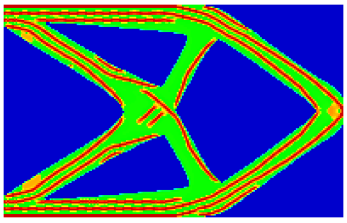

**(g)** Continuation step 7 ($\eta = 7$, $\beta = 12$)

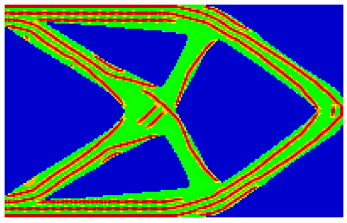

**(h)** Continuation step 9 ($\eta = 15$, $\beta = 20$)

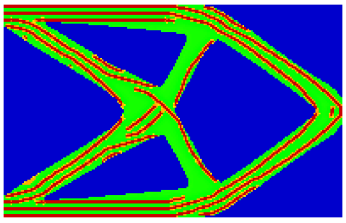

**(i)** Continuation step 12 ($\eta = 40$, $\beta = 50$)

**Figure 3.58:** Design evolution for the topology shown in Figure 3.49g. Note: initial guess is uniform.

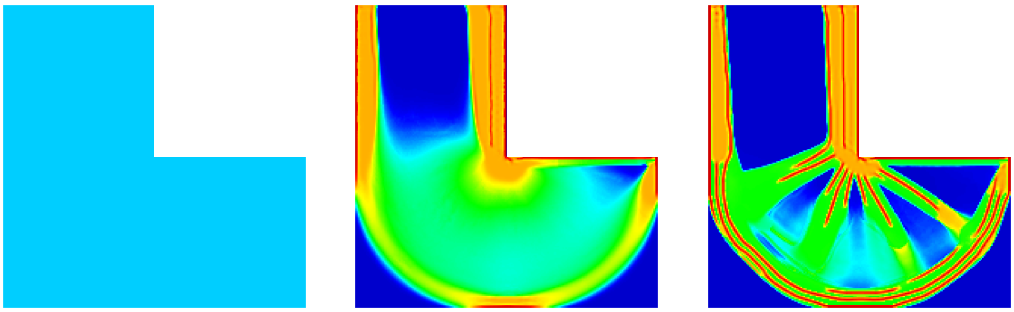

**(a)** Initial guess

**(b)** Continuation step 1 ($\eta = 0$, $\beta = 5$)

**(c)** Continuation step 2 ($\eta = 1$, $\beta = 6$)

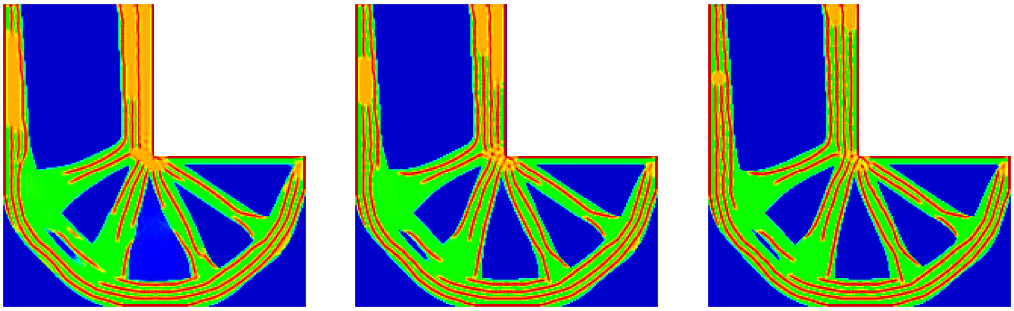

**(d)** Continuation step 3 ($\eta = 2$, $\beta = 7$)

**(e)** Continuation step 4 ($\eta = 3$, $\beta = 8$)

**(f)** Continuation step 5 ($\eta = 4$, $\beta = 9$)

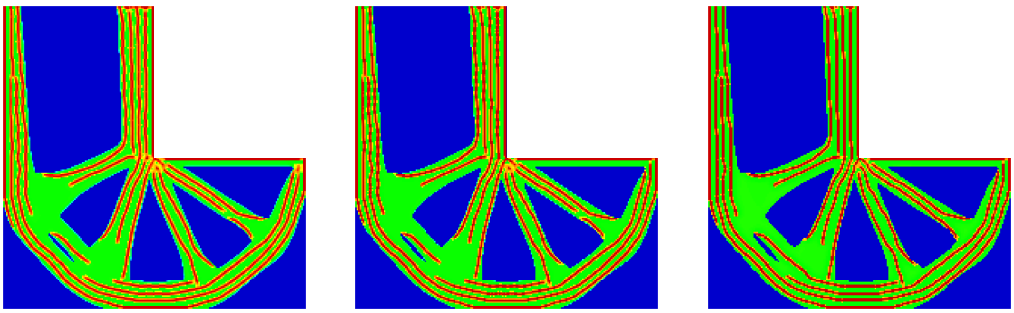

**(g)** Continuation step 6 ($\eta = 5$, $\beta = 10$)

**(h)** Continuation step 9 ($\eta = 15$, $\beta = 20$)

**(i)** Continuation step 12 ($\eta = 40$, $\beta = 50$)

**Figure 3.59:** Design evolution for the topology shown in Figure 3.54g. Note: initial guess is uniform.

#### 3.3.4.6 Smaller Length Scale, Finer Mesh Resolution, and Stiffness Ratio

To investigate the effect of length scale and mesh resolution, we apply the multi-phase DOP algorithm to the benchmark simply supported MBB beam problem (Figure 3.30) loaded at the midpoint of the beam at the top chord. Here, the finite element mesh is 480 $\times$ 160 (i.e. the size of each finite element is 0.125 units), which is two times finer than the previous mesh used in Section 3.3.4.2. Here we also reduce the minimum length scale of the component topology $r_{\min_T}$ from 2 units to 0.5 units. The half length scale of the fiber reinforcement are kept the same as before at 0.6 units in the x-direction and 0.2 units in the y-direction. An optimized MBB beam with the new minimum length scale and without any reinforcement is shown in Figure 3.60.

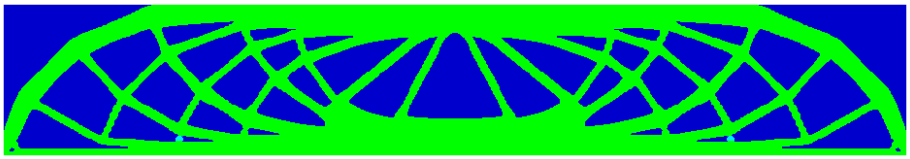

**Figure 3.60:** Optimized solution for MBB beam without any reinforcement

For stiffness ratio between the reinforcement and component of 3:1, we obtain optimized solutions shown in Figure 3.61 for reinforcement volume fraction of 12.5%, 20%, and 30% of $V_T$. We again see that the algorithm successfully optimizes both the placement of stiff reinforcement and the topology of the structure simultaneously. Similar to previous solutions with larger minimum length scale, the yarn reinforcement

is clearly identifiable and are strategically placed in the regions where stress and bending moment exist. As we give more reinforcement becomes available, the extra volume of yarns are placed at the web to take on the shear.

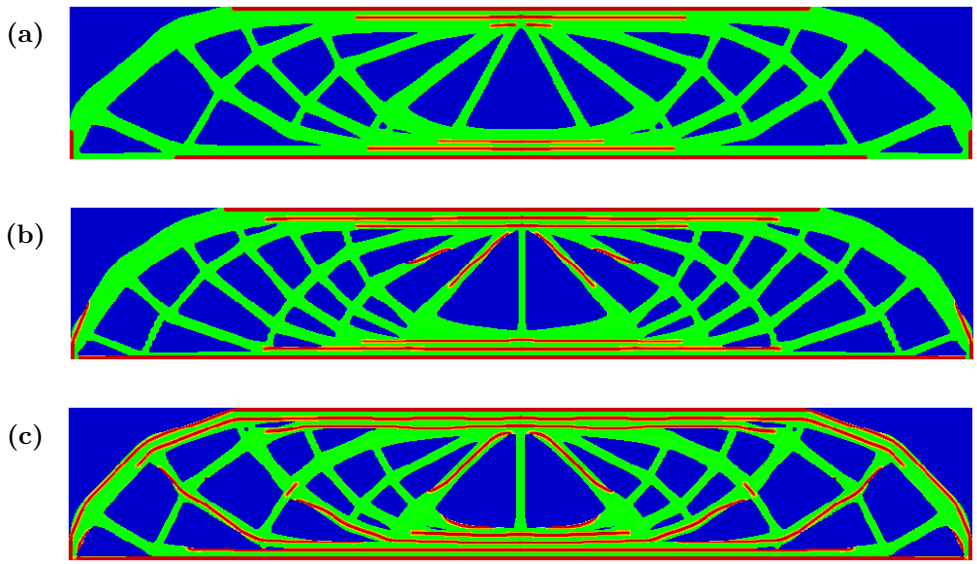


**Figure 3.61:** Optimized solution for simply supported beam with 3:1 stiffness ratio and continuous yarn reinforcement volume fraction of (a) 12.5%, (b) 20%, and (c) 30% of $V_T$.

We can see that by changing the component minimum length scale, the topology of the optimized solutions vary for different reinforcement volume fractions, which we did not see in the solutions with larger minimum length scale. This behavior becomes much more pronounced in the case where the stiffness ratio is increased to 24.5:1 to match the stiffness ratio between the CNT yarn and Ultem®. Figure 3.62 shows the optimized solutions for this case.

For this high stiffness ratio, the optimized solutions for the beam are very different

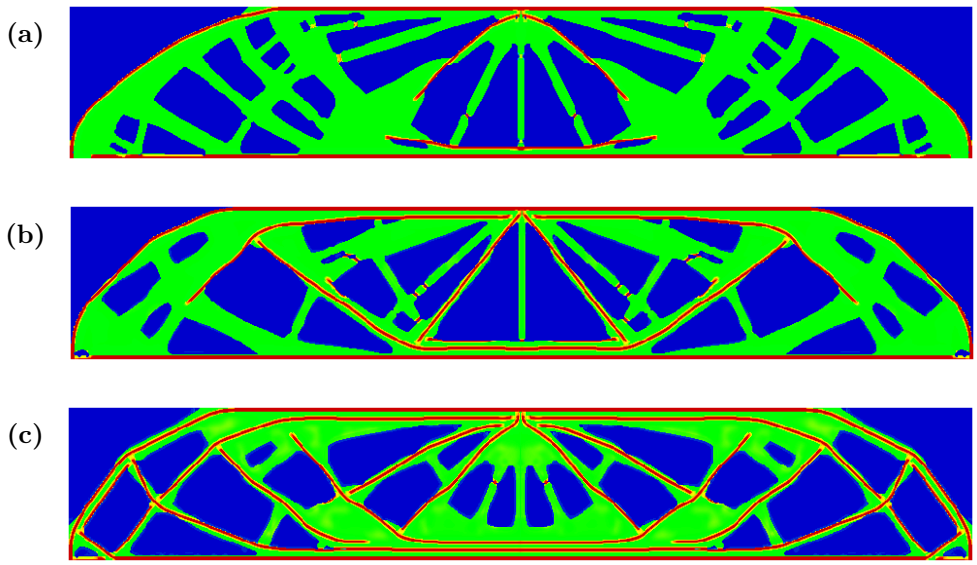


**Figure 3.62:** Optimized solution for simply supported beam with 24.5:1 stiffness ratio and continuous yarn reinforcement volume fraction of (a) 12.5%, (b) 20%, and (c) 30% of $V_T$.

both in terms of the yarn reinforcement layout and component topology from the previous solutions. For low yarn volume fraction, most of the yarn reinforcements are placed along the boundaries of the beam instead of concentrating at the top and bottom chords. This is because the yarn is much stiffer and thus less reinforcement is required to take on the bending stresses at the upper and lower chords. As we allow for more yarn volume in the component, the yarns are spread throughout the webs and we can observe that less compliant material is necessary in the webs near the ends of the beam when the volume of yarn reinforcement is high (see Figure 3.62c). This allows the algorithm to allocate the extra materials in middle of the beam to take on the bending stresses.

We would like to note that we ran into some convergence difficulty when we reduce the the length scale of the compliant phase in the cantilever beam problem. In this case we set the size of each finite element to be 0.1 units and reduce the minimum length scale of the component topology $r_{\min_T}$ to 0.3 units (from 1.2 units as previously used in Section 3.3.4.1). Here, the half length scale of the fiber reinforcement remains the same at $r_{\min_{D,x}} = 0.6$ units in the x-direction and $r_{\min_{D,y}} = 0.2$ units in the y-direction, making the length scale of the component about half the size of the fiber length in the x-direction and only 0.1 units bigger on the either side of fiber in the y-direction.

As we shrink the component topology length scale to approach the length scale of yarn, we observe that the algorithm has much harder time converging to solution with identifiable yarn reinforcement. This similar issue is also observed in Guest (2015) in the cases where the length scale of the compliant enclosure approaches the length scale of the stiff inclusion. In his work, Guest reported that the solutions contain high presence of phase mixing around the inclusion interface and becomes much worse when the the enclosure length scale gets smaller. Even though here the length scale of the component, not the enclosure, is reduced, we believe that the effect is the same as seen in Guest (2015) and warrants additional investigation.

## 3.4 Preventing Development of Partial Objects in 3-Phase Discrete Projection

From the results in Section 3.2.2, we observe several partial discrete objects at or near the boundaries of the component topology, as illustrated in Figure 3.63. This is because implementing the algorithm as presented in Section 3.2.1 allows partial objects to develop since the element volume fraction projecting discrete object $\rho_D$ is independent from element volume fraction projecting component topology $\rho_T$. Specifically, $\rho_D$ is allowed to be non-zero even when $\rho_T$ is equal to zero. This essentially means that discrete objects can be created in the void region near the boundary of the structure where part of the objects are projected on to the structure creating partial objects.

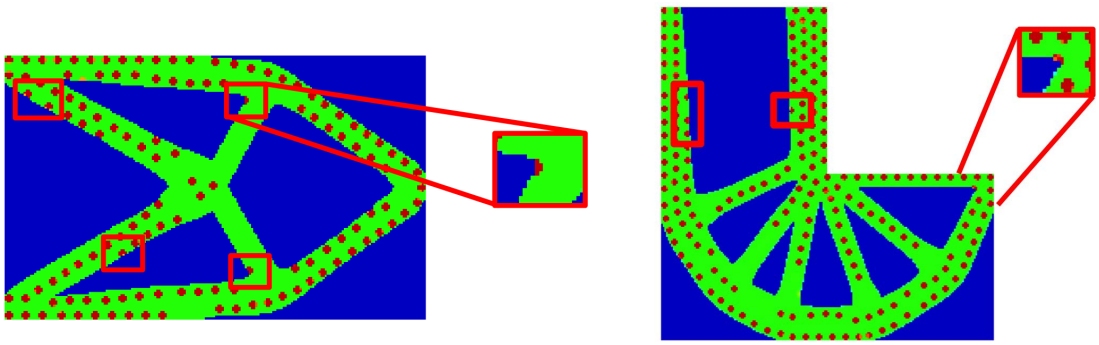

**Figure 3.63:** Development of partial objects near the boundaries of component topology in the optimized solutions of cantilever beam and L-bracket.

Inspection of $\rho_D$, $\rho_T$, and $\rho_D\rho_T$ of an optimized L-bracket solution with circular inclusion shown in Figures 3.34d and 3.63 illustrate this effect. It can be seen that in the regions where $\rho_T = 0$, $\rho_D$ takes on intermediate volume (see Figure 3.64a). This makes sense numerically because the gradient at these regions is zero. Since there is no incentive for the algorithm to drive $\rho_D$ to zero when $\rho_T = 0$, stiff objects can be created in these regions near the topology boundaries causing partial objects to develop as seen in Figure 3.64c.

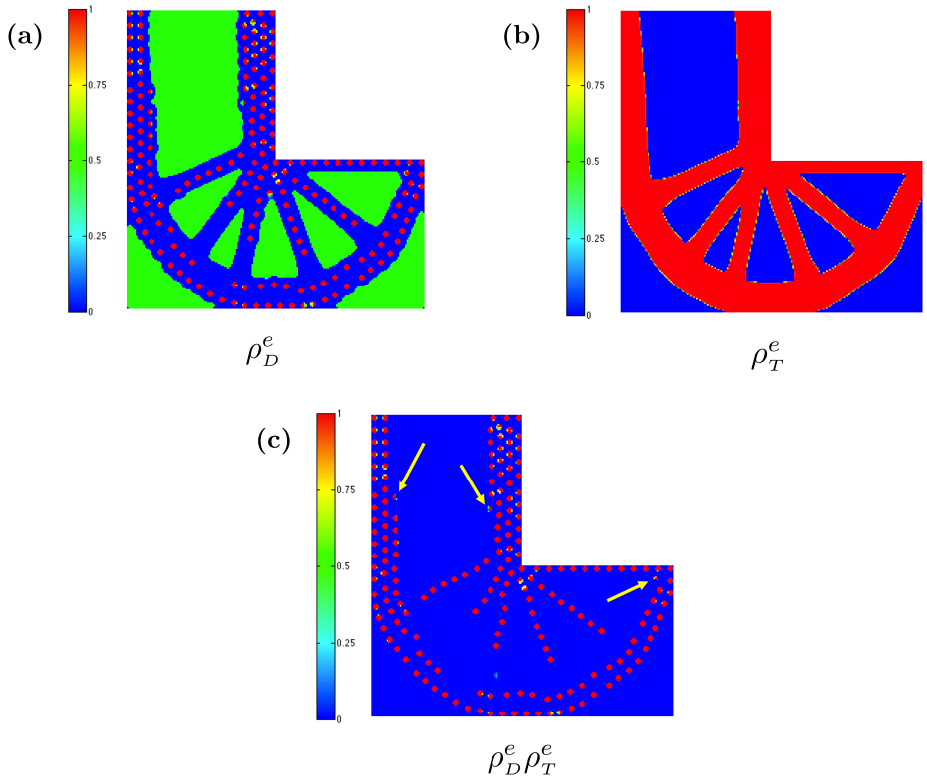


**Figure 3.64:** Illustration of $\rho_D$, $\rho_T$, and $\rho_D\rho_T$ of an optimized L-bracket solution with circular inclusion shown in Figures 3.34d and 3.63.

The technique, described in Section 3.2.1.4, in restricting projected length scale near the design domain boundaries cannot be applied in the context of restricting the length scale of the discrete object near the edges of the component topology because the topology is not known *a priori*. Instead, we propose restricting length scale near structure's boundaries by simply replacing a constraint function on the volume of stiff material with a constraint function on the volume of stiff material calculated only from $\rho_D^e(\boldsymbol{\phi}_D)$. The updated formulation for minimum compliance problems (Eq. (3.14)) then becomes:

$$\min_{\boldsymbol{\phi}_D, \boldsymbol{\phi}_T} \quad C = \mathbf{F}^{\mathrm{T}}\mathbf{d} \tag{3.34a}$$

$$\text{s.t.} \quad \mathbf{K}(\boldsymbol{\phi}_D, \boldsymbol{\phi}_T)\mathbf{d} = \mathbf{F} \tag{3.34b}$$

$$\sum_{\forall e \in \Omega} \rho_T^e(\boldsymbol{\phi}_T) v^e \leq V \tag{3.34c}$$

$$\sum_{\forall e \in \Omega} \rho_D^e(\boldsymbol{\phi}_D) v^e \leq V_s \tag{3.34d}$$

$$0 \leq \phi_i \leq \phi_{max} \quad \forall i \in \Omega \tag{3.34e}$$

and the updated formulation for maximum negative displacement of the compliant

inverter (Eq (3.16)) becomes:

$$\min_{\boldsymbol{\phi}_D,\boldsymbol{\phi}_T} \quad C = \max\left\{\mathbf{L}^{\mathrm{T}}\mathbf{d}_{\left(r_{\mathrm{minsmall}_T}\right)}, \mathbf{L}^{\mathrm{T}}\mathbf{d}_{\left(r_{\mathrm{minlarge}_T}\right)}\right\} \tag{3.35a}$$

$$\text{s.t.} \quad \mathbf{K}\left(\boldsymbol{\phi}_D, \boldsymbol{\phi}_{T_{\left(r_{\mathrm{minsmall}_T}\right)}}\right)\mathbf{d}_{\left(r_{\mathrm{minsmall}_T}\right)} = \mathbf{F} \tag{3.35b}$$

$$\mathbf{K}\left(\boldsymbol{\phi}_D, \boldsymbol{\phi}_{T_{\left(r_{\mathrm{minlarge}_T}\right)}}\right)\mathbf{d}_{\left(r_{\mathrm{minlarge}_T}\right)} = \mathbf{F} \tag{3.35c}$$

$$\sum_{\forall e\in\Omega} \rho_T^e\left(\boldsymbol{\phi}_{T_{\left(r_{\mathrm{min}_T}\right)}}\right) v^e \leq V_T \tag{3.35d}$$

$$\sum_{\forall e\in\Omega} \rho_D^e\left(\boldsymbol{\phi}_D\right) v^e \leq V_s \tag{3.35e}$$

$$0 \leq \phi_i \leq \phi_{max} \quad \forall i \in \Omega \tag{3.35f}$$

Since the adjusted constraint function on the stiff material volume $g_s$ solely depends on $\phi_D$, the sensitivity is then simply:

$$\frac{\partial g_s}{\partial \phi_{D,i}} = \sum_{\forall e\in\Omega} v^e \frac{\partial \rho_D^e}{\partial \phi_{D,i}} \qquad \forall i \in \boldsymbol{\phi}_D \tag{3.36}$$

By changing the calculation of the total volume stiff material used in structure from the product of $\rho_D^e$ and $\rho_T^e$ to only $\rho_D^e$, we are accounting for all the discrete objects being projected onto the design domain even in the void regions (i.e. when $\rho_D = 1$ and $\rho_T = 0$). In the case where stiff objects are being created near or outside of the topology boundaries, the volume of stiff objects used will be higher than the volume of stiff objects actually appearing inside the structure. This will result in either a violation on volume constraint or a structure that is underperformed because stiff

objects are being projected outside the structure, which will then drive the algorithm to project full discrete stiff objects completely inside the structure.

### 3.4.1 Comparison of Results

The proposed adjusted multi-material DOP algorithm (Eq. (3.34)) is demonstrated on benchmark cantilever beam, MBB beam, L-bracket, and compliant inverter problems with the same parameters defined in Section 3.2.2 for circular discrete particles reinforcement.

#### 3.4.1.1 Cantilever Beam

Figure 3.65 shows the optimized cantilever beam solutions with circular stiff inclusions using the adjusted multi-material DOP formulations. Table 3.18 and Figure 3.66 show comparison of results obtained between using the original formulation (Eq. (3.14)) and the adjusted formulation (Eq. (3.34)) for the cantilever beam problem.

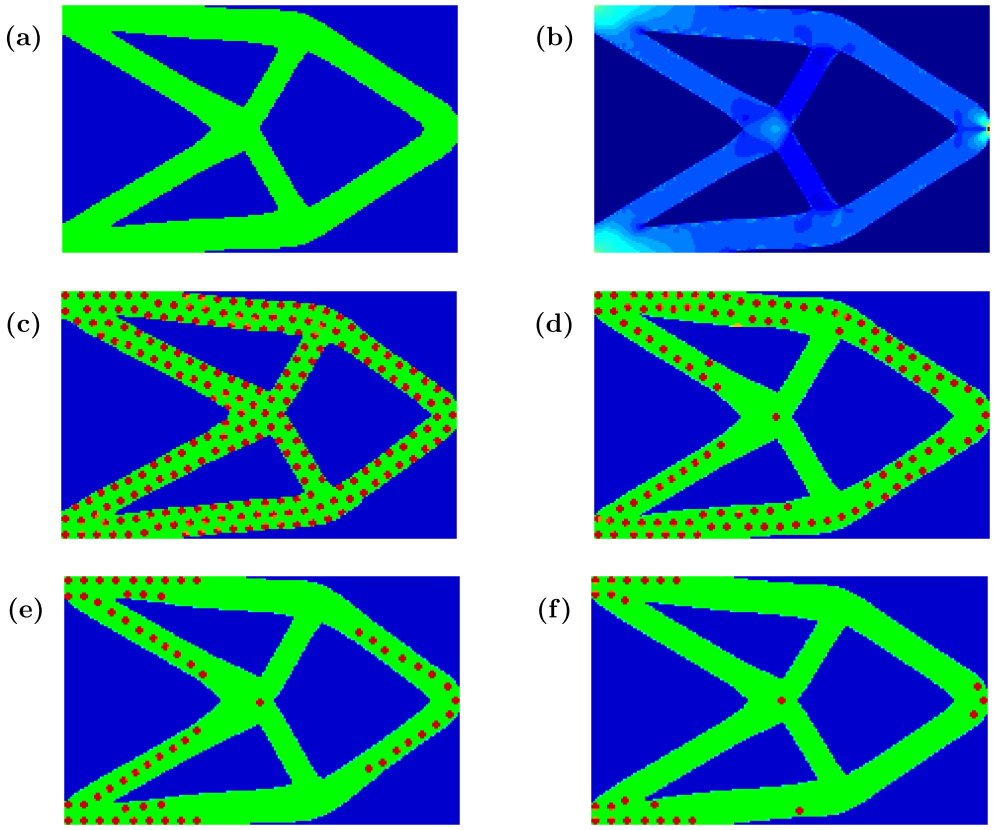


**Figure 3.65:** Cantilever beam results: (a) optimized solution using traditional monolithic formulation composed of compliant material with allowable total volume fraction $V_t = 40\%$, (b) von Mises stress plot for structure in (a), and optimized solutions using the adjusted multi-material DOP formulation (Eq. (3.34)) with allowable volume of stiff material (c) $V_s = 100\%$ of $V_T$ (i.e. packing problem), (d) $V_s = 15\%$ of $V_T$, (e) $V_s = 7.5\%$ of $V_T$, and (f) $V_s = 3\%$ of $V_T$.

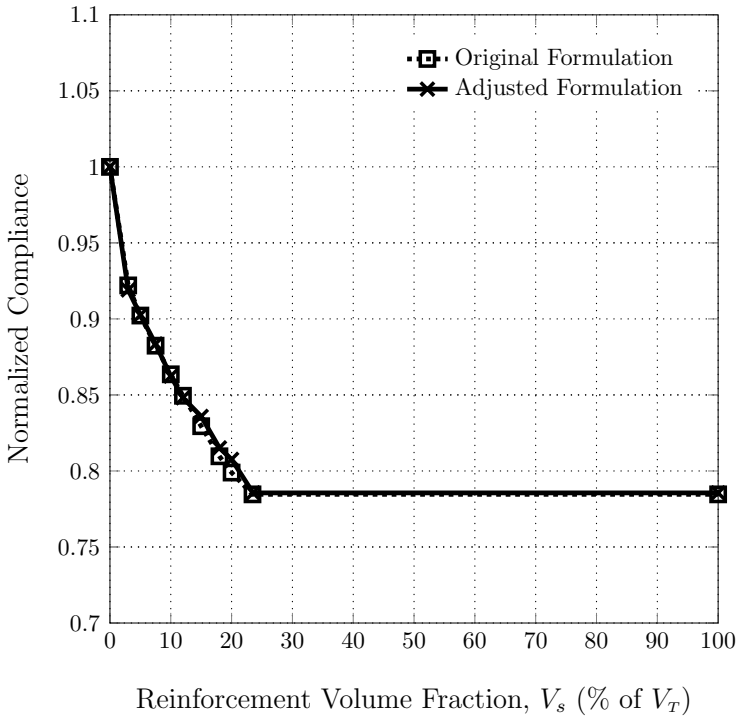


**Figure 3.66:** Normalized compliance for optimized cantilever beam solutions with stiff circular particles for original and updated formulations, and different reinforcement volume fractions; All values are normalized with the corresponding values for the optimized unreinforced cantilever beam.

**Table 3.18:** Cantilever beam results comparison between using original and adjusted multi-material DOP formulations.

| $V_{s,\text{given}}$ (%)* | Fig.‡ | Compliance‡ | $V_{s,\text{in}}$ (%)*,‡ | $V_{s,\text{out}}$ (%)*,‡ | # of partial objects‡ | % Stiffness gain†,‡ |
|---|---|---|---|---|---|---|
| 0 | 3.65a(3.28a) | 45.43 | 0 | 0 | 0 | 0 |
| 3 | 3.65f(3.28f) | 41.75 (41.89) | 3 (3) | 0 (74.2) | 0 (1) | 8.1 (7.8) |
| 7.5 | 3.65e(3.28e) | 40.13 (40.08) | 7.5 (7.5) | 0 (72) | 0 (0) | 11.6 (11.8) |
| 15 | 3.65d(3.28d) | 37.97 (37.68) | 13.2 (15) | 1.8 (66.2) | 1 (8) | 16.4 (17.1) |
| 100 | 3.65c(3.28c) | 35.69 (35.69) | 23.5 (23.4) | 57.1 (59) | 31 (27) | 21.4 (21.5) |

* $V_s, V_{s,\text{in}}, V_{s,\text{out}}$ are presented in % of $V_T$.

† These values represent percent stiffness gains over the unreinforced cantilever beam.

‡ The values for original formulation are presented inside the parentheses.

#### 3.4.1.2 MBB Beam

Figure 3.67 shows the optimized MBB beam solutions with circular stiff inclusions using the adjusted multi-material DOP formulations. Table 3.19 and Figure 3.68 show comparison of results obtained between using the original formulation (Eq. (3.14)) and the adjusted formulation (Eq. (3.34)) for the MBB beam problem.

**Table 3.19:** MBB beam results comparison between using original and adjusted multi-material DOP formulations.

| $V_{s,\text{given}}$ (%)* | Fig.‡ | Compliance‡ | $V_{s,\text{in}}$ (%)*,‡ | $V_{s,\text{out}}$ (%)*,‡ | # of partial objects‡ | % Stiffness gain†,‡ |
|---|---|---|---|---|---|---|
| 0 | 3.67a(3.31a) | 194.50 | 0 | 0 | 0 | 0 |
| 5 | 3.67g(3.31g) | 174.72 (174.62) | 5 (5) | 0 (48.6) | 0 (0) | 10.2 (10.2) |
| 10 | 3.67f(3.31f) | 164.19 (165.16) | 10 (10) | 0 (47.8) | 0 (0) | 15.6 (15.1) |
| 12.5 | 3.67e(3.31e) | 161.82 (162.07) | 12.5 (12.5) | 0 (46.8) | 0 (8) | 16.8 (16.7) |
| 15 | 3.67d(3.31d) | 160.10 (160.16) | 15 (15) | 0 (45.7) | 0 (12) | 17.7 (17.7) |
| 100 | 3.67c(3.31c) | 155.35 (155.55) | 23.6 (23.4) | 37.7 (38) | 60 (66) | 20.1 (20.0) |

* $V_s, V_{s,\text{in}}, V_{s,\text{out}}$ are presented in % of $V_T$.

† These values represent percent stiffness gains over the unreinforced MBB beam.

‡ The values for original formulation are presented inside the parentheses.

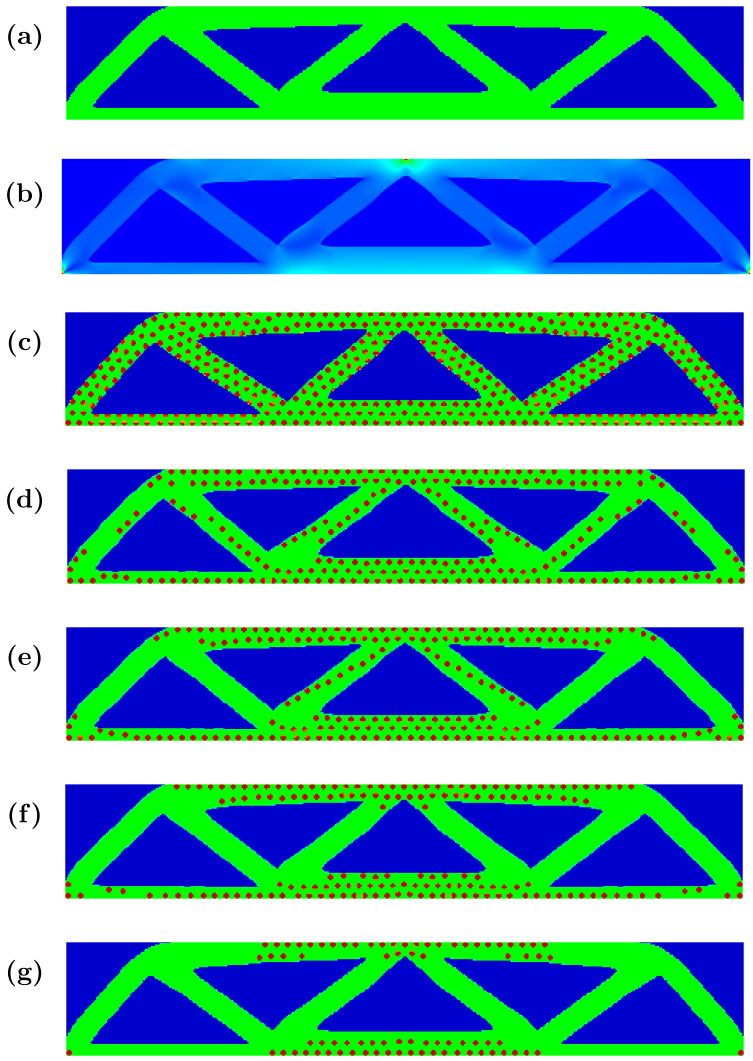


**Figure 3.67:** MBB beam results: (a) optimized solution using traditional monolithic formulation composed of compliant material with allowable total Volume fraction $V_T = 50\%$, (b) von Mises stress plot for structure in (a), and optimized solutions using the adjusted multi-material DOP formulation (Eq. (3.34)) with allowable volume of stiff material (c) $V_s = 100\%$ of $V_T$ (i.e. packing problem), (d) $V_s = 15\%$ of $V_T$, (e) $V_s = 12.5\%$ of $V_T$, (f) $V_s = 10\%$ of $V_T$, and (g) $V_s = 5\%$ of $V_T$.

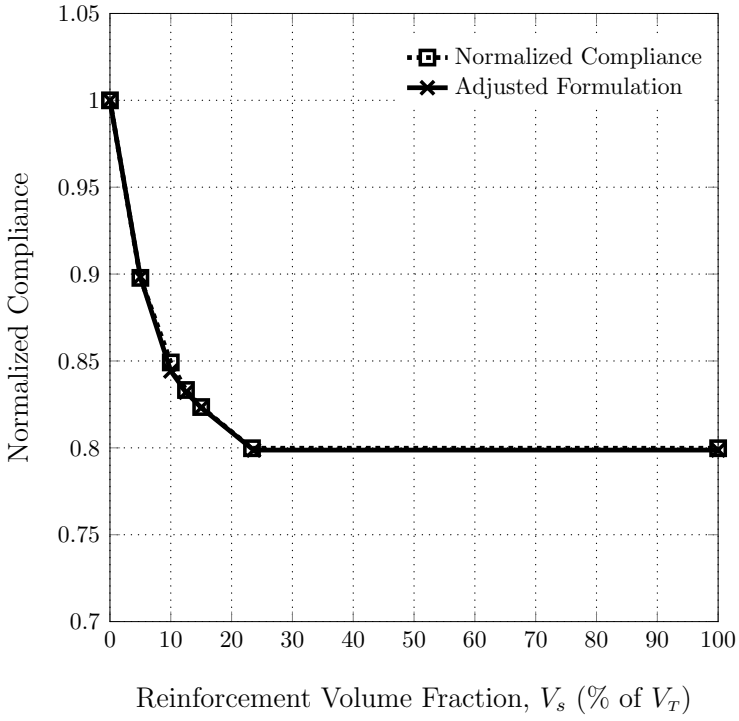


**Figure 3.68:** Normalized compliance for optimized MBB beam solutions with stiff circular particles for original and updated formulations, and different reinforcement volume fractions; All values are normalized with the corresponding values for the optimized unreinforced MBB beam.

#### 3.4.1.3 L-Bracket

Figure 3.69 shows the optimized L-bracket solutions with circular stiff inclusions using the adjusted multi-material DOP formulations. Table 3.19 and Figure 3.70 show comparison of results obtained between using the original formulation (Eq. (3.14)) and the adjusted formulation (Eq. (3.34)) for the L-bracket problem.

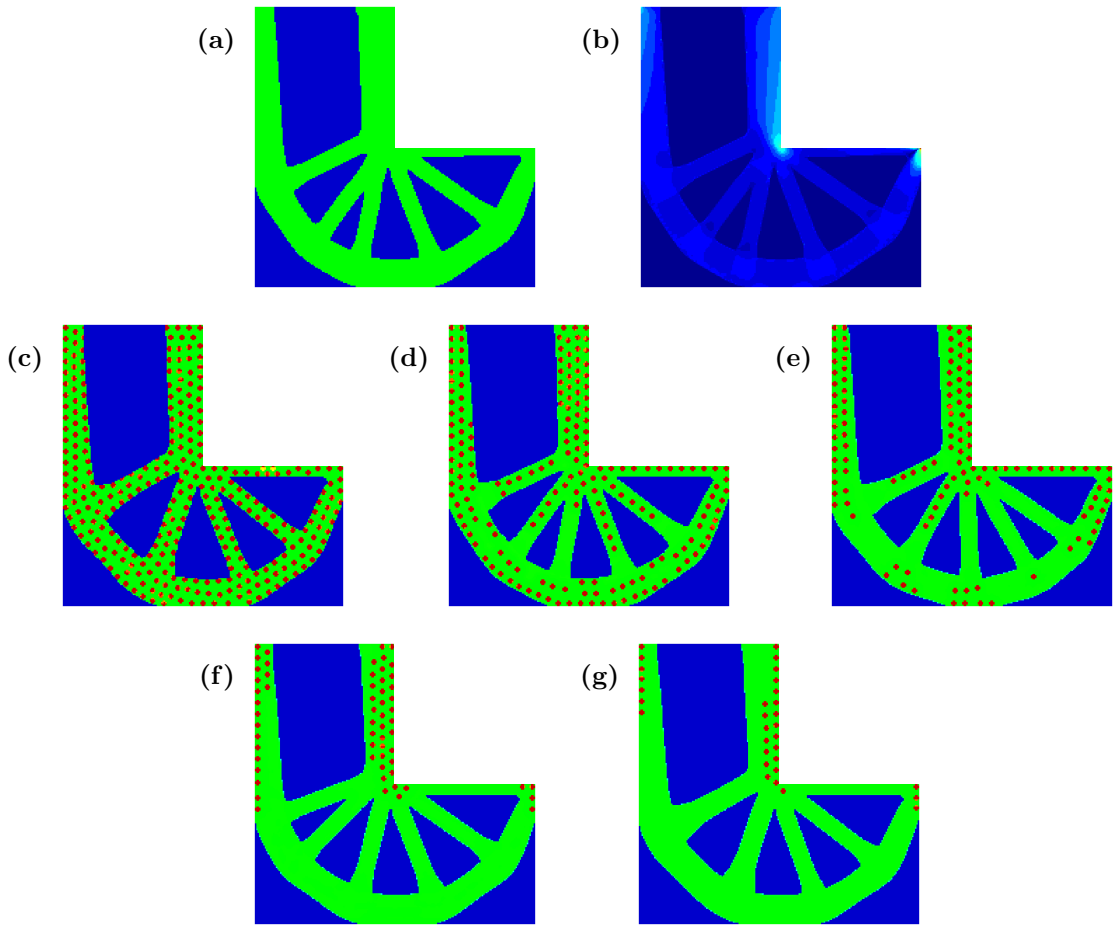


**Figure 3.69:** L-bracket results: (a) optimized solution using traditional monolithic formulation composed of compliant material with allowable total volume fraction $V_t = 40\%$, (b) von Mises stress plot for structure in (a), and optimized solutions using the adjusted multi-material DOP formulation (Eq. (3.34)) with allowable volume of stiff material (c) $V_s = 100\%$ of $V_T$ (i.e. packing problem), (d) $V_s = 15\%$ of $V_T$, (e) $V_s = 10\%$ of $V_T$,(f) $V_s = 5\%$ of $V_T$, and (g) $V_s = 2.5\%$ of $V_T$.

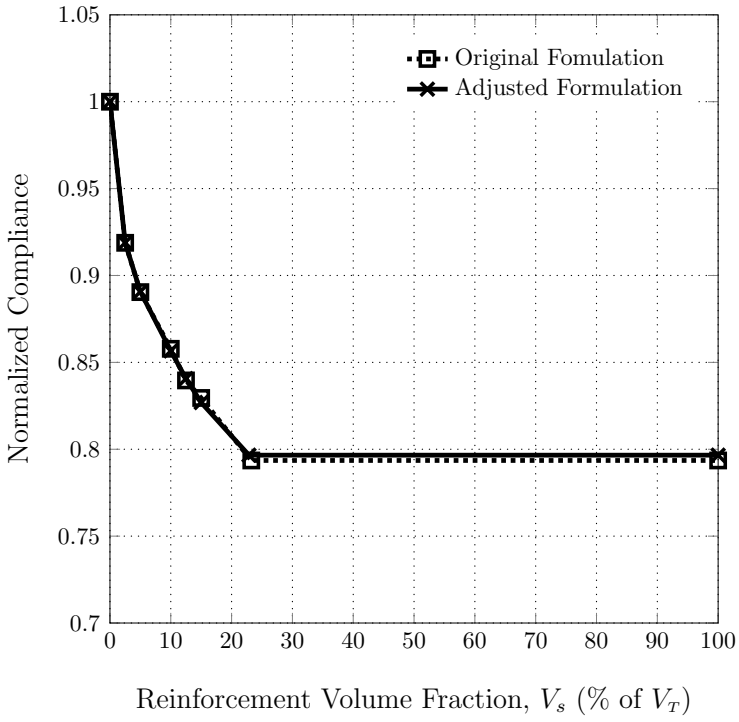


**Figure 3.70:** Normalized compliance for optimized L-bracket solutions with stiff circular particles for original and updated formulations, and different reinforcement volume fractions; All values are normalized with the corresponding values for the optimized unreinforced L-bracket.

**Table 3.20:** L-bracket results comparison between using original and adjusted multi-material DOP formulations.

| $V_{s,\text{given}}$ (%)* | Fig.‡ | Compliance‡ | $V_{s,\text{in}}$ (%)*,‡ | $V_{s,\text{out}}$ (%)*,‡ | # of partial objects‡ | % Stiffness gain†,‡ |
|---|---|---|---|---|---|---|
| 0 | 3.69a(3.34a) | 80.95 | 0 | 0 | 0 | 0 |
| 2.5 | 3.69g(3.34g) | 74.38 (74.38) | 2.5 (2.5) | 0 (49.5) | 0 (0) | 8.1 (8.1) |
| 5 | 3.69f(3.34f) | 72.10 (72.08) | 5 (5) | 0 (49.5) | 0 (0) | 10.9 (11.0) |
| 10 | 3.69e(3.34e) | 69.34 (69.44) | 10 (10) | 0 (48.3) | 0 (8) | 14.3 (14.2) |
| 15 | 3.69d(3.34d) | 66.94 (67.15) | 14.9 (15) | 0.1 (46.6) | 1 (5) | 17.3 (17.0) |
| 100 | 3.69c(3.34c) | 64.48 (64.24) | 22.9 (23.2) | 38.1 (37.2) | 20 (16) | 20.3 (20.6) |

* $V_s, V_{s,\text{in}}, V_{s,\text{out}}$ are presented in % of $V_T$.

† These values represent percent stiffness gains over the unreinforced L-bracket.

‡ The values for original formulation are presented inside the parentheses.

#### 3.4.1.4 Compliant Inverter

Figure 3.71 shows the optimized compliant inverter solutions with circular stiff inclusions using the adjusted multi-material DOP formulations. Table 3.21 and Figure 3.72 show comparison of results obtained between using the original formulation (Eq. (3.16)) and the adjusted formulation (Eq. (3.35)) for the compliant inverter problem.

**Table 3.21:** Compliant inverter results comparison between using original and adjusted multi-material DOP formulations.

| $V_{s,\text{given}}$ (%)* | Fig.‡ | Compliance‡ | $V_{s,\text{in}}$ (%)*,‡ | $V_{s,\text{out}}$ (%)*,‡ | # of partial objects‡ | % Displ. gain†,‡ |
|---|---|---|---|---|---|---|
| 0 | 3.71a(3.37a) | -191.68 | 0 | 0 | 0 | 0 |
| 2.5 | 3.71g(3.37g) | -203.41 (-204.01) | 2.5 (2.5) | 0 (102.6) | 0 (4) | 6.1 (6.4) |
| 5 | 3.71f(3.37f) | -204.37 (-209.63) | 5 (5) | 0 (102.4) | 0 (6) | 6.6 (9.4) |
| 10 | 3.71e(3.37e) | -213.94 (-213.68) | 10 (10) | 0 (102.9) | 0 (10) | 11.6 (11.5) |
| 12.5 | 3.71d(3.37d) | -219.31 (-214.23) | 12.5 (12.5) | 0 (102.5) | 0 (17) | 14.4 (11.8) |
| 100 | 3.71c(3.37c) | -220.57 (-216.08) | 22.9 (22.8) | 77.1 (100.0) | 48 (62) | 15.1 (14.3) |

* $V_s, V_{s,\text{in}}, V_{s,\text{out}}$ are presented in % of $V_T$.

† These values represent percent displacement gains over the unreinforced compliant inverter.

‡ The values for original formulation are presented inside the parentheses.

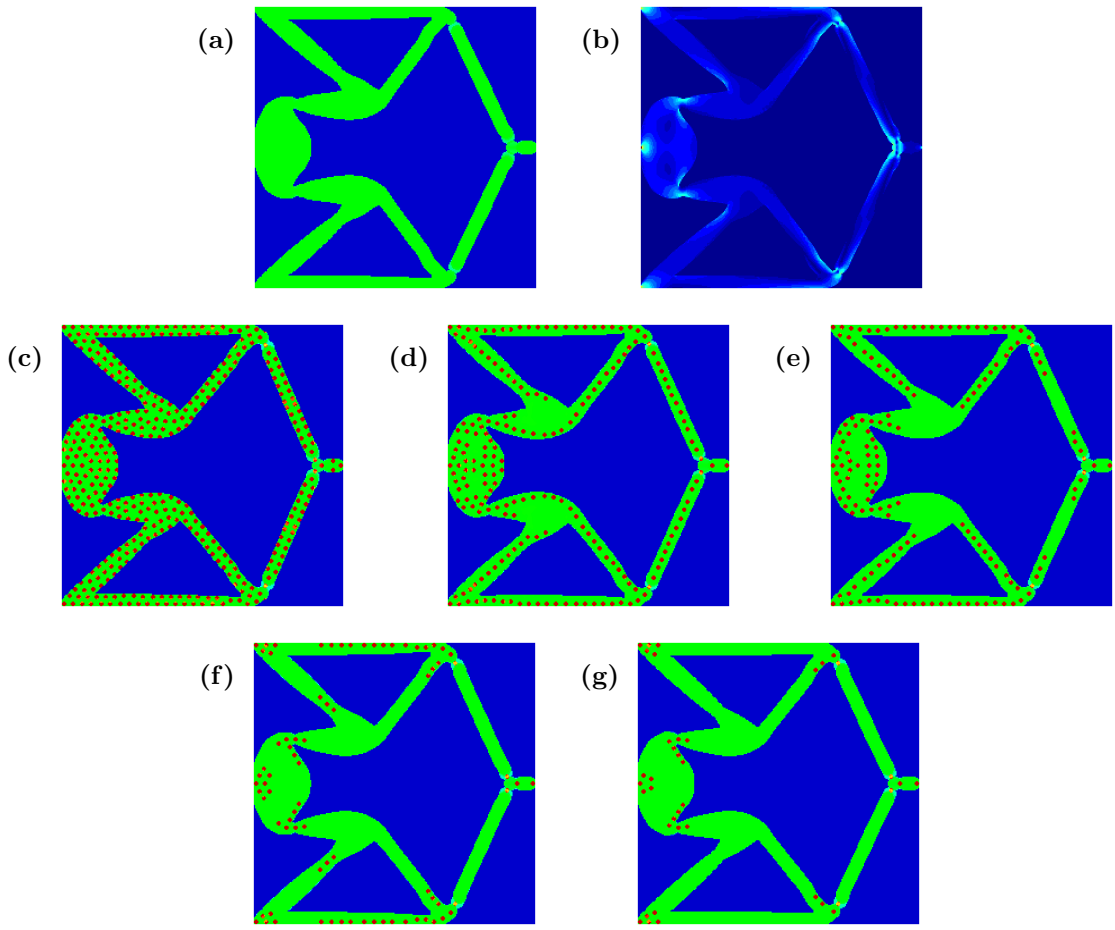


**Figure 3.71:** Compliant inverter results: (a) optimized solution using traditional monolithic formulation composed of compliant material with allowable total volume fraction $V_t = 30\%$, (b) von Mises stress plot for structure in (a), and optimized solutions using the adjusted multi-material DOP formulation (Eq. (3.35)) with allowable volume of stiff material (c) $V_s = 100\%$ of $V_T$ (i.e. packing problem), (d) $V_s = 12.5\%$ of $V_T$, (e) $V_s = 10\%$ of $V_T$,(f) $V_s = 5\%$ of $V_T$, and (g) $V_s = 2.5\%$ of $V_T$.

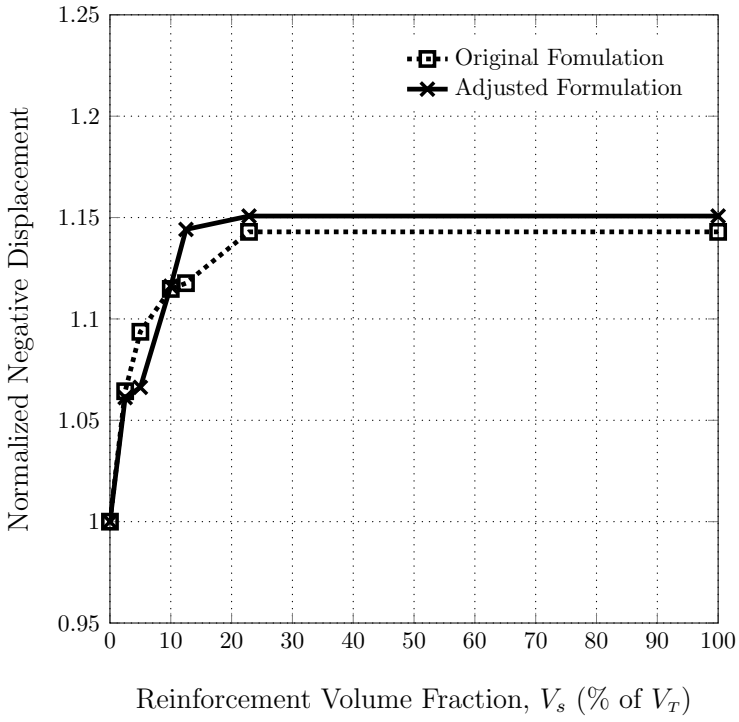


**Figure 3.72:** Normalized compliance for optimized compliant inverter solutions with stiff circular particles for original and updated formulations, and different reinforcement volume fractions; All values are normalized with the corresponding values for the optimized unreinforced compliant inverter.

### 3.4.2 Discussion

Using the adjusted formulation, the algorithm successfully reduces the the number of partial objects developed inside the topology down to zero in most of all the benchmark problems (see Tables 3.8-3.11). It is important to note that the algorithm cannot completely avoid creating partial discrete objects especially in the case of packing problem (Figures 3.65c, 3.67c, 3.69c, and 3.71c). This is because creating only full discrete objects may reduce overall structural performance if the only possible way to create full objects without violating the prescribed enclosure region length scale is to completely remove partial discrete objects.

Moreover, since the optimal packing volume fraction is not known *a priori*, we choose to set the maximum allowable stiff material volume $V_s$ to be equal to the maximum allowable of total material used $V_T$ as to avoid accidentally constraint the optimal packing volume. This subsequently leads to the constraint on the volume of stiff material being inactive in the packing problem when implementing either the original or the adjusted formulations, and therefore may require an alternative approach. This is a subject of future work.

We also observe that the volume of stiff particles outside the component topology $V_{s,\text{out}}$ is zero as expected for two reasons. First, the total volume of stiff material is calculated from the stiff particles developed both inside and outside of component topology. By constraining the volume of stiff material used over the entire domain (i.e. both inside and outside the component topology), the algorithm is forced to

create full discrete objects inside the topology as much as possible in order for it to count toward the stiffness of the structure without violating the required spaces between each object. Second, as the maximum allowable volume of stiff material decreases, more space in the component topology becomes increasingly available for the algorithm to place full discrete objects without violating the minimum spacing between two discrete objects. This result shows that the adjusted algorithm is working as expected.

Another worthy observation from the results is that the overall final topology of the structure as well as the layout of the discrete objects slightly differs between the two formulations. This behavior is as expected because the algorithm may need to re-arrange the layout of the objects as it tries to avoid creating partial objects and place full discrete objects inside the topology. It is also worth mentioning that the compliances obtained from using the original formulation and the adjusted formulation for all numerical examples are relatively the same with respect to their corresponding volume fractions. Based on these examples, both formulations gives solutions that are similar in structural performance. The adjusted formulation is, however, more suitable in the cases where the development of partial discrete objects are not permitted or favorable in the final topology.

## 3.5 Summary

This chapter proposed an extension to the Discrete Object Projection (DOP) approach for optimizing the layout of discrete embedded objects to simultaneously optimize the component topology. This is done by combining the Heaviside Projection Method (HPM) with multi-phase Rational Approximation of Material Properties (RAMP), which essentially adds an additional material phase to the DOP methodology. Since this is a projection-based approach, the length scales of discrete objects, spacing between the objects, and the length scales of the component are implicitly achieved through projection functions without requiring any additional constraints.

This approach has advantages over traditional multicomponent optimization approaches in that (1) no additional constraints are needed to achieve geometric constraints, (2) the number of embedded objects need not be defined *a priori*, (3) the analysis model does not require remeshing of finite element mesh bounded inside the embedded objects at each optimization iteration, and (4) the approach maintains the free-form nature of traditional topology optimization for both component and embedded objects (i.e. the embedded objects can be created, removed, or translated at any point during optimization), which ultimately facilitate the use of gradient-based algorithms.

The proposed methodology was used to optimize layout of the circular embedded objects and component topology in benchmark minimum compliance design problems of cantilever beam, MBB beam, L-bracket, and compliant inverter. The results

of these numerical examples show the successful implementation of the proposed algorithm, where the optimized component topologies contain identifiable discrete objects that are strategically placed in the locations subjected to high stress as well as the locations of the applied loads and supports. The optimized component topologies also resemble those obtained from traditional topology optimization. The results also show that by placing the reinforcement strategically, stiffness can be enhanced even in the cases where the given volume of the stiff reinforcement is small.

This methodology is further extended to consider a set of objects that must be chosen from a prescribed database. These objects may be of different sizes, shapes, and orientations, but they are predefined before optimization begins. This is different from prior works where objects were one shape and size (Guest, 2011, 2015) or where objects were allowed to vary its shape and size within prescribed length scale limits during optimization (Guest and Ha, 2014). An example of predefined object sets includes non-circular objects such as square and short fibers at different orientations.

The methodology is then extended to allow for creation discrete continuous fibers out of short fiber objects. This is achieved by allowing the short fibers to link at either or both ends and form a single long continuous fiber. Each of the short fibers can also be placed at different orientations resulting in free-form layout of the discrete continuous fibers. This method is specifically tailored to 3DP technologies that can fabricate continuous fiber-reinforced component parts, allowing designers to obtain topology-optimized reinforced component parts directly for manufacturing.

In this work, we also proposed a simple technique to reduce the number of partial discrete objects developed inside the optimized component topology by slightly modifying the volume constraint on the embedded objects to account for any part of the embedded objects that lies on the outside of the component topology. The results obtained using the updated formulation successfully shows the reduction of partial objects appearing inside the component topology.

It should be noted that while the algorithm shows great potential, overlapping objects are occasionally observed in the presented solutions with object sets, such as L-bracket with discrete short fibers and compliant inverter with discrete continuous fibers. In the case of discrete continuous fiber, the overlapping tends to occurs in higher volume fractions at the the location of high stresses. In particular, the phase mixing appears when the end of one fiber comes into the side of another fibers. Such overlapping can potentially be prevented with larger penalization or by applying robust topology optimization strategies like the ones presented in Sigmund (2009) and Gaynor et al. (2014). The robust strategies could be implemented in this work by introducing a "dilate" operator to simulate over-depositing of the enclosure regions, resulting in larger area of phase mixing which would be undesirable. This is also the subject of future work.

Lastly, as previously mentioned, we observe that the proposed algorithm has some difficulty converging to an optimized solution when the length scale of the compliant phase approaches the length scale of the stiff phase. This similar issue is observed in

Guest (2015), which shows that solutions with discrete objects are difficult to obtain in this situation. Even though in this dissertation, the length scale of the component, not the enclosure, is reduced, we believe that the effect is the same as seen in Guest (2015) and deserves additional investigation in the future research.

# Chapter 4

# Concluding Remarks and Recommendations for Future Work

In this dissertation, topology optimization of structures considering constructability and manufacturability is presented. The first part of this dissertation is dedicated to examining constructability issues that arise in topology optimization of truss structures and proposing new algorithms that incorporate constructability into the design. Three specific constructability issues involving oversized members, connection complexity, and many different member sizes are discussed and translated into cost metrics that can be directly incorporated into topology optimization formulations. The second part of this dissertation is focused on developing topology optimization algorithm for designing structures and component with embedded objects. In particular, we proposed an extension to an existing approach to simultaneously optimize the

layout of discrete embedded objects and the component topology. Further extension is also proposed to include different object shapes and orientation and enable the creation of discrete continuous fiber-like objects. Overall, this dissertation aims to bring the field of topology optimization in research one step closer to application in real-world operating condition.

Looking forward, besides the challenges in relations to minimum member size and nonlinear connection cost function previously discussed in Section 2.2, there are several recommendations for future exploration and expansion of the presented work. In the case of the proposed algorithms for constructability of trusses, it is important to note that since all of the proposed algorithms are independent of one another, the designer can choose to combine any of these cost functions together to achieve a desired structural efficiency and constructability properties.

These algorithms are also directly expandable to frame structures and 3D design domain. Other constructability criteria should also be explored for a complete performance and constructability-based design. An example of this would be to consider constructability of structures in the context of connection types. Different types of connections in structures require different level of complexity in construction process, which makes some more expensive than others. A study on optimized placement of these different types of connections based on cost would allow designers to explore tradeoffs between performance and constructability in this context. Another great criteria would be repeatability of member lengths in addition to member sizes (Zhu,

2015).

Although this dissertation focused on constructability issues in civil structural applications, the algorithms proposed here can be tailored and extended to other application, such as space structural applications, that may have contructability issues. In space applications, for instance, structural members will need to fit inside containers, therefore limiting the member sizes and lengths to certain dimensions for space travels. To further reduce cost, structural members may need to be of same size and length (i.e. repeatability).

Another important factor to consider is the quantification of constructability cost. A proper quantification of unit cost parameters, which are not the focus of this article, is thus necessary for a complete design optimization process. This is a nontrivial task and will require an expertise in market data and construction cost estimation. Nevertheless, the proposed algorithms have shown to perform effectively even for situations where the unit costs have not yet been completely quantified.

In the case of topology optimization of components and embedded objects, the implementation of the proposed multi-material DOP design methods and algorithm provides a gateway to a complete design of engineering components and materials that gain functionality from discrete objects. Although this work is motivated and tailored to 3DP technologies that can create continuous fiber-reinforced component parts, the framework can be adapted to other specific manufacturing technologies that fabricate component parts with discrete embedded objects.

# CHAPTER 4. CONCLUDING REMARKS AND RECOMMENDATIONS FOR FUTURE WORK

The general frame work of DOP can be extend to multiple phase having different material properties, multifunctionality (such as thermal and electrical conductivity), and 3D design domain. Extension to 3D design domain will allow designer to completely model the entire process of 3DP. For 3DP techniques that fabricate components layer-by-layer, the algorithm would optimized the layout of reinforcement in each layer separately since discrete object such as continuous fibers cannot be placed across different layer. Design in 3D domain will also allow designer to extend the methodology to design problems with more complicated loading conditions such as biaxial loading, where there are two directional load paths. In this case, the alignments of fibers may differ in different layers since each fiber cannot cross on top of another.

It is important to note that the proposed methodology is currently employed with an underlying assumption that the materials are isotropic. This assumption, however, becomes invalid in the cases where discrete objects have different properties in different directions (e.g. CNT yarns possess different properties in the longitudinal and radial directions). Components fabricated by certain additive manufacturing process, such as FFF, also exhibit anisotropic behavior dictated by orientation of parts during the printing process. This method should be extended to capture anisotropy relating to both materials and build directions.

Additionally, a future research in this area should also includes further investigation into the convergence challenges and difficulties that arises when the length scale

of the component approaches the length scale of embedded discrete objects. Even if the issue cannot be avoided, it is still important to understand and be aware of the potential limitations of the methodology.

Lastly, the developed topology optimization methodology should be validated through various case studies. Since the proposed methodology directly incorporates the manufacturing process directly into the algorithm, the optimized parts obtained from optimization can be directly fabricated without requiring any post-processing. The results from the experiments will not only evaluate the methodology, but will also provide feedback that can be used to refine the methodology as necessary.

# Bibliography

W. Achtziger. *Topology optimization of discrete structures: an introduction in view of computational and nonsmooth aspects. In: George I. N. Rozvany (ed)*, pages 57–100. Springer, Heidelberg, 1997. ISBN 978-3-7091-2566-3.

Aerojet Rocketdyne. Aerojet rocketdyne hot-fire tests additive manufactured components for the ar1 engine to maintain 2019 delivery, Jun 2015. URL `http://www.rocket.com/article/aerojet-rocketdyne-hot-fire-tests-additive-manufactured-components-ar1-engine-maintain-2019`. [Acessed on 07-07-2017].

L. Ambrosio and G. Buttazzo. An optimal design problem with perimeter penalization. *Calculus of Variations and Partial Differential Equations*, 1(1):55–69, 1993. doi: 10.1007/BF02163264.

O. Amir and O. Sigmund. Reinforcement layout design for concrete structures based on continuum damage and truss topology optimizaiton. *Structural and Multidisciplinary Optimization*, 47(2):157–174, 2013. doi: 10.1007/s00158-012-0817-1.

BIBLIOGRAPHY

A. Asadpoure, J. K. Guest, and L. Valdevit. Incorporating fabrication cost into topology optimization of discrete structures and lattices. *Structural and Multidisciplinary Optimization*, 51(2):385–396, 2015. doi: 10.1007/s00158-014-1133-8.

R. H. Baughman, A. A. Zakhidov, and W. A. de Heer. Carbon nanotubes: the route toward applications. *Science*, 297(5582):787–792, 2002. doi: 10.1126/science.1060928.

R. Behrou and J. K. Guest. Topology optimization for transient response of structures subjected to dynamic loads. *18th AIAA/ISSMO Multidisciplinary Analysis and Optimization Conference, AIAA AVIATION Forum, (AIAA 2017-3657),Denver, CO*, page 3657, 2017. doi: 10.2514/6.2017-3657.

M. P. Bendsøe. Optimal shape design as a material distribution problem. *Structural Optimization*, 1(4):193–202, 1989. doi: 10.1007/BF01650949.

M. P. Bendsøe and N. Kikuchi. Generating optimal topologies in structural design using homogenization method. *Computer Methods in Applied Mechanics and Engineering*, 71(2):197–224, 1988. doi: 10.1016/0045-7825(88)90086-2.

M. P. Bendsøe and O. Sigmund. Material interpolation schemes in topology optimization. *Archive of Applied Mechanics*, 69(9-10):635–654, 1999. doi: 10.1007/s004190050248.

BIBLIOGRAPHY

M. P. Bendsøe and O. Sigmund. *Topology Optimization: Theory, Methods and Applications*. Springer, Berlin, 2nd edition, 2003. ISBN 3-540-42992-1.

M. P. Bendsøe, A. R. Díaz, and N. Kikuchi. *Topology and Generalized Layout Optimization of Elastic Structures*, volume 227, pages 159–205. Springer, Dordrecht, 1993. doi: 10.1007/978-94-011-1804-0_13.

T. E. Bruns and D. A. Tortorelli. Topology optimization of non-linear elastic structures and compliant mechanisms. *Computer Methods in Applied Mechanics and Engineering*, 190(26-27):3443–3459, 2001. doi: 10.1016/S0045-7825(00)00278-4.

T. A. Campbell and O. S. Ivanova. 3d printing of multifunctional nanocomposites. *Nano Today*, 8(2):119–120, 2013. doi: https://doi.org/10.1016/j.nantod.2012.12.002.

J. V. Carstensen and J. K. Guest. New projection methods for two-phase minimum and maximum length scale control in topology optimization. *Proceedings of the AIAA AVIATION 2014 - 15th AIAA/ISSMO Multidisciplinary Analysis and Optimization Conference, Atlanta, GA, USA.*, pages 1–11, 2014.

K. Chizari, M. A. Daoud, A. R. Ravindran, and D. Therriault. 3d printing of highly conductive nanocomposites for the functional optimization of liquid sensors. *Small*, 12(44):6076–6082, 2016. doi: 10.1002/smll.201601695.

BIBLIOGRAPHY

C. K. Chua, K. F. Leong, and C. S. Lim. *Rapid Prototyping: Principles and Applications*. World Scientific, New Jersey, 2nd edition, 2003. ISBN 981-238-117-1.

J. D. Deaton and R. V. Grandhi. Stiffening of restrained thermal structures via topology optimization. *Structural and Multidisciplinary Optimization*, 48(4):731–745, 2013. doi: 10.1007/s00158-013-0934-5.

A. R. Díaz and O. Sigmund. Checkerboard patterns in layout optimization. *Structural Optimization*, 10(1):40–45, 1995. doi: 10.1007/BF01743693.

Discount Steel. ASTM A276-10 304 stainless steel round bar, Jul 2017. URL `https://www.discountsteel.com/items/304_Stainless_Steel_Round_Bar.cfm?item_id=218&size_no=1`. [Acessed on 07-08-2017].

W. S. Dorn, R. E. Gomory, and H. J. Greenberg. Automatic design of optimal structures. *Journal de Mecanique*, 3(1):25–52, 1964.

R. D. Farahani, H. Dalir, V. L. Borgne, L. A. Gautier, M. A. E. Khakani, M. Lévesque, and D. Therriault. Direct-write fabrication of freestanding nanocomposite strain sensors. *Nanotechnology*, 23(8):085502, 2012a. doi: 10.1088/0957-4484/23/8/085502.

R. D. Farahani, H. Dalir, V. L. Borgne, L. A. Gautier, M. A. E. Khakani, M. Lévesque, and D. Therriault. Reinforcing epoxy nanocomposites with functionalized carbon

nanotubes via biotinstreptavidin interactions. *Composites Science and Technology*, 72(12):1387–1395, 2012b. doi: 10.1016/j.compscitech.2012.05.010.

J. M. Gardner, G. Sauti, J.-W. Kim, R. J. Cano, R. A. Wincheski, C. J. Stelter, B. W. Grimsley, D. C. Working, and E. J. Siochi. Additive manufacturing of multifunctional components using high density carbon nanotube yarn filaments. *NASA Technical Reports (NF1676L-23685)*, 2016a.

J. M. Gardner, G. Sauti, J.-W. Kim, R. J. Cano, R. A. Wincheski, C. J. Stelter, B. W. Grimsley, D. C. Working, and E. J. Siochi. 3-d printing of multifunctional carbon nanotube yarn reinforced components. *Additive Manufacturing*, 12(A):38–44, 2016b. doi: 10.1016/j.addma.2016.06.008.

J. M. Gardner, C. J. Stelter, E. A. Yashin, and E. J. Siochi. High temperature thermoplastic additive manufacturing using low-cost, open-source hardware. *NASA Technical Reports (NASA/TM-2016-219344, L-20761, NF1676L-25721)*, 2016c.

A. T. Gaynor and J. K. Guest. Topology optimization considering overhang constraints: Eliminating sacrificial support material in additive manufacturing through design. *Structural and Multidisciplinary Optimization*, 54(5):1157–1172, 2016. doi: 10.1007/s00158-016-1551-x.

A. T. Gaynor, J. K. Guest, and C. D. Moen. Reinforced concrete force visualization and design using bilinear truss-continuum topology optimization. *ASCE Journal*

*of Structural Engineering*, 139(4):607–618, 2013. doi: 10.1061/(ASCE)ST.1943-541X.0000692.

A. T. Gaynor, N. A. Meisel, C. B. Williams, and J. K. Guest. Multiple-material topology optimization of compliant mechanisms created via polyjet three-dimensional printing. *Journal of Manufacturing Science and Engineering*, 136(6):1–10, 2014. doi: 10.1115/1.4028439.

A. R. Gersborg and C. S. Andreasen. An explicit parameterization for casting constraints in gradient driven topology optimization. *Structural and Multidisciplinary Optimization*, 44(6):875–881, 2011. doi: 10.1007/s00158-011-0632-0.

J. K. Guest. Topology optimization with multiple phase projection. *Computer Methods in Applied Mechanics and Engineering*, 199(1-4):123–135, 2009a. doi: 10.1016/j.cma.2009.09.023.

J. K. Guest. Imposing maximum length scale in topology optimization. *Structural and Multidisciplinary Optimization*, 37(5):463–473, 2009b. doi: 10.1007/s00158-008-0250-7.

J. K. Guest. A projection-based topology optimization approach to distributing discrete features in structures and materials. *Proceedings of the 9th World Congress on Structural and Multidisciplinary Optimization, Shizuoka, Japan.*, pages 1–10, 2011.

BIBLIOGRAPHY

J. K. Guest. Projection-based topology optimization using discrete object sets. *ASME International Design Engineering Technical Conference, Buffalo, NY, USA.*, pages 1–8, 2014. doi: 10.1115/DETC2014-35213.

J. K. Guest. Optimizing the layout of discrete objects in structures and materials: A projection-based topology optimization approach. *Computer Methods in Applied Mechanics and Engineering*, 283(5):330–351, 2015. doi: 10.1016/j.cma.2014.09.006.

J. K. Guest and S.-H. Ha. Optimizing inclusion shapes and patterns in periodic materials using discrete object projection. *Structural and Multidisciplinary Optimization*, 50(1):65–80, 2014. doi: 10.1007/s00158-013-1026-2.

J. K. Guest and J. H. Prévost. Optimizing multifunctional materials: Design of microstructures for maximized stiffness and fluid permeability. *International Journal Solids and Structures*, 43(22-23):7028–7047, 2006. doi: 10.1016/j.ijsolstr.2006.03.001.

J. K. Guest and M. Zhu. Casting and milling restrictions in topology optimization via projection-based algorithms. *Proceedings of the ASME Design Engineering Technical Conference, Chicago, IL, USA.*, 3(parts A and B):913–920, 2012. doi: 10.1115/DETC2012-71507.

J. K. Guest, J. H. Prévost, and T. Belytschko. Achieving minimum length scale in topology optimization using nodal design variables and projection functions.

BIBLIOGRAPHY

*International Journal for Numerical Methods in Engineering*, 61(2):238–254, 2004. doi: 10.1002/nme.1064.

J. K. Guest, A. Asadpoure, and S.-H. Ha. Eliminating beta-continuation from heaviside projection and density filter algorithm. *Structural and Multidisciplinary Optimization*, 44(4):443–453, 2011. doi: 10.1007/s00158-011-0676-1.

S.-Z. Guo, X. Yang, M.-C. Heuzeyb, and D. Therriault. 3d printing of a multifunctional nanocomposite helical liquid sensor. *Nanoscale*, 7:6451–6456, 2015. doi: 10.1039/c5nr00278h.

M. Gurau. Part 2: The world's first commercial all-cnt sheets, tape and yarns, Apr 2014. URL `http://www.nanocomptech.com/blog/need-to-know-part-2-sheets-tape-yarn`. [Acessed on 07-08-2017].

R. B. Haber, C. S. Jog, and M. P. Bendsøe. A new approach to variable-topology shape design using a constraint on perimeter. *Structural Optimization*, 11(1):1–12, 1996. doi: 10.1007/BF01279647.

B. Hubscher. Open for business: 3-d printer creates first object in space on international space station, Nov 2014. URL `https://www.nasa.gov/content/open-for-business-3-d-printer-creates-first-object-in-space-on-international-space-station`. [Acessed on 07-07-2017].

BIBLIOGRAPHY

S. Iijima. Helical microtubules of graphitic carbon. *Nature*, 354:56–58, 1991. doi: 10.1038/354056a0s.

M. Jansen, G. Lombaert, M. Diehl, B. S. Lazarov, O. Sigmund, and M. Schevenels. Robust topology optimization accounting for misplacement of material. *Structural and Multidisciplinary Optimization*, 47(3):317–333, 2013. doi: 10.1007/s00158-012-0835-z.

C. S. Jog and R. B. Haber. Stability of finite element models for distributed-parameter optimization and topology design. *Computer Methods in Applied Mechanics and Engineering*, 130(3-4):203–226, 1996. doi: 10.1016/0045-7825(95)00928-0.

Y. Kanno. Global optimization of trusses with constraints on number of different cross-sections: a mixed-integer second-order cone programming approach. *Computational Optimization and Applications*, 63(1):203–236, 2015. doi: 10.1007/s10589-015-9766-0.

J. Kato and E. Ramm. Optimization of fiber geometry for fiber reinforced composites considering damage. *Finite Elements in Analysis and Design*, 46(5):401–415, 2010. doi: 10.1016/j.finel.2010.01.001.

J. Kato and E. Ramm. Multiphase layout optimization for fiber reinforced composites considering a damage model. *Engineering Structures*, 49:202–220, 2013. doi: 10.1016/j.engstruct.2012.10.029.

BIBLIOGRAPHY

T. Kellner. Worlds first plant to print jet engine nozzles in mass production, Jul 2014. URL http://www.gereports.com/post/91763815095/worlds-first-plant-to-print-jet-engine-nozzles-in/. [Acessed on 07-07-2017].

J. H. Kim, S. Lee, M. Wajahat, H. Jeong, W. S. Chang, H. J. Jeong, J.-R. Yang, J. T. Kim, and S. K. Seol. Three-dimensional printing of highly conductive carbon nanotube microarchitectures with fluid ink. *ACS Nano*, 10(9):8879–8887, 2016. doi: 10.1021/acsnano.6b04771.

S. Lin, L. Zhao, J. K. Guest, T. P. Weihs, and Z. Liu. Topology optimization of fixed-geometry fluid diodes. *ASME Journal of Mechanical Design*, 137(8):081402, 2015. doi: 10.1115/1.4030297.

J. Lou, Z. Lou, S. Chen, L. Tong, and M. Y. Wang. A new level set method for systematic design of hinge-free compliant mechanisms. *Computer Methods in Applied Mechanics and Engineering*, 198(2):318–331, 2008. doi: 10.1016/j.cma.2008.08.003.

Markforged. Markforged 3d printers, 2017. URL https://www.symsolutions.com/3d-printing/markforged-3d-printers. [Acessed on 07-07-2017].

R. Matsuzaki, M. Ueda, M. Namiki, T.-K. Jeong, H. Asahara, K. Horiguchi, T. Nakamura, A. Todoroki, and Y. Hirano. Three-dimonsional printing of continuous-fiber composites by in-nozle impregnation. *Scientific Reports*, 6:23058, 2016. doi: 10.1038/srep23058.

BIBLIOGRAPHY

N. A. Meisel, A. M. Elliott, and C. B. Williams. A procedure for creating actuated joints via embedding shape memory alloys in polyjet 3d printing. *International Journal for Numerical Methods in Engineering*, 26(12):1498–1512, 2015. doi: 10.1177/1045389X14544144.

B. Peng, M. Locascio, P. Zapol, S. Li, S. L. Mielke, G. C. Schatz, and H. D. Espinosa. Measurements of near-ultimate strength for multiwalled carbon nanotubes and irradiation-induced crosslinking improvements. *Nature Nanotechnology*, 3(10): 626–631, 2008. doi: 10.1038/nnano.2008.211.

J. Petersson and O. Sigmund. Slope constrained topology optimization. *International Journal for Numerical Methods in Engineering*, 41(8):1417–1434, 1998. doi: 10.1002/(SICI)1097-0207(19980430)41:8⟨1417::AID-NME344⟩3.0.CO;2-N.

G. Postiglione, G. Natale, G. Griffini, and M. L. amd Stefano Turri. Conductive 3d microstructures by direct 3d printing of polymer/carbon nanotube nanocomposites via liquid deposition modeling. *Composites Part A: Applied Science and Manufacturing*, 76:110–114, 2015. doi: 10.1016/j.compositesa.2015.05.014.

T. A. Poulsen. A new scheme for imposing a minimum length scale in topology optimization. *International Journal for Numerical Methods in Engineering*, 57(6): 741–760, 2003. doi: 10.1002/nme.694.

Z. Qian and G. K. Ananthasuresh. Optimal embedding of rigid objects in the topology

design of structures. *Mechanics Based Design of Structures and Machines.*, 32(2): 165–193, 2004. doi: 10.1081/SME-120030555.

M. Schevenels, B. S. Lazarov, and O. Sigmund. Robust topology optimization accounting for spatially varying manufacturing errors. *Computer Methods in Applied Mechanics and Engineering*, 200(49-52):3613–3627, 2011. doi: 10.1016/j.cma.2011.08.006.

O. Sigmund. On the design of conpliant mechanisms using topology optimization. *Mechanics of Structures and Machines*, 25(4):493–524, 1997. doi: 10.1080/08905459708945415.

O. Sigmund. Morphology-based black and white filters for topology optimization. *Structural and Multidisciplinary Optimization*, 33(4-5):401–424, 2007. doi: 10.1007/s00158-006-0087-x.

O. Sigmund. Manufacturing tolerant topology optimization. *Acta Mechanica Sinica*, 25(2):227–239, 2009. doi: 10.1007/s10409-009-0240-z.

O. Sigmund and J. Petersson. Numerical instabilities in topology optimization: a survey on procedures dealing with checkerboards, mesh-dependencies and local minima. *Structural and Multidisciplinary Optimization*, 16(1):68–75, 1998. doi: 10.1007/BF01214002.

M. Stolpe and K. Svanberg. An alternative interpolation scheme for minimum com-

pliance topology optimization. *Structural and Multidisciplinary Optimization*, 22 (2):116–124, 2001. doi: 10.1007/s001580100129.

Stratasys Ltd. Fdm technology, 2017a. URL `http://www.stratasys.com/3d-printers/technologies/fdm-technology`. [Acessed on 07-07-2017].

Stratasys Ltd. Ultem 1010, 2017b. URL `http://www.stratasys.com/materials/fdm/ultem-1010`. [Acessed on 07-08-2017].

L. L. Stromberg, A. Beghini, W. F. Baker, and G. H. Paulino. Application of layout and topology optimization using pattern gradation for the conceptual design of buildings. *Structural and Multidisciplinary Optimization*, 43(2):165–180, 2011. doi: 10.1007/s00158-010-0563-1.

N. Strömberg. Topology optimization of structures with manufacturing and unilateral contact constraints by minimizing an adjustable compliance-volume product. *Structural and Multidisciplinary Optimization*, 42(3):341–350, 2010. doi: 10.1007/s00158-010-0502-1.

K. Svanberg. The method of moving asymptotes - a new method for structural optimization. *International Journal for Numerical Methods in Engineering.*, 24(2): 359–373, 1987. doi: 10.1002/nme.1620240207.

K. Svanberg. A globally convergent version of mma without linesearch. *in: G.I.N.*

*Rozvany, N. Olhoff (Eds), Proceedings of the First World Congress of Structural and Multidisciplinary Optimization (held in Goslar, Germany)*, pages 9–16, 1995.

B. M. Tymrak, M. A. Kreiger, and J. M. Pearce. Mechanical properties of components fabricated with open-source 3-d printers under realistic environmental conditions. *Materials and Design*, 5:242–246, 2014. doi: 10.1016/j.matdes.2014.02.038.

Y. Yang, J. K. Guest, and C. D. Moen. Optimizing reinforcement layout in concrete design considering constructability. *Proceedings of the 2014 PCI Convention and National Bridge Conference, Washington, D.C., USA*, pages 1–12, 2015a.

Y. Yang, C. D. Moen, and J. K. Guest. Three-dimensional force flow paths and reinforcement design in concrete via stress-dependent truss-continuum topology optimization. *ASCE Journal of Engineering Mechanics*, 141(1):04014106, 2015b. doi: 10.1061/(ASCE)EM.1943-7889.0000819.

Y. Yang, M. Zhu, M. D. Shields, and J. K. Guest. Topology optimization of continuum structures subjected to filtered white noise stochastic excitations. *Computer Methods in Applied Mechanics and Engineering*, 2017. doi: 10.1016/j.cma.2017.06.015.

L. Yin and G. K. Ananthasuresh. Topology optimization of compliant mechanisms with multiple materials using a peak function material interpolation scheme. *Structural and Multidisciplinary Optimization*, 23(1):49–62, 2001. doi: 10.1007/s00158-001-0165-z.

BIBLIOGRAPHY

L. Yin and G. K. Ananthasuresh. Design of distributed compliant mechanisms. *Mechanics Based Design of Structures and Machines*, 31(2):151–179, 2003. doi: 10.1081/SME-120020289.

M.-F. Yu, B. S. Files, S. Arepalli, and R. S. Ruoff. Tensile loading of ropes of single wall carbon nanotubes and their mechanical properties. *Physical Review Letters*, 84(24):5552, 2000a. doi: 10.1103/PhysRevLett.84.5552.

M.-F. Yu, O. Lourie, M. J. Dyer, K. Moloni, T. F. Kelly, and R. S. Ruoff. Strength and breaking mechanism of multiwalled carbon nanotubes under tensile load. *Science*, 287(5453):637–640, 2000b. doi: 10.1126/science.287.5453.637.

M. Zhou and G. I. N. Rozvany. The coc algorithm, part ii: Topological, geometrical and generalized shape optimization. *Computer Methods in Applied Mechanics and Engineering*, 89(1):309–336, 1991. doi: 10.1016/0045-7825(91)90046-9.

J. Zhu, W. Zhang, P. Beckers, Y. Chen, and Z. Guo. Simultaneous design of components layout and supporting structures using coupled shape and topology optimization technique. *Structural and Multidisciplinary Optimization*, 36(1):29–41, 2008. doi: 10.1007/s00158-001-0165-z.

M. Zhu. *Topology Optimization of Frame Structures: Design for Constructability and Stochastic Dynamic Loads*. PhD thesis, Johns Hopkins University, 2015.

# Vita

Saranthip Koh (née Rattanaserikiat) is originally from Thailand. She received B.S. in Civil & Environmental Engineering with a minor in Engineering Management from University of Massachusetts Amherst in 2011. Upon graduation, she enrolled in the M.S./Ph.D. program at Johns Hopkins University. During her times at Hopkins, Saranthip received Hoomes Rich Fellowship and the NSF's Modeling Complex System Integrative Graduate Education and Research Traineeship. She was also awarded the Teaching Assistant Award from the Civil Engineering Department of the G.W.C. Whiting School of Engineering. Her research focuses on the development of topology optimization algorithms for constructability and manufacturability of structures, which has given her an opportunity to work with researchers at NASA Langley Research Center. Her works have been presented at conferences organized by International Society for Structural and Multidisciplinary Optimization (ISSMO), American Society of Civil Engineers (ASCE), and American Society of Mechanical Engineers (ASME).